Freie Universität Berlin

Optical simulation of complex nanostructured solar cells with a reduced basis method

Dissertation zur Erlangung des Grades
eines Doktors der Naturwissenschaften (Dr. rer. nat.)
am Fachbereich Mathematik und Informatik
der Freien Universität Berlin

von

Martin Hammerschmidt

Berlin

2015

Betreuer und Erstgutachter:
Prof. Dr. Frank Schmidt

Freie Universität Berlin
Fachbereich Mathematik und Informatik
Arnimallee 2-6
14195 Berlin

Zuse Institute Berlin
Computational Nano Optics Group
Takustraße 7
14195 Berlin

Zweitgutachter:
Prof. Dr. Bernd Rech

Technische Universität Berlin
Fakultät Elektrotechnik und Informatik
Marchstraße 23
10587 Berlin

Helmholtz-Zentrum Berlin für Materialien und Energie
Institut für Silizium-Photovoltaik
Kekuléstraße 5
12489 Berlin

Drittgutachter:
Prof. Dr. Ralf Kornhuber

Freie Universität Berlin
Fachbereich Mathematik und Informatik
Arnimallee 2-6
14195 Berlin

Datum der Disputation: 10. Juni 2016

Eidesstattliche Erklärung

Hiermit versichere ich an Eides statt, die vorliegende Arbeit selbstständig und ausschließlich unter Benutzung der angegebenen Quellen und Hilfsmittel verfasst zu haben.

Ich erkläre weiterhin, dass die vorliegende Arbeit nicht im Rahmen eines anderen Promotionsverfahrens eingereicht worden ist.

Unterschrift: _____

Datum: _____

Abstract

Simulations of optical processes and complex nanostructured devices have become omnipresent in recent years in several fields of current research and industrial applications, not limited to the field of photovoltaics. Devices or processes are optimized with respect to a certain objective where the underlying physical processes are described by partial differential equations. In photovoltaics and photonics electromagnetic fields are investigated which are governed by Maxwell's equations.

In this thesis a reduced basis method for the solution of the parameter dependent electromagnetic scattering problem with arbitrary parameters is developed. The method is developed with the specific challenges arising in optical simulations of thin-film silicon solar cells in mind. These are large in domain size and have a complex three-dimensional structure, making optimization tasks infeasible if high-accuracy of the electromagnetic field solution is required. The application of the empirical interpolation methods allows to expand an arbitrary parameter dependence affinely. Thus not only geometries, but also material tensors and source fields can be parameterized. Additionally, the required non-linear post-processing steps of the electromagnetic field to derive energy fluxes or volume absorption are addressed. The reduced basis method allows to reduce the computational costs by orders of magnitude compared to efficient finite element solvers.

In addition, an efficient tailored domain decomposition algorithm is presented to model incoherent layers or illuminations in optical systems efficiently. This is of particular interest for solar cells in superstrate configuration where the absorber is illuminated through a glass substrate.

The developed methods are employed in application examples taken from collaborations with experimentalists active in the joint lab "BerOSE"[1]. The optical model of a thin-film silicon multi-junction with incoherent light-trapping is characterized in great detail. The computational gains through hybrid, hp adaptive finite elements are studied and the incoherent domain decomposition algorithm is applied to model a more realistic light-trapping by the glass substrate.

The numerical examples of a hexagonal nano-hole array and multi-junction silicon solar cell with a tunable intermediate reflector layer show that the reduced basis method is well suited as a forward solver for modeling and optimization tasks arising in photovoltaics and photonics. Reduced models for illumination and geometric parameters are built providing up to five orders of magnitude savings in computational costs. Resonance phenomena present in the nano-hole array example are detected and the model adapts itself automatically.

---

[1]Berlin Joint Lab for Optical Simulations for Energy Research (BerOSE)

Acknowledgement

My thesis project provided me with the unique opportunity to gain insight into the theoretical aspects of the numerics research at Zuse Institute Berlin (ZIB) and its applications at the same time. In modeling and simulating solar cells I was also challenged to regard the experimental and industrial research aspects of photovoltaics through the cooperation with the Helmholtz-Zentrum Berlin für Materialien und Energie (HZB) and the industrial partner Masdar PV.

First and foremost I would like to express my sincere gratitude to my advisor Prof. Dr. Frank Schmidt for his continued support during this thesis project. He introduced me to the field of computational nanooptics and always had an open door to share his knowledge with me and to encourage and advice me when encountering difficulties.

I am deeply grateful to Dr. Daniel Lockau for sharing his knowledge and insights into the working principles of solar cells, their optical modeling and optimization during countless discussions.

I am profoundly indebted to Dr. Jan Pomplun for his advice on the theory and support in the implementation of the reduced basis method.

I would also like to express my sincere gratitude to Dr. Sven Burger and Dr. Lin Zschiedrich for their continuous willingness to debate aspects of modeling, physics and numerics. Their constructive criticism always helped to advance ideas.

I am very thankful to Prof. Dr. Christiane Becker, Dr. Bernd Stannowski and Dr. Simon Kirner of HZB and Kompetenzzentrum Dünnschicht- und Nanotechnologie für Photovoltaik Berlin (PVcomB) for the fruitful collaboration and discussions on the optics of solar cells and light trapping structures and for the material data and cell setups provided.

I thank Dr. Andreas Heidelberg, Dr. Jens-Hendrik Zollondz and Tim Frijnts from Masdar PV for the discussions on solar cell modeling and insights into the industrial applications of solar cell research.

I am very thankful to my colleague Philipp Gutsche for carefully proofreading the manuscript and his many useful remarks. I also thank Dr. Daniel Lockau, Dr. Sven Burger and Dr. Klaus Jäger for their corrections on selected chapters.

I very much enjoyed the atmosphere and countless useful discussions within the computational nanooptics group at ZIB. For this I am very thankful to the past and present members of our group including Dr. Benjamin Kettner, Dr. Benjamin Wohlfeil, Prof. Dr. Kirankumar Hiremath, Dr. Mark Blome, Carlo Barth, Maria Rozova, Phillip Manley, Sven Herrmann, Therese Blome and Xavier García Santiago who have not yet been mentioned.

Last but certainly not least, I am endlessly grateful for the unreserved support of my family over the last years. They always supported my decisions and continuously expressed interest in my work, progress and achievements.

Contents

Contents

List of Figures

List of Tables

Acronyms

μPDE parameter dependent partial differential equation. 2, 64, 66

μc-Si micro-crystalline silicon. 10, 110–112, 126, 127

a-Si amorphous silicon. 10, 110–112, 114, 125–127

ACF autocorrelation function. 18

ACL autocorrelation length. 18, 126

AFM atomic force microscopy. 16–18, 126

Ag silver. 111, 126

ARC anti-reflective coating. 14, 15, 47

AZO ZnO:Al - aluminium doped zinc oxide. 11, 15, 16, 125, 126

BZO ZnO:B - boron doped zinc oxide. 11, 16, 119, 125–127

CVD chemical vapor deposition. 17

DEIM Discrete Empirical Interpolation Method. 76

DtN Dirichlet-to-Neumann. 34

EIM Empirical Interpolation Method. 63, 64, 76–78, 90, 92, 97, 100, 105–108, 128, 129, 135, 137

EQE external quantum efficiency. 9, 16, 113, 118, 119, 139

FEM Finite Element Method. 1, 4, 19, 21, 26, 35, 37, 64, 65, 69, 88–90, 92, 96, 100, 127, 131

FFT fast Fourier transform. 18

FTO SnO_2:F - fluorine doped tin oxide. 11, 16, 17, 110, 111, 114, 115, 118, 121, 124, 125

HZB Helmholtz-Zentrum Berlin für Materialien und Energie. 3, 127, 143

Acronyms

IRL intermediate reflector layer. 125–128, 133, 136, 139–141, 144

j$_{sc}$ short-circuit current density. 9, 50, 63

MA moving average. 51, 61, 118, 121–123

MPI Message Passing Interface. 92

ODE ordinary differential equation. 64

PDE partial differential equation. 1, 2, 21, 23, 26, 35, 63–65, 143

PML Perfectly Matched Layer. 34, 35

POD Proper Orthogonal Decomposition. 56

PSD power spectral density. 18

PV photovoltaics. 7, 8, 113

PVcomB Kompetenzzentrum Dünnschicht- und Nanotechnologie für Photovoltaik Berlin. 3, 111, 127

RBM Reduced Basis Method. 2, 5, 19, 59, 63, 64, 69, 72, 77, 79, 85, 87, 91–93, 100, 124

RMS root mean squared roughness. 18, 126

SCM successive constraint method. 73

SVD Singular Value Decomposition. 56

TCO transparent conductive oxide. 10, 11, 16, 17, 119, 121, 125, 126

TFSSC thin-film silicon solar cell. 2, 5, 7, 10, 16, 17, 93, 124, 125

ZIB Zuse Institute Berlin. 152, 153

ZnO zinc oxide. 111, 126

1. Introduction

Climate change and nuclear disasters have driven governments around the world to effect change in the global energy supply. At the forefront of this development is the demand for a decarbonized and sustainable energy supply for an exponentially growing world population. Furthermore, the economic development of the newly industrializing nations has added to the demand for resources and energy. The field of green photonics summarizes efforts to address these arising global challenges by means of optical technologies. This comprises the development and use of more energy efficient light sources [Moser et al., 2014, Wolff et al., 2015], optical sensors and production technologies [Pfleging et al., 2014]. It also includes energy technologies to harvest solar energy through photovoltaic energy conversion [Stannowski et al., 2013] or artificial photosynthesis [Abdi et al., 2013].

The optical devices considered in green photonics oftentimes require the consideration of wave optical effects due to their structure sizes in the order of nanometers. Predictive numerical simulations of optical effects in nanophotonic devices are a useful tool for their design and optimization. They further allow to understand optical effects and novel devices. The simulation and modeling of these devices thus require the solution of Maxwell's equations, the set of partial differential equations (PDEs) describing electromagnetic fields.

This setting of a system whose physical properties or processes are described by a PDE is common in applied sciences and engineering applications. As solutions of these PDEs modeling temperature distributions, mechanical stresses, fluid dynamics or electromagnetic fields are analytical only in specific cases, numerical solvers rely on discretization schemes such as finite differences [Yee and Others, 1966, Taflove and Hagness, 2005], finite volumes [Hermeline, 2004], the discontinuous Galerkin [Hesthaven and Warburton, 2010, Li and Huang, 2012] or Finite Element Method (FEM) [Monk, 2003, Demkowicz, 2006]. The numerical solution of the discretized systems is generally computationally expensive as the examined devices and hence the discrete systems are growing larger in size and more complex. Oftentimes the desired numerical accuracy of the discretization schemes cannot be achieved or only part of a device is modeled as the resulting computation times might equate to hours or days.

The computational effort makes detailed numerical studies and optimizations of

systems governed by PDEs oftentimes infeasible in practical applications. Commonly the devices depend on parameters varying geometrical features such as widths or heights of structural components or other material properties. In the context of photonic devices scans over wavelength and incidence angle of the illumination sources are frequent. Typically, a large number of solutions of the parameter dependent partial differential equation (µPDE) are computed for multiple design parameters and/or configurations in these tasks. This is referred to as a *many-query* context which often arises in applications such as optimization or inverse problems like parameter estimation. In other contexts the budget for computational expenses is limited by time constraints. This is referred to as a *real-time* context. It is for example encountered in on-line process control.

Generally, the solution of the PDE itself is of lesser interest for the device optimization. Instead derived quantities of the solutions called *outputs of interest* are employed as goal functions. Hence, in many applications it is convenient to derive an *input-output relationship*. This is typically achieved by interpolation of pre-computed solutions which offers computationally inexpensive input-output relationships at the expense of neglecting the underlying physical processes as only the output data enters. We employed and compared different interpolation strategies in [Hammerschmidt et al., 2014b] for model problems from optical critical dimension metrology and solar cell modeling.

A different approach is to derive a reduced model for the µPDE by a low-dimensional approximation of the (very) high-dimensional problem. A promising strategy to be used in model order reduction is the Reduced Basis Method (RBM). It allows to split the computation in an expensive reduction step executed first and an inexpensive second phase during which solutions can be computed extremely fast. A more detailed historical review of the method is presented in Section 5.1.

1.1. Challenges in optical simulations of solar cells

In photovoltaics the need for better, more efficient devices has led to the simultaneous development of new cell concepts and a refinement of existing technologies. Especially in silicon solar cells the optics of the device are of a great importance, as silicon based solar cells suffer from insufficient absorption of the incident solar irradiation due the indirect bandgap of the absorber material. Hence, advanced cell concepts and photonic structures must be found to trap light inside the solar cell absorber. Optical simulations are indispensable in this process. However, there are a number of modeling challenges to overcome.

Rigorous optical simulations of large scale, three dimensional, complex nanostructured solar cells are computationally expensive. This especially holds for solar cells relying on light trapping provided by random textures as most thin-film silicon solar cells (TFSSCs) do. The statistical nature of the texturing of the interfaces between adjacent cell layers requires either large domains with the correct treatment of the heterogeneous exterior domains or an artificial periodification and subsequent aver-

aging over Monte Carlo samples [Lockau, 2012]. Furthermore, the vertical device structure exhibits layers and geometrical features on multiple scales. Very thin layers and tiny features on the nanometer scale are optically relevant and cannot be omitted in a discretization, one also has to account for the glass substrate which is several mm thick. This discrepancy in scale leads to high-frequency oscillations in the computed reflection which are not observed in experiments where imperfections and averaging effects are present. Additionally, neither the sun nor the experimentally used light sources provide the perfect coherent illumination fields used in models of solar cells. These incoherence effects are difficult to model and naive implementations depend on high computational effort.

All the above mentioned challenges lead to a large number of simulations to be run to predict the optical response of a solar cell in experiments accurately. Optimizations of specific layer thicknesses or feature sizes and studies of the influence of material parameters add to the already large, and possibly high-dimensional, parameter spaces considered in these tasks. Hence, reduced models are sought allowing to compute solutions to Maxwell's equations with arbitrary parameter dependencies with low computational effort. A particular challenge in this context are non-linear outputs of interest whose evaluation can be a bottleneck for large computational domains.

1.2. Thesis contribution

This thesis addresses some of the challenges in optical simulations of nanostructured solar cells presented above. It contributes a tailored domain decomposition method that in itself is suited to reduce computation times in solar cell modeling by decomposing the cell model into smaller, easier to handle subdomains. Further, this method is exploited to model incoherent layers or illuminations more efficiently. An orthogonal decomposition is employed to reduce evaluation times in computing quadratic outputs of interest.

The main contribution of this thesis is a reduced basis method for the electromagnetic scattering problem with arbitrary parameter dependencies and non-linear outputs of interest. While a previous implementation [Pomplun, 2010] was limited to geometrical parameter variations, the method presented here allows to include non-geometrical parameters varying material properties or illumination sources as well. This is essential for the modeling of solar cells. The same holds for the non-linear outputs of interest which are rarely addressed in current research where the main focus is on linear outputs.

Furthermore, the methods developed in this thesis are extensively studied in model examples motivated by the close collaboration to experimentalists from Helmholtz-Zentrum Berlin für Materialien und Energie (HZB) and Kompetenzzentrum Dünnschicht- und Nanotechnologie für Photovoltaik Berlin (PVcomB). They are designed to introduce and promote the developed mathematical tools in the application field of photonic devices. The numerical examples demonstrate the possibility to build

reduced models for geometrical and non-geometrical parameters with high-accuracy allowing to compute field enhancements in a photonic crystal or solar cell absorptance with a very dense sampling previously impractical to compute and use in optimizations. In addition, we show that a very accurate geometrical modeling of the cell topography including all layers is possible with the underlying finite element solver JCMsuite and that an incoherent domain coupling yields more realistic estimates of substrate light trapping with reasonable computational costs.

1.3. Thesis outline

This thesis is structured into five main chapters. In Chapter 2 the basic principles of the photovoltaic energy conversion are presented. The energy conversion process, its limits and the concept of multi-junction solar cells are discussed in Sections 2.1. The optical properties of silicon based solar cells are presented in Section 2.2 where the concept of light-trapping is introduced and optical modeling of silicon solar cells with randomly textured interfaces is discussed.

In Chapter 3 the mathematical background of the methods presented in this thesis is established. Results from functional analysis are recapitulated in Section 3.1. These are essential for the weak formulation of the electromagnetic scattering problem in Section 3.2. A review of Maxwell's equations and a brief introduction to the Finite Element Method are also included in this section. Section 3.3 contains a scattering matrix domain decomposition method based on a Fourier plane wave basis. A semi-analytical method for layered media is introduced in Section 3.3.4.

Chapter 4 proposes an algorithm to include incoherent layers or illumination sources into rigorous optical simulation through means of a domain decomposition approach. The principle of incoherent light and existing modeling approaches for it in the context of solar cells are reviewed in Sections 4.1 and 4.2. The proposed domain decomposition method is introduced in Section 4.3 with an orthogonal decomposition strategy to speed up computations of quadratic outputs of interest.

Chapter 5 comprises the main contribution of this thesis, a reduced basis method for optical simulations of solar cells. A historical review of the method precedes the presentation of the state-of-the-art reduced basis approximation and the self-adaptive construction of a basis in Sections 5.3 and 5.6. The specific requirements of a reduced basis method with respect to solar cell modeling, the parameterization of the electromagnetic scattering problem and the inclusion of quadratic outputs of interest, are discussed in Sections 5.5 and 5.7.

The numerical examples in Chapter 6 demonstrate the efficacy of the methods presented in this thesis. Three application examples from collaborations with experimentalists in the field of solar cell research are investigated. In Section 6.1 the reduced basis technique for Maxwell's equations is applied to a photonic crystal made of silicon exhibiting resonance phenomena in the field solution. The arising errors of the reduced basis and the empirical interpolation approximations are discussed in detail.

The remaining examples concern the simulation of multi-junction solar cells. The focus of these examples is to establish a rigorous optical modeling setting for TFSSC including incoherent light trapping. We investigate the use of our implementation for this context in Section 6.2 and discuss aspects of the modeling and discretization with finite element methods as well. The final example in Section 6.3 demonstrates the efficacy of the Reduced Basis Method for Maxwell's equation for the optimization of the optical properties of a large nanostructured thin-film silicon solar cell.

2. Photovoltaics Basics

The photovoltaic conversion of sunlight into electricity is one of the cornerstones of a sustainable energy supply for a growing world economy. The demand for renewable energy production is consistently greater than the supply. The world wide installed peak power of photovoltaics (PV) installations surpassed $170\,\mathrm{GW_p}$[1] in 2014 and more than $200\,\mathrm{GW_p}$ are estimated for 2015 [IEA, 2015]. Although these are impressive growth rates, PV still only accounts for about one percent of the world's electricity supply. In Germany 6.9% of the net electricity production in 2014 was supplied by more than 1.5 million PV installations with a peak power of $38.5\,\mathrm{GW_p}$ [Wirth, 2015]. A continued steady growth demands for higher cell efficiencies, more energy, cost and environmentally efficient production. The productions costs have been significantly reduced over the last decade, for example by employing more efficient cell designs.

This chapter introduces the fundamental physical process of photovoltaic energy conversion, cell concepts and limiting principles in Section 2.1. A detailed discussion of the optical properties of TFSSC in Section 2.2 comprising light trapping concepts and the optical modeling concludes it. Terms and challenges presented here are essential for the numerical examples presented in Chapter 6.

2.1. Physics of solar energy conversion in thin-film silicon solar cells

This sections gives a brief overview of the working principles of photovoltaics in general and silicon thin-film solar cells in particular. It starts with a brief review of the photovoltaic energy conversion and presents fundamental limits of energy conversion and the device structure of multi-junction thin-film solar cells. An in depth description can be found in many textbooks such as the well written book by Würfel [Würfel, 2009].

2.1.1. Photovoltaic energy conversion

The conversion of electromagnetic field energy to electric energy in a semiconductor works by converting to electro-chemical energy first. Energy transferred from the electromagnetic field excites bound electrons from the valence band to the conduction band of the absorber. The absence of an electron in the valence band is

---

[1] $\mathrm{W_p}$ or "watt-peak" charaterizes a the nomimal output power of a module

referred to as a *hole*. Absorption of photons with sufficient energy to bridge the energy *bandgap*

$$E_G = E_C - E_V$$

between valence and conduction band is the most important process in solar cells. In order to obtain a working PV device, these pairs of charges (the excited electron and the hole) have to be separated subsequently, otherwise they recombine and their energy is lost.

The generated electrons and holes diffuse through the material to the boundaries. Using n- and p-doped barrier layers at the contacts in a semiconductor solar cell, one can discriminate the extracted charge species. The boundary interface between the p-type and n-type layers is called a pn-junction. The different doping levels in the boundary layers imply a potential difference which drives the different species to the doped contacts: holes to p-type, electrons to n-type. In solar cell absorbers with short diffusion lengths, like amorphous silicon, this additional drift acting in the right directions improves the extraction efficiency. Several other contacting schemes have been developed, but are of lesser interest for this work as all solar cells presented herein are based on the pn-junction.

2.1.2. Efficiency limits

The electric power output $P = j \cdot V$ of a solar cell depends on its operating conditions. The relation between the current j and voltage V is described by a non-linear characteristic

$$j = j_{sc} + j_R \left(\exp\left(\frac{qV}{kT}\right) - 1 \right) \tag{2.1}$$

where q, k_B and T are the elementary charge, the Boltzmann constant and the temperature. The reverse saturation current j_R depends on diffusion lengths of electrons and holes as well as their recombination rates. The axis intersections of the current-voltage characteristic are given by the short-circuit current j_{sc} (no voltage) and the open-circuit voltage V_{oc} (no current). The open-circuit voltage is given by

$$V_{oc} = \frac{k_B T}{q} \ln\left(1 - \frac{j_{sc}}{j_R} \right). \tag{2.2}$$

The V_{oc} decreases with larger cell thicknesses.

The short circuit current is the current produced by absorbed photons. Although the incident photon exciting an electron-hole pair may carry additional energy beyond the bandgap of the material, this excess energy cannot be extracted as the carriers thermalize on much shorter time scales then they can be extracted. Hence only one pair of charge carriers can be created by every incident photon with energy beyond the bandgap. The maximal short-circuit current is thus depends only on the

number of incident photons noted as the solar photon flux density Φ. It is given by

$$j_{sc} = -e \int_{E_G}^{\infty} EQE(\lambda)\Phi(\lambda)\,\mathrm{d}\lambda \tag{2.3}$$

with the external quantum efficiency (EQE). This is the probability of an incident photon to generate an electron-hole pair and is ideally close to unity. The short-circuit current density decreases with increasing bandgap. Due to thermalization losses, the incident power is of lesser interest than the spectral photon flux Φ. It is obtained by scaling the incident power with the inverse of the photon energy $E_{ph} = \hbar\omega = 2\pi h_p c_0/\lambda$ where Planck's constant h_p enters.

The current-voltage characteristic (2.1) has a distinct operating point at which the power output P_{MPP} is maximized. It is called the maximum power point. Ideally, the fill factor

$$FF = \frac{P_{MPP}}{j_{sc}V_{oc}}$$

relating P_{MPP} and the product of j_{sc} and V_{oc} is close to one.

As the V_{oc} (2.2) depends on the short-circuit current and increases with the bandgap E_G, the bandgap of the absorber material limits the efficiency

$$\eta = \frac{j_{sc}V_{oc}FF}{P_{sun}}$$

of a solar cell. For solar irradiation under standardized conditions with the AM1.5G spectrum (cf. Section 2.2) shown in Figure 2.2 the optimal bandgaps lie between 1.1 eV and 1.5 eV with a maximum efficiency of 33.7% at 1.34 eV. This limit is known as the Shockley–Queisser limit [Shockley and Queisser, 1961]. The optimum is very broad, making crystalline silicon with E_G=1.12 eV and 29% maximum efficiency a good, although not optimal candidate for a single junction solar cell material.

A major limiting factor of the solar cell efficiency is the thermalization loss by photons with excess energy beyond the bandgap. The photon energy does not enter the formulas above which only depend on the number of photons with energies beyond the bandgap. If a collection of every photon with all of its energy was possible, 42% of the incident power could be theoretically converted.

The theoretical limit of the short-circuit current density (j_{sc}) of a crystalline silicon solar cells is $j_{sc} = 46$ mA cm^{-2} and cell records of 41.8 mA cm^{-2} have been reported for a cell with 25.6% efficiency and a V_{oc} of 740 mV [Green et al., 2015].

2.1.3. Multi-junction thin-film solar cells

To overcome the limitations of a solar cell with a single junction as assumed above, multiple cells using different absorber materials with different bandgaps can be combined. They can either be arranged side-by-side or in series behind each other. Using spectrum splitting optics such as prisms, different spectral intervals of the incident light can be focused on spatially separate cells. However, this is more expensive from
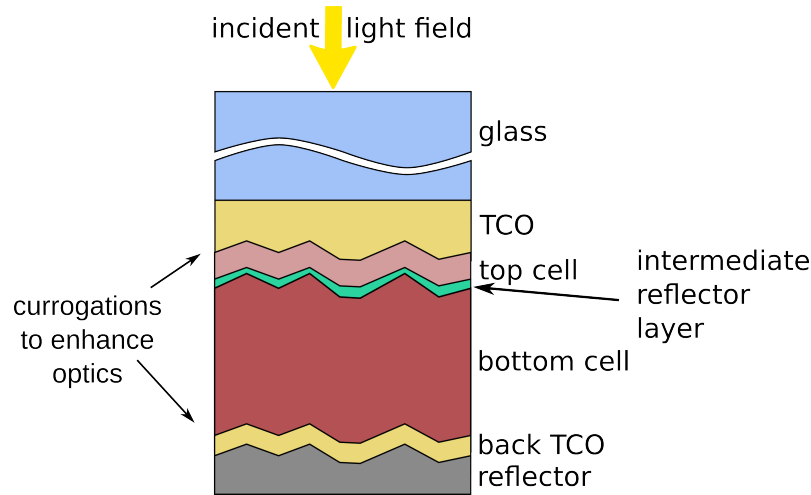
Figure 2.1.: Simplified vertical device schematic of a tandem thin-film silicon solar cell in superstrate configuration.

an engineering point of view as it requires tracking of the sun's position, than placing the subcells in series into the light path ordered by highest to lowest bandgap.

A very common combination is to combine two or three subcells. In fact, the highest ever demonstrated cell efficiency relies on a four subcell concept [Green et al., 2015]. A combination of two subcells (a *tandem* configuration) is oftentimes used to boost the efficiency of TFSSC by combining a high bandgap, thin, amorphous silicon (a-Si) top cell with a much thicker, lower bandgap, micro-crystalline silicon (μc-Si) bottom cell. This promises cell efficiencies of theoretically up to 36% [Würfel, 2009] and devices with over 12% efficiencies have been demonstrated by several groups [Green et al., 2015, Stannowski et al., 2013]. The monolithic integration of the subcells requires careful balancing of the different currents generated by the subcells under illuminations. Either they are contacted individually, which drastically increases complexity in cell design and production, or the subcells are connected in series. In this case the total current generated by the device is limited by the minimum of the currents of the subcells.

In Figure 2.1 the vertical device structure of an a-Si/μc-Si tandem cell is depicted schematically. In the shown superstrate configuration, incident light passes through the glass substrate first and is subsequently scattered by surface corrugations of the transparent conductive oxide (TCO). In this tandem configuration the thinner amorphous silicon subcell is referred to as a *top cell* and the second, microcrystalline subcell is called *bottom cell*. A back contact and reflector complete the structure. An intermediate reflector layer may also be introduced in the optical path. Apart from the glass / TCO interface all material interfaces are corrugated due to artificial or naturally occurring textures.

The electric circuit is closed by contacting front and back TCO. As the name suggests, these materials must be optically transparent but conducting. These are conflicting goals and the improvement of TCOs is challenging for material scientists.
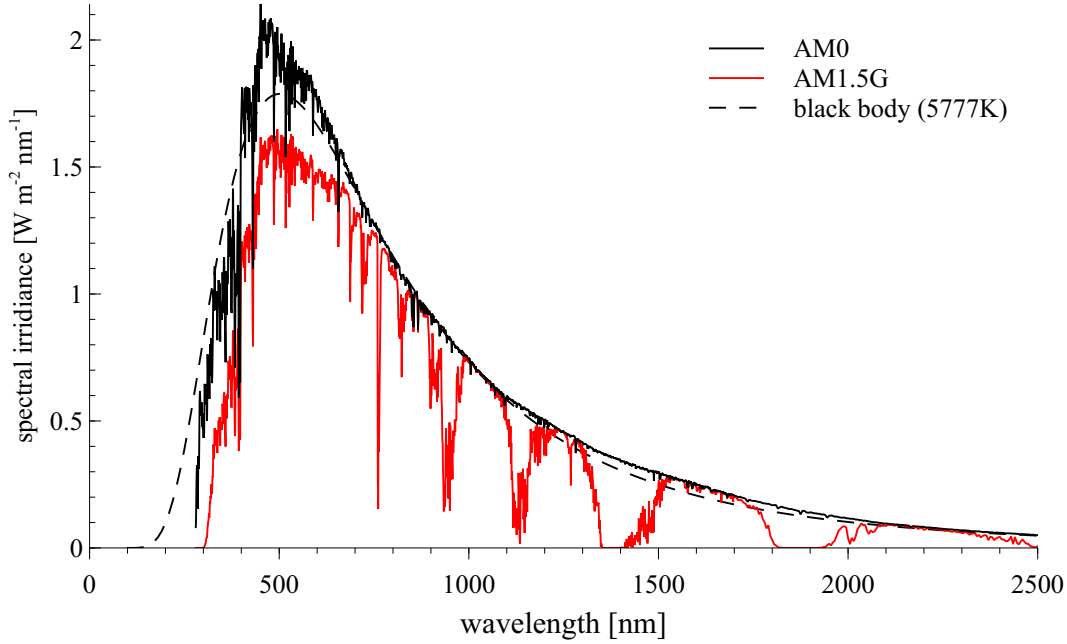
Figure 2.2.: The solar irradiance spectra AM0(black) and AM1.5G(red) have their maxima in the visible part of the spectrum around 500 nm. The AM0 spectrum [NREL, 2015] fits well to the spectrum of a black body (dashed line) at the surface temperature of the sun (T_{sun}=5777 K). The AM1.5G spectrum includes atmospheric absorption and scattering effects and thus has less power. It exhibits several distinct grooves which are related to absorption lines of atmospheric gases (mainly water vapor, carbon dioxide and nitrogen based gases).

Commonly employed TCOs are ZnO:Al - aluminium doped zinc oxide (AZO), ZnO:B - boron doped zinc oxide (BZO) and SnO_2:F - fluorine doped tin oxide (FTO).

2.2. Optics of thin-film silicon solar cells

The solar spectrum in space above the earth's atmosphere can be roughly approximated by the spectrum emitted by a black body at a temperature T_{sun}=5777 K [NASA, 2015]. At the surface of the earth the spectrum is slightly different due to scattering and absorption in the atmosphere which can be observed in Figure 2.2. A standardized spectrum AM1.5G [NREL, 2015] is used for experimental comparison and simulations which is meant to represent standard conditions in mid-latitudes. AM1.5 stands for an air mass that is 50% larger than at normal incidence corresponding to a zenith incidence of 48.2°. It corresponds to an illumination with an energy current density of 1 kWm^{-2}.

As discussed in the previous section, due to thermalization losses for solar cells the incident power is of lesser interest than the spectral photon flux. In Figure

2.3 the photon flux is shown instead of the spectral energy current density. The maximum of the photon flux is observed to be around 640 nm; red shifted compared to the maximum of the spectral energy current density in Figure 2.2. However, even beyond the visible spectrum a large number of photons are present in the spectrum and can thus contribute to the cell current if they are absorbed. The hatched area in Figure 2.3 contains half of the total number of photons below 1100 nm. This indicates, that the near infrared part of the spectrum can contribute substantially to the photo current in a silicon solar cell. The bandgap position of amorphous silicon (indicated by the vertical black line) is very close to the median of this photon distribution, which motivates the popular choice of a-Si as a high-bandgap material in thin-film silicon tandem configurations.
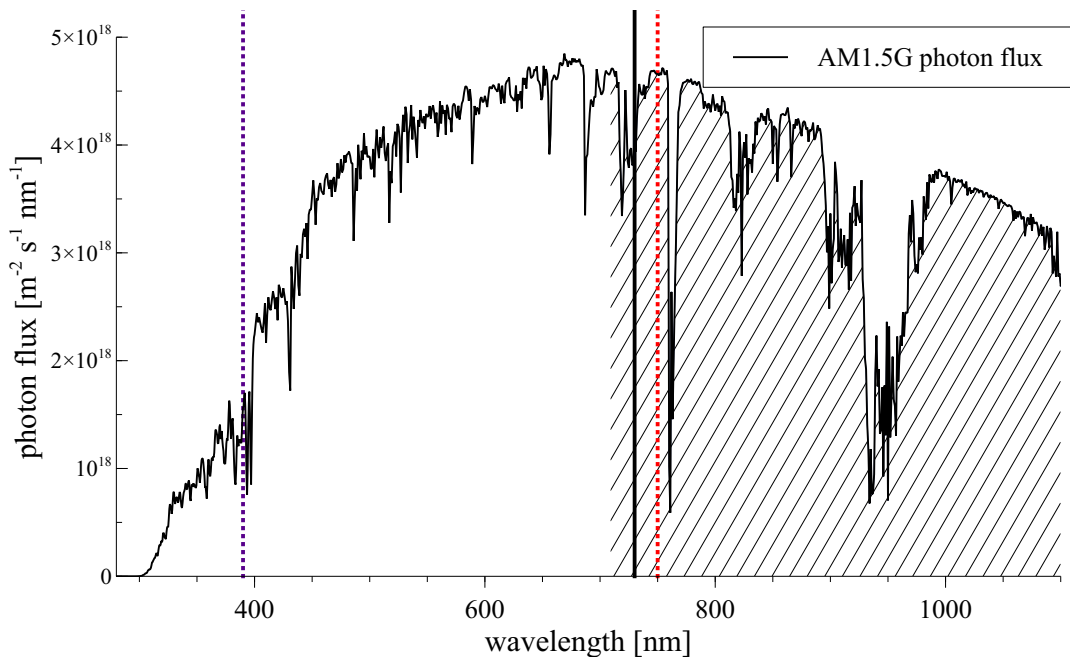
Figure 2.3.: The spectral photon flux corresponds to the number of solar photons included in the AM1.5G spectrum (black line). It is shown up to the band edge of silicon at 1100 nm. In contrast to the irradiance spectrum in Figure 2.2, the maximum is slightly red shifted and broader. As guidance to the eye the limits of the visible spectrum are marked as dotted lines (violet and red). The hatched area contains 50% of the photons with energies larger than the band edge of silicon. The vertical black line marks the band edge of amorphous silicon (assumed to be 1.7 eV).
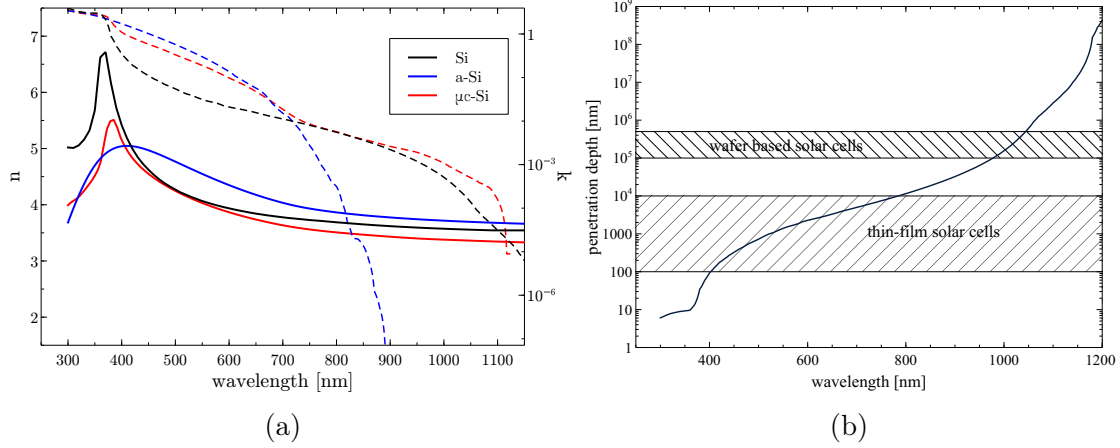
Figure 2.4.: (a): Real (solid lines) and imaginary part (dashed lines) of the refractive index of crystalline (black), amorphous (blue) and microcrystalline silicon (red). Data provided by PVcomB. (b): The black line shows the penetration depth of incident light in crystalline silicon for wavelengths of interest. The hatched areas mark typically used absorber thicknesses in wafer and thin-film technologies. The absorber thicknesses employed in wafer cell concepts are sufficient to absorb nearly all the light in a single pass up to 1100 nm wavelength. In thin-film devices the absorber thicknesses are insufficient to absorb photons of wavelength larger than 700-800 nm in a single pass.

2.2.1. Light trapping

An ideal solar cell absorbs all incident photons in the absorber layer. Intensity decays according the exponential Lambert-Beer law

$$I(d) = I_0 \exp\{-\alpha d\}. \tag{2.4}$$

One of the most widely used absorber materials is silicon [Wirth, 2015]. Its abundance in the earths crust (second only to oxygen) and non-toxicity make it the most viable option to base a renewable world energy supply on [Saga, 2010]. In contrast to other absorber materials, such as GaAs or InP, which are direct semiconductors, silicon is an indirect semiconductor. Thus it exhibits relatively poor absorption of photons whose energy is close to the band edge. The result is a relatively poor absorption efficiency. In Figure 2.4a the real (solid line) and imaginary part (dashed line) of the refractive indices of crystalline (black), amorphous (blue) and microcrystalline silicon (red) is shown. Note the logarithmic scale for the imaginary parts.

Figure (2.4b) depicts the penetration depth

$$d_{pen} = \frac{1}{\alpha} = \frac{\lambda}{4\pi \, \mathfrak{Im}\,\{n\}}$$

(where n is the refractive index) of the incident photons in crystalline silicon. This quantity is derived from (2.4) and measures the depth an electromagnetic field can reach as its intensity decays to $1/e$. The penetration depth in silicon increases by orders of magnitude over the spectrum. Typically employed absorber thicknesses (indicated as hatched areas) are insufficient to absorb all of the incident photons. Especially in the near infrared this severely limits the short-circuit current density as there still are a large number of photons in the spectrum (cf. discussion in the previous section). This imperfect absorption makes management of the incident light a key issue in solar cell optimization. The objective is to enhance the optical path of the incident light as much as possible in order to have similar absorption as in much thicker absorbers. An obvious improvement is the introduction of a back reflector designed to reflect light reaching the back side of the absorber layer back into it. Thus the path length of the light effectively doubles.

Although the use of planar slabs as absorbing layers is beneficial for the electrical properties, they are not optimal for the optics of the solar cell. The high refractive index $n \in [3.5, 7)$ of silicon leads to large reflection losses in excess of 30% in bare planar slabs. It also allows for light to be *trapped* inside the absorber layer by total internal reflection due to contrast in refractive indices between the absorber material and air. Anti-reflective coatings (ARCs) based on index matching or destructive interferences can be used to reduce reflection losses. Perfect transmission for a single wavelength can be achieved for a coating with thickness $d = \lambda/4$, but for a broad spectrum multiple layers have to be used, rendering the ARC much more complex. Furthermore, the anti-reflection effect works in both directions and hence light cannot be trapped any more as it is easily out-coupled.

A similar effect anti-reflection effect can be achieved through corrugations of the absorber layer. In addition, these corrugations scatter light away from the incidence angle, thus increasing the light path within the absorber layer. A study of scattering and non-scattering anti-reflection designs can be found in [Lockau et al., 2014b]. A plethora of different concepts and structures to scatter and trap light efficiently within the absorber layer have been presented. Figure 2.5 (ii-iv) depicts some concepts that are commonly discussed in addition to the discussed anti-reflective coating in Figure 2.5 (i):

periodic scatterers A periodic nano-structuring, such as a grating, scatters light very efficiently into discrete angles and allows to focus light into specific spatial regions. The list of possible structures comprises a number of different 1D and 2D gratings, i.e. binary, blazed and sinusoidal gratings or arrays of scatterers such as (inverted) pyramids and nanowires [Zeng et al., 2006, Krč et al., 2011, Čampa et al., 2009, Yu et al., 2010a, Mavrokefalos et al., 2012, Christesen et al., 2012, Schmitt et al., 2012, Kowalczewski et al., 2013, Paetzold, 2013, Lockau et al., 2014b, Lockau et al., 2014c, Becker et al., 2014].

random scatterers A random or disordered nano-texturing scatters an incident light beam into a continuum of angles. The randomization of the interface angles leads to broadband anti-reflection and scattering effects. The shape
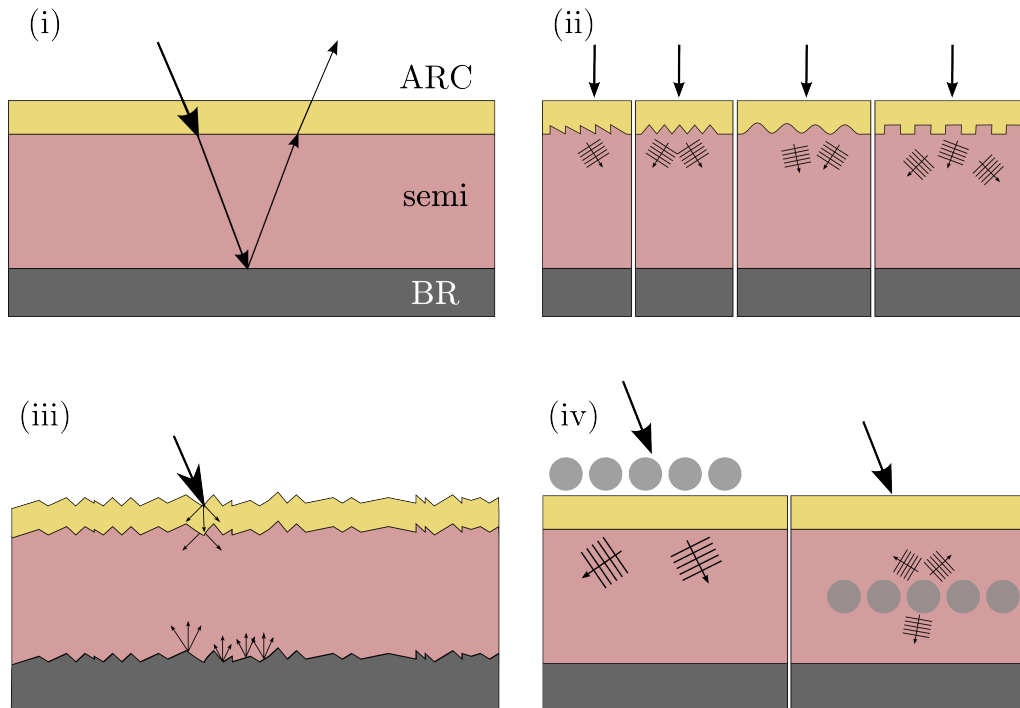
Figure 2.5.: Schematics of four different light-management concepts employed in solar cell research. *(i)* An anti-reflective coating can be employed to reduce reflections and a back reflector doubles the light path inside of the semiconductor absorber layer. *(ii)*: Periodic textures scatter incident light into discrete angles. The unit cell shape and period may vary. *(iii)*: A random texture scatters light into a variety of angles accepting incident light from all angles. *(iv)*: (Metallic) nano-particles allow for tailored light-scattering at the front of the solar cell absorber or scatter light and enhance optical near-fields inside the absorber layer.

of the texture may range from densely packed, high-aspect ratio, needle-like structures (black silicon) to much larger, etched craters in AZO [Yablonovitch, 1982, Campbell and Green, 1987, Krč et al., 2003, Koynov et al., 2006, Fahr et al., 2011, Ferry et al., 2011, Jovanov et al., 2013].

nano-particles Nano-scale particles at the interface of an absorber have a scattering effect as well. Tailoring size and shape, the scattering can be directed as well. Metallic nano-particles within the absorber layer scatter light and can lead to an enhanced plasmonic near-field in the vicinity of the particle which leads to absorption enhancements [Schaadt et al., 2005, Fahr et al., 2009, Deceglie et al., 2012, Schmid et al., 2014, Schmid and Manley, 2014].

The design and optimization of nano-photonic scattering structures for light-management is a field of intense research and many different light-trapping concepts have been investigated both experimentally and theoretically. This intense work has

led to the derivation of theoretical limits for light-path or absorption enhancements different concepts. A review of these can be found in [Sprafke and Wehrspohn, 2012]. The most important limit being the *geometric limit* derived by Yablonovitch [Yablonovitch, 1982] which is often named in his honor. Assuming a scattering surface with ideal diffuse (or Lambertian) scattering properties, weak-absorption in a slab much thicker than the incident wavelength and a perfect reflector, the light-path can be enhanced by a factor of at most

$$\alpha_{Yab} = 4n^2$$

where n is the real part of the refractive index. There are multiple possibilities to derive this limit without using the wave characteristics of light, hence the name geometric limit. For grating structures and very thin absorber layers, absorption enhancements can exceed this limit by a factor of π [Yu et al., 2010b] through coupling to high-quality resonances with high intensities. By accepting light from the entire half-space, but restricting the emission cone of light to a very small solid angle Θ, the absorption enhancement factor is

$$\alpha_{e_{cone}} = \frac{4n^2}{\sin^2(\Theta)}.$$

In [Sprafke and Wehrspohn, 2012] this is referred to as "ultra-light trapping".

Several light-trapping concepts have been demonstrated with the promise to exceed the geometrical limit experimentally. Only a handful of them are industrially viable or compatible with current manufacturing techniques. The industry standard as of 2015 for (tandem) TFSSCs is still the use of a randomly textured TCO. Out of the above mentioned candidate materials, BZO and etched AZO provide light-scattering superior to FTO.

2.2.2. Optical modeling

The efficiency considerations in Section 2.1.2 rely to great extend on the short-circuit current density in (2.3) which is the integral over the EQE weighted with spectral solar photon flux. In solar cell optimization the wavelengths resolved EQE is often used as a figure of merit instead. The EQE measures the probability of an incident photon at a specific energy to be collected as a charge carrier pair at the contact. Optical simulations allow to compute the cell absorptance and to estimate the EQE of a solar cell assuming perfect carrier collection, i.e. neglecting all electrical loss mechanisms. Figures 6.15 and 6.16 show simulated EQE curves and absorptance plots.

Underlying all considerations in this work is a fully parameterized optical solar cell model. This model builds on the work presented in [Lockau, 2012]. The model is based on measured data wherever applicable, for example refractive indices and geometric parameters such as thicknesses and textures measured by atomic force

microscopy (AFM). The thin-film solar cells in superstrate configuration are modeled as layered media stacks with different cell domains separated by arbitrary interface textures. This emulates the production of solar cells by chemical vapor deposition (CVD) where cell layers are deposited in sequence on top of each other, starting with a substrate layer. In all examples presented in this work the substrate is FTO on glass, but other TCOs can be and have been considered as well. A specialized meshing pipeline for these geometries, as presented in great detail in [Lockau, 2012], is used to generate the geometrical models of the TFSSCs. For more general, three-dimensional, nano-photonic structures other meshing tools are more suitable and have been employed to generate for example the meshes in Section 6.1.

Approximate methods have been successfully employed to account for random textures in solar cells for years [Leblanc et al., 1994, Krč et al., 2003, Jäger et al., 2012, Jäger, 2012]. Rigorous treatments however are a more recent phenomenon [Rockstuhl et al., 2007, Lockau, 2012, Isabella et al., 2014, Jäger et al., 2015] with the major restrictions being computation time and domain sizes. The modeled tandem solar cells have a randomly rough interface texture which extends over several cm^2 before being separated by electric circuits in the real world. However, incident light does not propagate to the limits of the absorber layer but will be absorbed within (possibly many) micrometers of absorber materials. These lateral dimensions still push the the boundaries of current computing capabilities for rigorous Maxwell solvers if modeled as an isolated domain. For modeling purposes and especially for experimental comparability, it is crucial to account for light being scattered across the lateral boundaries of the computational domain. Commonly periodic boundary conditions are employed to serve as artificial boundary conditions at the lateral boundaries of the computational domains. Thus, light scattered out of one boundary re-enters on the opposite side. The random, infinitely extended texture is thus restricted to a periodic unit cell with small lateral dimensions in the range of a few micrometers [Lockau et al., 2013]. A Monte-Carlo sampling over several of these unit cells generally provides reasonable approximations of the solar cell optics.

We employ different methods to include random textures into periodic unit cells:

- periodification of AFM data,

- mirroring of AFM data,

- generation of synthetic data with similar statistics.

Each of these methods has drawbacks. The substrate roughness can be directly investigated by means of AFM which provides the basis for all methods. The random structure of the substrate texture prohibits the direct use of measured AFM data as an interface texture in periodic setups. Periodification of patches taken from AFM data at the domain sizes suitable for 3D simulations may lead to distortions of the surface morphology in these smaller patches. Mirroring of smaller patches along x and y axis yields periodic patches by design, but may also introduce rims and ridges along the mirror axis. However, this method allows to model larger unit cells,

provided the illumination shares the same symmetry. This is the case for most solar cell simulations where normally incident light is used.

The morphologic statistics derived from AFM data allow to generate synthetic textures based on height autocorrelation length (ACL) and root mean squared roughness (RMS). These are derived from a radial fit of the (height) autocorrelation function (ACF)

$$\gamma(f; \boldsymbol{d}) = \frac{\int_{\mathbb{R}^2} f(\boldsymbol{r}) f(\boldsymbol{r} + \boldsymbol{d}) \, \mathrm{d}\boldsymbol{r}}{\sigma^2} \tag{2.5}$$

where $\boldsymbol{d} \in \mathbb{R}^2$ and $f : \mathbb{R}^2 \to \mathbb{R}$ is a height distribution with variance σ^2. It can be efficiently computed via fast Fourier transform (FFT) if f is periodic or periodified. Assuming the height distribution is isotropic, it can be represented by a radial ACF with only a distance variable d. Fitting the radial formulation of (2.5) by a Gaussian distribution

$$\gamma(d; \sigma_{RMS}, L_{ACL}) = \sigma_{RMS}^2 \exp\left(\frac{3}{2}\left(\frac{d}{L_{ACL}}\right)^2\right), \tag{2.6}$$

defines the ACL parameter L_{ACL} and the RMS parameter σ_{RMS}. This information is readily available for a variety of morphologies. Some authors use other constants or exponents in the exponential, leading to different definitions of the autocorrelation length.

As the ACF is related to the power spectral density (PSD) (Wiener-Khinchin theorem, [Goodman, 2000])

$$\gamma(f; \boldsymbol{d}) = \int_{\mathbb{R}^2} \frac{\hat{f}^{\mathsf{T}}(\boldsymbol{k}) \hat{f}(\boldsymbol{k})}{\sigma^2} e^{i\boldsymbol{k}\cdot\boldsymbol{d}} \, \mathrm{d}\boldsymbol{k} = \int_{\mathbb{R}^2} PSD(\boldsymbol{k}) e^{i\boldsymbol{k}\cdot\boldsymbol{d}} \, \mathrm{d}\boldsymbol{k},$$

we can use it to generate a random distribution with the same ACF by introducing random phases in the inverse transform

$$z(\boldsymbol{r}) = FFT^{-1}\left(\sigma_{RMS}\sqrt{PSD(\boldsymbol{k})} e^{i\phi_{rand}}\right).$$

This technique and is described in detail in [Wu, 2000] and applied to solar cell modeling [Lockau et al., 2011, Lockau, 2012, Hammerschmidt et al., 2013]. It also allows for a controllable variation of surface statistic parameters which was used in [Kirner et al., 2014].

3. Mathematical Basics

The following chapter reviews the mathematical basis required for the formulation and the solution of Maxwell's equations with the Finite Element Method and the theoretical understanding and analysis of the Reduced Basis Method presented in Chapter 5. We start with a summary of the necessary definitions and results from functional analysis in Section 3.1. This comprises the concept of Hilbert spaces, the variational formulation and the function spaces used in this thesis. In Section 3.2 we review Maxwell's equations as the fundamental set of equations modeling light-matter interaction in thin-film solar cells and photonic nanostructures. The electromagnetic scattering problem and its weak formulation, the discretization with finite elements and appropriate boundary conditions are presented in this context. A few remarks in Section 3.3 on domain decomposition methods focused on the concepts used in Chapter 4 conclude this chapter.

3.1. Functional analysis

The introduction of the electromagnetic scattering problem and its solution with finite elements requires terms, concepts and notations from functional analysis. Specifically Hilbert and Sobolev spaces and their properties are required to describe and solve Maxwell's equations numerically. A comprehensive introduction to functional analysis is found in [Werner, 2011] where the following definitions are adapted from.

3.1.1. Hilbert spaces

The definition of a $\mathbb{K}$-Hilbert space over a field $\mathbb{K} = \mathbb{C}$ or $\mathbb{K} = \mathbb{R}$ requires some preliminary work. We recall the definitions of a norm $\|\cdot\|_X$ and a normed vector space $(X, \|\cdot\|_X)$:

Definition 3.1 (Norm). Let X be a $\mathbb{K}$-vector space. A function

$$\|\cdot\|_X : X \to [0, \infty)$$

is called **norm**, if the following axioms are satisfied $\forall x, y \in X$ and $\forall \lambda \in \mathbb{K}$:

(i) $\|\lambda x\|_X = |\lambda| \|x\|_X$,

(ii) $\|x + y\|_X \leq \|x\|_X + \|y\|_X$,

(iii) $\|x\|_X = 0 \Rightarrow x = 0$.

The pair $(X, \|\cdot\|_X)$ is called a **normed vector space**.

For any $x, y \in X$ a metric $d(x,y) = \|x - y\|_X$ is induced by this norm. This allows for a definition of sequences and terms like convergence. For a Hilbert space we need the concept of a complete space:

Definition 3.2 (Complete normed spaces). A normed space X in which all Cauchy sequences converge is called **complete** or **Banach space**.

Furthermore we require an additional map to be defined on the vector space X

Definition 3.3 (Inner product). Let X be a $\mathbb{C}$-vector space. A map

$$(\cdot, \cdot)_X : X \times X \to \mathbb{K}$$

is called **inner product** or **scalar product**, if the following axioms are satisfied $\forall x, y, z \in X$ and $\forall \lambda \in \mathbb{K}$:

(i) $(x + y, z)_X = (x, z)_X + (y, z)_X$,

(ii) $(x, \lambda y)_X = \lambda (x, y)_X$,

(iii) $(x, y)_X = \overline{(y, x)_X}$,

(iv) $(x, x)_X \geq 0$,

(v) $(x, x)_X = 0 \iff x = 0$,

where the bar denotes complex conjugation. The pair $(X, (\cdot, \cdot)_X)$ is called an **inner product space**.

We call two elements of X **orthogonal** if $(x, y)_X = 0$. These definitions combined define a Hilbert space:

Definition 3.4 (Hilbert space). A normed vector space $(X, \|\cdot\|_X)$ is called *pre-Hilbert space*, if an inner product $(\cdot, \cdot)_X : X \times X \to \mathbb{K}$ with $(x, x)_X = \|x\|_X \quad \forall x \in X$ exists. A complete pre-Hilbert space is called **Hilbert space**.

We recall some properties of linear operators mapping a Hilbert space X to another Hilbert space Y. Particularly, the case of $Y = \mathbb{K}$ is of interest.

Definition 3.5 (Dual space). Let X be a $\mathbb{K}$-Hilbert space. The space of all bounded / continuous linear maps $\cdot : X \to \mathbb{K}$ is called the **dual space** and denoted X'. Its elements are **bounded/continuous linear functionals**. With

$$(cF)(x) = cF(x)$$
$$(F + G)(x) = F(x) + G(x)$$

for $F, G \in X', x \in X, c \in \mathbb{K}$ and the **dual norm** $\|\cdot\|_{X'}$ given by

$$\|F\|_{X'} = \sup_{x \in X} \frac{|F(x)|}{\|x\|_X},$$

X' is a Banach space. $F(x)$ is oftentimes shortened to Fx.

Remark. As both X and $\mathbb{K}$ are normed spaces, continuity and boundedness of $F \in X'$ are equivalent (cf. [Werner, 2011] Theorem II.1.2).

The following theorem allows to identify elements of the space X' with elements of the Hilbert space X and vice versa.

Theorem 3.6 (Riesz representation theorem). *For each $F \in X'$, there exists a unique $f \in X$ such that*
$$F(x) = (f, x)_X \quad \forall x \in X.$$

*Furthermore, $\|F\|_{X'} = \|f\|_X$ holds. We call f the **Riesz representation** of F.*

Corollary 3.7 (Riesz representer of anti-linear form). *The Riesz representer of an anti-linear form F, that is*

$$F(x + y) = F(x) + F(y),$$
$$F(\lambda x) = \overline{\lambda} F(x),$$

is a unique $f \in X$ such that

$$F(x) = (x, f)_X \quad \forall x \in X.$$

Proof. $G(x) = \overline{F(x)}$ is a linear form, hence Theorem 3.6 applies. The Definition 3.3 (iii) of the inner product yields the result. □

3.1.2. Variational formulation

The Finite Element Method presented in Section 3.2.4 requires the partial differential equation to be stated in weak form. This variational formulation is based on bilinear or sesquilinear forms.

Definition 3.8 (Sesquilinear form). Let X be a $\mathbb{K}$ Hilbert space. A mapping

$$a(\cdot, \cdot) : X \times X \to \mathbb{K}$$

is called **bilinear** ($\mathbb{K} = \mathbb{R}$) or **sesquilinear** ($\mathbb{K} = \mathbb{C}$) **form**, if $\forall x, y, z \in X, \forall \lambda, \mu \in \mathbb{K}$

$$a(\lambda x + \mu y, z) = \overline{\lambda} a(x, z) + \overline{\mu} a(y, z)$$
$$a(x, \lambda y + \mu z) = \lambda a(x, y) + \mu a(x, z)$$

3. Mathematical Basics

Definition 3.9 (continuity, coercivity)**.** A sesquilinear form $a(\cdot, \cdot)$ on a normed space X is

(*i*) **bounded** or **continuous** if there exists a constant $\mathbb{R}^+ \ni \gamma < \infty$ such that

$$|a(x, y)| \leq \gamma \|x\|_X \|y\|_X \quad \forall x, y \in X. \tag{3.1}$$

The smallest constant γ satisfying (3.1) is called the **continuity constant** of a.

(*ii*) **coercive** if there exists a constant $\mathbb{R}^+ \ni \alpha > 0$ such that

$$|a(x, x)| \geq \alpha \|x\|_X^2 \quad \forall x \in X. \tag{3.2}$$

The largest constant α satisfying (3.2) is called the **coercivity constant** of a.

(*iii*) **hermitian** or **symmetric** if:

$$a(x, y) = \overline{a(y, x)} \quad \forall x, y \in X.$$

In the following, we focus on sesquilinear forms on $\mathbb{C}$-Hilbert spaces as they are required for the variational formulation of Maxwell's equation later on. The results for bilinear forms hold analogously. We will make use of the following properties:

Corollary 3.10. *Let $a(\cdot, \cdot)$ be a bounded sesquilinear form. There exists a unique bounded linear operator $T : X \to X$ such that*

$$a(x, y) = (T(x), y)_X \quad \forall x, y \in X.$$

The operator norm of T is the continuity constant $y > 0$ satisfying (3.1).

Proof. For every $x \in X$ $a(x, \cdot)$ is a linear, bounded functional and according to Theorem 3.6 we can find the Riesz representer $A_x \in X$ such that $a(x, y) = (A_x, y)_X \quad \forall x \in X$. We define $T(x) := A_x$. The operator norm of T is

$$\|T\| = \sup_{x \in X} \frac{\|T(x)\|}{\|x\|} = \sup_{x \in X} \frac{\|a(x, \cdot)\|_{X'}}{\|x\|} = \sup_{x \in X} \sup_{y \in X} \frac{a(x, y)}{\|x\| \|y\|} = \gamma$$

where we used $\|T(x)\| = \|a(x, \cdot)\|_{X'}$. $\qquad \square$

We now turn to variational problems given by sesquilinear forms. The prototype of such a problem is the following:

Problem 1. Let $a(\cdot, \cdot)$ be a bounded, coercive sesquilinear form on a Hilbert space X and $f \in X'$. Find $u \in X$ such that

$$a(u, v) = f(v) \quad \forall v \in X \tag{3.3}$$

The following lemma states the existence and uniqueness of solutions of Problem 1.

Lemma 3.11 (Lax-Milgram). *Let X be a Hilbert space. Suppose $a(\cdot,\cdot) : X \times X \to \mathbb{C}$ is a bounded, coercive sesquilinear form. Then for each $f \in X'$ there exists a unique solution $u \in X$ to (3.3) and*

$$\|u\|_X \leq \frac{\gamma}{\alpha}\|f\|_{X'},$$

where γ and α are the continuity and coercivity constants.

This famous Lax-Milgram lemma (also known as Lax-Milgram theorem) relies on the coercivity of the sesquilinear form $a(\cdot,\cdot)$. A generalization of this lemma for non-coercive sesquilinear forms uses the inf-sup constant β instead.

Definition 3.12 (Inf-sup constant). Let $a(\cdot,\cdot)$ be a sesquilinear form on a normed space X. The **inf-sup constant** β of $a(\cdot,\cdot)$ is given by

$$\beta = \inf_{x \in X} \sup_{y \in X} \frac{|a(x,y)|}{\|x\|_X \|y\|_X}.$$

$a(\cdot,\cdot)$ satisfies the **Babuška-Brezzi condition**, if $\beta > 0$.

With the Babuška-Brezzi condition the existence and uniqueness of solutions to Problem 1 can be extended to non-coercive sesquilinear forms.

Lemma 3.13 (Generalized Lax-Milgram). *Let X be a Hilbert space. Suppose $a(\cdot,\cdot) : X \times X \to \mathbb{C}$ is a bounded sesquilinear form which satisfies the Babuška-Brezzi condition. Then for each $f \in X'$ there exists a unique solution $u \in X$ to (3.3) and*

$$\|u\|_X \leq \frac{\gamma}{\beta}\|f\|_{X'},$$

where γ and β are the continuity and inf-sup constants of $a(\cdot,\cdot)$, respectively.

3.1.3. Function spaces

The variational formulation of Maxwell's equation involves Sobolev spaces of scalar and vector valued functions. These are an important class of Hilbert spaces of particular interest for the solution of PDEs in weak form. Before turning to Sobolev spaces, we recall some results on integration which always refers to Lebesque integration on $\Omega \subseteq \mathbb{R}^n$.

L^p **spaces** We define the space of p-integrable functions $\mathcal{L}^p(\Omega)$ as

$$\mathcal{L}^p(\Omega) := \left\{ f : \Omega \to \mathbb{K}, f \text{ measurable}, \int_\Omega |f(\boldsymbol{r})|^p \, \mathrm{d}\boldsymbol{r} < \infty \right\}, \quad 1 \leq p < \infty$$

$$\|f\|_{\mathcal{L}^p(\Omega)}^* := \left(\int_\Omega |f(\boldsymbol{r})|^p \, \mathrm{d}\boldsymbol{r} \right)^{1/p}, \quad f \in \mathcal{L}^p(\Omega)$$

3. Mathematical Basics

The case $p = \infty$ is defined in the following sense:

$$\mathcal{L}^\infty(\Omega) := \left\{ f : \Omega \to \mathbb{K}, f \text{ measurable}, \|f\|^*_{\mathcal{L}^\infty(\Omega)} < \infty \right\}$$

$$\|f\|^*_{\mathcal{L}^\infty(\Omega)} := \operatorname{ess\,sup} f = \inf_{c \in \mathbb{R}} \left\{ |f| < c \text{ almost everywhere } \right\}$$

$\|f\|^*_{\mathcal{L}^p(\Omega)}$ is only a semi-norm on $\mathcal{L}^p(\Omega)$ as $\forall f \in N : \|f\|^*_{\mathcal{L}^p(\Omega)} = 0$ where

$$N := \{ f \mid f = 0 \text{ almost everywhere } \}.$$

In the quotient space

$$L^p(\Omega) := \mathcal{L}^\infty(\Omega)/N$$

functions f and g are identified if $f - g = 0$ almost everywhere. Elements of $L^p(\Omega)$ are equivalence classes $[f]$ of functions f. We may chose a single representation of a class to represent it whenever the result does not depend on the specific choice of the representation.

All $L^p(\Omega), 1 \le p \le \infty$ are Banach spaces, but only the space of square-integrable functions $L^2(\Omega)$ is a Hilbert space. In $L^2(\Omega)$ we have the inner product

$$(u, v)_{L^2(\Omega)} = \int_\Omega \overline{u(\boldsymbol{r})} v(\boldsymbol{r}) \, \mathrm{d}\boldsymbol{r} \tag{3.4}$$

with the associated norm

$$\|u\|_{L^2(\Omega)} = \left((u, u)_{L^2(\Omega)} \right)^{1/2} = \left(\int_\Omega |u(\boldsymbol{r})|^2 \, \mathrm{d}\boldsymbol{r} \right)^{1/2}.$$

Sobolev spaces The definition of Sobolev spaces relies on the concept of weak derivatives. Before introducing their definition we note another function space and introduce the multi-index notation $\alpha = (\alpha_1, \ldots, \alpha_n)^\intercal \in \mathbb{N}$ with $|\alpha| = \sum_{i=1}^n \alpha_i$. This abbreviates the notation of the derivative of a function $v : \Omega \to \mathbb{K}$:

$$D^\alpha v = \partial_{x_1}^{\alpha_1} \partial_{x_2}^{\alpha_2} \cdots \partial_{x_n}^{\alpha_n} v$$

Definition 3.14 (Continuously differentiable functions). We denote

$$\mathcal{C}^k(\Omega) = \{ v \in \mathcal{C}(\Omega) \mid D^\alpha v \in \mathcal{C}(\Omega), |\alpha| \le k \in \mathbb{N} \}$$

the set of k times continuously differentiable functions $\phi : \Omega \to \mathbb{R}$ with compact support in Ω. We call $C_0^\infty(\Omega)$ the set of **test functions**.

Definition 3.15 (Weak derivative). Let $u \in L^1(\Omega)$. We call $w \in L^1(\Omega)$ satisfying

$$\int_\Omega \overline{u} D^\alpha v \, \mathrm{d}\boldsymbol{r} = (-1)^{|\alpha|} \int_\Omega \overline{w} v \, \mathrm{d}\boldsymbol{r} \quad \forall v \in \mathcal{C}_0^\infty(\Omega)$$

the **weak αth partial derivative** of u.

If w exists, it is uniquely determined and we write $D^\alpha u := w$. The existence of (weak) partial derivatives gives rise to the definition of Sobolev spaces.

Definition 3.16 (Sobolev space)**.** The Sobolev space $W^{k,p}$ is defined as

$$W^{k,p} := \{u \in L^p(\Omega) \,|\, D^\alpha u \in L^p(\Omega) \quad \forall \alpha \in \mathbb{N}^n \text{ with } 0 \le |\alpha| \le k\}\,.$$

We abbreviate $W^{k,2} = H^k(\Omega)$ and note that

$$(u,v)_{H^k(\Omega)} = \sum_{|\alpha| \le k} \int_\Omega \overline{D^\alpha u} D^\alpha v \,\mathrm{d}\boldsymbol{r}$$

is a scalar product on $H^k(\Omega)$ which induces the norm

$$\|u\|_{H^k(\Omega)} = \left(\sum_{|\alpha| \le k} \int_\Omega \overline{D^\alpha u} D^\alpha u \,\mathrm{d}\boldsymbol{r} \right)^{1/2}\,.$$

The existence of the scalar product distinguishes $H^k(\Omega)$ from the Banach spaces $W^{k,p}(\Omega)$, making it a Hilbert space.

H(curl,Ω) spaces The solution of Maxwell's equations are vector fields in $\mathbb{R}^3$ thus we need to extend the concepts of Sobolev spaces from scalar to vector valued functions. This poses no problem as the definition of the L^2 inner product (3.4) easily extends to vectorial functions. For $\boldsymbol{u} = (u_1, u_2, u_3)^\mathsf{T} \in (L^2(\Omega))^3$ and $\boldsymbol{v} = (v_1, v_2, v_3)^\mathsf{T} \in (L^2(\Omega))^3$ (3.4) becomes

$$(u,v)_{(L^2(\Omega))^3} = \int_\Omega \sum_{i=1}^3 \overline{u_i} v_i \,\mathrm{d}\boldsymbol{r}$$

and similarly the norm

$$\|u\|_{(L^2(\Omega))^3} = \left((u,u)_{(L^2(\Omega))^3} \right)^{1/2}\,.$$

In Maxwell's equations we find the differential operators $\nabla\times$ and $\nabla\cdot$ acting on three-dimensional vectorial functions which are defined as

$$\mathbf{curl}\ \boldsymbol{u} = \nabla \times \boldsymbol{u} = (\partial_{x_2} u_3 - \partial_{x_3} u_2, \partial_{x_3} u_1 - \partial_{x_1} u_3, \partial_{x_1} u_2 - \partial_{x_2} u_1)^\mathsf{T}$$

and

$$\mathbf{div}\ \boldsymbol{u} = \nabla \cdot \boldsymbol{u} = \sum_{i=1}^3 \partial_{x_i} u_i$$

for $\boldsymbol{u} \in (L^2(\Omega))^3$ with weak partial derivatives.

This allows to define the following Hilbert space which we will employ in solving Maxwell's equations numerically.

Definition 3.17 (H(**curl**,Ω))**.** We define the space of three-dimensional vectorial functions $\boldsymbol{u} \in (L^2(\Omega))^3$ with **curl** $\boldsymbol{u} \in (L^2(\Omega))^3$ as

$$H(\mathbf{curl}, \Omega) = \left\{ \boldsymbol{u} \in (L^2(\Omega))^3 \,|\, \nabla \times \boldsymbol{u} \in (L^2(\Omega))^3 \right\}$$

with the corresponding norm

$$\|u\|_{H(\mathbf{curl},\Omega)} = \left(\|\boldsymbol{u}\|_{(L^2(\Omega))^3}^2 + \|\nabla \times \boldsymbol{u}\|_{(L^2(\Omega))^3}^2 \right)^{1/2} .$$

This Hilbert space is of fundamental importance for solutions to Maxwell's equations as its elements correspond to solutions with finite energy.

3.2. Maxwell's equations and the electromagnetic scattering problem

This sections serves as a brief introduction to the set of equations stated by James Clerk Maxwell (1831-1879) 150 years ago. This set of equations is named in his honor and consists of two pairs of coupled PDEs relating six fields. These fields describe the dynamical behavior of electromagnetic fields and its interactions with matter. In this section we start with the classical macroscopic Maxwell's equations, introduce a harmonic time-dependence and consider the specific problem setting of scattering of an electromagnetic fields by an obstacle. We conclude this section by deriving the weak formulation of the time-harmonic electromagnetic scattering problem and its solution using FEM discretizations with the appropriate boundary conditions to model transparent boundaries in isolated domains. The derivativation and notation follows the FEM chapter of [Lavrinenko et al., 2014].

3.2.1. Maxwell's equations

The electromagnetic field at a spatial coordinate $\boldsymbol{r} \in \mathbb{R}^3$ at time $t \in \mathbb{R}$ is described by four real-valued vector functions: the electric field strength $\boldsymbol{E}$, the magnetic field strength $\boldsymbol{H}$, the electric flux density $\boldsymbol{D}$ and the magnetic flux density $\boldsymbol{B}$.

The sources of an electromagnetic field are the macroscopic static charge distributions ρ, a scalar quantity, or the macroscopic electric current densities $\boldsymbol{j}$, a vectorial quantity. We state the Maxwell's equations in differential form together with their

commonly used names:

Faraday's law of induction

$$\frac{\partial \boldsymbol{B}}{\partial t} + \nabla \times \boldsymbol{E} = 0, \qquad (3.5\text{a})$$

Coulomb's law

$$\nabla \cdot \boldsymbol{D} = \rho, \qquad (3.5\text{b})$$

Ampère's law

$$\frac{\partial \boldsymbol{D}}{\partial t} - \nabla \times \boldsymbol{H} = -\boldsymbol{j}, \qquad (3.5\text{c})$$

absence of magnetic monopoles

$$\nabla \cdot \boldsymbol{B} = 0. \qquad (3.5\text{d})$$

The conservation of charges in the field equations (3.5a) and (3.5c) requires the divergence conditions (3.5b) and (3.5d) to hold. This can be seen by taking the divergence of (3.5a) and (3.5c)

$$\nabla \cdot \frac{\partial \boldsymbol{B}}{\partial t} = 0 \quad \text{and} \quad \nabla \cdot \frac{\partial \boldsymbol{D}}{\partial t} + \nabla \cdot \boldsymbol{j} = 0 \qquad (3.6)$$

where $\nabla \cdot (\nabla \times \boldsymbol{x}) = 0$ for any vector $\boldsymbol{x}$ is used. The continuity equation of the electric charge

$$\nabla \cdot \boldsymbol{j} + \frac{\partial \rho}{\partial t} = 0 \qquad (3.7)$$

is obtained by adding the divergence of (3.5c) and the time derivative of (3.5b). Together, (3.7) and (3.6) yield

$$\frac{\partial}{\partial t} \nabla \cdot \boldsymbol{B} = \frac{\partial}{\partial t} (\nabla \cdot \boldsymbol{D} - \rho) = 0$$

Maxwell's equations require 12 components of the vector fields $\boldsymbol{E}, \boldsymbol{H}, \boldsymbol{D}$ and $\boldsymbol{B}$ to be fixed but constitute only 8 equations. In addition, not all quantities are independent. Namely, $\boldsymbol{E}$ and $\boldsymbol{B}$ are linked as can be shown quickly: Introducing a vector potential $\boldsymbol{A}$ satisfying

$$\boldsymbol{B} = \nabla \times \boldsymbol{A},$$

which is motivated by (3.5d), we get

$$\nabla \times \left(\boldsymbol{E} + \frac{\partial \boldsymbol{A}}{\partial t} \right) = 0$$

instead of (3.5a). The vanishing **curl** of this expression allows to express it as the gradient of a scalar potential Φ, i.e.

$$-\nabla \Phi = \boldsymbol{E} + \frac{\partial \boldsymbol{A}}{\partial t}.$$

This means, only four components of $\boldsymbol{E}$ and $\boldsymbol{B}$ are independent. In total we require six additional equations to fix all components. These are called constitutive relations describing the dependence of electric flux density and magnetic field on the electric

field and magnetic flux density

$$\boldsymbol{D} = \boldsymbol{D}(\boldsymbol{E}, \boldsymbol{B}),$$
$$\boldsymbol{H} = \boldsymbol{H}(\boldsymbol{E}, \boldsymbol{B}).$$

In this work we assume all bodies to be at rest and assume a harmonic dependence on time t with angular frequency $\omega > 0$, that is

$$\boldsymbol{E}(\boldsymbol{r}, t) = \mathfrak{Re}\left\{ \hat{\boldsymbol{E}}(\boldsymbol{r}, \omega) e^{-i\omega t} \right\}, \tag{3.8a}$$

$$\boldsymbol{H}(\boldsymbol{r}, t) = \mathfrak{Re}\left\{ \hat{\boldsymbol{H}}(\boldsymbol{r}, \omega) e^{-i\omega t} \right\}. \tag{3.8b}$$

and similarly $\boldsymbol{D}, \boldsymbol{B}, \boldsymbol{j}$ and ρ. As physical fields are always real valued, taking the real part is a necessity. The quantities denoted with hats are complex-valued functions contain phase information called phasors. Multiplying these quantities with a phase factor $e^{-i\omega t}$ and taking the real part recovers the real valued physical quantity at a point $\boldsymbol{r}$ at time t.

In the following we will consider only time-harmonic fields and hence will drop the hat notation. The time-harmonic Maxwell's equations are now derived from (3.5) by applying the time derivative

$$\frac{\partial}{\partial t} \to -i\omega$$

and now read

$$\nabla \times \boldsymbol{E} - i\omega \boldsymbol{B} = 0, \tag{3.9a}$$

$$\nabla \cdot \boldsymbol{D} = \rho, \tag{3.9b}$$

$$\nabla \times \boldsymbol{H} + i\omega \boldsymbol{D} = \boldsymbol{j}, \tag{3.9c}$$

$$\nabla \cdot \boldsymbol{B} = 0. \tag{3.9d}$$

The continuity condition (3.7) becomes

$$\nabla \cdot \boldsymbol{j} - i\omega\rho = 0. \tag{3.10}$$

Assuming linear material relationships, the constitutive equations read as

$$\boldsymbol{D} = \epsilon \boldsymbol{E}, \tag{3.11a}$$

$$\boldsymbol{H} = \mu \boldsymbol{B}, \tag{3.11b}$$

$$\boldsymbol{j} = \sigma \boldsymbol{E} + \boldsymbol{j}_i. \tag{3.11c}$$

where ϵ, μ and σ are the permittivity, permeability and conductivity tensors. Here we assume that the electric current density can be split into a conducting part $\sigma \boldsymbol{E}$ depending linearly on the electric field and an impressed part $\boldsymbol{j}_i$. We can rewrite

the set of equations (3.9) into a single, second order equation for the electric field $\boldsymbol{E}$

$$\nabla \times \mu^{-1} \nabla \times \boldsymbol{E} - \omega^2 \varepsilon \boldsymbol{E} = i\omega \boldsymbol{j}_i. \tag{3.12}$$

To facilitate the transformation, we introduced the complex permittivity tensors

$$\varepsilon = \epsilon + i\frac{\sigma}{\omega} \tag{3.13}$$

and used the constitutive material equations (3.11) and Maxwell's equations (3.9c) to transform (3.9a):

$$
\begin{aligned}
\nabla \times \boldsymbol{E} - i\omega \boldsymbol{B} &= 0 && \overset{(3.11)}{\Longleftrightarrow} \\
\mu^{-1} \nabla \times \boldsymbol{E} - i\omega \boldsymbol{H} &= 0 && \overset{\nabla \times \cdot}{\Longrightarrow} \\
\nabla \times \mu^{-1} \nabla \times \boldsymbol{E} - i\omega \nabla \times \boldsymbol{H} &= 0 && \overset{(3.9c)}{\Longleftrightarrow} \\
\nabla \times \mu^{-1} \nabla \times \boldsymbol{E} - i\omega(\boldsymbol{j} - i\omega \boldsymbol{D}) &= 0 && \overset{(3.11)}{\Longleftrightarrow} \\
\nabla \times \mu^{-1} \nabla \times \boldsymbol{E} - i\omega(\sigma \boldsymbol{E} + \boldsymbol{j}_i - i\omega\epsilon \boldsymbol{E}) &= 0 && \Longleftrightarrow \\
\nabla \times \mu^{-1} \nabla \times \boldsymbol{E} - i\omega(\sigma - i\omega\epsilon)\boldsymbol{E} &= i\omega \boldsymbol{j}_i && \overset{(3.13)}{\Longleftrightarrow} \\
\nabla \times \mu^{-1} \nabla \times \boldsymbol{E} - \omega^2 \varepsilon \boldsymbol{E} &= i\omega \boldsymbol{j}_i
\end{aligned}
$$

A special solution of (3.12) for homogeneous media with constant ε and μ without impressed current sources $\boldsymbol{j}_i$ is a plane wave

$$\boldsymbol{E}(\boldsymbol{r}) = \boldsymbol{E}_0 e^{i\boldsymbol{k}\cdot\boldsymbol{r}} \tag{3.14}$$

with $\boldsymbol{k}, \boldsymbol{E}_0 \in \mathbb{C}^3$ if $\boldsymbol{k} \cdot \boldsymbol{E}_0 = 0$ and $k = \sqrt{\boldsymbol{k} \cdot \boldsymbol{k}} = \sqrt{|k_1|^2 + |k_3|^2 + |k_3|^2} = \omega\sqrt{\mu\varepsilon}$. We call $\boldsymbol{k}$ the wave-vector with wave number k. The plane wave *propagates* in a direction $\boldsymbol{r}_0$ provided $\mathfrak{Re}\{\boldsymbol{k} \cdot \boldsymbol{r}_0\} > 0$. It is *evanescent* in direction $\boldsymbol{r}_0$ if $\mathfrak{Im}\{\boldsymbol{k} \cdot \boldsymbol{r}_0\} > 0$.

3.2.2. Weak formulation of the Time-Harmonic Electromagnetic Scattering Problem

The electromagnetic scattering problem describes the interaction of an incident electromagnetic field with a scatterer S located within a bounded domain of interest Ω_{int} with boundary $\partial\Omega_{int} = \Gamma$. The schematic in Figure 3.1 depicts this setup with an arbitrarily shaped scatter S and a polygonal domain boundary Γ with outer normal $\boldsymbol{n}$. The incident field $\boldsymbol{E}_{in}$ is a solution to Maxwell's equations in the exterior $\Omega_{ext} = \mathbb{R}^3 \setminus \Omega_{int}$ with permeability μ_{ext} and permittivity ε_{ext}. It enters the domain Ω_{int}, interacts with the scatterer S and excites a scattered electromagnetic field $\boldsymbol{E}_{sc}$. This scattered field is *outward radiating*, i.e. it leaves Ω_{int} through the boundary Γ and does not (re-)enter Ω_{int}. The total electromagnetic field in Ω_{ext} is
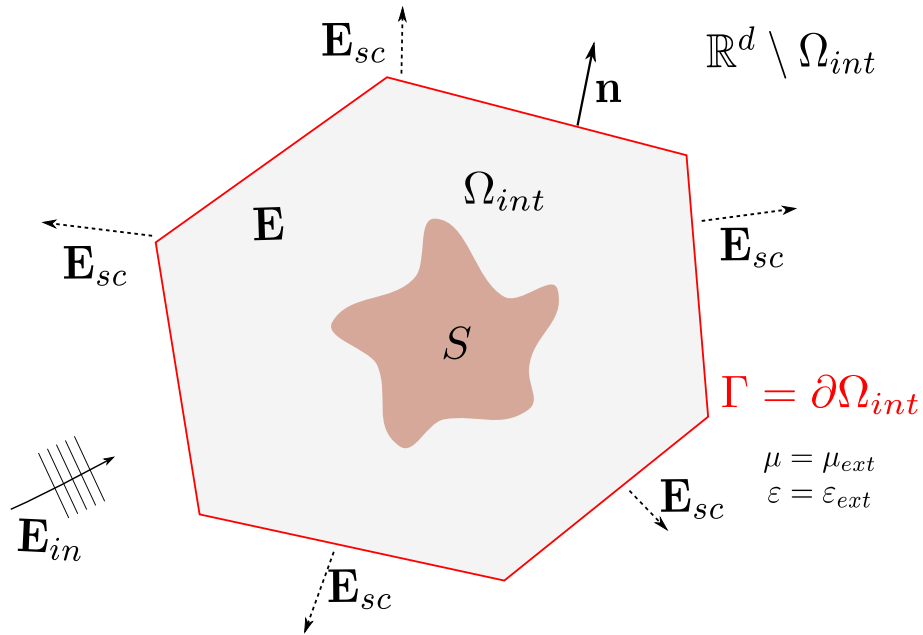
Figure 3.1.: Schematic depiction of scattering of an electromagnetic field by a scatterer S inside a domain Ω_{int}. The incoming field $\mathbf{E}_{in}$ enters the domain Ω_{int} through the boundary Γ where it is the source for the electromagnetic field $\mathbf{E}$. The scattered electromagnetic field $\mathbf{E}_{sc}$ originates in Ω_{int} and is strictly outward radiating into the exterior $\Omega_{ext} = \mathbb{R}^3 \setminus \Omega$ with permeability μ_{ext} and permittivity ε_{ext}.

the superposition of $\boldsymbol{E}_{in}$ and $\boldsymbol{E}_{sc}$

$$\boldsymbol{E} = \boldsymbol{E}_{in} + \boldsymbol{E}_{sc}.$$

In order to arrive at a well-posed problem formulation we need to impose appropriate boundary conditions at Γ and at $\|\boldsymbol{r}\| \to \infty$. We demand, that the scattered electric field asymptotically resembles a transversal plane wave traveling radially away from the origin. The following definition guarantees this property in more formal way.

Definition 3.18 (Silver-Müller Radiation Condition)**.** A solution $\boldsymbol{E}_{sc}$ to Maxwell's equations is called **(strictly) outward radiating** if it satisfies the **Silver-Müller radiation condition**

$$\lim_{r \to \infty} r \left(\nabla \times \boldsymbol{E}_{sc}(\boldsymbol{r}) \times \boldsymbol{r}_0 - i \frac{\omega \sqrt{\varepsilon_{ext}\mu_{ext}}}{c_0} \boldsymbol{E}_{sc}(\boldsymbol{r}) \right) = 0$$
$$\text{uniformly for all directions } \boldsymbol{r}_0,$$

where $\boldsymbol{r} \in \mathbb{R}^3$ is the spatial coordinate with norm $r = \|\boldsymbol{r}\|$ and $\boldsymbol{r}_0 = r^{-1}\boldsymbol{r}$, ε_{ext} and μ_{ext} are the permittivity and permeability in the exterior domain and c_0 the speed of light in vacuum.

This definition is a necessary condition for the unique solvability of the following strong formulation of the electromagnetic scattering problem which is the prototypical problem considered throughout this thesis.

Problem 2 (Electromagnetic scattering problem - strong formulation)**.** For given Ω_{int} with boundary Γ:
Find $\boldsymbol{E}$ such that

(*i*) the electric field $\boldsymbol{E}$ satisfies Maxwell's equations in the interior Ω_{int}:

$$\nabla \times \mu^{-1} \nabla \times \boldsymbol{E} - \omega^2 \varepsilon \boldsymbol{E} = \boldsymbol{j}_i \text{ in } \Omega_{int}$$

(*ii*) the scattered electric field $\boldsymbol{E}_{sc}$ satisfies Maxwell's equations in the exterior domain $\Omega_{ext} = \mathbb{R}^3 \setminus \Omega_{int}$:

$$\nabla \times \mu_{ext}^{-1} \nabla \times \boldsymbol{E}_{sc} - \omega^2 \varepsilon_{ext} \boldsymbol{E}_{sc} = 0 \text{ in } \Omega_{ext}$$

(*iii*) the tangential component of the electric field is continuous (boundary condition at Γ)

$$\boldsymbol{n} \times \left(\boldsymbol{E} - \boldsymbol{E}_{sc} - \boldsymbol{E}_{in} \right)|_\Gamma = 0 \tag{3.15}$$

where the incident electric field $\boldsymbol{E}_{in}$ satisfies Maxwell's equations in the exterior domain Ω_{ext}

(*iv*) the scattered electric field $\boldsymbol{E}_{sc}$ is strictly outward radiating, i.e. it fulfills the Silver-Müller radiation condition 3.18 (boundary condition at $\|r\| \to \infty$).

3. Mathematical Basics

In the following, we do not consider problems with impressed current sources, i.e. from now on

$$\boldsymbol{j}_i = 0.$$

We observe that $\boldsymbol{E}_{in}$ enters the problem formulation only at the boundary Γ.

The weak formulation of the electromagnetic scattering problem is readily derived from (3.12). Instead of $\boldsymbol{E}$, we we denote $\boldsymbol{u} \in \mathcal{X}$ the electric field with a function space $\mathcal{X}$ to be specified later. We multiply (3.12) with the complex conjugate of a test function $\boldsymbol{v} \in (\mathcal{C}_0^\infty)^3$ and subsequently integrate over $\mathbb{R}^3$:

$$\int_{\mathbb{R}^3} \overline{\boldsymbol{v}} \cdot \left(\nabla \times \mu^{-1} \nabla \times \boldsymbol{u} - \omega^2 \varepsilon \boldsymbol{u} \right) \, \mathrm{d}\boldsymbol{r} = 0.$$

Integrating by parts we find

$$\int_{\mathbb{R}^3} \overline{\nabla \times \boldsymbol{v}} \cdot \mu^{-1} \nabla \times \boldsymbol{u} - \omega^2 \overline{\boldsymbol{v}} \cdot \varepsilon \boldsymbol{u} \, \mathrm{d}\boldsymbol{r} = 0 \tag{3.16}$$

where the arising boundary term vanishes at infinity due to the compact support of $\boldsymbol{v}$. We split the integral into the interior and exterior parts defined over Ω_{int} and Ω_{ext}, use $\boldsymbol{u} = \boldsymbol{u}_{sc} + \boldsymbol{u}_{in}$ in Ω_{ext} and ensure that (3.15) holds:

$$\int_{\Omega_{int}} \overline{\nabla \times \boldsymbol{v}} \cdot \mu^{-1} \nabla \times \boldsymbol{u} - \omega^2 \overline{\boldsymbol{v}} \cdot \varepsilon \boldsymbol{u} \, \mathrm{d}\boldsymbol{r}$$

$$+ \int_{\Omega_{ext}} \overline{\nabla \times \boldsymbol{v}} \cdot \mu^{-1} \nabla \times \boldsymbol{u}_{sc} - \omega^2 \overline{\boldsymbol{v}} \cdot \varepsilon \boldsymbol{u}_{sc} \, \mathrm{d}\boldsymbol{r}$$

$$+ \underbrace{\int_{\Omega_{ext}} \overline{\nabla \times \boldsymbol{v}} \cdot \mu^{-1} \nabla \times \boldsymbol{u}_{in} - \omega^2 \overline{\boldsymbol{v}} \cdot \varepsilon \boldsymbol{u}_{in} \, \mathrm{d}\boldsymbol{r}}_{:=\mathfrak{I}} = 0 \tag{3.17}$$

The last integral $\mathfrak{I}$ can be rewritten into a boundary integral over Γ by means of the vector identity

$$\nabla (\boldsymbol{a} \cdot \boldsymbol{b}) = \boldsymbol{b} \cdot (\nabla \times \boldsymbol{a}) - \boldsymbol{a} \cdot (\nabla \times \boldsymbol{b}),$$

the assumption that $\boldsymbol{u}_{in}$ is a solution to Maxwell's equations in the exterior and Gauß's theorem:

$$\mathfrak{I} = \int_{\Omega_{ext}} \nabla \cdot \left(\overline{\boldsymbol{v}} \cdot \mu^{-1} \nabla \times \boldsymbol{u}_{in} \right) + \overline{\boldsymbol{v}} \cdot \nabla \times \mu^{-1} \nabla \times \boldsymbol{u}_{in} - \omega^2 \overline{\boldsymbol{v}} \cdot \varepsilon \boldsymbol{u}_{in} \, \mathrm{d}\boldsymbol{r}$$

$$= \int_{\Omega_{ext}} \nabla \cdot \left(\overline{\boldsymbol{v}} \cdot \mu^{-1} \nabla \times \boldsymbol{u}_{in} \right) + \overline{\boldsymbol{v}} \cdot \underbrace{\left(\nabla \times \mu^{-1} \nabla \times \boldsymbol{u}_{in} - \omega^2 \varepsilon \boldsymbol{u}_{in} \right)}_{=0} \, \mathrm{d}\boldsymbol{r}$$

$$= \int_{\partial \Omega_{ext}} \overline{\boldsymbol{v}} \cdot \mu^{-1} \nabla \times \boldsymbol{u}_{in} \, \mathrm{d}\boldsymbol{s} = - \int_{\Gamma} \overline{\boldsymbol{v}} \cdot \mu^{-1} \nabla \times \boldsymbol{u}_{in} \, \mathrm{d}\boldsymbol{s}.$$

Now (3.17) reads

$$
\int_{\Omega_{int}} \overline{\nabla \times \boldsymbol{v}} \cdot \mu^{-1} \nabla \times \boldsymbol{u} - \omega^2 \overline{\boldsymbol{v}} \cdot \varepsilon \boldsymbol{u} \, \mathrm{d}\boldsymbol{r} + \int_{\Omega_{ext}} \overline{\nabla \times \boldsymbol{v}} \cdot \mu^{-1} \nabla \times \boldsymbol{u}_{sc} - \omega^2 \overline{\boldsymbol{v}} \cdot \varepsilon \boldsymbol{u}_{sc} \, \mathrm{d}\boldsymbol{r}
$$
$$
= \int_{\Gamma} \overline{\boldsymbol{v}} \cdot \mu^{-1} \nabla \times \boldsymbol{u}_{in} \, \mathrm{d}\boldsymbol{s}. \tag{3.18}
$$

In the following, it is useful to abbreviate

$$
a_{int}(\boldsymbol{v}, \boldsymbol{u}) = \int_{\Omega_{int}} \overline{\nabla \times \boldsymbol{v}} \cdot \mu^{-1} \nabla \times \boldsymbol{u} - \omega^2 \overline{\boldsymbol{v}} \cdot \varepsilon \boldsymbol{u} \, \mathrm{d}\boldsymbol{r} \tag{3.19}
$$

and

$$
a_{ext}(\boldsymbol{v}, \boldsymbol{u}_{sc}) = \int_{\Omega_{ext}} \overline{\nabla \times \boldsymbol{v}} \cdot \mu^{-1} \nabla \times \boldsymbol{u}_{sc} - \omega^2 \overline{\boldsymbol{v}} \cdot \varepsilon \boldsymbol{u}_{sc} \, \mathrm{d}\boldsymbol{r}. \tag{3.20}
$$

Next, we introduce an auxiliary function $\boldsymbol{g}$ with support only in the vicinity of Γ which is tangentially continuous and fulfills

$$
\boldsymbol{g}|_{\Gamma} = \boldsymbol{u}_{in}|_{\Gamma}. \tag{3.21}
$$

This function helps to include the continuity condition (3.15) in the weak formulation. We write

$$
\boldsymbol{u}_{sc} = (\boldsymbol{u}_{sc} + \boldsymbol{g}) - \boldsymbol{g} := \boldsymbol{w} - \boldsymbol{g}. \tag{3.22}
$$

We replace $\boldsymbol{u}_{sc}$ in (3.18) and use the abbreviations

$$
a_{int}(\boldsymbol{v}, \boldsymbol{u}) + a_{ext}(\boldsymbol{v}, \boldsymbol{w} - \boldsymbol{g}) = \int_{\Gamma} \overline{\boldsymbol{v}} \cdot \mu^{-1} \nabla \times \boldsymbol{u}_{in} \, \mathrm{d}\boldsymbol{s}
$$
$$
\Longleftrightarrow a_{int}(\boldsymbol{v}, \boldsymbol{u}) + a_{ext}(\boldsymbol{v}, \boldsymbol{w}) - a_{ext}(\boldsymbol{v}, \boldsymbol{g}) = \int_{\Gamma} \overline{\boldsymbol{v}} \cdot \mu^{-1} \nabla \times \boldsymbol{u}_{in} \, \mathrm{d}\boldsymbol{s}
$$
$$
\Longleftrightarrow a_{int}(\boldsymbol{v}, \boldsymbol{u}) + a_{ext}(\boldsymbol{v}, \boldsymbol{w}) = a_{ext}(\boldsymbol{v}, \boldsymbol{g}) + \int_{\Gamma} \overline{\boldsymbol{v}} \cdot \mu^{-1} \nabla \times \boldsymbol{u}_{in} \, \mathrm{d}\boldsymbol{s}. \tag{3.23}
$$

By construction $\boldsymbol{u}$ and $\boldsymbol{w}$ are defined on Ω_{int} and Ω_{ext}, respectively, but are continuous across Γ, thus we can define

$$
\boldsymbol{u}_w = \begin{cases} \boldsymbol{u}(\boldsymbol{r}) & \boldsymbol{r} \in \Omega_{int}, \\ \boldsymbol{w}(\boldsymbol{r}) & \boldsymbol{r} \in \Omega_{ext}. \end{cases}
$$

Inserting this definition into (3.23) we obtain

$$
a_{int}(\boldsymbol{v}, \boldsymbol{u}_w) + a_{ext}(\boldsymbol{v}, \boldsymbol{u}_w) = a_{ext}(\boldsymbol{v}, \boldsymbol{g}) + \int_{\Gamma} \overline{\boldsymbol{v}} \cdot \mu^{-1} \nabla \times \boldsymbol{u}_{in} \, \mathrm{d}\boldsymbol{s}. \tag{3.24}
$$

Finally, we can state the weak formulation of the electromagnetic scattering problem.

We have not yet specified the proper function space $\mathcal{X}$ for $\boldsymbol{u}$. In order for the integrals to exist, we must demand $\nabla \times \boldsymbol{u}$ to be integrable. This makes $\mathcal{X} = \mathrm{H}(\mathbf{curl}, \mathbb{R}^3)$ the proper choice as function space.

Problem 3 (Electromagnetic scattering problem - weak formulation)**.** Let the incident field $\boldsymbol{u}_{in}$ and its tangential component $\nabla \times \boldsymbol{u}_{in}$ be given on Γ. For arbitrary $\boldsymbol{g}$ satisfying (3.21) we have the following variational formulation of the electromagnetic scattering problem:

Find $\boldsymbol{u} \in \mathrm{H}(\mathbf{curl}, \mathbb{R}^3)$ such that

$$a(\boldsymbol{v}, \boldsymbol{u}) = f(\boldsymbol{v}) \quad \forall \boldsymbol{v} \in \mathrm{H}(\mathbf{curl}, \mathbb{R}^3) \tag{3.25}$$

where

$$a(\boldsymbol{v}, \boldsymbol{u}) = \int_{\mathbb{R}^3} \overline{\nabla \times \boldsymbol{v}} \cdot \mu^{-1} \nabla \times \boldsymbol{u} - \omega^2 \overline{\boldsymbol{v}} \cdot \varepsilon \boldsymbol{u} \, \mathrm{d}\boldsymbol{r}. \tag{3.26}$$

and

$$f(\boldsymbol{v}) = \int_{\Omega_{ext}} \overline{\nabla \times \boldsymbol{v}} \cdot \mu^{-1} \nabla \times \boldsymbol{g} - \omega^2 \overline{\boldsymbol{v}} \cdot \varepsilon \boldsymbol{g} \, \mathrm{d}\boldsymbol{r} + \int_{\Gamma} \overline{\boldsymbol{v}} \cdot \mu^{-1} \nabla \times \boldsymbol{u}_{in} \, \mathrm{d}\boldsymbol{s}. \tag{3.27}$$

3.2.3. Transparent boundary conditions

The electromagnetic scattering Problem 3 is stated on an unbounded domain. For the numerical solution it is split in a bounded domain Ω_{int} enclosing the scatterer and an unbounded exterior Ω_{ext}. A mathematically correct formulation must obey the radiation boundary condition, i.e. it must account for radiation out of the computational domain Ω_{int} to infinity by imposing a *transparent boundary condition* on $\Gamma = \partial \Omega_{int}$. Only for specific instances it is possibly to describe the transparent boundaries by means of Dirichlet-, Neumann- or Robin-boundary conditions, for example by employing a Dirichlet-to-Neumann (DtN) operator. Generally, the straight-forward discretization and application of artificial boundary conditions introduces artificial, unphysical reflections from the boundaries which no longer satisfy the radiation condition in Definition 3.18, i.e. the scattered field is no longer strictly outward radiating.

Different concepts and transparent boundary conditions have been introduced. Among them the Perfectly Matched Layer method [Berenger, 1994] has emerged as the most widely used. The idea of this method is a complex continuation of the Maxwell's equation to a complex coordinate system. In the complex deformed coordinate system propagating and oscillating waves are deformed to exponentially decaying waves. If the decay at a finite distance $\rho > 0$ is sufficiently approximated, a zero Dirichlet boundary condition can be imposed without distorting the solution.

The complex stretching of the coordinate system in the exterior is indicated in Figure 3.2. In this trapezoidal coordinate system the coordinate stretching $(x, \xi) \mapsto (x, (1 + i\sigma)\xi)$ works along the distance coordinate ξ. The Perfectly Matched Layer (PML) also allows for structured exterior domains. As the coordinate stretching
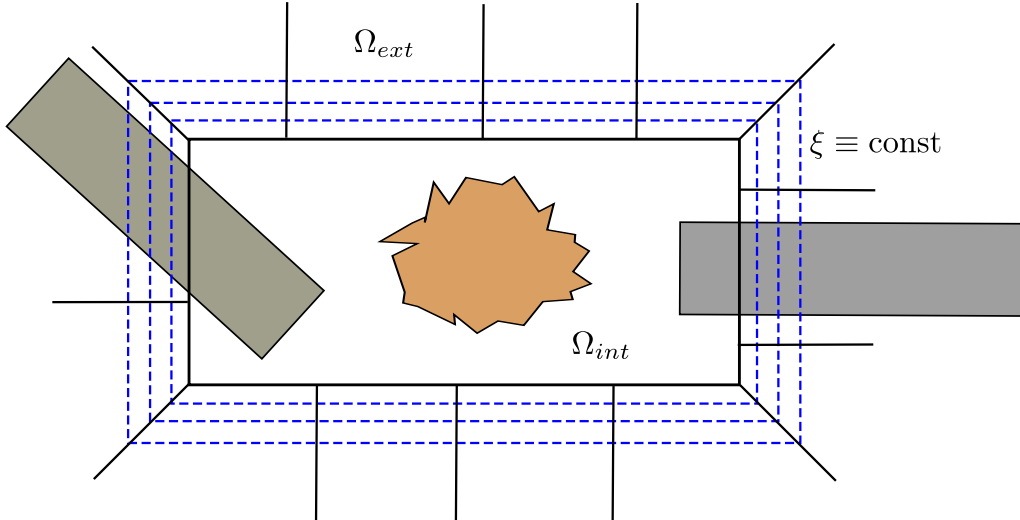
Figure 3.2.: Schematic of a trapezoidal coordinate system in the structured exterior of a domain Ω_{int}. The dotted lines mark lines of constant distance coordinates ξ.

is applied to the continuous problem the resulting weak formulation is identical to Problem 3 except for a transformation of the permeability and permittivity tensors in Ω_{ext}. It thus integrates naturally in the FEM discretization presented in the next section. A detailed presentation of the PML in general and the adaptive PML used throughout this thesis in particular can be found in [Zschiedrich, 2009].

Other concepts for transparent boundary conditions comprise Green's tensor methods [Paulus and Martin, 2001], mode-matching methods and the use of infinite elements [Cecot et al., 2003]. An elegant characterization of the radiation condition in Definition 3.18 for time-harmonic fields is the pole condition method [Schmidt, 2002, Hohage et al., 2003a]. The outgoing solutions are characterized by the location in the complex plane of the poles of their Laplace transformation with respect to a generalized distance variable. It has been shown to be equivalent to the PML [Hohage et al., 2003b] and can be used to detect spurious modes in resonance mode computations [Kettner, 2012].

3.2.4. hp finite element discretization

This section serves as only as a brief introduction to the Finite Element Method. For a more general introduction we refer to [Braess, 2007] and to [Monk, 2003, Demkowicz, 2006, Demkowicz et al., 2007, Lavrinenko et al., 2014] for the specifics of FEM for Maxwell's equation.

A natural way to solve a PDE numerically is to use the weak formulation of the PDE and to replace the function space of the continuous problem V by a finite

dimensional subspace V_h. For Problem 3 we hence choose

$$V_h \subset V = \mathrm{H}(\mathbf{curl}, \Omega).$$

As V_h is a subspace of $\mathrm{H}(\mathbf{curl}, \Omega)$ we call V_h a *conforming finite element space* and note

$$\mathcal{N} = \dim V_h < \infty.$$

The discrete analog to Problem 3 reads

Problem 4 (Finite element approximation). Find $\boldsymbol{u}_h \in V_h$ such that

$$a(\boldsymbol{v}_h, \boldsymbol{u}_h) = f(\boldsymbol{v}_h) \quad \forall \boldsymbol{v}_h \in V_h. \tag{3.28}$$

Let $B = \{\boldsymbol{\xi}_1, \boldsymbol{\xi}_2, \dots \boldsymbol{\xi}_{\mathcal{N}}\}$ be a basis of V_h and

$$\boldsymbol{u}_h = \sum_{i=1}^{\mathcal{N}} \alpha_i \boldsymbol{\xi}_i$$

the expansion of the solution $\boldsymbol{u}_h$ of (3.28) in it. As $\operatorname{span} B = V_h$ it is sufficient in Problem 4 to demand (3.28) to hold for all $\boldsymbol{\xi} \in B$. This simplifies (3.28) to the linear system of equations

$$a\left(\boldsymbol{\xi}_j, \sum_{i=1}^{\mathcal{N}} \alpha_i \boldsymbol{\xi}_i\right) = \sum_{i=1}^{\mathcal{N}} a(\boldsymbol{\xi}_j, \boldsymbol{\xi}_i)\alpha_i = f(\boldsymbol{\xi}_j), \quad j = 1, \dots \mathcal{N} \tag{3.29}$$

or in matrix-vector notation

$$\mathcal{A}\boldsymbol{\alpha} = \boldsymbol{f} \tag{3.30}$$

with $\mathcal{A}_{i,j} = a(\xi_i, \xi_j)$, $\boldsymbol{f}_i = f(\xi_i)$ and the unknown coefficient vector $\boldsymbol{\alpha}_i = \alpha_i$.

A finite element subspace V_h must be constructed such that (3.30) is solvable with reasonable computational effort, i.e. $\mathcal{A}$ should be sparse. In finite element methods this is achieved by using basis or ansatz functions which have a small support in Ω. The name of the method arises from the discretization of Ω into a mesh of a finite number of disjoint geometrical elements K_i with $\cup_i K_i = \Omega$. The subscript h usually refers to the typical size of the elements, e.g. the radius of the circumscribed sphere. On each element K a space of polynomials P_K up to order p is chosen together with a set of linear functionals Σ_K called *degrees of freedom*. The triple (K, P_K, Σ_K) is called a *finite element* and must be unisolvant, i.e. Σ_K must uniquely determine a basis of P_K.

Constructing finite elements and corresponding subspaces suitable for Maxwell's equations is still a question of research. Avoiding *unphysical* or *spurious* solutions is a necessity. A discussion of different finite elements and associated spaces for the electromagnetic fields is out of the scope of this introduction. For a detailed overview we refer to [Monk, 2003, Demkowicz et al., 2007, Zaglmayr, 2006, Bergot and Duruflé, 2013]. Here we quote some of the principles and key ideas in constructing

these spaces. The analysis of the variational Problem 3 reveals complications, if the finite element space is a subspace of the kernel of the **curl**-operator. The Helmholtz-decomposition is thus used to factor out the null-space of the **curl**-operator. The correct way to construct finite element spaces starts with the following sequence

$$H^1(\Omega)/\mathbb{R} \xrightarrow{\nabla} \mathrm{H}(\mathbf{curl}, \Omega) \xrightarrow{\nabla\times} \mathrm{H}(\mathbf{div}, \Omega) \xrightarrow{\nabla\cdot} L^2(\Omega)$$

called the de-Rham complex [Jänich, 2005]. Functions are identified as elements of the quotient space $H^1(\Omega)/\mathbb{R}$ if they only differ by a constant. The diagram indicates, that for a function $p \in H^1(\Omega)/\mathbb{R}$ the gradient ∇p lies in $\mathrm{H}(\mathbf{curl}, \Omega)$. In addition, the range of the operator ∇ is the kernel of the **curl** operator whose range is $L^2(\Omega)$. If this diagram holds, we call the sequence *exact*. On simply connected subsets $\Omega \subseteq \mathbb{R}^3$ this is fulfilled.

We demand for finite dimensional subspaces

$$\begin{aligned} W_h &\subset H^1(\Omega) \\ V_h &\subset \mathrm{H}(\mathbf{curl}, \Omega) \\ S_h &\subset \mathrm{H}(\mathbf{div}, \Omega) \\ Z_h &\subset L^2(\Omega) \end{aligned}$$

to fulfill the corresponding sequence

$$W_h \xrightarrow{\nabla} V_h \xrightarrow{\nabla\times} S_h \xrightarrow{\nabla\cdot} Z_h$$

exactly. This guarantees, that each element function $v_h \in V_h$ contained in the kernel of the **curl**-operator is the gradient of a scalar potential, i.e. we have

$$\nabla \times v_h = 0 \Rightarrow \exists \phi \in W_h : v_h = \nabla\phi.$$

Our implementation [Pomplun et al., 2007] uses a full family of Nédélec's edge elements [Nedelec, 1980] including tetrahedra, hexahedra, prisms and pyramids [Bergot et al., 2010, Bergot and Duruflé, 2013]. They have been proven to have optimal convergence rates and can be used directly in hybrid meshes [Bergot and Marc, 2013]. Table 3.1 lists the dimensions of these optimal finite element spaces for different element types.

In FEM textbooks Céa's Lemma, the discrete analog to the Lax-Milgram Lemma 3.13, is usually employed to derive error bounds for the error between exact and approximate solutions $u \in V$ and $u_h \in V_h$ for a coercive bilinear form $a(\cdot, \cdot)$. It states, that the approximation error of the Galerkin solution is bounded by the best-approximation in V_h with discretization independent constants. A generalization to non-coercive sesquilinear forms holds with the Babuška-Brezzi condition (cf. Definition 3.12). Hence, the FEM solution is the best approximation of the solution to Maxwell's equation in V_h. Furthermore, we have convergence of the discrete to the continuous solution with uniform mesh refinements, also called h-refinements.

The convergence rate is limited by the minimum of the polynomial degree p of the ansatz functions and the regularity r of the solution [Demkowicz et al., 2007]:

$$\|u - u_h\|_{\mathrm{H}(\mathbf{curl},\Omega)} \leq C\mathcal{N}^{-\min(p,r)}$$

In a uniform p-refinement the convergence rate is only limited by the regularity. The regularity of the solution of Maxwell's equations is reduced at boundaries or material interfaces, where singularities may occur. Using *a posteriori* error estimates to steer locally adaptive h-refinements, the converge rate is thus limited only by the polynomial degree of the ansatz functions. Typically, large elements with high polynomial degrees provide a good approximation provided the solution is analytic. The drawback of a fixed polynomial degree p for all elements is the investment of numerical effort even if the solution is of lower regularity where the high-order ansatz functions do not provide a benefit. The *hp*-adaptivity [Demkowicz et al., 2007] resolves this handicap by allowing for different polynomial degrees to be set on each element. Choosing both h and p adaptively leads to exponential convergence in case of unlimited regularity.

A posteriori adaptive h- and p-refinements require the solution to be known to steer refinements. This becomes infeasible for larger problems in three spatial dimensions. Oftentimes there is *a priori* knowledge about the physics of the solution and location of singularities. In this case, the initial mesh can be pre-refined to adapt to the local regularity and create ideally Optimal Initial Meshes [Demkowicz et al., 2007]. These allow to observe exponential convergence rates for uniform p-refinements even pre-asymptotically. In order to optimize the numerical effort, the polynomial degree can then adapted to the local mesh size. Estimating the error in simple test problems over each element allows to set the polynomial degree *a priori* according to a user-specified global accuracy level.

Table 3.1.: Dimension of optimal finite element spaces for different element types derived in [Bergot and Duruflé, 2013].

element \ order	1	2	3	4	5	6	7	8
tetrahedron	6	20	45	84	140	216	315	440
prism	15	52	120	228	385	600	882	1240
hexahedron	27	96	225	432	735	1152	1701	2400
pyramid	10	35	81	154	260	405	595	836

3.3. Scattering matrix domain decomposition

A domain decomposition method is a numerical strategy to subdivide computations into problems on subdomains and coordinate the solutions between adjacent subdomains in order to solve the full problem. The subproblems can be solved independently of each other thus allowing for parallelization. There are several ways to update the solutions on the interface between subdomains by either choosing an iterative approach and/or overlapping subdomains [Schädle et al., 2007]. Another possibility are Mortar methods [Wohlmuth, 2000, Hollaus et al., 2010] where variables only acting on the interface are introduced and the solution is ensured via Lagrange multipliers. Non-iterative methods usually leave a smaller and coarser problem to be solved on the skeleton.

In this section we derive a non-overlapping domain, non-iterative decomposition method based on scattering matrices in a Fourier plane wave basis. We also briefly recall a semi-analytical method for layered media in Section 3.3.4. These are the building blocks for the incoherent coupling algorithm presented in Chapter 4. In contrast to the previous sections we reserve bold symbols for (complex) vectors and denote fields with roman letters to distinguish $\boldsymbol{E} \in \mathbb{C}^M$ and $E : \mathbb{R}^3 \to \mathbb{C}^3$.

3.3.1. Fourier plane wave basis

In the following we assume a computational domain Ω with transparent boundary conditions in $\pm z$ direction and a two-fold Bloch-periodic behavior of the electromagnetic field. This means for lattice vectors $\boldsymbol{a}_1$ and $\boldsymbol{a}_2 \in \mathbb{R}^3$ we have

$$E(\boldsymbol{r} + \boldsymbol{a}_i) = E(\boldsymbol{r})e^{i\boldsymbol{k}_B \cdot \boldsymbol{a}_i} \tag{3.31}$$

with the Bloch-vector $\boldsymbol{k}_B$ and $\boldsymbol{a}_i \in \{\boldsymbol{a}_1, \boldsymbol{a}_2\}$. Associated with $\boldsymbol{a}_i$ is a reciprocal grid vector $\boldsymbol{b}_i$ defined by

$$\boldsymbol{a}_i \cdot \boldsymbol{b}_j = 2\pi \delta_{i,j}. \tag{3.32}$$

For simplicity we will assume the grid vectors to lie in the xy plane.

The Fourier transform of the electric field in the exterior domain Ω^+ with respect to the $z = z_0$ hyperplane is an infinite sum in case of the assumed two-fold periodicity.

$$E(\boldsymbol{r}) = \sum_{n_1 \in \mathbb{Z}} \sum_{n_2 \in \mathbb{Z}} \boldsymbol{E}^+_{n_1,n_2} e^{i\boldsymbol{k}^+(n_1,n_2) \cdot \boldsymbol{r}} + \boldsymbol{E}^-_{n_1,n_2} e^{i\boldsymbol{k}^-(n_1,n_2) \cdot \boldsymbol{r}} \tag{3.33}$$

with the complex amplitudes $\boldsymbol{E}^+_{n_1,n_2}$ and $\boldsymbol{E}^-_{n_1,n_2} \in \mathbb{C}^3$, the wave vectors $\boldsymbol{k}^\pm(n_1,n_2) = (\boldsymbol{k}_\perp(n_1,n_2), \pm k_z(n_1,n_2))^\intercal$ where $\boldsymbol{k}_\perp(n_1,n_2) = n_1\boldsymbol{b}_1 + n_2\boldsymbol{b}_2 \in \mathbb{R}^2$ with the x,y components of the reciprocal grid vectors $\boldsymbol{b}_i$. $k_z(n_1,n_2)$ is defined by

$$k_z(n_1,n_2) = \sqrt{k_m^2 - \|\boldsymbol{k}_\perp(n_1,n_2)\|^2} \in \mathbb{C} \tag{3.34}$$

$$\Omega^+$$

$$\Omega$$

$$\Omega^-$$

Ω_1
Γ_1
Ω_2
Γ_2
Ω_3
Ω_4 Γ_3
Ω_5 Γ_4

$$\Omega_{i-1}$$

Ω_{i-1}^- $\cdots\cdots\Gamma_{i-1}$
Ω_i^+

$$\Omega_i$$

Ω_i^-
$\cdots\cdots\Gamma_i$
Ω_{i+1}^+

$$\Omega_{i+1}$$

(a)   (b)
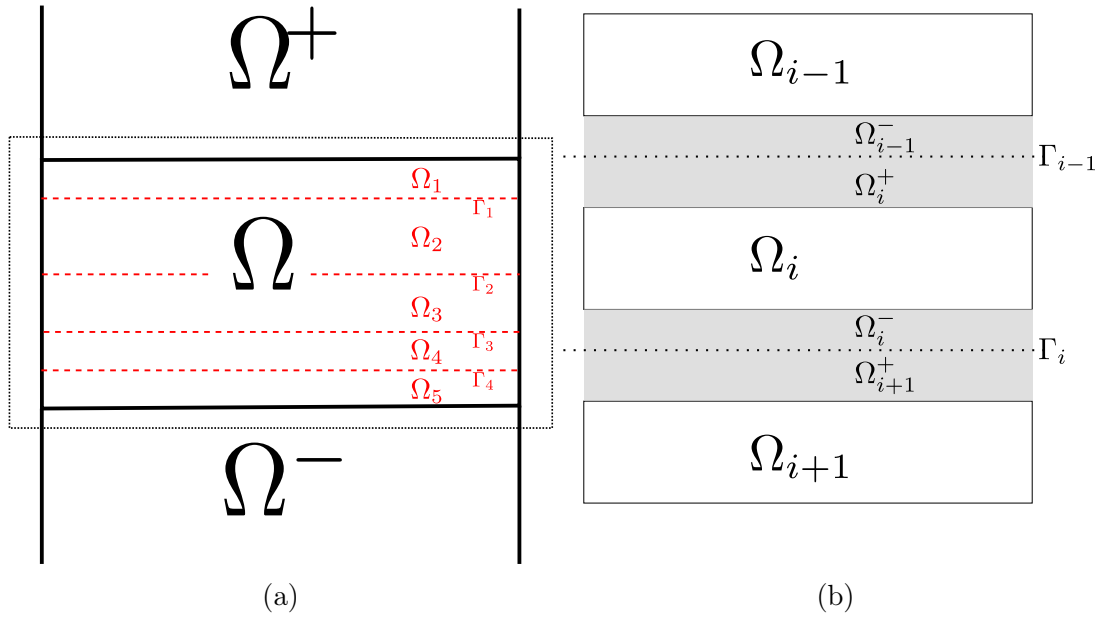
Figure 3.3.: (a) Schematic depiction of an isolated, layered domain Ω with half-infinite sub- and superspaces Ω^- and Ω^+. The subdomains $\Omega_1 - \Omega_5$ are separated by the boundaries $\Gamma_1 - \Gamma_4$.
(b) Schematic and labeling for the scattering matrix computation detailed in Section 3.3.2. The subdomains are isolated individually by introducing artificial, half-infinite sub- and superspaces Ω_i^- and Ω_i^+ in place of the boundaries Γ_i and Γ_{i-1}.

with the wavenumber $k_m = 2\pi n/\lambda_0$ depending on the refractive index n of the material and the vacuum wavelength λ_0.

If we assume a non-absorptive material, k_m is a real number and we can distinguish two cases for $k_z = k_z(n_1, n_2)$:

- $\mathfrak{Re}\{k_z\} > 0, \mathfrak{Im}\{k_z\} = 0$, i.e. $\|\boldsymbol{k}_\perp(n_1, n_2)\| \leq k_m$. $E(\boldsymbol{r}) = \boldsymbol{E}^\pm_{n_1,n_2} e^{i\boldsymbol{k}^\pm(n_1,n_2)\cdot\boldsymbol{r}}$ is called an upward/downward *propagating* plane wave.

- $\mathfrak{Re}\{k_z\} = 0, \mathfrak{Im}\{k_z\} > 0$, i.e. $\|\boldsymbol{k}_\perp(n_1, n_2)\| > k_m$. $E(\boldsymbol{r}) = \boldsymbol{E}^+_{n_1,n_2} e^{i\boldsymbol{k}^+(n_1,n_2)\cdot\boldsymbol{r}}$ is called an *evanescent* plane wave in z-direction. Due to $\mathfrak{Im}\{k_z\} > 0$ it decays exponentially, i.e. $\lim_{z\to\infty} e^{ik_z z} = 0$.

We call

$$E^\uparrow(\boldsymbol{r}) = \sum_{n_1\in\mathbb{Z}}\sum_{n_1\in\mathbb{Z}} \boldsymbol{E}^+_{n_1,n_2} e^{i\boldsymbol{k}^+(n_1,n_2)\cdot\boldsymbol{r}}$$

and

$$E^\downarrow(\boldsymbol{r}) = \sum_{n_1\in\mathbb{Z}}\sum_{n_1\in\mathbb{Z}} \boldsymbol{E}^-_{n_1,n_2} e^{i\boldsymbol{k}^-(n_1,n_2)\cdot\boldsymbol{r}}$$

the up- and downward propagating spectrum in the upper half space. The amplitudes $\boldsymbol{E}^\pm_{n_1,n_2}$ depend on the z coordinate z_0 of the plane. By applying a phase shift $e^{\mp ik_z(n_1,n_2)z_0}$ they can be pulled back to $z = 0$ which we choose as a common reference plane.

In most applications the full Fourier series (3.33) of E is truncated and not all Fourier modes are kept or computed. We refer to such a truncation as a *k-spacing*. A formal definition reads

Definition 3.19 (k-spacing). A *k-spacing* is a finite set $\mathfrak{K} = \{(n_i, m_i)\ i = 1 : N\,|\,n_i, m_i \in \mathbb{Z}\}$ of N diffraction orders.

A common k-spacing would be the set of all propagating Fourier modes. The expansion of an electric field with respect to a k-spacing $\mathfrak{K}$ is

$$E(\boldsymbol{r}) = \sum_{(n_1,n_2)\in\mathfrak{K}} \boldsymbol{E}^+_{n_1,n_2} e^{i\boldsymbol{k}^+(n_1,n_2)\cdot\boldsymbol{r}} + \boldsymbol{E}^-_{n_1,n_2} e^{i\boldsymbol{k}^-(n_1,n_2)\cdot\boldsymbol{r}}. \tag{3.35}$$

A field u_{in} incident from Ω^+ excites a scattered field E_{sc} in Ω, Ω^+ and Ω^-. The scattered field E_{sc} is outward radiating hence its Fourier series expansion in Ω^+ and Ω^- with respective k-spacings $\mathfrak{K}_+$, $\mathfrak{K}_-$ is

$$E_{sc}(\boldsymbol{r}) = \sum_{(n_1,n_2)\in\mathfrak{K}_+} \boldsymbol{E}^+_{n_1,n_2} e^{i\boldsymbol{k}^+(n_1,n_2)\cdot\boldsymbol{r}} \quad \text{in} \quad \Omega^+ \tag{3.36}$$

$$E_{sc}(\boldsymbol{r}) = \sum_{(n_1,n_2)\in\mathfrak{K}_-} \boldsymbol{E}^-_{n_1,n_2} e^{i\boldsymbol{k}^-(n_1,n_2)\cdot\boldsymbol{r}} \quad \text{in} \quad \Omega^- \tag{3.37}$$

The same holds true for illumination from Ω^-.

Remark (Polarizations). The electric field of a plane wave can be split into two orthogonal polarizations, i.e. $\boldsymbol{E}^{\pm}_{n_1,n_2} = \boldsymbol{p}_1 p_1 + \boldsymbol{p}_2 p_2$ with $\boldsymbol{p}_1, \boldsymbol{p}_2 \in \mathbb{R}^3, \boldsymbol{p}_1 \cdot \boldsymbol{p}_2 = 0$ and $p_1, p_2 \in \mathbb{C}$. In the definition of $\boldsymbol{E}_{sc}$ we did not account for this. Doubling up each integer pair in $\mathfrak{K}$ allows to distinguish the different polarizations. Henceforth, we assume this to be the case but keep the same notation to avoid additional indices.

The choice of reference polarizations allows to express the amplitudes $\boldsymbol{E}^{\pm}_{n_1,n_2}$ by complex scalars $E^{\pm}_{n_1,n_2}$, the *Fourier coefficients*, if we allow the members of $\mathfrak{K}$ to appear twice. The scattered field in Ω^+ and Ω^- can thus be associated with the vector

$$\boldsymbol{E}_{sc} = \left(\underbrace{E^+_{n_1,m_1}, \ldots, E^+_{n_{N_+},m_{N_+}}}_{\text{coefficients from (3.36)}}, \underbrace{E^-_{n_1,m_1}, \ldots, E^-_{n_{N_-},m_{N_-}}}_{\text{coefficients from (3.37)}} \right)^{\mathsf{T}} = (\boldsymbol{E}_+, \boldsymbol{E}_-)^{\mathsf{T}} \qquad (3.38)$$

In the (non-homogeneous) interior domain Ω the electric field can no longer be written as a superposition of plane waves with respect to a k-spacing $\mathfrak{K}$. However, the illuminating field u_{in} in Ω^+ or Ω^- can be characterized like in (3.36) and (3.37) with the propagation directions switched. Similarly to (3.38) it can be expressed as $\boldsymbol{E}_{in}$. The linearity of Maxwell's equations thus allows to describe the scattered electromagnetic field E_{sc} at $\boldsymbol{r} \in \Omega$ as the superposition of fields excited by plane waves associated with $\mathfrak{K}$. We denote these fields u_l if the incident field is a plane wave associated with the l-th element of $\mathfrak{K}$. We use the same ordering as before, i.e. first sources in Ω_+ on $\mathfrak{K}^+$ followed by those in Ω_- on $\mathfrak{K}^-$. This yields

$$E_{sc}(\boldsymbol{r}) = \sum_{l=1}^{N} E^{in}_l u_l(\boldsymbol{r}) \quad , \boldsymbol{r} \in \Omega \qquad (3.39)$$

with $N = N_+ + N_-$. Here N_+ and N_- denote the cardinalities of $\mathfrak{K}^+$ and $\mathfrak{K}^-$. Collecting complex electric field amplitudes of u_l at $\boldsymbol{r}$ in $\mathcal{U}(\boldsymbol{r}) \in \mathbb{C}^{3 \times N}$ allows to rewrite (3.39) as

$$E_{sc}(\boldsymbol{r}) = \mathcal{U}(\boldsymbol{r}) \boldsymbol{E}_{in} \quad , \boldsymbol{r} \in \Omega. \qquad (3.40)$$

3.3.2. Scattering matrices for isolated domains

We define a scattering matrix for the simple isolated geometry depicted in Figure 3.3a with homogeneous, isotropic and infinite half-spaces Ω^+ and Ω^-. The association of every illuminating field with a vector $\boldsymbol{E}_{in}$ of Fourier coefficients motivates the definition of a scattering matrix $\mathcal{T}$.

Definition 3.20 (Scattering matrix). A *scattering matrix* characterizes the scattering of an incident field by a scatterer located in a spatial domain Ω with homogeneous, isotropic and infinite half-spaces Ω^+ and Ω^- in terms of k-spacings $\mathfrak{K}_+$, $\mathfrak{K}_-$ with cardinalities N_+ and N_-. The i-th column of a scattering matrix

$\mathcal{T} \in \mathbb{C}^{(N_+ + N_-) \times (N_+ + N_-)}$ is the response of the underlying system, represented as $\boldsymbol{E}_{sc}$ as in (3.38), when illuminated by a plane wave of normalized amplitude associated with the i-th element of $\mathfrak{K} = \mathfrak{K}_+ \cup \mathfrak{K}_-$.

Remark (Reflection and Transmission). A scattering matrix $\mathcal{T}$ can be subdivided into four submatrices $\mathcal{T}_{j,i}, i, j = 1, 2$. Numbering Ω^+ and Ω^- top to bottom, the response or scattered field in the same domain is characterized by the square matrix $\mathcal{T}_{i,i} \in \mathbb{C}^{N_i \times N_i}$. This response is referred to as *reflection*. The response in the opposing domain Ω_j is given by the rectangular matrix $\mathcal{T}_{j,i} \in \mathbb{C}^{N_j \times N_i}$. This response is referred to as *transmission*.

3.3.3. Domain decomposition and coupling conditions on interfaces

In this section we present the domain decomposition algorithm based on scattering matrices and the corresponding coupling conditions which must hold on the interface between neighboring subdomains. Instead of using an iterative domain decomposition algorithm like a Schwarz method [Quarteroni and Valli, 1999] to ensure the coupling conditions on $\{\Gamma_i\}_{i=1}^{N_\Omega - 1}$ we solve directly for the coupling conditions. The idea of the domain decomposition presented here is targeted at a commonly encountered layered or stacked geometry depicted schematically in Figure 3.3a. Oftentimes the computational domain Ω consists of - or can be vertically split into - smaller, non-overlapping subdomains $\{\Omega_i\}_{i=1}^{N_\Omega}$, numbered from top to bottom. Following the domain decomposition concept we aim to compute the solution of Maxwell's equations on each subdomain separately. As adjacent subdomains Ω_i and Ω_{i+i} share a common boundary $\Gamma_i = \{\boldsymbol{r} = (x, y, z)^\intercal \in \mathbb{R}^3 \,|\, z = \gamma_i \in \mathbb{R}\}$, the electric fields E_i in Ω_i and E_{i+1} in Ω_{i+1} must match on Γ_i. We refer to the ensemble $\{\Omega_i\}$ as a *stack*. The algorithm presented here is based on the following assumption.

Assumption 1 (ϵ-Separability). *We assume constant, isotropic permeability and permittivity tensors in the vicinity $\Gamma_i^\epsilon = \{\boldsymbol{r} = (x, y, z)^\intercal \in \mathbb{R}^3 \,|\, |z - \gamma_i| < \epsilon\}$ of Γ_i.*

In the previous section we derived a scattering matrix for a single, isolated domain Ω. We thus isolate each subdomain by introducing artificial, homogeneous, isotropic, infinite sub- and superspaces Ω_i^- and Ω_i^+ below and above each Ω_i. In Figure 3.3b this is depicted schematically. Matching exterior domains for neighboring subdomains, i.e. the chosen permittivities and permeabilities on Ω_i^- and Ω_{i+1}^+ should be identical, and k-spacings are required. This allows us to compute scattering matrices $\mathcal{T}^i$ for every subdomain individually.

A solution to Maxwell's equation requires the total electric field $E = E_{in} + E_{sc}$ on the shared boundary Γ_i between Ω_i and Ω_{i+1} to match. As $\Gamma_i = \Omega_i^- \cap \Omega_{i+1}^+$, we can describe E on Γ_i in two separate ways. Regarding the subproblem for Ω_i first, we have illumination (i.e. upward propagating fields) incident from Ω_i^- and scattered (i.e. downward propagating) fields. The latter are either caused by reflection of the incident field in the same domain or fields transmitted through the domain.

3. Mathematical Basics

As in (3.40) we denote $\mathcal{U} = (\mathcal{U}_+ \, \mathcal{U}_-) = \boldsymbol{U}(\boldsymbol{r}) \in \mathbb{C}^{3 \times N}$ the collective amplitudes of plane waves associated with the upward and downward propagating Fourier modes in $\mathfrak{K} = \mathfrak{K}_i^- = \mathfrak{K}_{i+1}^+$ at an arbitrary but fixed point $\boldsymbol{r} \in \Gamma_i$. Similarly we use the vector notation for the Fourier coefficients of the incident fields $\boldsymbol{E}_i^\pm$. This yields $E_{in} = \mathcal{U}_+ \boldsymbol{E}_i^-$ for this illumination and the scattered fields become $E_{sc,1} = \mathcal{U}_- \mathcal{T}_{2,2}^i \boldsymbol{E}_i^-$ and $E_{sc,2} = \mathcal{U}_- \mathcal{T}_{2,1}^i \boldsymbol{E}_i^+$ where we used the scattering matrix $\mathcal{T}^i$ to relate illuminating fields to scattered fields. An examination of the subproblem for Ω_{i+1}^+ yields related expressions: $\boldsymbol{E}_{in} = \mathcal{U}_- \boldsymbol{E}_{i+1}^+$ and $\boldsymbol{E}_{sc} = \mathcal{U}_+ \mathcal{T}_{1,1}^{i+1} \boldsymbol{E}_{i+1}^+ + \mathcal{U}_+ \mathcal{T}_{1,2}^{i+1} \boldsymbol{E}_{i+1}^-$. Note the changed propagating direction of illumination and scattered fields compared to the previous case. These considerations lead to the following equation in $\boldsymbol{r}$:

$$\mathcal{U}_+ \boldsymbol{E}_i^- + \mathcal{U}_- \left(\mathcal{T}_{2,1}^i \boldsymbol{E}_i^+ + \mathcal{T}_{2,2}^i \boldsymbol{E}_i^- \right) = \mathcal{U}_- \boldsymbol{E}_{i+1}^+ + \mathcal{U}_+ \left(\mathcal{T}_{1,1}^{i+1} \boldsymbol{E}_{i+1}^+ + \mathcal{T}_{1,2}^{i+1} \boldsymbol{E}_{i+1}^- \right) \quad (3.41)$$

As (3.41) must hold for every $\boldsymbol{r} \in \Gamma_i$ and arbitrary $\mathcal{U}$ we immediately find

$$\boldsymbol{E}_i^- = \mathcal{T}_{1,1}^{i+1} \boldsymbol{E}_{i+1}^+ + \mathcal{T}_{1,2}^{i+1} \boldsymbol{E}_{i+1}^-$$
$$\boldsymbol{E}_{i+1}^+ = \mathcal{T}_{2,1}^i \boldsymbol{E}_i^+ + \mathcal{T}_{2,2}^i \boldsymbol{E}_i^- \quad (3.42)$$

The interface conditions for Γ_0 and Γ_{N_Ω} are trivial. The matching conditions (3.42) for all interfaces Γ_i can be collected in a *stack matrix* $\mathcal{S}$ by traversing the interfaces top to bottom. The resulting matrix

$$\mathcal{S} = \begin{pmatrix} \mathcal{I} & & & & & & & & \\ -\mathcal{T}_{2,1}^1 & -\mathcal{T}_{2,2}^1 & \mathcal{I} & & & & & & \\ & \mathcal{I} & -\mathcal{T}_{1,1}^2 & -\mathcal{T}_{1,2}^2 & & & & & \\ & -\mathcal{T}_{2,1}^2 & -\mathcal{T}_{2,2}^2 & \mathcal{I} & & & & & \\ & & \mathcal{I} & -\mathcal{T}_{1,1}^3 & -\mathcal{T}_{1,2}^3 & & & & \\ & & -\mathcal{T}_{2,1}^3 & -\mathcal{T}_{2,2}^3 & \mathcal{I} & & & \\ & & & \mathcal{I} & \ddots & & & \\ & & & & & \ddots & & \\ & & & & & -\mathcal{T}_{2,2}^{N-1} & \mathcal{I} & \\ & & & & & \mathcal{I} & -\mathcal{T}_{1,1}^N & -\mathcal{T}_{1,2}^N \\ & & & & & & & \mathcal{I} \end{pmatrix}$$

is block tridiagonal. In the same way we collect the Fourier coefficients $\boldsymbol{E}_i = (\boldsymbol{E}_i^+ \, \boldsymbol{E}_i^-)$ of all subdomains Ω_i in a vector. The global illumination source of the stack can be encoded as an illumination source $\boldsymbol{s}_{in}$. Thus we find the system

$$\mathcal{S} \boldsymbol{w} = \boldsymbol{s}_{in} \quad (3.43)$$
$$\boldsymbol{w} = \mathcal{S}^{-1} \boldsymbol{s}_{in}$$

The solution $\boldsymbol{w}$ of (3.43) is a complex valued vector containing Fourier coefficients of

all incoming fields in the subproblems. Its dimension is determined by the number of interfaces and the cardinalities of the k-spacings involved.

The incoherent domain decomposition algorithm in Section 4.3 relies on this concept. In the Appendix A.1 we look at the common case of coupling of two domains and derive a relation to iterative methods.

3.3.4. Semi-analytical method for layered media

In case of homogeneous, isotropic, non-magnetic materials separated by planar interfaces the solution can be computed very efficiently using semi-analytical approaches. The solution to Maxwell's equation for plane wave illumination in such *layered media* or *multilayer* stacks is oftentimes computed with a transfer matrix method. Many variations, descriptions and implementations exist. Classically, these are formulated in S- or T-matrix formalisms using 2×2 matrices describing reflection and transmission at planar interfaces. Here, the Fresnel coefficients enter. Likewise, propagation within each uniform layer is described by a matrix containing phase shifts and dampings. Multiplication of these matrices readily yields the scattering matrix of the layered media. This method does not allow to access the fields within a layer directly which is required if one wants to attribute attenuation to a specific layer. For more detailed insights we refer to the extensive literature on multi-layer [Harbecke, 1986, Santbergen et al., 2013] and Fourier Modal Methods [Li, 1996, Lavrinenko et al., 2014, Gutsche, 2014].

In the following we briefly present a semi-analytical method to compute the amplitudes of the fields within every layer simultaneously. This approach is previously documented in [Lockau, 2012] and in [Pomplun, 2006] in greater detail. In the Appendix A.2 we additionally derive the electric field energy within the stack analytically. As above we assume the stack to oriented along the z-axis. Instead of traversing the N domains as before, we now focus on the interface conditions for the different Fourier-modes. The assumption of homogeneous isotropic materials allows to represent the electromagnetic field as Fourier-modes as there are no field discontinuities in z-direction. The individual plane waves are not coupled by the layers or interfaces thus it suffices to investigate one. In the following we use the numbering presented in Figure 3.4 and focus on a single mode $\boldsymbol{u}$. Inside every layer i we split the mode into up and down propagating plane waves $\boldsymbol{u}_i^+$ and $\boldsymbol{u}_i^-$ whose zero-phase planes we choose to be $z = z_{i-1}$ and $z = z_i$. These are marked with dots in Figure 3.4 and ensure decreasing field amplitudes with increasing propagation distance from the interfaces. The layers 0 and $N+1$ are assumed to be infinite.

In every layer we have three degrees of freedom for the amplitudes of the propagating waves as the wave vectors $\boldsymbol{k}_i^{\pm}$ are already determined by the Fourier mode considered and the material parameters ε_i, μ_i in the layer. In total we have $3 \cdot 2 \cdot (N+2)$ degrees of freedom. As

$$\boldsymbol{k}_i^{\pm} \cdot \boldsymbol{u}_i^{\pm} = 0 \tag{3.44}$$

must hold in every layer we collect $2N + 2$ conditions in the stack. In the infinite layers only outgoing fields are unknown and treated the same way whereas incoming fields are known. Hence they fulfill (3.44) trivially. However, they are prescribes as right hand sides and fix additional 6 degrees of freedom. The remaining $4N + 4$ conditions are fixed by the continuity conditions for the tangential components of $\boldsymbol{E}$ and $\boldsymbol{H}$ and the normal components of $\boldsymbol{D}$ and $\boldsymbol{B}$ derived from Maxwell's equations [Nolting, 1990]. These read

$$(\varepsilon_i \boldsymbol{u}_i - \varepsilon_{i+1} \boldsymbol{u}_{i+1}) \cdot \boldsymbol{n} = 0$$
$$(\nabla \times \boldsymbol{u}_i - \nabla \times \boldsymbol{u}_{i+1}) \cdot \boldsymbol{n} = 0$$
$$(\boldsymbol{u}_i - \boldsymbol{u}_{i+1}) \times \boldsymbol{n} = 0$$
$$\left(\mu_i^{-1} \nabla \times \boldsymbol{u}_i - \mu_{i+1}^{-1} \nabla \times \boldsymbol{u}_{i+1}\right) \times \boldsymbol{n} = 0$$

and must hold across the $N + 1$ material interfaces.

These conditions form a linear system which can be solved very fast for a given layered media stack with materials $\{\varepsilon_i, \mu_i\}_{i=1}^{N}$ and thicknesses $\{d_i = z_i - z_{i-1}\}_{i=1}^{N}$.
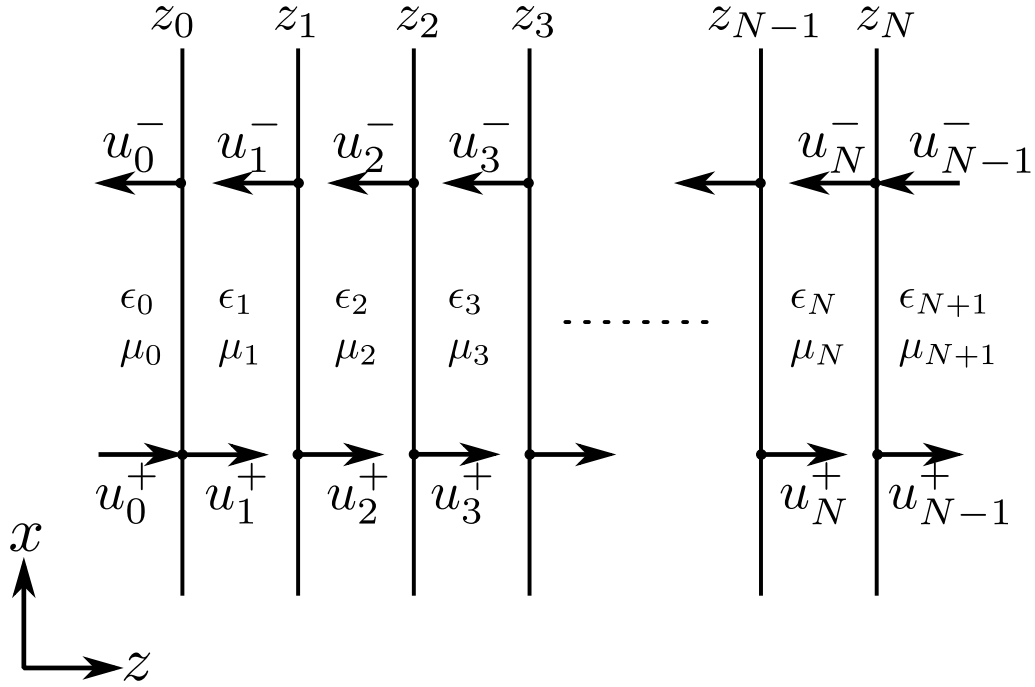

Figure 3.4.: Labeling of the layered media stack and fields involved in algorithm is described in the text. The vertical lines mark interfaces at the position $z_i \in \mathbb{R}$. The arrows indicate propagating directions of the fields $\boldsymbol{u}_i$ in layer i with permittivity ε_i and permeability μ_i. The zero-phase planes are determined by the dots.

4. Incoherence in Rigorous Optical Simulations

This chapter presents a tailored domain decomposition algorithm that allows to model incoherent light efficiently in rigorous optical simulations. The application of the algorithm is the frequently encountered setup of a substrate coupled to a nano-photonic device which is common for the type of solar cells investigated in this thesis. The key contribution here is the use of the domain decomposition framework to model incoherence and an efficient method to compute quadratic outputs of interest.

The chapter starts with a brief introduction to incoherence in Section 4.1 where its effects are described and polarization incoherence is modeled. Additionally the spectral decomposition of an incoherent light source is presented and the averaging of derived field quantities is introduced. Existing modeling approaches for incoherent light in the context of solar cells are presented in Section 4.2. The proposed domain decomposition method is presented in Section 4.3. Here, the averaging for a coherent summation of fields is discussed before the orthogonal decomposition is derived to speed up computations. The details of the algorithm are presented and discussed in the context of previous concepts.

4.1. Introduction to incoherence

Electromagnetic waves (like any kind of wave) only exhibit stationary interference patterns if they are correlated in time and space. This ability of a wave to interfere with itself or other waves constructively enables many physical effects and related technologies such as the anti-reflective coating (cf. Section 2.2.1), lithography or lasing. In Figure 4.1 the intensity pattern of a coherent (4.1b), partially coherent (4.1c) and incoherent (4.1d) superposition is depicted. The sun and thermal light sources in general emit uncorrelated or *incoherent* radiation. At macro scales geometrical optics or "ray tracing" is sufficient to describe refraction and scattering of light as only the (incoherent) light intensity is of importance. With feature sizes of scattering structures and layer thicknesses on the nanoscale, this is not the case for optical wavelengths and coherent wave optical effects have to be considered.

4.1.1. Polarization incoherence in solar cell modeling

Rigorous modeling requires a coherent illumination source with a well defined polarization. Modeling polarization incoherence for a plane wave illumination source

(a)

(b) coherence pattern   (c) partial coherence pattern   (d) incoherence pattern
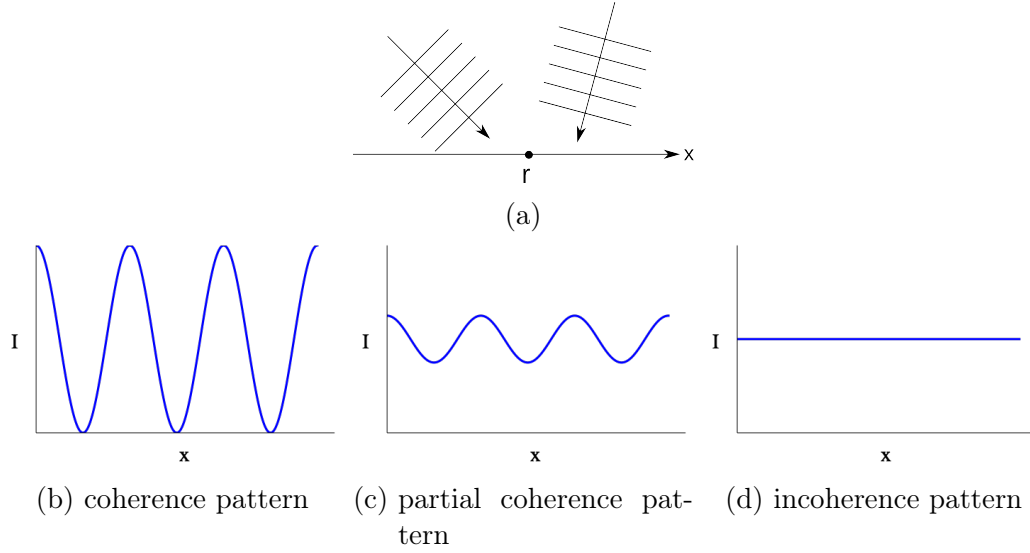
Figure 4.1.: Schematic of electromagnetic fields (depicted as plane waves in (a)) interfering at a point r on the x-axis. Resulting interference patterns in case of (b) coherent, (c) partially coherent or (d) incoherent fields.

is simple. The incident plane wave $\boldsymbol{E}_{in}$ amplitude can be written as the sum of two orthogonal, normalized field components

$$\boldsymbol{E}_{in} = \alpha_1 \boldsymbol{E}_{in}^1 + \alpha_2 \boldsymbol{E}_{in}^2$$

with $\boldsymbol{E}_{in}^1 \cdot \boldsymbol{E}_{in}^2 = 0$ and $\alpha_1, \alpha_2 \in \mathbb{C}$. Exploiting the linearity of Maxwell's equations allows to decompose the resulting scattered field into components

$$\boldsymbol{E}_{sc} = \alpha_1 \boldsymbol{E}_{sc}^1 + \alpha_2 \boldsymbol{E}_{sc}^2$$

as well. For the scattered fields we can no longer assume orthogonality. In consequence, the intensity of the scattered field becomes

$$\|\boldsymbol{E}_{sc}\|^2 = \|\alpha_1 \boldsymbol{E}_{sc}^1 + \alpha_2 \boldsymbol{E}_{sc}^2\|^2 = |\alpha_1|^2 \|\boldsymbol{E}_{sc}^1\|^2 + |\alpha_2|^2 \|\boldsymbol{E}_{sc}^2\|^2 + 2\Re\mathfrak{e}\left\{\alpha_1 \alpha_2 \boldsymbol{E}_{sc}^1 \cdot \boldsymbol{E}_{sc}^2\right\}.$$

In general, the last term does not vanish. However, averaging over all possible polarizations eliminates this term. This is easily demonstrated by parameterizing the amplitude of the incident wave

$$\boldsymbol{E}_{in}(\theta) = a\left(\cos(\theta)\boldsymbol{E}_{in}^1 + \sin(\theta)\boldsymbol{E}_{in}^2\right)$$

where $a \in \mathbb{C}, \theta \in [0, 2\pi]$ and averaging of the angular parameter yields

$$
\begin{aligned}
\langle \boldsymbol{E}_{sc}(\theta) \rangle_\theta &= \frac{|a|^2}{2\pi} \int_0^{2\pi} \cos^2(\theta) \|\boldsymbol{E}_{sc}^1\|^2 + \sin^2(\theta) \|\boldsymbol{E}_{sc}^2\|^2 \, \mathrm{d}\theta \\
&\quad + \frac{|a|^2}{2\pi} \int_0^{2\pi} 2\mathfrak{Re} \left\{ \sin(\theta) \cos(\theta) \boldsymbol{E}_{sc}^1 \cdot \boldsymbol{E}_{sc}^2 \right\} \, \mathrm{d}\theta \\
&= \frac{|a|^2}{2} \left(\|\boldsymbol{E}_{sc}^1\|^2 + \|\boldsymbol{E}_{sc}^2\|^2 \right).
\end{aligned}
\tag{4.1}
$$

Thus the incoherent average over all possible polarizations is obtained by computing the average of two orthogonal polarizations.

4.1.2. Spectral decomposition of an incoherent source

In a monochromatic, coherent wave the field amplitude is constant whereas the phase varies with time. Typically, this is not the case for real-world light sources and the amplitudes are only constant within a (small) *coherence* time. Furthermore, the light has a spectral bandwidth $\Delta\omega$ instead of a single frequency ω_0. The Fourier transform allows to write every polychromatic light field as a superposition of monochromatic light sources. In case of an incoherent illumination, the power spectral density of the source can be used to determine the response of an optical system to the illumination by weighting the responses of monochromatic illuminations according to the spectral density. This approach is usually used for solar cell modeling to compute the implied photo-currents by weighting the computed monochromatic absorption with the spectral density of the sun depicted in Figure 2.3.

In the field of partial coherence the *mutual coherence function*

$$
\Gamma(\boldsymbol{r}_1, \boldsymbol{r}_2, \tau) = \lim_{T \to \infty} \frac{1}{2T} \int_{-T}^{T} F(\boldsymbol{r}_1, t) F(\boldsymbol{r}_2, t + \tau) \, \mathrm{d}t
$$

introduced by [Born and Wolf, 1999] is used to describe the correlation of a field F at two points $\boldsymbol{r}_1, \boldsymbol{r}_2$ at time delay τ. A similar *mutual spectral density* is obtained by Fourier transformation of the time-dependent source fields to characterize the correlation with itself in time. In [Lockau, 2012] this was used to justify the monochromatic plane wave as a source model for solar illumination.

The spectral density is related to the auto-correlation of a signal via the Wiener-Khinchin-theorem [Goodman, 2000]. In Section 2.2.2 we exploited this already for a spatial signal but the same can be done for a temporal signal. In [Sarrazin et al., 2013, Herman et al., 2014] this is used to derive an incoherence function

$$
I(\omega) = \tau_c \sqrt{\frac{\ln 2}{\pi^3}} e^{-\frac{\ln 2}{\pi^2} \tau_c^2 \omega^2}
\tag{4.2}
$$

with a Gaussian spectral density depending on the coherence time τ_c of a stochastic

modulation of a temporal signal. This is a model of a monochromatic source with a finite coherence time. A similar model is obtained by disturbing the temporal signal of a monochromatic wave by a stochastic modulation and subsequent Fourier transformation of a simulated signal [Lee et al., 2012].

4.1.3. Averaging of derived quantities

We can use the spectral decomposition of the (partially) incoherent source to compute incoherent averages of quantities derived from the electromagnetic field in analog to (4.1). A common application, for example in optical simulations of solar cells, is the determination of optical losses in terms of volume absorption

$$A = 2\omega \Im\mathfrak{m} \left\{ \int_\Omega E \cdot \overline{D} \,\mathrm{d}\boldsymbol{r} \right\} = 2\omega \Im\mathfrak{m} \left\{ \int_\Omega \frac{1}{4} E \cdot \overline{\varepsilon E} \,\mathrm{d}\boldsymbol{r} \right\} \tag{4.3}$$

which requires the volume integration of the electric field energy density, which is a (quadratic) nonlinear function of the electric field. The energy flux in homogeneous, transparent media is another example for a derived quantity.

Instead of regarding the frequency spectrum as in the previous section, we use the wavelength dependent spectrum $\xi : \lambda \mapsto [0, \infty)$. We denote the wavelength dependent quantity $J(\lambda) = J(E(\lambda))$. The averaged quantity $<J>$ is

$$<J> = \int_\Lambda \xi(\lambda) J(\lambda) \,\mathrm{d}\lambda. \tag{4.4}$$

Here $\Lambda \subset [0, \infty)$ denotes the wavelength interval of interest which is usually small and bounded. This notation covers the equi-distribution used in Section 4.1.1, Gaussian-distribution used in Section 4.1.2 and the weighting by the solar photon flux in Section 2.1.2 in computations of the j_{sc}. We thus make no assumptions on the weighting function ξ.

The case of averaging a linear quantity is trivial and thus omitted here. Here, we assume the derived quantity J to be the volume or surface integral over a quadratic function of the electromagnetic field E, i.e. $J(\lambda) = \int_\Omega \mathfrak{j}(\lambda, \boldsymbol{r}) \,\mathrm{d}\boldsymbol{r}$ with density $\mathfrak{j}$. In the following we thus restrict the computation to the product $\boldsymbol{E}^H \boldsymbol{E}$ (here $\boldsymbol{E}^H$ denotes the complex conjugate transpose to be distinguished from the component wise complex conjugate $\overline{\boldsymbol{E}}$) which is the major building block of (4.3). A scalar permittivity $\varepsilon \in \mathbb{C}$ can be moved out of the density in (4.3) easily, giving rise to this product. A non-scalar permittivity tensor can be treated similarly, but would introduce additional terms which complicate notation without providing additional insights.

4.2. Modeling approaches for incoherence

Modeling (partially) incoherent electromagnetic fields has been an active field in recent years and several models and algorithms have been suggested. Models either address the response of a structure if the illumination source is (partially) incoherent or derive the response of a structure that removes coherence.

A typical example of the latter is found in the field of multilayer or thin-film systems [Harbecke, 1986]. Here a layer that does not exhibit interference effects in reflection or transmission measurements is called an *incoherent layer*. Typically, these layers are thicker than the coherence length of the illumination source and/or the layer interfaces are not plan parallel as assumed in the models. As these layers remove phase correlations between the illumination and the scattered light, the phase is usually neglected and only the amplitudes are investigated. These models have been adapted to the field of thin-film solar cells and combined with the scalar scattering theory [Krč et al., 2003]. Here, the field is split into a coherent beam and a separate incoherent beam.

Another approach to model incoherent layers in multilayer films is averaging over multiple simulations. The availability of efficient semi-analytical methods (cf. Section 3.3.4) allows to compute the same structure multiple times with varying thicknesses [Prentice, 2000] or by randomization of the phase shift introduced by the incoherent layer [Santbergen et al., 2013]. We will demonstrate the equivalence of both methods in Section 4.3.3.

Modeling of incoherent illumination generally relies on the spectral decomposition of the source field as outlined in Section 4.1.2. This allows to regard the incoherent source as the superposition of monochromatic fields which are correlated according to the spectral density [Sarrazin et al., 2013, Lee et al., 2012]. A modulation of the transient signal by a modulating function with randomized jump intervals can be analyzed numerically by its Fourier transform [Lee et al., 2012] or used as the motivation for a parameterized spectral density [Sarrazin et al., 2013]. Like in the multilayer case, where an average is applied, these models rely on a convolution of the coherent response of a complex optical system with the spectral density. As it is applied after coherent computations, it acts as a moving average filter on the computed coherent spectrum. Thus the response of the system can be easily investigated under varying coherence lengths of the illumination. In Section 6.2.6 the effect of this filtering is demonstrated for a solar cell model.

A very frequently encountered experimental setup, where a thick substrate layer is part of the optical system, has been investigated by multiple groups as well. This configuration is commonly found in applications ranging from photonic crystals [Becker et al., 2014], solar cells [Lockau, 2012] and light-emitting diodes [Zschiedrich et al., 2012]. Here, a nano-photonic system containing subwavelength sized features is coupled to a glass substrate or a multilayer stack of several mm thickness. The substrate is generally assumed to be an incoherent layer, i.e. it does not show interference effects in reflection or transmission measurements even if the incident light is coherent.

This setup poses a challenge to rigorous simulation routines such as the finite element method due to the large discrepancy in scales between the substrate and the rest of the device. Usually, the glass layer is not accounted for and the illumination is modeled as incident from an infinite half-space with a correction for the initial reflection at the air/substrate interface using Fresnel's equations.

As drastically reducing the size of the substrate, to bring the different scales into a regime suitable for example for a FEM discretization, distorts the solution, iterative approaches [Abass et al., 2013, Lockau et al., 2011, Lockau, 2012] have been used to include the substrates. Here, like in ray-tracing methods based on geometrical optics, the path of the light or its energy is traced between the substrate and the solar cell or photonic device. After every pass through the photonic device, the absorption within it is calculated and the reflected fraction of light is propagated to the substrate/air interface. Here it either is transmitted and thus no longer accounted for, or it is reflected back towards the nano-photonic part of the device. In case of a solar cell, the amount of light trapped by total internal reflection due to scattering into large angles can be significant, especially at long wavelengths where absorption is poor.

These iterative methods are easily implemented, but are inefficient as they require possibly many iteration or passes for the incident light to be fully absorbed or transmitted. This means multiple solutions have to be computed. Furthermore, in all of the passes the absorption within the photonic system has to be computed. This operation can be expensive as well if the discretization has a large number of degrees of freedom $\mathcal{N}$. The number of floating point operations involved in its computation is $O(\mathcal{N}^2)$.

A different approach is taken in [Čampa et al., 2013]. They scale down and adjust the thickness of the substrate layer to eliminate or match the phase of the reflected wave thus mimicking incoherent reflection. The elimination requires particular knowledge about the phase shift introduced by the structure beneath the substrate which is only directly available in layered media and for plane wave illumination. Using this knowledge, the interference fringes in the measured reflection can be eliminated by adjusting the layer thicknesses and averaging the simulation results. In more realistic setups, they adjust the thickness to shift the phase of the reflected wave by π such that in the superposition of the solutions the interference term vanishes. However, this only eliminates the interference term of one diffraction order with itself. The specular direction introduces the most visible fringes, thus the correction is applied with respect to it. The method cannot correct for interference fringes excited by multiple diffraction orders as present in strongly scattering structures.
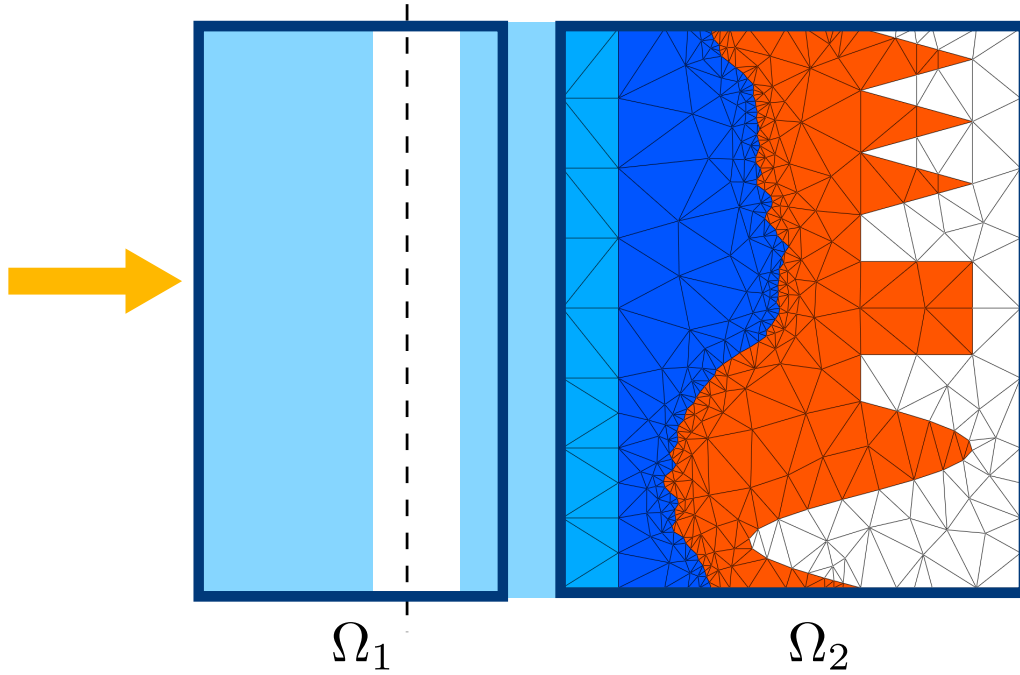
Figure 4.2.: Schematic of the tailored domain decomposition proposed. The two domains are indicated by the rectangles and have domain sizes on different scales. Adaptive finite elements are employed to discretize the scattering structure with features on nanoscales. The much larger homogeneous or simply structured domain is treated with semi-analytical methods.

4.3. Incoherent coupling domain decomposition algorithm

In this section we present an algorithm suited to couple domains incoherently. The algorithm is aimed at a frequently encountered setup depicted in Figure 4.2. The idea of the algorithm is quickly summarized:

(i) Decompose the incoming incoherent electromagnetic field spectrally.

(ii) Accelerate the computations using a tailored domain decomposition method by exploiting the structure of the computational domain.

(iii) Accelerate the evaluation of nonlinear output functionals using an orthogonal decomposition.

In the following we focus on the last steps as the spectral decomposition is already addressed in Section 4.1.2.

As in Section 3.3, where we adapt the notation and concepts from, we assume that the computational domain Ω can be split into subdomains Ω_i. This setup is schematically shown in Figure 4.2. Here the domains are indicated by rectangles.

One is a simply structured domain Ω_1, either a single homogeneous or a layered media consisting of multiple such layers. The second domain Ω_2 is complex and nano-structured. This assumption is fulfilled by typical setups in solar cell or light emitting diode simulations.

We further assume a large discrepancies in the size of the domains involved. In typical application examples this ranges from $O(1000)$ wavelength for Ω_1 to $O(10)$ wavelengths for the complex 3D domain Ω_2. This discrepancy in scale leads to a vastly different sensitivity of the solution with respect to changes in domain size or frequency of the incident light. We state this explicitly for later reference.

Assumption 2 (Low wavelength sensitivity). *We assume a robust behavior of the fields $\mathcal{U}$ in Ω_2 with respect to the wavelength. Hence $\frac{\partial}{\partial \lambda} \mathcal{U}$ is assumed do be negligible in $\Lambda \subset [0, \infty)$ denoting the parameter interval of interest.*

The domain decomposition algorithm outlined in Section 3.3 relies on scattering matrices (cf. Definition 3.20) mapping incident electromagnetic fields represented as Fourier coefficients in the Fourier plane wave basis to the scattered electromagnetic fields excited by the incident fields. We can exploit the structures of Ω to find the appropriate numerical tool best suited for each subdomain independently. The simple structure of Ω_1 allows to determine its scattering matrix $\mathcal{T}_{LM}$ rapidly using a semi-analytical method outlined in Section 3.3.4. The complex structured domain Ω_2 containing subwavelength sized features requires a rigorous treatment with an adaptive finite element discretization to derive the scattering matrix $\mathcal{T}_{FE}$. The subscript reflects the applied numerical tool: LM for layered media represents a semi-analytical method whereas FE stands for finite elements.

The domain decomposition algorithm uses the stack matrix $\mathcal{S}$ constructed from the scattering matrices $\mathcal{T}_i$ of the subdomains Ω_i to compute the weights $\boldsymbol{w}$ as the solution of the linear system (3.43). The computational effort required to construct $\mathcal{S}$ and to compute $\boldsymbol{w}$ from $\mathcal{S}$ and $\boldsymbol{s}_{in}$ is negligible compared to the computational effort required to derive the scattering matrices $\mathcal{T}_i$ for the subdomains Ω_i.

4.3.1. Incoherent average in case of a coherent summation of fields

In the following we derive an incoherent average as in (4.4) for a coherent super-position of electromagnetic fields. This is the natural setting for the domain decomposition method based on scattering matrices where each column of the matrix represents the scattered electromagnetic field in the exterior of the computational domain in a Fourier plane wave basis. In the interior the scattered electromagnetic field is not necessarily decomposable into plane waves. For homogeneous media this is possible and there are analytical formulas to compute even quadratic quantities as assumed here. In Appendix A.2 this is shown explicitly. In the following we will assume the scattered field to be a finite element field.

In Section 3.3 we used N plane waves on k-spacings $\mathfrak{K}$ as incident fields on a domain Ω. We denoted the scattered field excited by the j-th incident field at

$\boldsymbol{r} \in \Omega$ as $\boldsymbol{u}_j(\boldsymbol{r}) \in \mathbb{C}^3$ and found the scattered field $E(\boldsymbol{r}) = \sum_{j=1}^{N} w_j u_j(\boldsymbol{r})$ where w_j are the weights describing the decomposition of the global illumination field. To facilitate reading we drop the spatial coordinate $\boldsymbol{r}$ and use it only to highlight spatial dependence explicitly.

The density $j(\lambda, \boldsymbol{r})$ becomes $j(\lambda) = j(\lambda, \boldsymbol{r}) := E(\lambda, \boldsymbol{r})^H E(\lambda, \boldsymbol{r})$ and similarly $u_j(\boldsymbol{r}) = u_j$.

$$
\begin{aligned}
j(\lambda) = E(\lambda)^H E(\lambda) &= \left(\sum_{j=1}^{N} w_j u_j(\lambda) \right)^H \left(\sum_{k=1}^{N} w_k u_k(\lambda) \right) \\
&= \sum_{j=1}^{N} |w_j|^2 \|u_j(\lambda)\|^2 + \sum_{j=1}^{N} \sum_{\substack{k=1 \\ k \neq j}}^{N} \overline{w_j} w_k u_j(\lambda)^H u_k(\lambda) \\
&= \sum_{j=1}^{N} |w_j|^2 \|u_j(\lambda)\|^2 + 2 \sum_{j=1}^{N} \sum_{k>j}^{N} \mathfrak{Re} \left(\overline{w_j} w_k u_j(\lambda)^H u_k(\lambda) \right)
\end{aligned}
$$

As the spectral average and the volume integration are interchangeable, we find for the averaged density $<j>$

$$
<j> = \int_{\Lambda} \xi(\lambda) j(\lambda) \, d\lambda = \int_{\Lambda} \xi(\lambda) \left(\sum_{j=1}^{N} w_j u_j(\lambda) \right)^H \left(\sum_{k=1}^{N} w_k u_k(\lambda) \right) d\lambda \tag{4.5}
$$

$$
= \sum_{j=1}^{N} \int_{\Lambda} \xi(\lambda) |w_j(\lambda)|^2 \|u_j(\lambda)\|_2^2 \, d\lambda \tag{4.6}
$$

$$
+ 2 \sum_{j=1}^{N} \sum_{k>j}^{N} \mathfrak{Re} \left(\int_{\Lambda} \xi(\lambda) \overline{w_j(\lambda)} w_k(\lambda) u_j(\lambda)^H u_k(\lambda) \, d\lambda \right). \tag{4.7}
$$

This incoherent average is unsuited for most applications even if the wavelength integral is evaluated numerically. This ansatz demands the evaluation of $N + \frac{N(N+1)}{2}$ volume integrals over products of electric fields u_j in (4.6) and (4.7) per wavelength and is thus infeasible to compute. However, this representation allows to distinguish the incoherent part (4.6) and oscillating part (4.7).

4.3.2. Orthogonal decomposition for quadratic outputs of interest

Searching for more efficient ways to compute the volume integral over the averaged density in (4.6) and (4.7) we move to a matrix-vector notation. As in Section 3.3 we use $\mathcal{U} \in \mathbb{C}^{3 \times N}$ to denote the collective field amplitudes of the N fields u_j at a spatial coordinate $\boldsymbol{r}$. This allows to write $E(\boldsymbol{r}) = \mathcal{U}(\boldsymbol{r}) \boldsymbol{w}$ with the weight vector $\boldsymbol{w} \in \mathbb{C}^N$ with the i-th component $(\boldsymbol{w})_i = w_i$. Similarly, $\boldsymbol{U}_i \in \mathbb{C}^N$ is the transpose of

_

the i-th row of the matrix $\mathcal{U}$.

Using the above notation we rewrite (4.5) as

$$\int_\Lambda \xi(\lambda)\mathsf{j}(\lambda)\,\mathrm{d}\lambda = \int_\Lambda \xi(\lambda)\,(\mathcal{U}\boldsymbol{w})^H\,(\mathcal{U}\boldsymbol{w})\,\mathrm{d}\lambda = \int_\Lambda \xi(\lambda)\sum_{i=1}^3 ((\mathcal{U}\boldsymbol{w})_i)^H\,(\mathcal{U}\boldsymbol{w})_i\,\mathrm{d}\lambda$$

$$= \int_\Lambda \xi(\lambda)\sum_{i=1}^3\left\{\sum_{j,k=1}^N \overline{(\boldsymbol{U}_j)_i w_j}w_k(\boldsymbol{U}_k)_i\right\}\mathrm{d}\lambda$$

$$= \int_\Lambda \xi(\lambda)\sum_{i=1}^3 \boldsymbol{U}_i^H\mathcal{W}^H\boldsymbol{U}_i. \tag{4.8}$$

In the last line we used the following definition implicitly.

Definition 4.1 (Weight matrix). The matrix $\mathcal{W} = \boldsymbol{w}\boldsymbol{w}^H \in \mathbb{C}^{N\times N}$ with entries

$$\mathcal{W}_{jk} = \overline{w_j(\lambda)}w_k(\lambda)$$

is called a *weight matrix*. $\mathcal{W}$ is hermitian by construction.

The fact that $\mathcal{W}$ is hermitian allows to apply the following theorem.

Theorem 4.2 (Schur and spectral decomposition). *For any matrix $\mathcal{M} \in \mathbb{C}^{N\times N}$ a unitary matrix $\mathcal{Q} \in \mathbb{C}^{N\times N}$ and an upper triangular matrix $\mathcal{D} \in \mathbb{C}^{N\times N}$ exist such that*

$$\mathcal{M} = \mathcal{Q}\mathcal{D}\mathcal{Q}^H.$$

If $\mathcal{M}$ is hermitian, $\mathcal{D}$ is real, diagonal and its entries are the eigenvalues of $\mathcal{M}$ and the columns of $\mathcal{Q}$ form an orthonormal basis of $\mathbb{C}^N$. If $\mathcal{M}$ is positive semi-definite the spectral decomposition and the Schur decomposition coincide.

The theorem and its proof can be found in different versions in textbooks [Deufl-hard and Hohmann, 1993] and the original article [Schur, 1909]. It is a special case of the more general Singular Value Decomposition (SVD). As we are only dealing with the case of quadratic matrices, we refrain from speaking of a SVD or a Proper Orthogonal Decomposition (POD).

We use $\mathcal{W}^H = \mathcal{W} = \mathcal{Q}^H\mathcal{D}\mathcal{Q}$ in (4.8) and write $\boldsymbol{q}_k$ for the k-th column of $\mathcal{Q}$. $\boldsymbol{q}_k$ is an eigenvector of $\mathcal{W}$ corresponding to the k-th eigenvalue $d_{kk} \in \mathbb{R}$, the diagonal

entry of $\mathcal{D}$. With these notations we continue (4.8) for $<\mathsf{j}>$

$$
\int_\Lambda \xi(\lambda) \sum_{i=1}^3 \boldsymbol{U}_i^H \mathcal{W} \boldsymbol{U}_i = \int_\Lambda \xi(\lambda) \sum_{i=1}^3 \boldsymbol{U}_i^H \mathcal{Q} \mathcal{D} \mathcal{Q}^H \boldsymbol{U}_i \, \mathrm{d}\lambda
$$

$$
= \int_\Lambda \xi(\lambda) \sum_{i=1}^3 \left(\mathcal{Q}^H \boldsymbol{U}_i\right)^H \mathcal{D} \left(\mathcal{Q}^H \boldsymbol{U}_i\right) \, \mathrm{d}\lambda
$$

$$
= \int_\Lambda \xi(\lambda) \sum_{i=1}^3 \left\{ \sum_{k=1}^N \sum_{j=1}^N \overline{(\mathcal{Q}^H)_j \boldsymbol{U}_i} d_{kj} (\mathcal{Q}^H)_k \boldsymbol{U}_i) \right\} \, \mathrm{d}\lambda
$$

$$
= \int_\Lambda \xi(\lambda) \sum_{i=1}^3 \left\{ \sum_{k=1}^N d_{kk} \overline{(\mathcal{Q}^H)_k \boldsymbol{U}_i} (\mathcal{Q}^H)_k \boldsymbol{U}_i) \right\} \, \mathrm{d}\lambda
$$

$$
= \int_\Lambda \xi(\lambda) \sum_{i=1}^3 \left\{ \sum_{k=1}^N d_{kk} \overline{\boldsymbol{q}_k^H \boldsymbol{U}_i} \boldsymbol{q}_k^H \boldsymbol{U}_i) \right\} \, \mathrm{d}\lambda
$$

$$
= \int_\Lambda \xi(\lambda) \sum_{k=1}^N d_{kk} \left\{ \sum_{i=1}^3 \overline{\boldsymbol{q}_k^H \boldsymbol{U}_i} \boldsymbol{q}_k^H \boldsymbol{U}_i) \right\} \, \mathrm{d}\lambda
$$

$$
= \int_\Lambda \xi(\lambda) \sum_{k=1}^N d_{kk} \left\{ (\mathcal{U}\overline{\boldsymbol{q}_k})^H (\mathcal{U}\overline{\boldsymbol{q}_k}) \right\} \, \mathrm{d}\lambda \tag{4.9}
$$

This expression is convenient as $\mathcal{D}$ is usually not of full rank and only a few eigenvalues contribute to the integral. Without loss of accuracy it is possible to restrict the summation in (4.9) to $d_{kk} \neq 0$.

$$
<\mathsf{j}> = \int_\Lambda \xi(\lambda) \sum_{\substack{k=1 \\ d_{kk} \neq 0}}^N d_{kk} \left\{ (\mathcal{U}\overline{\boldsymbol{q}_k})^H (\mathcal{U}\overline{\boldsymbol{q}_k}) \right\} \, \mathrm{d}\lambda \tag{4.10}
$$

Special case: constant fields

We return to the case of coupled domains. As noted above, the computational effort required to compute $\boldsymbol{w}$ is negligible compared to the computation of the scattering matrices $\mathcal{T}_i$ for the subdomains Ω_i or the computation of a single volume integration of the density. The same holds for the orthogonal decomposition of the weight matrix. Even with the reduced costs of computing at most N volume integrals, it is impractical to evaluate the averaged density expression (4.10) as it requires the coherent solutions for all $\lambda \in \Lambda$.

However, it is possible to compute an approximation to (4.10) for specific cases where Assumption 2 holds. This assumption allows to treat the fields u_k and thus the matrix $\mathcal{U}$ as independent of λ in Λ. This leads to the following approximation

of (4.10)

$$
\begin{aligned}
<\mathsf{j}> &= \int_\Lambda \xi(\lambda) \sum_{i=1}^{3} \boldsymbol{U}_i^H \mathcal{W} \boldsymbol{U}_i \, \mathrm{d}\lambda \\
&\approx \sum_{i=1}^{3} \boldsymbol{U}_i^H \left(\int_\Lambda \xi(\lambda) \mathcal{W} \, \mathrm{d}\lambda \right) \boldsymbol{U}_i = \sum_{i=1}^{3} \boldsymbol{U}_i^H <\mathcal{W}> \boldsymbol{U}_i \\
&= \sum_{\substack{k=1 \\ d_{kk} \neq 0}}^{N} d_{kk} \left\{ (\mathcal{U}\overline{\boldsymbol{p}_k})^H (\mathcal{U}\overline{\boldsymbol{p}_k}) \right\}
\end{aligned}
\tag{4.11}
$$

where $\boldsymbol{p}_k$ denotes the eigenvector of $<\mathcal{W}>$, the incoherently averaged weight matrix. If the fields are actually independent of λ, the approximation is error free.

4.3.3. Incoherent coupling algorithm

Based on the findings in the previous sections we can present an algorithm to efficiently calculate the effects of an incoherent illumination or an incoherent layer for the setup depicted in Figure 4.2. The substrate Ω_{LM} is simply structured and can be treated semi-analytically (cf. Section 3.3.4), whereas the nano-structured subdomain Ω_{FE} is discretized using adaptive finite elements. Based on Assumption 2 we treat the fields in Ω_2 as independent of λ which also means $\mathcal{T}_{FE}$ is constant over Λ. This is justified due to separation of scales between the Ω_{LM} and the cell Ω_{FE}.

The spectral average over $\mathcal{W}$ can be computed explicitly. As $\mathcal{T}_{FE}$ is constant only $\mathcal{T}_{LM}$ needs to be reevaluated to construct $\mathcal{S}$ for changing λ which is assumed to be a fast operation. Computing this scattering matrix comprises solving N independent, semi-analytical problems whose computational costs only depend on the number of layers involved. As mentioned in Section 4.2 the wavelength of the illumination and the thickness of a layer inside a multilayer stack are interchangeable as a closer look into the algorithm in Section 3.3.4 reveals.

The thicknesses $d_i = z_i - z_{i-1}$ of layer i with z_i taken from Figure 3.4 enter only in the forward and backward propagation within each layer to state the coupling condition on the opposing interface to the adjacent layer. This is achieved by a multiplication of the amplitudes with the phase factor $\phi = e^{ik_z(\boldsymbol{k}_\perp)d_i}$ where the dependence of $k_z(\boldsymbol{k}_\perp)$ on the wavelength is known (cf. (3.34) in Section 3.3.1). Hence we can obtain the solution for λ' instead of λ by adjusting d_i to $d_i' = d_i k_z(\boldsymbol{k}_\perp)(k_{z'}(\boldsymbol{k}_\perp))^{-1}$. Note that we need to adjust every layer thickness differently according to $\boldsymbol{k}_\perp$. Computing $\mathcal{T}_{LM}$ for a different wavelength can thus be achieved by adjusting the thickness for each plane wave of the k-spacing first and subsequent re-computation.

However, when aiming at an incoherent coupling of two domains a neglect of the adjusting step for wavelength or thickness for each member of the k-spacing provides an additional benefit of decoupling the diffraction orders. As $k_z(\boldsymbol{k}_\perp)$ depends not

only on the wavelength but also on $\boldsymbol{k}_\perp$, keeping a constant layer thickness d while changing the wavelength introduces different phase shifts for different $\boldsymbol{k}_\perp$. This reduces interference effects between the fields excited by these plane waves in the nano-structured subdomains.

The Algorithm 1 is split into three phases. First, the proper Fourier plane wave basis i.e. the k-spacing for the scattering matrices has to be chosen and the corresponding scattering matrix $\mathcal{T}_{FE}$ of the complex structured domain is computed using an adaptive finite element discretization. Reusing the LU decomposition of the finite element system matrix helps to reduce computational costs by handling multiple sources simultaneously. Next, the incoherent illumination is spectrally decomposed and its statistical variation is encoded in a variation of the simply structured domain. This concludes the first phase. In analog to the Reduced Basis Method presented in Chapter 5 we can call this the *offline* phase.

Subsequently we can now compute the scattering matrix $\mathcal{T}_{LM}$ of the simple domain for a number of parameters very quickly using one of the inexpensive semi-analytical methods presented in Section 3.3.4. For every λ we can combine the scattering matrices of the simple and complex structured domains to form the stack matrix $\mathcal{S}$ and solve the stack system. In addition, we update the weight matrix $\mathcal{W}$. We call this the *online* phase.

This yields a sequence of solutions to the Maxwell's equation of the coupled system for varying parameters encoded in the Fourier plane wave basis. In a post processing step these can be used to compute the incoherently averaged quantities of interest. The orthogonal decomposition presented in Section 4.3.2 reduces the computational cost for this step drastically thus making the computation feasible. We call this the *post processing* phase.

The algorithm presented above is not limited to two domains and can easily be extended to multiple domains. Also the light is not required to be incident from the substrate side as shown in Figure 4.2. The domain decomposition algorithm works in any of these cases. However, the orthogonal decomposition for quadratic outputs of interest in Section 4.3.2 relies on the Assumption 2. Thus the incoherent part of the algorithm will only reduce costs as long as the quantity of interest is derived from the domain assumed to have low sensitivity with respect to the wavelength.

4.3.4. Comparison to other approaches

The algorithm presented here combines ideas from other approaches to gain a computationally advantageous method. Note, that we have assumed the parameter λ to be the wavelength, but we have not exploited this fact anywhere. We can treat λ to be a general parameter changing material properties or geometrical sizes equivalently. This means, all the presented modeling approaches in Section 4.2 can be treated in this framework. It allows to model an incoherent layer like it is common practice in the multilayer or thin-film community. The usually applied averaging is feasible as the changes are reflected in adaptations of the layered media and not the finite element block. The same holds true for a randomization of the phase in the

---

Algorithm 1 incoherent coupling of two domains

---

*%% **offline** - initialization of quantities*
determine k-spacing $\mathfrak{K}$
compute scattering matrix $\mathcal{T}_{FE}$ of the complex structured domain
determine illumination statistics $\{\lambda_k, \boldsymbol{s}_{in}^k, \xi_k\}_{k=1}^M$
initialize weight matrix $\mathcal{W} \leftarrow 0$

*%% **online** - solution of coupled systems*
for $k \in \{1, \ldots, M\}$ **do**
   compute scattering matrix of simply structured domain $\mathcal{T}_{LM}(\lambda_k)$
   build stack matrix $\mathcal{S}_{\lambda_k} \leftarrow \{\mathcal{T}_{FE}, \mathcal{T}_{LM}\}$
   solve $\mathcal{S}_{\lambda_k} \boldsymbol{w} = \boldsymbol{s}_{in}^k$
   update weight matrix $\mathcal{W} \leftarrow \mathcal{W} + \xi_k \boldsymbol{w}\boldsymbol{w}^H$
end for

*%% **post processing** - compute incoherent average with orthogonal decomposition*

compute orthogonal decomposition of weight matrix $\mathcal{W}$ resulting in $\mathcal{Q}$ and $\mathcal{D}$
initialize $I \leftarrow 0$
while $|d_k| > tol$ **do**
   $I \leftarrow I + \int_V d_k \left(\mathcal{U}\overline{\boldsymbol{q}_k}\right)^H \left(\mathcal{U}\overline{\boldsymbol{q}_k}\right) \mathrm{d}\boldsymbol{r}$
   $j \leftarrow j + 1$
end while

---

layer which can be achieved by a thickness adjustment of a layer.

Likewise an incoherent light source can be modeled. Computing its spectral decomposition, and adapting the layer thickness of the layered media to reflect changes in wavelength, allows to compute the incoherent averages without significantly increased cost over the expense of computing the scattering matrix of the complex structured block for the central wavelength. As only the spectral decomposition of the source into monochromatic fields is required to compute the average, the derivation of said decomposition does not play a role. In this context a modulation of the transient field is identical to a theoretical or statistical model of the effects of such a modulation. Also the effect of a moving average (MA) filter can be included into the computation of the average itself without additional cost.

The main advantage over iterative models lies in the reduced cost of the coupled problem. In Appendix A.1 we demonstrate the connection of an iterative approach to the direct solution for the coupling conditions. Obviously it is possible to implement an iterative procedure using the scattering matrices of both domains directly to mimic the methods in [Abass et al., 2013] and [Lockau et al., 2011, Lockau, 2012]. Depending on the dimension of the k-spacing N and the eigenvalue spectrum of the averaged weight matrix, the number of volume integrations might be lower for the iterative procedure.

The method of [Čampa et al., 2013] of averaging two simulations for adapted thicknesses can profit from the domain decomposition approach provided the computation of the scattering matrix is not more expensive then solving two finite element problems. However, this should always be the case as the usage of a direct solver allows to scale optimally with the number of right hand sides. Furthermore, due to the tailored decomposition of the domains it is not necessary to discretize large, homogeneous substrates with finite elements like they do, but more efficiently with semi-analytical methods.

5. A Reduced Basis Method for Optical Simulations of Nanostructured Thin-Film Solar Cells

Optimizations of optical properties of nanostructured solar cells are challenging as it requires accounting for various interdependent parameters to be included. In general, the cells are optimized with respect to the short-circuit current density. As outlined in Chapter 2, this usually means to optimize structures with regard to light-trapping at the band edge where absorption is poor. The time and computational resources required to compute the forward solutions during the optimization procedure can render an optimization procedure to become infeasible as for example the wavelength integration of the absorptance within the absorber layer cannot be too sparse to provide a meaningful approximations to the j_{sc}. Reduced order models are well suited to address these *many-query* situations.

In this chapter we present a Reduced Basis Method for the solution of parameterized non-coercive PDEs such as the time-harmonic electromagnetic scattering problem underlying the optical simulations of solar cells. It allows to split the solution of the problem into an expensive offline step executed only once, and an online evaluation with low computational demands. The reduced model is built self-adaptively and allows to compute non-linear outputs of interest orders of magnitude faster than the approximated original problem.

We start with a brief historical review of the method in Section 5.1. In Section 5.2 we define the problem and quantities of interest. The construction of the reduced basis and the estimation of approximation errors are presented in Sections 5.3 and 5.4. An efficient offline-online decomposition requires an affine parameter dependence. In Section 5.5 we employ the Empirical Interpolation Method to construct an affine decomposition for the electromagnetic scattering problem for any parameter dependence. The self-adaptive construction in the offline phase is presented in Section 5.6. Non-linear outputs of interest and their inclusion in the reduced basis formalism are addressed in Section 5.7. The computational costs involved in building a reduced basis are examined in Section 5.8. The chapter is concluded by a brief consideration of high-performance computing aspects in relation to the constructing of a reduced basis in Section 5.9.

5.1. Historical review

The RBM is a promising strategy to be used in model order reduction of μPDEs. It provides a low-dimensional approximation of a (very) high-dimensional problem which implies a structure on the manifold of solutions of the μPDE with respect to the parameter μ. The RBM is observed to converge exponentially and for special cases this has been proven as well [Maday et al., 2002, Binev et al., 2011]. It is widely investigated for applications ranging from structural dynamics [Farhat et al., 2014, Afonso et al., 2009], option pricing [Haasdonk et al., 2012], modeling concentrations of ions in lithium-ion batteries [Lass and Volkwein, 2013], non-linear convection-diffusion in [Drohmann et al., 2011] to hierarchical flow systems such as blood vessels [Maday and Rønquist, 2002, Iapichino et al., 2012, Iapichino et al., 2014]. The investigated PDEs include Stoke's equation [Iapichino et al., 2014], the heat [Bui-Thanh et al., 2008] and Helmholtz equation [Maday and Rønquist, 2002]. A comprehensive overview of the method can be found in [Rozza et al., 2008]. The literature on Maxwell's equations is not as extensive but starting with [Jabbar and Azeman, 2004] several groups have investigated the transient case [Mancini and Volkwein, 2013] as well as the time-harmonic case [Pomplun, 2010, Chen et al., 2011, Benner and Schneider, 2013].

The RBM was introduced for a parametric setting in nonlinear analysis of structures [Almroth et al., 1978, Noor and Peters, 1980]. These early works were restricted to a single parameter and lacked the currently used *a posteriori* estimators and sampling procedures as well as rigorous error bounds. Nowadays the RBM has been extended to more general PDE and ordinary differential equation (ODE) contexts and is mostly used in the real-time or multi-query context where inexpensive and therefore very many or extremely fast solutions of a μPDE are sought after. The appeal of this method relies in the offline-online splitting of the solution process into two phases: an expensive *offline* procedure and an inexpensive *online* phase. Ideally the reduced basis can be evaluated in the online phase at very low computational costs with a guaranteed accuracy. The objective is thus to fully decouple the evaluation of the reduced basis from the dimension $\mathcal{N}$ of the underlying FEM discretization of the μPDE during the online phase. The decoupling requires an affinity in the parameter dependence and many problems can be modeled with an affine parameter dependence. However, for general non-linearities this was not possible until the development of the Empirical Interpolation Method (EIM) allowed for an affine expansion of parameter dependencies. The RBM is historically based on a variational formulation and a finite element discretization but other discretization schemes (e.g. finite volumes) exist.

5.2. Problem definition and quantities of interest

The time-harmonic electromagnetic scattering problem 2 relates an input (e.g. material distributions, source fields) to an output via a parameterized PDE. Its solution

is the electromagnetic field, a physical quantity that oftentimes is of lesser interest. Instead, derived quantities of this field are more commonly investigated, for example the coefficients of its Fourier transform, the power fluxes between different (sub-) domains or the electric field energy contained within a (sub-) domain. In a more general setting these notions are not only applicable to the time-harmonic electromagnetic scattering problem, but to any parameterized system relating inputs to outputs via a PDE where quantities of interest are given as functionals of the PDE-solution. In the following we consider real valued parameters $\mu \in \mathfrak{D} \subset \mathbb{R}^d$ where $\mathfrak{D}$ is assumed to be bounded and consider output quantities s_l and s_q where the subscripts distinguish between linear and quadratic quantities throughout this chapter. We state the following input-output relationships for linear and quadratic quantities of interest:

Problem 5. For a given input parameter $\mu \in \mathfrak{D} \subset \mathbb{R}^d$, compute the linear and quadratic outputs of interest

$$s_l(\mu) = l(u(\mu)),$$
$$s_q(\mu) = q(u(\mu)),$$

where $u(\mu) \in X$ satisfies the following weak formulation:
Find $u(\mu) \in X$ such that:

$$a(v, u(\mu); \mu) = f(v; \mu), \quad \forall v \in X \tag{5.1}$$

Here $a(\cdot, \cdot; \mu)$ is a bilinear form describing the weak formulation of a parameter dependent PDE. The outputs are given by a linear functional $l(\cdot) \in (X)'$ and a quadratic functional $q(\cdot) = \tilde{q}(\cdot, \cdot)$, where $\tilde{q}$ is bilinear, respectively.

In general, (5.1) is not solvable in the classical sense. Instead, a numerical method is employed to discretize this variational equation. As stated earlier, the FEM offers many advantages in this context and is generally the method of choice. Assuming a FEM discretization we can state discretized input-output relationships:

Problem 6 (Truth-Approximation). For a given input parameter $\mu \in \mathfrak{D} \subset \mathbb{R}^d$, compute the linear and quadratic outputs of interest

$$s_l(\mu) = l(u^{\mathcal{N}}(\mu)),$$
$$s_q(\mu) = q(u^{\mathcal{N}}(\mu)),$$

where $u^{\mathcal{N}}(\mu) \in X^{\mathcal{N}}$ satisfies the following weak formulation:
Find $u^{\mathcal{N}}(\mu) \in X^{\mathcal{N}}$ such that:

$$a(v, u^{\mathcal{N}}(\mu); \mu) = f(v; \mu), \quad \forall v \in X^{\mathcal{N}} \tag{5.2}$$

The solution of (5.2) in the finite element space $X^{\mathcal{N}} \subset X$ requires the inversion of a large sparse matrix of dimension $\mathcal{N}$, where $\mathcal{N} = \dim X^{\mathcal{N}}$ is usually in the order

of at least $1 \cdot 10^6$ for real world 3D applications. This makes the direct evaluation of the truth approximation for a set $\{\mu_1, \mu_2, \mu_3, \dots\}$ of distinct parameters in many query applications infeasible as a single evaluation may require considerable computational resources. In particular this rules out real-time applications, because a single inversion can take hours.

5.3. Reduced basis approximation and construction

The purpose of the reduced basis approximation is to provide a low-dimensional approximation of the high-dimensional Problem 6 that allows for rapid evaluations for a set of parameters. It is based on the assumption, that the manifold of solutions of the µPDE with respect to all the parameters $\mu \in \mathfrak{D}$

$$\mathfrak{M}^{\mathcal{N}} = \{u^{\mathcal{N}}(\mu) \text{ is a solution to } (5.2) \mid \mu \in \mathfrak{D}\} \subset X^{\mathcal{N}}$$

can be approximated well by low dimensional subspace $X_N \subset \mathfrak{M}^{\mathcal{N}}$. If this assumption holds true, i.e.

$$\mathfrak{M}^{\mathcal{N}} \approx X_N \subset X^{\mathcal{N}},$$

it is reasonable to assume that solutions of the following reduced problem are good approximations of $u^{\mathcal{N}}(\mu)$, the solution of (5.2):

Problem 7 (Reduced Problem)**.** For a given input parameter $\mu \in \mathfrak{D} \subset \mathbb{R}^d$, compute the outputs of interest

$$s_l(\mu) = l(u_N(\mu)),$$
$$s_q(\mu) = q(u_N(\mu)),$$

where $u_N(\mu)$ satisfies the following weak formulation:
Find $u_N(\mu) \in X_N$ such that:

$$a(v, u_N(\mu); \mu) = f(v; \mu), \quad \forall v \in X_N \tag{5.3}$$

We refer to X_N as a reduced basis space with dimension N. A more formal definition reads:

Definition 5.1 (Snapshots, Reduced Basis and Reduced Basis Spaces)**.** Let $D_N = \{\mu_1, \dots, \mu_N\} \subset \mathfrak{D}$ a set of distinct parameter and $\{u^{\mathcal{N}}(\mu_i)\}_{i=1}^N$ the set of corresponding (linearly independent) solutions of (5.2). We refer to $u^{\mathcal{N}}(\mu_i)$ as the *snapshot* corresponding to the parameter μ_i. Then

$$X_N = \text{span}_{i=1,\dots,N}\{u^{\mathcal{N}}(\mu_i)\}$$

is a N-dimensional (Lagrange)- *reduced basis space*. A basis $\Phi_N = \{\phi_1, \dots, \phi_N\} \subset X_N \subset X$ of a reduced basis space X_N is called a *reduced basis*.
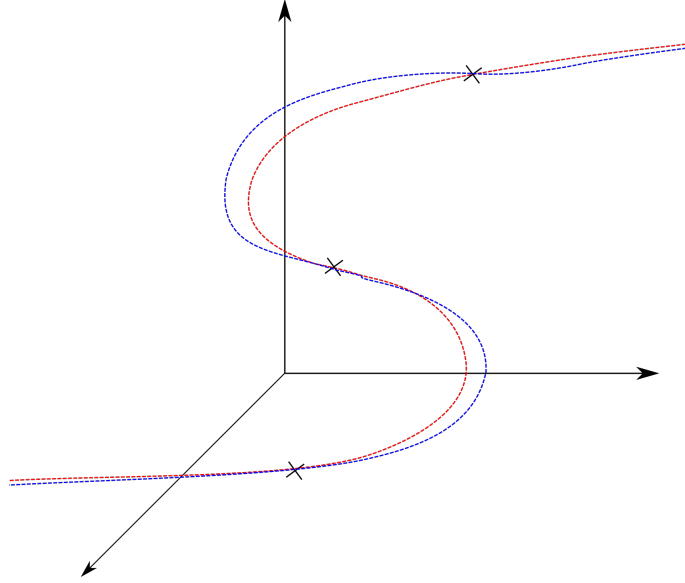
Figure 5.1.: Schematic of the solution manifold $\mathfrak{M}$ (red). A point on it corresponds to a solution of (5.2) a parameter $\mu \subset \mathfrak{D}$. The *snapshots* are marked as crosses. An approximation of the manifold based on the reduced basis space spanned by these snapshot solutions is shown in blue.

Figure 5.1 shows the solution manifold $\mathfrak{M}^{\mathcal{N}}$, a reduced basis space X_N and some snapshots $u^{\mathcal{N}}(\mu_i)$. It is possible to define other reduced basis spaces, for example Hermite and Taylor spaces which include (high-order) derivatives of snapshot solutions with respect to the parameter into the reduced basis space as well, but this work refers to Lagrangian reduced basis spaces only. The assumption of linear independence leads to nested or hierarchical reduced basis spaces with increasing number of snapshots

$$X_1 \subset X_2 \subset \cdots X_N \subset \mathfrak{M}^{\mathcal{N}}.$$

With sufficiently large N these spaces should approximate $\mathfrak{M}^{\mathcal{N}}$ "reasonably well". In the literature the concept of Kolmogorow N-width is used to measure the quality of such an approximation. The challenging task remains to find appropriate reduced basis spaces with $N << \mathcal{N}$ such that Problem 7 can be solved orders of magnitude faster than the truth approximation 6.

5.3.1. Offline-online decomposition

The Definition 5.1 of the reduced basis space X_N indicates the use of solutions of the truth approximation as basis functions. Computing these snapshots is the main cost in the *offline* or *assembling* phase of the reduced basis as the truth approximation has to be solved N times. In this phase we invest computational resources in order to benefit in the *online* of much reduced computational costs. The variational

formulation (5.3) is solved in X_N and its solution $u_N(\mu)$ exhibits the expansion

$$u_N(\mu) = \sum_{i=1}^{N} \alpha_i(\mu)\phi_i.$$

Using a Galerkin projection onto the basis Φ_N of X_N reduces (5.3) to the equivalent formulation

$$\sum_{i=1}^{N} \alpha_i(\mu)a(\phi_i, \phi_j; \mu) = f(\phi_j; \mu) \quad \forall \phi_j \in \Phi_N.$$

This is a linear system

$$\mathcal{A}_N(\mu)\boldsymbol{\alpha} = \boldsymbol{f}_N(\mu)$$

in the N unknown coefficients $\boldsymbol{\alpha} = (\alpha_i)_{i=1,\dots,N}$ with the matrix

$$\mathcal{A}_N(\mu) = (a(\phi_i, \phi_j; \mu))_{i,j=1,\dots,N}$$

and right-hand side

$$\boldsymbol{f}_N(\mu) = (f(\phi_i; \mu))_{i,j=1,\dots,N}.$$

Thus in the (online) evaluation phase the computation of the solution requires only the inversion of this low-dimensional system. Assembling this parameter dependent system however depends on the number of degrees of freedom in the underlying finite element approximation as the basis functions are of dimension $\mathcal{N}$. Hence it is of critical importance to decouple the assembly of this system from $\mathcal{N}$.

We observe that in case of an affine parameter dependence

$$a(v, u; \mu) = \sum_{q=1}^{Q_A} \theta_q^A(\mu)a_q(v, u)$$

$$f(v; \mu) = \sum_{q=1}^{Q_f} \theta_q^f(\mu)f_q(v)$$

of the (sesqui-) linear forms a and f, this is readily achieved as linearity allows to write

$$\mathcal{A}_N(\mu) = \sum_{q=1}^{Q_A} \theta_q^A(\mu)\mathcal{A}_N^q$$

$$\boldsymbol{f}_N(\mu) = \sum_{q=1}^{Q_f} \theta_q^f(\mu)\boldsymbol{f}_N^q$$

with

$$\mathcal{A}_N^q = (a_q(\phi_i, \phi_j))_{i,j=1,\dots,N}, \tag{5.4a}$$

$$\boldsymbol{f}_N^q = (f(\phi_i))_{i=1,\dots,N}. \tag{5.4b}$$

In this case the assembling only requires the summation of Q_A $N \times N$ matrices and Q_f vectors and is thus independent of $\mathcal{N}$. The $\mathcal{N}$ dependent matrices $\{\mathcal{A}_N^q \,|\, q = 1,\dots,Q_A\}$ and vectors $\{\boldsymbol{f}_N^q \,|\, q = 1,\dots,Q_f\}$ can be precomputed in the offline phase. The output quantities can be similarly reduced to an offline computable part depending on $\mathcal{N}$ which allows for only N dependent evaluation costs in the online phase. In Section 5.8 we list the steps and the operation counts involved in assembling and solving the reduced system with its output functionals.

Although the Finite Element Method and the Reduced Basis Method seem similar there are distinct differences. The reduced basis method generates a very low dimensional model for a specific problem. Its use of ansatz functions with a global support leads to dense albeit very small linear systems. This is in opposition to FEM where locally supported ansatz functions generate large but sparse systems.

5.4. A posteriori error estimation

The reliability of the reduced basis method relies on accurate approximation of the solution to the truth approximation and efficient methods to compute and control approximation errors. In particular the desired self-adaptive construction of a reduced basis requires not only tight and effective error bounds but computable ones. In this section we present rigorous bounds for the approximation errors for the solution and quantities of interest. We furthermore derive computable error estimators suitable for an offline-online decomposition thus allowing for efficient evaluation of the error bound in the construction of the reduced basis.

5.4.1. Error bounds

In this section we present errors bounds for the residual of the primal problem in the dual norm. The following theorem is the basis for the *a posteriori* error estimates derived later.

Theorem 5.2 (Primal error bounds)**.** *The residual*

$$r^{pr}(\cdot; \tilde{u}) : X \to \mathbb{C}, v \mapsto r^{pr}(v; \tilde{u}) = f(v) - a(v, \tilde{u}) \tag{5.5}$$

of the approximate solution $\tilde{u} \in \tilde{X} \subset X$ and the inf-sup constant β of $a(\cdot, \cdot)$ bound the error $e = u - \tilde{u}$ of the approximate solution to the exact solution $u \in X$. It holds:

$$\|e\|_X \leq \frac{1}{\beta} \|r^{pr}(\cdot; \tilde{u})\|_{X'}.$$

Proof. Using Corollary 3.10 we find a map $T : X \mapsto X$ relating $a(x, \cdot) \in X'$ for every $x \in X$ to the Riesz representer $A_x \in X$ such that $a(x, y) = (A_x, y)_X \quad \forall y \in X$. For $A_x \in X$ we have

$$0 < \beta \|e\|_X \|A_x\|_X \leq |a(A_x, e)|. \tag{5.6}$$

This follows from the Definition 3.12 of β where the supremum is attained at the Riesz representer $A_x \in X$.

The residual also fulfills

$$a(v, e) = a(v, u) - a(v, \tilde{u}) = f(v) - a(v, \tilde{u}) = r^{pr}(v; \tilde{u}) \quad \forall v \in X$$

as u is the exact solution. Inserting the Riesz representer $v = A_x$ yields

$$a(A_v, u - \tilde{u}) = r^{pr}(A_v; \tilde{u}) \leq \|r^{pr}(\cdot; \tilde{u})\|_{X'} \|A_v\|_X. \tag{5.7}$$

Combining (5.6) and (5.7) and eliminating $\|A_x\|$ concludes the proof.

$\square$

The theorem allows to bound the errors of the continuous quantities of interest. The following Lemma bounds the error of the linear quantity of interest.

Lemma 5.3. *For a linear quantity of interest we find*

$$|s_l - \tilde{s}_l| \leq \frac{1}{\beta} \|l(\cdot)\|_{X'} \|r^{pr}(\cdot; \tilde{u})\|_{X'}.$$

Proof. Linearity of $l(\cdot)$ allows to apply Theorem 5.2:

$$\begin{aligned}
|s_l - \tilde{s}_l| =& |l(u) - l(\tilde{u})| = |l(u - \tilde{u})| \\
\leq & \|l(\cdot)\|_{X'} \|e\|_X \\
\leq & \frac{1}{\beta} \|l(\cdot)\|_{X'} \|r^{pr}(\cdot; \tilde{u})\|_{X'}.
\end{aligned}$$

$\square$

In case of a quadratic function of interest s_q we obtain the similar result exploiting the properties of the locally Lipschitz-continuous, bounded functional.

Lemma 5.4. *For a quadratic quantity of interest we find*

$$|s_q - \tilde{s}_q| \leq \frac{L_q}{\beta^2} \left(\gamma \|r^{pr}(\cdot; \tilde{u})\|_{X'} \|f\|_{X'} + \|r^{pr}(\cdot; \tilde{u})\|_{X'}^2 \right)$$

where $L_q = \sup_{w \in X} \frac{|q(w)|}{(w,w)_X} > 0$ and γ the continuity constant of $a(\cdot, \cdot; \mu)$.

Proof. The quadratic functional $q(v) = \tilde{q}(v, v)$ allows to expand

$$\tilde{s}_q = q(\tilde{u}) = q(u + e) = q(u) + q(e) + \tilde{q}(u, e) + \tilde{q}(e, u).$$

Hence with the continuity of q and the constant L_q we find

$$
\begin{aligned}
|s_q - \tilde{s}_q| &= |q(e) + \tilde{q}(u, e) + \tilde{q}(e, u)| \\
&\leq L_q \left(\|e\|_X^2 + 2\|e\|_X \|u\|_X \right).
\end{aligned}
$$

Now we apply Theorem 5.2 to bound $\|e\|_X$:

$$
\|e\|_X^2 + 2\|e\|_X \|u\|_X \leq \frac{1}{\beta} \|r^{pr}(\cdot; \tilde{u})\|_{X'} \|u\|_X + \frac{1}{\beta^2} \|r^{pr}(\cdot; \tilde{u})\|_{X'}^2
$$

Applying the Lax-Milgram Lemma 3.13 to bound $\|u\|_X$ gives the desired result.

$\square$

5.4.2. Error estimators

According to the error bounds for the residual and quantities of interest estimating the dual norm of the residual is key in determining a tight error estimate. A numerical evaluation of it in $X^{\mathcal{N}} \subset X$ starts with the Riesz representer $R_N^{pr}(\mu) \in X$ of the anti-linear, parameter dependent residual $r^{pr}(\cdot; \tilde{u}(\mu))$, i.e.

$$
(v, R_N^{pr}(\mu))_{X^{\mathcal{N}}} = r^{pr}(v; \tilde{u}(\mu)) \quad \forall v \in X^{\mathcal{N}}. \tag{5.8}
$$

Solving (5.8) directly has the same costs as the solution of the truth approximation in addition to the costs of computing $\|r^{pr}(\cdot; \tilde{u}(\mu))\|_{(X)'} = \|R_N^{pr}(\mu)\|_{X^{\mathcal{N}}}$ which again depends on $\mathcal{N}$. Assuming once more that $a(\cdot, \cdot; \mu)$ and $f(\cdot; \mu)$ can be affinely decomposed we can recover an efficient offline-online decomposition of the dual norm of the residual. Exploiting the linearity of the scalar product and recalling the definition of $r^{pr}(\cdot; \tilde{u}(\mu))$ in (5.5) we thus find

$$
\begin{aligned}
(v, R_N^{pr}(\mu))_{X^{\mathcal{N}}} &= f(v; \mu) - a(v, \tilde{u}(\mu)) = \sum_{q=1}^{Q_f} \theta_q^f(\mu) f_q(v) - \sum_{q=1}^{Q_A} \theta_q^A(\mu) a_q(v, \tilde{u}(\mu)) \\
&= \sum_{q=1}^{Q_f} \theta_q^f(\mu) f_q(v) - \sum_{q=1}^{Q_A} \sum_{i=1}^{N} \theta_q^A(\mu) \alpha_i(\mu) a_q(v, \phi_i)
\end{aligned}
$$

where we expanded $\tilde{u}$ in the basis Φ of X_N. Finding Riesz representers of the anti-linear functionals $f_q(\cdot)$ and $a_q(\cdot, \phi)$ by solving

$$
q \in \{1, \ldots, Q_f\}: \quad f_q(v) = (v, F_q)_{X^{\mathcal{N}}} \quad \forall v \in X^{\mathcal{N}} \tag{5.9a}
$$

$$
q \in \{1, \ldots, Q_A\}, i \in \{1, \ldots, N\}: \quad a_q(v, \phi_i)_X = (v, A_q^i)_{X^{\mathcal{N}}} \quad \forall v \in X^{\mathcal{N}} \tag{5.9b}
$$

allows to rewrite

$$
R_N^{pr}(\mu) = \sum_{q=1}^{Q_f} \theta_q^f(\mu) F_q - \sum_{q=1}^{Q_A} \sum_{i=1}^{N} \theta_q^A(\mu) A_q^i
$$

and hence we find

$$\|R_N^{pr}(\mu)\|^2 = \sum_{q,q'=1}^{Q_f} \overline{\theta_q^f(\mu)}\theta_{q'}^f(\mu)(F_q, F_{q'})_{X^{\mathcal{N}}}$$

$$- 2\mathfrak{Re}\left\{\sum_{q=1}^{Q_f}\sum_{q'=1}^{Q_A}\sum_{i=1}^{N} \overline{\theta_q^f(\mu)}\theta_{q'}^A(\mu)(F_q, A_{q'}^i)_{X^{\mathcal{N}}}\right\}$$

$$+ \sum_{q,q'=1}^{Q_A}\sum_{i,i'=1}^{N} \overline{\theta_q^A(\mu)}\theta_{q'}^A(\mu)\alpha_i(\mu)\overline{\alpha_{i'}(\mu)}\left(A_q^{i'}, A_{q'}^i\right)_{X^{\mathcal{N}}}. \tag{5.10}$$

The $\mathcal{N}$ dependent scalar products $(F_q, F_{q'})_{X^{\mathcal{N}}}, (F_q, A_{q'}^i)_{X^{\mathcal{N}}}$ and $(A_q^{i'}, A_{q'}^i)_{X^{\mathcal{N}}}$ can be computed offline. In the online phase $\|R_N^{pr}(\mu)\|^2$ can be computed independently of $\mathcal{N}$. Owing to Theorem 5.2 we can construct a rigorous, $\mathcal{N}$-independent error estimator for the reduced basis

$$\Delta_N(\mu) = \frac{1}{\beta(\mu)}\|R_N^{pr}(\mu)\|_{X^{\mathcal{N}}}. \tag{5.11}$$

Similarly we can also derive rigorous estimators for the resulting errors in the output quantities

$$\Delta_N^l(\mu) = \|l(\cdot)\|_{(X^{\mathcal{N}})'}\Delta_N(\mu),$$

$$\Delta_N^q(\mu) = \frac{L_q}{\beta(\mu)}\left(\gamma\|f\|_{X'}\Delta_N(\mu) + \Delta_N(\mu)^2\right).$$

The necessary constants are usually not known hence we rather use the relative difference between an evaluation in X_N and X_{N-1} as indicators for the quality of the approximation. We denote these

$$\eta_N^l = \frac{\|s_N^l - s_{N-1}^l\|_{L_\infty}}{\|s_N^l\|_{L_\infty}}, \tag{5.12}$$

$$\eta_N^q = \frac{\|s_N^q - s_{N-1}^q\|_{L_\infty}}{\|s_N^q\|_{L_\infty}} \tag{5.13}$$

for $N \geq 2$.

5.4.3. Inf-sup constant

The certification of the accuracy of a RBM relies on rigorous error estimates. These estimates require the computation of the parameter dependent inf-sup constant $\beta(\mu)$ for every parameter μ in the parameter space $\mathfrak{D}$. In the following we explore a way to compute $\beta(\mu)$.

As a sesquilinear form $a(\cdot, \cdot)$ is linear in the second argument on X and $\forall v \in X$:

$a(v, \cdot) \in X'$. Hence Definition 3.12 can be restated equivalently as:

$$\beta = \inf_{v \in X} \frac{\|a(v, \cdot)\|_{X'}}{\|v\|_X}. \tag{5.14}$$

Due to the Riesz-representation Theorem 3.6 we can find a map

$$T : X \to X$$
$$v \mapsto Tv$$

such that

$$a(v, \cdot) = (Tv, \cdot)_X \quad \forall v \in X \tag{5.15}$$

With (5.15) we reformulate (5.14):

$$\begin{aligned}
\beta &= \inf_{v \in X} \frac{\|a(v, \cdot)\|_{X'}}{\|v\|_X} \\
&= \inf_{v \in X} \frac{\|(Tv, \cdot)_X\|_{X'}}{\|v\|_X} \\
&= \inf_{v \in X} \frac{\|Tv\|_X}{\|v\|_X} \\
&= \inf_{v \in X} \frac{(Tv, Tv)_X}{\|v\|_X \|Tv\|_X}
\end{aligned} \tag{5.16}$$

using $\|(\cdot, Tv)_X\|_{X'} = \sup_{w \in X} \frac{|(w, Tv)_X|}{\|w\|_X} = \|Tv\|_X$.

We obtain

$$\beta^2 = \inf_{v \in X} \frac{(Tv, Tv)_X}{(v, v)_X}$$

by squaring (5.16) and can interpret the right-hand side of this equation as the Rayleigh quotient of the symmetric, positive definite eigenvalue problem:

Find $(x, \lambda) \in X \times \mathbb{R}$ such that

$$(Tv, Tx)_X = \lambda(v, x)_X \quad \forall v \in X. \tag{5.17}$$

The inf-sup constant β now corresponds to the square root of the smallest eigenvalue λ_{min} of (5.17):

$$\beta = \sqrt{\lambda_{min}}$$

Estimation of $\beta\mu$ for reduced basis error estimates Solving the discretized eigenvalue problem (5.17) of size $\mathcal{N}$ directly for all parameter $\mu \in \mathfrak{D}$ is infeasible. In recent years the successive constraint method (SCM) [Huynh et al., 2007, Chen et al., 2008, Chen et al., 2009] is usually employed to construct lower bounds $\beta^{LB} < \beta$ for the inf-sup constant by solving small linear optimization problems. It is observed that this method converges poorly thus leading to high computational complexity

[Hess et al., 2014]. In [Hess et al., 2014] four different estimators (upper-bound-SCM, MinRes-, Galerkin-estimators, and Kriging-interpolation) are evaluated in a coplanar waveguide-setting at GHz frequencies. Their investigation reveals the MinRes-estimator introduced in [Maday and Rønquist, 2002] to be the most accurate. However, these estimators approximate the discrete stability constant, but are not lower bounds.

The electromagnetic scattering problem is stated in an unbounded domain. In these conditions, the inf-sup constant is nearly unaffected by small parameter perturbations in the interior. This will be demonstrated by the numerical examples in Chapter 6. Hence for almost constant $\beta(\mu)$ replacing it by a constant β_0 has little effect on the error estimates presented before. We take β_0 to be the minimum over a finite subset $\mathfrak{D}_\beta$ of $\mathfrak{D}$. It is beneficial to choose $\mathfrak{D}_\beta$ the set of snapshot locations as we already have access to the LU decomposition of the system matrix $\mathcal{A}(\mu)$ there. This serves to reduce computational costs as we will demonstrate in the following.

Direct computation of discrete constant In order to compute β, we solve the discrete analog of (5.17). We call $\mathcal{H} \in \mathbb{C}^{\mathcal{N} \times \mathcal{N}}$ the inner product matrix of $X_\mathcal{N} \subset X$, i.e. $(x, y)_{X_\mathcal{N}} = \boldsymbol{x}^H \mathcal{H} \boldsymbol{y}$. With the finite element matrix $\mathcal{A} \in \mathbb{C}^{\mathcal{N} \times \mathcal{N}}$, we have $a(v, w) = \boldsymbol{v}^H \mathcal{A} \boldsymbol{w}$ and find $\mathcal{T}$ by means of

$$a(v, w) = (Tv, w)_X \quad \forall v, w \in X_\mathcal{N}$$
$$\implies \quad \boldsymbol{v}^H \mathcal{A} \boldsymbol{w} = \boldsymbol{v}^H \mathcal{T}^H \mathcal{H} \boldsymbol{w} \quad \forall \boldsymbol{v}, \boldsymbol{w} \in \mathbb{C}^\mathcal{N}$$
$$\iff \quad \mathcal{A} = \mathcal{T}^H \mathcal{H}$$
$$\iff \quad \mathcal{A} \mathcal{H}^{-1} = \mathcal{T}^H$$
$$\iff \quad \mathcal{T} = \mathcal{H}^{-H} \mathcal{A}^H. \tag{5.18}$$

In $X_\mathcal{N}$ this allows to rewrite the left-hand side in (5.17) as follows

$$\begin{aligned}
(Tv, Tx)_X &= (\mathcal{T}\boldsymbol{v})^H \mathcal{H} \mathcal{T} \boldsymbol{x} \\
&= \boldsymbol{v}^H \mathcal{T}^H \mathcal{H} \mathcal{T} \boldsymbol{x} \\
&\overset{(5.18)}{=} \boldsymbol{v}^H (\mathcal{H}^{-H} \mathcal{A}^H)^H \mathcal{H} \mathcal{H}^{-H} \mathcal{A}^H \boldsymbol{x} \\
&= \boldsymbol{v}^H \mathcal{A} \mathcal{H}^{-1} \mathcal{H} \mathcal{H}^{-H} \mathcal{A}^H \boldsymbol{x} \\
&= \boldsymbol{v}^H \mathcal{A} \mathcal{H}^{-H} \mathcal{A}^H \boldsymbol{x}
\end{aligned}$$

As $\boldsymbol{v} \in X^\mathcal{N}$ is arbitrary, solving (5.17) is now equivalent to

$$\mathcal{A} \mathcal{H}^{-H} \mathcal{A}^H \boldsymbol{x} = \lambda \mathcal{H} \boldsymbol{x} \tag{5.19}$$

We can solve (5.19) by an inverse power iteration detailed in Algorithm 2. It requires the inversion of the system matrix $\mathcal{A}$ and the inner product matrix $\mathcal{H}$. The LU decomposition of $\mathcal{H}$ has to be computed only once provided sufficient memory

---

Algorithm 2 Inverse power iteration algorithm to compute β

---

invert $\mathcal{H}, \mathcal{A}$

$i \to 0$, $q_0 = \frac{x_0}{\|x_0\|_X}$

while not converged **do**

    Solve $\mathcal{A}\mathcal{H}^{-H}\mathcal{A}^H x_{i+1} = \mathcal{H}q_i$ by

$$x_{i+1} = \mathcal{A}^{-H}\mathcal{H}^H\mathcal{A}^{-1}\mathcal{H}q_i$$

    Set

$$\lambda_{i+1} = \frac{x_{i+1}^H \mathcal{A}\mathcal{H}^{-H}\mathcal{A}^H x_{i+1}}{x_{i+1}^H \mathcal{H}x_{i+1}}$$

    Set

$$q_{i+1} = \frac{x_{i+1}}{\|x_{i+1}\|_X}$$

    $i \to i+1$

end while

return $\beta = \sqrt{\lambda_{i+1}}$

---

is available to store it for future use. The same holds for the LU decomposition of the system matrix which in case of a reduced basis snapshot location has already been computed.

5.5. Parameterization of the electromagnetic scattering problem

The electromagnetic scattering Problem 2 depends on a number of parameters that might be interdependent on each other. The offline-online decomposition in $\mathcal{N}$ dependent and independent operations presented in Section 5.3 relies on an affine parameter dependence of the bilinear form. A commonly encountered affine decomposition of the sesquilinear form a is

$$a(v, u; \{\omega, \mu, \varepsilon\}) = (\nabla \times v, \mu^{-1}\nabla \times u) - \omega^2(v, \varepsilon u)$$
$$= a_\mu(v, u) - \omega^2 a_\varepsilon(v, u),$$

resulting an affine decomposition with respect to the frequency ω and supposedly parameter independent sesquilinear forms $a_\mu(v, u), a_\varepsilon(v, u)$. Similar affine decompositions in ε, μ exist as well. However, when considering dispersive materials these decompositions are no longer affine as ε, μ are functions of ω. Likewise, for geometrical parameter variations this is not true and other affine decompositions must be used. In [Pomplun, 2010] the affine decomposition of Maxwell's equations with

respect to geometrical parameterizations used piecewise linear transformations of topologically equivalent meshes which fulfill the affine geometry precondition.

Whereas in [Pomplun, 2010] the implementation was limited to geometrical parameter variations, we aim to lift this restriction and aspire to include all parameters in our reduced basis method. This comprises material parameters, such as permittivity and permeability, as well as source parameters, such as incidence angle and frequency of the illumination. The restriction to real valued parameter domains $\mathfrak{D} \subset \mathbb{R}^d$ requires separate modeling of real and imaginary parts of complex valued quantities, i.e. the permittivity. In practice this restriction is of no consequence as $\mathbb{C}$ can be identified as $\mathbb{R}^2$.

5.5.1. Empirical Interpolation Method

Interpolating arbitrary functions is a challenging task if little information is available *a priori*. Classically, Lagrangian interpolation methods have been used with great success for polynomial functions and have found their way into various textbooks on numerics [Deuflhard and Hohmann, 1993]. Questions on existence and uniqueness of the interpolant are followed by discussions of optimally chosen interpolation points and algorithms. For example in the one dimensional case Gauss-Chebyshev nodes provide an optimal choice of interpolation points and define a unique Lagrangian interpolation operator. Although the theory of polynomial interpolation is very well documented and fairly extensive, a number of open questions remain when a more general set of non-polynomial or complex shaped, high dimensional domains are investigated. In these cases oftentimes optimal interpolation points are unknown or demand tailored and complicated implementations.

The demand for a general purpose, a-posteriori error controlled interpolation scheme has led to the introduction of the Empirical Interpolation Method (EIM) [Barrault et al., 2004] and its discrete analog the Discrete Empirical Interpolation Method (DEIM) [Chaturantabut and Sorensen, 2009, Chaturantabut and Sorensen, 2010]. These methods have been used with great success in connection with reduced basis methods [Grepl et al., 2007, Eftang et al., 2010a] and the algorithmic ideas demonstrate several similarities as both methods rely on snapshots. In fact, the interpolation points have been referred to as "magic points" [Maday et al., 2007] in praise of their efficiency in interpolating general classes of functions. This qualification is justified by the observation of the good interpolation behavior of the empirical interpolant compared to known optimal solutions for model problems.

In the following we briefly present the general idea of EIM and demonstrate its convergence properties with respect to several examples. For more detailed explanations and proofs the reader is referred to [Barrault et al., 2004, Maday et al., 2007, Chaturantabut and Sorensen, 2009, Chaturantabut and Sorensen, 2010]

Construction of affine approximation We present the empirical interpolation for a parameter dependent function $g : \Omega \times \mathfrak{D} \mapsto \mathbb{R}$ where we assume $g(\cdot, \mu) \in$

$L_\infty(\Omega)$ $\forall \mu \in \mathfrak{D}$ with a non-affine dependence on the parameter $\mu \in \mathfrak{D} \subset \mathbb{R}^d$. The idea is to find an approximation

$$g(\boldsymbol{r};\mu) \approx I_Q\left[g(\cdot;\mu)\right](\boldsymbol{r}) = \sum_{q=1}^{Q} \theta_q(\mu) g_q(\boldsymbol{r})$$

with scalar functions $\theta_q : \mathbb{R}^d \mapsto \mathbb{R}$ and a "collateral reduced basis" $\{g_q\}_{q=1}^{Q}$.

Like in a reduced basis approximation the empirical interpolation approximates the parametric manifold $\mathfrak{M} = \{g(\cdot;\mu) \,|\, \mu \in \mathfrak{D}\}$ by Q snapshots. The EIM, in contrast to RBM, does not rely on a Galerkin projection of the snapshots. Instead a linear system for the interpolation coefficient θ_q is derived by demanding the interpolation to be exact at Q interpolation nodes $\boldsymbol{r}_q$ chosen by the algorithm.

The approximation is constructed iteratively. We start by defining a set of interpolation points $\mathfrak{R} = \{\boldsymbol{r}_1, \ldots, \boldsymbol{r}_Q\}$ and parameters $\mathfrak{P} = \{\mu_1, \ldots, \mu_Q\}$ and the collateral reduced basis $\mathfrak{Q} = \{\xi_1, \ldots, \xi_Q\}$ which are generating functions $\{g(\cdot;\mu_1), \ldots, g(\cdot;\mu_Q)\}$ associated with $\mathfrak{P}$.

We initialize the set with a starting parameter $\mathfrak{P}_1 = \{\mu_1\}$ such that $g(\cdot;\mu_1) \neq 0$ and the set of interpolation points $\mathfrak{R}_1 = \{\boldsymbol{r}_1\}$ where $\boldsymbol{r}_1 = \mathrm{argmax}_{\boldsymbol{r}\in\Omega} \|g(\boldsymbol{r};\mu_1)\|_\infty$. We than set $\xi_1 = g(\cdot;\mu_1)\|g(\boldsymbol{r}_1;\mu_1)\|_\infty^{-1}$ and set $\mathfrak{Q} = \{\xi_1\}$. Associated with these choices is the interpolation operator I_Q. For $Q > 1$ we define recursively:

- $\mu_Q = \mathrm{argmax}_{\mu\in\mathfrak{D}} \|g(\cdot;\mu) - I_{Q-1}\left[g(\cdot;\mu)\right]\|_\infty, \quad \mathfrak{P}_Q = \mathfrak{P}_{Q-1} \cup \{\mu_Q\}$

- $\boldsymbol{r}_Q = \mathrm{argmax}_{x\in\Omega} \|g(\cdot;\mu_Q) - I_{Q-1}\left[g(\cdot;\mu_Q)\right]\|_\infty, \quad \mathfrak{R}_Q = \mathfrak{R}_{Q-1} \cup \{\boldsymbol{r}_Q\}$

- $\xi_Q = \dfrac{g(\cdot;\mu_Q)-I_{Q-1}\left[g(\cdot;\mu_Q)\right]}{\|g(\boldsymbol{r}_Q;\mu_Q)-I_{Q-1}\left[g(\boldsymbol{r}_Q;\mu_Q)\right]\|_\infty}, \quad \mathfrak{Q}_Q = \mathfrak{Q}_{Q-1} \cup \{\xi_Q\}$

In implementations $\mathfrak{D}$ and Ω are replaced by finite subsets which makes the solution of the optimization problems feasible. The resulting basis $\mathfrak{Q}$ is not orthogonal but hierarchical and bounded as $\xi_q(\boldsymbol{r}_q) = 1 \,\forall q \leq Q$. The algorithmic construction resembles the Greedy-Algorithm 3 used to construct a reduced basis. It is discussed in detail in Section 5.6.1.

The interpolation operator $I_Q[\cdot]$ at $\mu \in \mathfrak{D}$ is defined as follows: With $\mathfrak{R}_Q$ and $\mathfrak{Q}_Q$ constructed as above we define the matrix $\mathcal{Q} = (\xi_j(\boldsymbol{r}_i))_{i,j=1}^{Q}$ and the vector $\boldsymbol{g} = (g(\boldsymbol{r}_i;\mu))_{i=1}^{Q}$. The solution $\boldsymbol{\theta}$ of

$$\mathcal{Q}\boldsymbol{\theta} = \boldsymbol{g}$$

gives rise to the interpolant $I_Q\left[g(\cdot;\mu)\right] = \sum_{q=1}^{Q} \theta_q \xi_q(\cdot)$. The matrix $\mathcal{Q}$ is lower triangular with a unit diagonal and hence always invertible. The cost associated with the computation of $\boldsymbol{\theta}$ is $O(Q^2)$.

Theorem 5.5 (*A posteriori* error estimate)**.** *Let I_Q and $I_{Q'}$ be empirical interpolants for $Q' > Q$ with $\mathfrak{Q}_Q \subset \mathfrak{Q}_{Q'}$ and $\mathfrak{R}_Q \subset \mathfrak{R}_{Q'}$ defined as above. Let $\mathcal{Q} = (\xi_j(\boldsymbol{r}_i))_{i,j=Q+1}^{Q'}$.*

For $\mu \in \mathfrak{D}$ we define $\boldsymbol{\delta} := (g(\boldsymbol{r}_i; \mu) - I_Q\left[g(\cdot; \mu)\right](\boldsymbol{r}_i))_{i=Q+1}^{Q'}$ and compute $\boldsymbol{\theta}' = \mathcal{Q}^{-1}\boldsymbol{\delta}$. If

$$I_Q\left[g(\cdot; \mu)\right] \in \text{span}(\mathfrak{Q}_{Q'}) \tag{5.20}$$

the following a posteriori *error bound for the interpolation error holds*

$$\|g(\cdot; \mu) - I_Q\left[g(\cdot; \mu)\right]\|_\infty \leq \Delta_{Q,Q',\infty}^g(\mu) = \|\boldsymbol{\theta}'\|_1 = \sum_{i=Q+1}^{Q'} |\theta_i'|$$

The assumption (5.20) generally does not hold and the estimator is not a rigorous upper bound. On the other hand the error bound is inexpensive to evaluate as it only requires one additional evaluation of $g(\cdot; \mu)$ for $Q' = Q + 1$. Rigorous error bounds exist [Eftang et al., 2010a] depending on the parametric derivatives of the approximated functions.

The Lebesque constant $\Lambda_Q = \sup_{x\in\Omega} \sum_{q=1}^Q |v_q(x)|$, where v_q are the characteristic functions of $\text{span}(\mathfrak{Q}_Q)$ satisfying $v_q(\boldsymbol{r}_i) = \delta_{qi}$, allows to bound the approximation error *a priori*. In [Barrault et al., 2004, Maday et al., 2007] it is proven that the EIM approximation satisfies

$$\|I_Q\left[g(\cdot; \mu)\right] - g(\cdot; \mu)\|_\infty \leq (1 + \Lambda_Q) \inf_{v\in\text{span}(\mathfrak{Q}_Q)} \|g(\cdot; \mu) - v\|_\infty. \tag{5.21}$$

The tight bound $2^Q - 1$ for Λ_Q is shown in [Barrault et al., 2004, Maday et al., 2007]. In practice the observed behavior is much better as found in the cited papers and in the numerical examples in Chapter 6.

The affine approximation of the bilinear form with the empirical interpolant leads to a different, interpolated truth approximation. In this thesis we refer to this approximation as the truth approximation with empirical interpolation.

Problem 8 (Truth-Approximation with empirical interpolation)**.** Let I_{Q^A} and I_{Q^f} be empirical interpolants for the sesquilinear form $a(\cdot, \cdot)$ and the linear form $f(\cdot)$. For a given input parameter $\mu \in \mathfrak{D} \subset \mathbb{R}^d$, compute the linear and quadratic outputs of interest

$$s_l(\mu) = l(u^{\mathcal{N}}(\mu)),$$
$$s_q(\mu) = q(u^{\mathcal{N}}(\mu)),$$

where $u^{\mathcal{N}}(\mu) \in X^{\mathcal{N}}$ satisfies the following weak formulation:
Find $u^{\mathcal{N}}(\mu) \in X^{\mathcal{N}}$ such that:

$$I_{Q^A}\left[a(v, u^{\mathcal{N}}(\mu); \mu)\right] = I_{Q^f}\left[f(v; \mu)\right], \quad \forall v \in X^{\mathcal{N}} \tag{5.22}$$

5.5.2. Implementation details

Our reduced basis implementation is based on JCMsuite. In the following we consider the treatment of parameter dependencies in optical simulations of nano-

photonic systems with it. We distinguish parameterizations of geometrical features from non-geometrical features.

Geometrical parameters Geometrical parameter dependencies are incorporated into the grid generation process in our implementation. By explicitly defining point derivatives in the layout of the geometry to be modeled, geometrical deformations with respect to parameters are included automatically into the underlying grid and are treated separately from non-geometrical parameters which are not deforming the grid. These parameters can describe and vary geometrical properties of three dimensional objects, among them length, width and height, as well as radii of circles and cylinders, or sidewall angles. Whereas the material properties may enter affinely in the weak formulation, the geometrical parameters generally do not. In many regards the geometrical variations prove the most difficult to handle in the parameterization, as the reduced basis construction requires topologically equivalent grids. The generation of meshes suitable for reduced basis computations capable of handling large deformations is part of our current research.

Non-geometrical parameters A general work flow for simulating optical properties of nanostructured devices starts and ends in a scripting language. Typically a set of user defined templates is used to generate the solver input for a given set of parameters. This usually includes steps to load and interpolate measured data (such as refractive indices) as well as modeling sources (for example rotating and scaling the k-vector of a plane wave). These templates can execute complex operations based on the input (entered as key-value pairs), but eventually keywords are substituted for their values.

Our RBM implementation relies on the scripting interfaces offered by JCMsuite to MATLAB and Python. It uses named parameters and passes key-value pairs to the scripting interfaces, executes any scripts necessary and substitutes the key words to obtain the required input which is subsequently processed by the program. Internally the required data is cached and calls to the scripting interfaces are bundled to reduce the number of overall calls as for example the overhead including startup times of MATLAB can make up several seconds. This procedure allows for very flexible usage and has the main advantage of exposing a wide range of parameterizations to be defined in a high level scripting environment. In contrast to replicating a lot of functionality of a higher level language in a low level implementation this embedded scripting interface is much more versatile and efficient. The possible downside of this approach is the excess burden for the user to define self-sustained templates that accept only the named parameters.

5.6. Self-adaptive reduced basis assembly

This section presents strategies to build Lagrange reduced basis spaces X_N. In Section 5.3 we did not specify how to choose the parameter locations $D_N = \{\mu_1, \ldots, \mu_N\}$

where the snapshots $u_i = u^{\mathcal{N}}(\mu_i)$ are computed. As the online costs of the reduced basis depend on the dimension N we attempt to choose D_N such that the resulting space $X_N = \mathrm{span}_{i=1,\ldots,N}\{u^{\mathcal{N}}(\mu_i)\}$ approximates the solution manifold $\mathfrak{M}^{\mathcal{N}}$ over $\mathfrak{D}$ well. Hence, for a given N we want to include as much information about $\mathfrak{M}^{\mathcal{N}}$ in X_N as possible, i.e. we aim to choose X_N as the optimal approximation in terms of linear subspaces of $\mathfrak{M}$. In these cases one usually is restricted to determine the snapshot locations by solving an optimization problem. The definition of "best" depends on the chosen metric $d(\cdot,\cdot) : X \times X \mapsto \mathbb{R}^+$.

In case of a single parameter $\mathfrak{D} \subset \mathbb{R}$ it is oftentimes possible to determine optimal snapshot locations. These are however not necessarily identical to optimal interpolation points for the output of interest [Maday et al., 2007] which are known to be Chebychev nodes. In high dimensional parameter spaces there is usually less or no a priori knowledge for optimal choices available.

5.6.1. Greedy snapshot selection

Instead of a direct construction of a N-dimensional subspace of X the idea is to use the available information during the construction phase and build X_N self-adaptively. The use of the inexpensive *a posteriori*-estimators (cf. Section 5.4.2) allows to assess how well the solution for a parameter $\mu \in \mathfrak{D}$ is approximated in a given reduced basis space X_N. The most common strategy is thus a "greedy" selection of the worst resolved parameter over a finite dimensional training set $\mathfrak{D}_{train} \subset \mathfrak{D}$ and subsequent enrichment of the reduced basis space by the corresponding snapshot solution. The inclusion of this parameter location into the reduced basis yields the maximal improvement in terms of approximating $\mathfrak{M}^{\mathcal{N}}$. This strategy has been shown to yield optimally chosen N-dimensional subspaces [Binev et al., 2011] with respect to Kolmogorow-N-width and exponential convergence rates for elliptic problems.

The Greedy algorithm 3 works as follows: A first snapshot parameter μ_1 is selected at random and the corresponding snapshot $u(\mu_1)$ is computed as a solution to the truth approximation. This allows to define an error estimate Δ_1. For the selection of the next snapshot this error estimate is evaluated over $\mathfrak{D}_{train}$ and the parameter corresponding to the largest error estimate is selected as the new snapshot parameter. This procedure is repeated until the maximum of the error estimate over the training set is smaller than the user specified tolerance level ϵ or a maximum dimension N_{max} has been reached.

In Algorithm 3 the algorithm is outlined in more detail. Here, additional steps are mentioned such as the construction of Δ_i. This summarizes the offline tasks necessary to construct the reduced basis, i.e. the projections of the snapshot onto the reduced basis. These steps are described in Section 5.3.1 for the affine decomposition and in Section 5.4.2 for the residual error estimate. The choice of the error indicator in Algorithm 3 influences the result. The choice of one of the error indicators for the output quantities instead of $\Delta_N(\cdot)$ possibly leads to a smaller basis but might not approximate the field solution $u^{\mathcal{N}}(\mu)$ as well. Conversely this is guaranteed by the continuity of the output quantities.

The listed algorithm also includes steps to compute lower bounds β^{LB} for the inf-sup-constant β. In Section 5.4.3 we commented on the estimation of β^{LB}. These enter the estimates and are listed for completeness.

Algorithm 3 Self-adaptive construction of the reduced basis space X_N by greedy selection of snapshots

---

    choose training set $\mathfrak{D}_{train} \subset \mathfrak{D}$, maximal reduced basis dimension N_{max} and error threshold ϵ

2: choose $\mu_1 \in \mathfrak{D}_{train}$ at random, compute snapshot $u_{\mathcal{N}}(\mu_1)$
    set $X_1 = \text{span}\{u_{\mathcal{N}}(\mu_1)\}$

4: orthonormalize X_1
    compute $\beta^{LB} = \beta(\mu_1)$

6: construct Δ_1
    refine $\mathfrak{D}_{train}$

8: $\mu_2 = \text{argmax}_{\mu \in \mathfrak{D}_{train}} \Delta_1(\mu)$
    $i \to 2$

10: **while** $\Delta_{i-1}(\mu_i) \geq \epsilon$ **and** $i \leq N_{max}$ **do**
      compute snapshot $u_{\mathcal{N}}(\mu_i)$

12:     set $X_i = X_{i-1} \cup \text{span}\{u_{\mathcal{N}}(\mu_i)\}$
      orthonormalize X_i

14:     compute $\beta^{LB} = \min\{\beta^{LB}, \beta(\mu_i)\}$
      construct Δ_i

16:     refine $\mathfrak{D}_{train}$
      $\mu_{i+1} = \text{argmax}_{\mu \in \mathfrak{D}_{train}} \Delta_i(\mu)$

18:     $i \to i + 1$
    end while

The computed snapshots are also orthogonalized against each other using a Gram-Schmidt procedure. The orthogonality improves the numerical stability.

Adaptive refinement and partitioning of $\mathfrak{D}_{train}$

The underlying assumption for the reduced basis computation is a smooth solution manifold $\mathfrak{M}$. This is usually measured as small Kolmogorow-N-width, a measure hard to compute. The contrary is usually readily observed *a posteriori* if a high number of reduced basis functions is required in the construction of the reduced order model. An analytical parameter dependence or high regularity of the solution is uncommon in real-world applications where these features are, if at all, only observed locally thus requiring at least a sufficiently dense approximation $\mathfrak{D}_{train}$ of $\mathfrak{D}$. Even with the optimal strategy, the choice of the training set $\mathfrak{D}_{train}$ has significant influence on the computation times and size of the reduced basis. In [Haasdonk et al., 2011] three problems are mentioned:

(i) over-fitting of too small training sets,

(ii) long training times in high dimensional parameter spaces,

(iii) possibly large number of reduced basis functions resulting in long online evaluation times.

Their strategies to overcome these drawbacks include locally adaptive grid refinements of $\mathfrak{D}_{train}$ with penalties for long non-refinement history and adaptive parameter domain partition. These are closely related to the hp strategy presented in [Eftang et al., 2010a]. Here h-refinements corresponds to locally adaptive partitioning of the parameter domain. This limits the computational complexity in the online phase as the parameter domain is split into subdomains $\mathfrak{D}_i$ if a given number N_{max} of reduced basis functions is considered insufficient to approximate the output of interest over the parameter domain as a whole. Allowing for variable maximal reduced basis space dimensions N_{max}^i in the Greedy enrichment within the subdomains yields the hp strategy.

All these strategies yield possibly very many bases for subdomains, each satisfying the global dimension limit N_{max} and error tolerances. The linear systems to be solved in the online phase are still small through the locality in parameter domain.

Locality beyond partitioning

The domain partitioning suggested in [Eftang et al., 2010a, Haasdonk et al., 2011] yield independent reduced bases for adjacent subdomains which may lead to the choice of parameter locations close to or on the boundary. Hence they require computation of effectively redundant truth solutions for close-by parameter values as the subdomain reduced bases do not share basis functions. This is a major drawback of the refinement strategies based on tessellation of the parameter domain. Alternative approaches are suggested in [Maday and Stamm, 2013] and [Amsallem et al., 2009]. Amsallem proposed an interpolation in the tangent space of the underlying Grassmanian manifold for parameterized linear structural dynamics. Instead of directly interpolating between snapshots to generate an approximation for new parameter values, they map them to the tangent space at a reference point, interpolate in the tangent space, before pulling back. In their specific case, reduced order models are built for symmetric positive definite matrices (mass, damping and stiffness) belonging to simple matrix manifolds whose structure is exploited, thus allowing for online computation of the mapping and interpolation.

The innovative idea proposed by Maday uses local approximation spaces spanned by the N snapshots closest to a parameter μ. The distance is measured by an empirical, problem specific metric based on the Hessian matrix of the output functional in each parameter point accounting for anisotropies in the parameter dependence. The Greedy strategy is then adapted to use a varying training set chosen optimally with the problem specific distance metric. The aim is to uniformly distribute the points of the trainings set $\mathfrak{D}_{train}$ with respect to the constructed metric. This advantage comes at the expense of a higher online complexity as the parameter specific reduced

basis space is constructed online and can only partially precomputed with higher offline effort.

Our implementation

The strategies presented above all require significant overhead in tessellation and tracking grid refinements as well as partitioning. In case of a locally adaptive snapshot selection the online phase might even become substantially more expensive. In many applications users choose to query the reduced model for very specific parameter locations which are oftentimes known a priori or may include areas of particular interest. We thus adapt our training set strategy accordingly starting with a hypercube enclosing $\mathfrak{D}$. This step is listed in Algorithm 3 as "refine $\mathfrak{D}_{train}$".

The user may provide an initial training set $\mathfrak{D}^0_{train}$ which is subsequently expanded through adaptive refinement following the general idea of [Haasdonk et al., 2011]. To overcome the curse of dimensionality we refrain from global refinements of $\mathfrak{D}_{train}$ in each Greedy iteration and furthermore allow for cells to be only split according to the steepest parameter derivatives. This limits the exponential growth of the training set through bisections.

5.6.2. Dual strategies

The use of the adjoint or dual problem can significantly improve convergence rates for the quantities of interest as it measures the "slack" of the solution with respect to the outputs in Problem 6. This we will briefly investigate in the following. The dual problem is derived from the corresponding Lagrange function with the primal variable $u \in X$ and dual variable $w \in X^{du}$ as follows. Starting with the derivatives of the Lagrangian

$$L(u, w) = s(u) + f(w) - a(w, u)$$

with respect to the primal variable u we obtain

$$L'_u(u, w)(v) = s'_u(u)(v) - a'_u(w, u)(v)$$

The dual problem is now found as

$$L'_u(u, w)(v) = 0, \quad \forall v \in X^{du}.$$

In case of a linear output

$$s(u) = s_l(u) = l(u) = (l, u) \text{ for } l \in X'$$

this reads as:

Problem 9 (Dual Problem - linear case). Let $u \in X$. Find $w \in X^{du}$ such that:

$$a(w, v) = -l(v), \quad \forall v \in X^{du}$$

The quadratic case with

$$s(u) = s_q(u) = (u, Qu) \text{ for } Q \in X'$$

is slightly more complicated but similar:

Problem 10 (Dual Problem - quadratic case). Let $u \in X$. Find $w \in X^{du}$ such that:

$$a(w, v) = -(u, Qv) - (v, Qu), \quad \forall v \in X^{du}$$

In case of the Maxwell scattering problem the input-output relationship is not compliant as the sesquilinear form $a(\cdot, \cdot)$ is not complex symmetric and the right hand side differs from the primal problem. A dual corrected approximation of the output of interest [Pierce and Giles, 2000] of the primal problem using an approximation of the dual solution w is given by

$$\tilde{s}^{pd} = \tilde{s} - r^{pr}(w, u)$$

which is bounded by (cf. [Pomplun, 2010])

$$|\tilde{s}^{pd} - \tilde{s}| \leq \frac{1}{\beta} \|r^{pr}(\cdot, u)\|_{X'} \|r^{du}(\cdot, w)\|_{X'}.$$

Here $r^{pr}(w, u)$ denotes the primal residual which is evaluated at the dual solution and $r^{du}(w; u)$ the corresponding residual of the dual problem.

In many publications [Sommer et al., 2015, Pomplun and Schmidt, 2010] these dual corrected output of interest are employed to improve convergence. Most focus on linear outputs though quadratic outputs are not drastically more complicated in this context. The drawback of this improved convergence is the necessity to construct a separate reduced basis for the dual problem and the X_N^{du}. The Galerkin orthogonality of the residual prohibits the use of $X_N^{du} = X_N$ as the correction $r^{pr}(w, u)$ would vanish thus requiring a separate reduced basis space $X_N^{du} \neq X_N$. Note that the sesquilinear form $a(\cdot, \cdot)$ is the same in primal as in the dual problem (linear and quadratic). This allows to compute the dual bases for Problems 9 and 10 efficiently using the same approximation of the left hand side as in the primal problem. However, the dual corrected output of interest requires a solution of the dual problem for every output of interest. In the typical setup described in this work usually a larger number of outputs is considered. Especially for this configuration the overhead of computing multiple reduced bases for dual problems might not be compensated by the improved converge rates of the dual correction.

5.7. Quadratic quantities of interest

Many applications require the investigation and optimization of power fluxes or energy transformation processes. Flux and density integration post processing of arbitrary flux or density type tensor fields hence are of great interest for many studies. Computation of power fluxes via integration of the Poynting vector fluxes $\boldsymbol{S} = \mathfrak{Re}\left\{\boldsymbol{E} \times \overline{\boldsymbol{H}}\right\}$ across the boundaries of subdomains and integration of the electric energy density $\frac{1}{4}\boldsymbol{E}\cdot\overline{\boldsymbol{D}}$ over subdomains are among the most common. In contrast to linear outputs of interest such as the Fourier transform of the scattered electromagnetic field, these quantities are quadratic functionals of the electric field. As much of the literature on RBMs is focused on linear functionals, this post processing step for the RBM is thus presented in more detail in this section.

5.7.1. Expanded formulation for quadratic outputs

A method to include general quadratic outputs of the form

$$s_q(u;\mu) = l(u;\mu) + q(u,u;\mu),$$

where $q(\cdot,\cdot;\mu)$ and $l(\cdot;\mu)$ are (sesqui-)linear forms, into a reduced basis formulations is an expanded problem formulation. In [Huynh and Patera, 2007] it is presented for stress intensity factors in fracture mechanics and in [Sen, 2007] for power fluxes in acoustics. The idea underlying this formulation is essentially the simultaneous computation of the solution u and the adjoint state z for the quadratic(-linear) output, allowing to compute the quadratic output of interest as a *linear*, compliant output. The extended formulation thus requires the computation of a pair (u, z) as solutions of the following system:

$$a(v, u; \mu) = f(v; \mu) \quad \forall v \in X \tag{5.23a}$$

$$a(z, v; \mu) = q(u, v; \mu) + \frac{1}{2}l(v; \mu) \quad \forall v \in X \tag{5.23b}$$

Setting

$$w^+ = \frac{1}{2}\left(u + z\right)$$

$$w^- = \frac{1}{2}\left(u - z\right)$$

allows to reformulate (5.23) as

$$a(v, w^+; \mu) + a(v, w^-; \mu) = f(v; \mu) \quad \forall v \in X \tag{5.24a}$$

$$a(w^+, v; \mu) - a(w^-, v; \mu) = q(w^+, v; \mu) + q(w^-, v; \mu) + \frac{1}{2}l(v; \mu) \quad \forall v \in X. \tag{5.24b}$$

For all $v^+, v^- \in X$ we obtain by adding (5.24a) and (5.24b)

$$
\begin{aligned}
a(v^+, w^+; \mu) + a(v^+, w^-; \mu) \\
+ a(w^+, v^+; \mu) - a(w^-, v^+; \mu) \\
- q(w^+, v^+; \mu) - q(w^-, v^+; \mu) = f(v^+; \mu) + \frac{1}{2} l(v^+; \mu)
\end{aligned}
$$

and subtracting (5.24a) from (5.24b)

$$
\begin{aligned}
a(w^+, v^-; \mu) - a(w^-, v^-; \mu) \\
- a(v^-, w^+; \mu) - a(v^-, w^-; \mu) \\
- q(w^+, v^-; \mu) - q(w^-, v^-; \mu) = -f(v^-; \mu) + \frac{1}{2} l(v^-; \mu)
\end{aligned}
$$

again two equations. This set of equations is equivalent to

$$
A(\mathcal{V}, \mathcal{W}; \mu) = F(\mathcal{V}; \mu) \quad \forall \mathcal{V} \in \mathcal{X} \tag{5.25}
$$

where $\mathcal{X} = X \times X$, $\mathcal{W} = (w^+, w^-)$, $\mathcal{V} = (v^+, v^-)$ and the sesquilinear form $A : \mathcal{X} \times \mathcal{X} \times \mathfrak{D} \to \mathbb{C}$ and linear form $F : \mathcal{X} \times \mathfrak{D} \to \mathbb{C}$ are defined as

$$
\begin{aligned}
A(\mathcal{V}, \mathcal{W}; \mu) =& a(v^+, w^+; \mu) + a(v^+, w^-; \mu) \\
& - a(v^-, w^+; \mu) - a(v^-, w^-; \mu) \\
& + a(w^+, v^+; \mu) - a(w^-, v^+; \mu) \\
& + a(w^+, v^-; \mu) - a(w^-, v^-; \mu) \\
& - q(w^+, v^+; \mu) - q(w^-, v^+; \mu) \\
& - q(w^+, v^-; \mu) - q(w^-, v^-; \mu) \\
F(\mathcal{V}; \mu) =& f(v^+; \mu) - f(v^-; \mu) + \frac{1}{2} l(v^+; \mu) + \frac{1}{2} l(v^-; \mu)
\end{aligned}
$$

Evaluating the compliant output functional $F(\mathcal{W}; \mu)$ at the solution $\mathcal{W}$ of (5.25) is now equivalent to computing the quadratic output in the original problem. This

can be quickly checked:

$$
\begin{aligned}
F(\mathcal{W}; \mu) &= f(w^+; \mu) - f(w^-; \mu) + \frac{1}{2}l(w^+; \mu) + \frac{1}{2}l(w^-; \mu) + \\
&= f(w^+ - w^-; \mu) + \frac{1}{2}l(w^+ + w^-; \mu) \\
&= f(z; \mu) + \frac{1}{2}l(u; \mu) \\
&= a(z, u; \mu) + \frac{1}{2}l(u; \mu) \\
&= q(u, u; \mu) + \frac{1}{2}l(u; \mu) + \frac{1}{2}l(u; \mu) \\
&= q(u, u; \mu) + l(u; \mu) \\
&= s_q(u; \mu)
\end{aligned}
$$

Assessment of the expanded formulation

The benefit of this formulation is obviously the evaluation of the quadratic output as a linear functional, thus being suited for a standard reduced basis formalism. Furthermore, a compliant output does not require a primal-dual formulation as in the linear, non-compliant case to achieve similar convergence rates.

The downside of this formulation is the requirement to solve (5.25) which is of dimension $\dim(\mathcal{X}) = 2\dim(X)$. Hence in a discretized system this is equivalent to the inversion of a system with twice the number of unknowns. Even though in the RBM this operation is only executed in the offline phase while the online costs are not affected, this renders the extended formulation infeasible for large, non-coercive systems with $\dim(X)$ in the order of millions. In addition, this approach does not scale well for multiple quadratic outputs.

5.7.2. Density integration

The electric field energy density is given by $w_e = \frac{1}{4}\boldsymbol{E} \cdot \overline{\boldsymbol{D}}$ as an expression of the electric field $\boldsymbol{E}$ and the electric displacement field $\boldsymbol{D}$ and similarly the magnetic field energy density by $w_m = \frac{1}{4}\boldsymbol{H} \cdot \overline{\boldsymbol{B}}$ with the magnetic field $\boldsymbol{H}$ and the magnetic flux density $\boldsymbol{B}$. In the following we focus on the electric field energy density. Assuming $\boldsymbol{D} = \varepsilon\boldsymbol{E}$ holds, w_e appears as a quadratic form:

$$
w_e(\boldsymbol{E}) = \frac{1}{4}\boldsymbol{E} \cdot \overline{\boldsymbol{D}} = \frac{1}{4}\boldsymbol{E} \cdot \overline{\varepsilon\boldsymbol{E}}. \tag{5.26}
$$

The energy densities itself are usually of minor interest whereas the integrated quantity, the electric field energy $W_e = \int_\Omega w_e \, d\boldsymbol{r}$ contained within a (sub-) domain Ω, are of greater importance. The electric field energy allows for example to compute the volume absorption within the domain (cf. Section 2.2.2). Usually a numeric quadrature rule of sufficiently high order is used to compute this integral in the

finite element context. This is an efficient strategy if the integration has to be done only once (cf. also Section 4.3.2), even though this post processing step can become very expensive.

Reduced basis formalism

Let $\Phi_N = \{\phi_i, i = 1, \ldots, N\}$ a basis of the reduced basis space X_N. We expand the reduced basis solution $u_N(\mu)$ in this basis

$$u_N(\mu) = \sum_{i=1}^{N} \alpha_i(\mu)\phi_i$$

and evaluate W_e for u_N

$$W_e(u_N(\mu)) = \frac{1}{4} \int_{\Omega} \sum_{i=1}^{N} \alpha_i(\mu)\phi_i \cdot \overline{\varepsilon(\mu) \sum_{j=1}^{N} \alpha_j(\mu)\phi_j} \, \mathrm{d}r$$

$$= \sum_{i,j=1}^{N} \alpha_i(\mu)\overline{\alpha_j(\mu)} \frac{1}{4} \int_{\Omega} \phi_i \cdot \overline{\varepsilon(\mu)\phi_j} \, \mathrm{d}r$$

$$= \sum_{i,j=1}^{N} \alpha_i(\mu)\overline{\alpha_j(\mu)} \, Q(\phi_i, \phi_j; \mu)$$

$$= \boldsymbol{\alpha}(\mu)^\mathsf{T} \mathcal{Q}(\mu)\overline{\boldsymbol{\alpha}(\mu)}$$

Note that evaluating $\mathcal{Q}(\mu) \in \mathbb{C}^{N \times N}$ for a given μ requires N^2 volume integrations of snapshot solutions ϕ_i. Thus this procedure becomes highly inefficient as it requires all snapshot solutions to be stored along with their shape functions and implies costs in the order of $N^2\mathcal{N}^2$. However, we can employ once again an empirical interpolation scheme to recover an affine expansion in the parameter. In this case this has to be done with respect to the permittivity tensor ε instead of the complete FEM system matrix. This leads to a set of parameters $\{\mu_1, \ldots, \mu_{Q_{PP}}\}$ which is in generally distinct from the one used in the empirical interpolation of the FEM system. Using this set $\varepsilon(\mu)$ reads

$$\varepsilon(\mu) = \sum_{k=1}^{Q_{PP}} \theta_k(\mu)\varepsilon(\mu_k) \tag{5.27}$$

and subsequently the matrix entries become

$$\mathcal{Q}(\mu)_{i,j} = Q(\phi_i, \phi_j; \mu) = \frac{1}{4} \int_{\Omega} \phi_i \cdot \overline{\varepsilon(\mu)\phi_j} \, \mathrm{d}r = \sum_{k=1}^{P} \theta_k(\mu) \frac{1}{4} \int_{\Omega} \phi_i \cdot \overline{\varepsilon(\mu_k)\phi_j} \, \mathrm{d}r$$

$$= \sum_{k=1}^{Q_{PP}} \theta_k(\mu) Q(\phi_i, \phi_j; \mu_k).$$

To distinguish between subdomains $\Omega_{id} \subset \Omega$ we furthermore have to restrict the integral to Ω_{id} and treat all of the $\mathbf{I}$ disjoint subdomains $\{\Omega_{id_1}, \Omega_{id_2}, \ldots \Omega_{\mathbf{I}}\}$ separately. As a simplification we do not use separate empirical interpolants for the restricted permittivity tensors $\varepsilon|_{\Omega_{id}}$. This is justified as an affine expansion interpolating ε on Ω does so on subdomains $\Omega_{id} \subset \Omega$ as well. Theoretical savings in requiring fewer expansion terms in a subdomain compared to a global approach have to be balanced against a more complicated implementation managing separate empirical interpolants for subdomains.

Offline phase

Naturally we aim at reducing online costs as much as possible. Thus it is necessary to compute the entries $Q_{id}(\phi_i, \phi_j; \mu_k)$ during the offline phase which still is an expensive step as it requires $Q_{PP}N^2$ integrations for every subdomain Ω_{id}. Note that Q is only symmetric if ε is real valued, i.e. the materials are non-absorptive. However, we can exploit the nature of the reduced basis elements ϕ_i which can be expanded in the underlying finite element basis $\{\zeta_1, \ldots, \xi_{\mathcal{N}}\}$ themselves. Using the expansion $\phi_i = \sum_{l_i=1}^{\mathcal{N}} \beta_{l_i} \zeta_{l_i}$ we can rewrite $Q_{id}(\phi_i, \phi_j; \mu_k)$ once more as

$$Q_{id}(\phi_i, \phi_j; \mu_k) = \sum_{l_i=1}^{\mathcal{N}} \sum_{l_j=1}^{\mathcal{N}} \beta_{l_i} \overline{\beta_{l_j}} \frac{1}{4} \int_{\Omega_{id}} \zeta_{l_i} \cdot \overline{\varepsilon(\mu_k)\zeta_{l_j}} \, \mathrm{d}r = \boldsymbol{\beta}_i^{\mathsf{T}} \mathfrak{Q}_{id}(\mu_k) \overline{\boldsymbol{\beta}_j}. \tag{5.28}$$

Assembling $\mathfrak{Q}_{id}^k = \mathfrak{Q}_{id}(\mu_k)$ is closely linked to assembling the mass matrix in the FEM system matrix $\mathcal{A}$. Computing the matrix entry $Q_{id}(\phi_i, \phi_j; \mu_k)$ results in a Galerkin projection step involving the finite element coefficient vectors $\boldsymbol{\beta}_i, \boldsymbol{\beta}_j$ of the snapshot solutions ϕ_i, ϕ_j and the matrix $\mathfrak{Q}_{id}^k$. The computational effort is reduced by restricting the assembly process to degrees of freedom associated with Ω_{id} and likewise selection of the associated entries of $\boldsymbol{\beta}$.

Summarizing the previous steps:

(i) Empirical interpolation of $\varepsilon(\cdot)$ with respect to $\{\mu \,|\, \mu \in \mathfrak{D}\}$.

(ii) Assembly of required matrices $\{\mathfrak{Q}_{id}^k\}$.

These two steps are independent of the reduced basis assembling steps and can thus be executed prior to the computation of the first snapshot (or in parallel). The addition of a new snapshot requires the projection step (5.28) to be executed with respect to every previous snapshot and for all matrices. This results in $(2N-1)Q_{PP}\mathbf{I}$ total projections.

Online phase

In the online phase we can compute the electric field energy contained in the subdomain Ω_{id} very efficiently for an arbitrary $\mu \in \mathfrak{D}$. We start by determining the

Table 5.1.: Operation count of the offline and online phases for different algorithmic
steps.

phase	step	operation count
offline	system assembly for EIM	$O(Q_A \mathcal{N})$
	computation of snapshots solutions[1]	$O(N \mathcal{N}^2)$
	Gram-Schmidt orthogonalization	$O(N^2 \mathcal{N})$
	matrix projection	$O(Q_A N^2 \mathcal{N})$
	residual error estimate: inner product matrix[1]	$O(\mathcal{N}^2)$
	residual error estimate: substitutions	$O(N(Q_f + Q_A)\mathcal{N})$
	residual error estimate: scalar products	$O(N^2(Q_f + Q_A)^2 \mathcal{N})$
	linear output of interest	$O(N\mathcal{N})$
	quadratic output of interest: assembly	$O(Q_{PP}\mathcal{N})$
	quadratic output of interest: projection	$O(Q_{PP}N^2 \mathcal{N})$
online	assembly of reduced system	$O(Q_A N^2)$
	solution of reduced system	$O(N^3)$
	residual error estimate	$O(Q_A^2 N^2)$
	linear output of interest	$O(N)$
	quadratic output of interest	$O(Q_{PP} N^2)$

empirical interpolation coefficients $\boldsymbol{\theta}(\mu)$ (5.27) first. Then we can use the coefficient
vector $\boldsymbol{\alpha}$ of (5.7.2) to compute $W_e^{id}(u_N(\mu))$ as follows:

$$W_e^{id}(u_N(\mu)) = \sum_{k=1}^{Q_{PP}} \theta_k(\mu) \boldsymbol{\alpha}^\mathsf{T} \mathcal{Q}_{id}^k \overline{\boldsymbol{\alpha}} \tag{5.29}$$

5.8. Operation count

In the previous sections we did not examine the computational costs in constructing
the reduced basis approximation. We thus discriminate the operation count between
offline and online phase. An overview of all steps involved with associated operation
count is found in Table 5.1.

Offline, the EIM requires assembling Q_A FEM systems. The sparse FEM system
of dimension $\mathcal{N}$ has to be solved for N snapshots. The complexity of this opera-

---

[1]Actual costs depend on the sparsity structure of the FEM system matrix. The complexity $O(\mathcal{N}^2)$
noted here is based on the observed cpu times listed in Table 6.4.

tions depends on several factors such as the structure, storage format and number of non-zero entries. In practical applications we usually observe complexity resembling $O(\mathcal{N}^2)$ as listed in Section 6.2.2. The snapshots are orthogonalized to increase numeric stability. This involves computing N^2 projections of the snapshots onto each other. Subsequently they are projected onto the Q_A system matrices (cf. (5.4)). As these are sparse, the number of operations is $O(Q_A N^2 \mathcal{N})$. The residual error estimator requires the computation of several Riesz representers (cf. (5.9)). However, a single LU decomposition of the inner product matrix $\mathcal{H}$ is sufficient to compute these together with $N(Q_f + Q_A)$ forward/backward substitutions. Subsequently, the $N^2(Q_f + Q_A)^2$ scalar products in (5.10) are computed.

The costs for linear outputs amount to $O(N\mathcal{N})$. For the quadratic output in Section 5.7.2 we need to distinguish the assembly of the Q_{PP} terms and the projection. The assembly is related to the FEM system assembly thus the costs are comparable. These matrices are sparse as well, hence the cost for the projections (5.28) are $O(Q_{PP} N^2 \mathcal{N})$.

In the online phase it is sufficient to assemble Q_A reduced systems which amounts to $O(Q_A N^2)$ operations. The inversion of the dense RB system amounts to $O(N^3)$ operations and an additional $O(N)$ operations is required for the evaluation of a linear output of interest. The evaluation of the residual error estimate requires $O(Q_A^2 N^2)$. The quadratic output of interest has approximately the same costs as it requires $O(Q_{PP} N^2)$ operations.

5.9. Reduced Basis Method and high performance computing

The RBM demands a lot of computational resources during the offline phase. High-performance computing centers offer supercomputers with performance in the peta-flop/s regime. Naturally one seeks to develop strategies to optimally use the resources available and distribute the workload whenever possible. In terms of high performance computing parallelization is key. The authors of [Knezevic and Peterson, 2011] note several opportunities for parallelization, including

- $\mathcal{N}$ dependent operations should be executed in parallel if possible,

- the Greedy search is embarrassingly parallel.

The first is easily addressed. The underlying finite element toolbox of JCMsuite heavily relies on thread parallelization wherever feasible. Namely matrix-vector operations as well as the solution of the linear system make efficient use of the available processing power through use of the OpenMP framework. The Greedy search requires evaluations of the error estimator for any parameter $\mu_t \in \mathfrak{D}_{train}$ during the argmax computation. Parallelizing this operations directly reduces computation times and scales optimally with the number of cores. However, it demands a thread

safe implementation of the reduced basis solution and error estimation, an operation that terminates within milliseconds. In real world application problems with $\mathcal{N} \approx 10^6$ the $\mathcal{N}$ operations clearly determine the offline computation times and the Greedy search is negligible even in high-dimensional parameter spaces (hours vs. seconds).

Current high-performance systems or super-computing clusters often use nodes with 64 GB main memory [HLRN, 2015, LRZ, 2015] whereas large-memory systems are rare. Hence computing nodes in supercomputers are generally too small to compute a reduced model for a larger problem on their own. We thus find a more challenging restriction in the available memory of a single machine. During the offline phase our RBM implementation assembles and stores a number of large sparse matrices of dim $\leq \mathcal{N}$. This is required by the EIM employed for both the parameter dependent system matrix and the matrices used in the post processes for subdomains. These possibly large storage requirements may prohibit the solution of the linear system to be executed on the same machine. The strategies to circumvent this include

- reassembling the matrices each time they are required,

- writing matrices to disk,

- using more than one physical machine.

The first is only a last resort as the overhead of reassembling $Q_A + Q_{PP}$ FEM matrices in every iteration is tedious. Offloading large matrices to disk is possible but produces overhead in reading and writing. The latter strategy requires the simultaneous use of at least two machines which further increases the computational requirements. Provided we have a computing cluster at our disposal, we can leverage the advantages process parallelization in addition to thread parallelization. Using Message Passing Interface (MPI) we can exchange information and data between different processes within the cluster and use different machines for assembling and solution of the linear systems. Thus the matrix inversion can be done on a machine or a cluster with sufficient memory, whereas another machine keeps the matrices in memory and transfers the matrix to be inverted to the other processes.

6. Numerical Examples

In this chapter numerical results are presented demonstrating the efficacy of the methods presented in the previous chapters. Most of theses examples are adapted from previous indicated publications. They demonstrate in great detail the flexibility of the implementation and the properties of the presented methods.

The reduced basis method relies on the assumption that the solution manifold can be approximated well by snapshot solutions. In case of a structure exhibiting resonant behaviour the field solution changes drastically with small variations of a parameter. In the first example in Section 6.1, the efficacy of the Reduced Basis Method for such a case is demonstrated. A reduced model is derived for photonic crystal made of silicon. The arising errors of the reduced basis and the Empirical Interpolation approximations are discussed in detail.

The following examples concern the simulation of multi-junction solar cells. The inclusion of incoherent layers in rigorous optical simulations. The focus of this examples is to establish a rigorous optical modeling setting for TFSSC including incoherent light trapping. On this basis we investigate the use of Reduced Basis Method and our implementation for this context in detail and demonstrate convergence properties again.

6.1. Hexagonal nano-hole array: a reduced basis for a photonic crystal

The following numerical example demonstrates the efficacy of the Reduced Basis Method for Maxwell's equation in case resonance phenomena occur. Results presented in this example were published in [Hammerschmidt et al., 2015b]. In this section we present a short motivational review of previous work, before presenting the optical model the reduced basis is built on. A detailed discussion and analysis of the approximation errors are presented next. The simulation results of the reduced model conclude this section.

6.1.1. Review and motivation

Photonic crystals are periodic structures that inhibit propagation of electromagnetic waves of frequencies within a specific frequency band called photonic band gap. The commonly used Distributed Bragg reflector is a one-dimensional photonic crystal consisting of a stack of multiple layers with different refractive indices. It can be used as an ideal reflector for specific wavelength λ_0 or a wavelength interval using

a large number of repeating pairs of materials whose thicknesses are close to $\frac{\lambda_0}{4n}$ where n is the refractive index. The alternation of materials leads to a constructive interference pattern which gives rise to a photonic stop band of wavelengths which are reflected by the layer stack almost perfectly.

The same principle applies to higher spatial dimensions where repeating material patterns are introduced through (nano-) structuring of materials for example in gratings [Joannopoulos et al., 2011, Yablonovitch, 1993]. Hexagonal arrays of holes in a high-index material are among the most frequently investigated structures. They give rise to pronounced photonic band gaps and are envisioned to be used in a variety of applications such as solar cell light management or up-conversion as well as optical sensing.

In [Becker et al., 2014] we investigated the absorption properties and the excitation of high-intensity near-fields within periodic, conical cavities (or *nanoholes*) of a silicon slab. We computed near-field enhancements as an increased electromagnetic field energy density in and 100 nm above the cavity normalized by the same quantity for the incident field in free space. The resonance bands depicted in Figure 6.1a were also observed in experimental reflection measurements and a good agreement between experimental and numerical results was found in the cited reference. The photonic crystal exhibits several distinct resonances with high quality factors in both polarizations which strongly depend on the wavelength and incidence angle of the illumination. They correspond to resonance modes excited in the photonic crystal structure. We found enhancements larger than a factor of 500 in [Becker et al., 2014] and subsequently found even higher enhancements for specific optical modes. The highest field enhancements correspond to excitation of Bloch modes in the crystal. Even if the highest field intensities are confined within the silicon crystal, the leakage into the cavity is substantial and encourages the afore mentioned applications.

The main numerical result of [Becker et al., 2014] is thus the field enhancement patterns of the nanohole array for all symmetry directions of the lattice. In Figure 6.1a such a pattern is shown for p-polarized illumination from the upper half-space tilted along the $\Gamma - K$ direction. Several distinct resonances are visible, corresponding to resonance modes of the photonic crystal. The field enhancement for $\theta = 17°$ in Figure 6.1b exhibits a number of high quality resonances over a broad spectrum. The resonance marked in red has a field enhancement larger than 230 and a full width half maximum smaller than 1.5 nm. It is isolated and drifts only slightly in resonance wavelength as can be seen in the rectangle marked in Figure 6.1a.

A slight red-shift compared to the experimental results was observed in the numerical simulations. The confidence in the accuracy of the numerical simulations allowed to conclude that this shift is due to small deviations of the experimentally realized structures to the model geometry. The deviations of the geometric parameters are readily investigated using a reduced basis model for the geometric and illumination parameters. Furthermore, many of the envisioned applications profit from broadband field enhancements. A reduced basis can be employed to optimize geometric parameters for the desired applications.
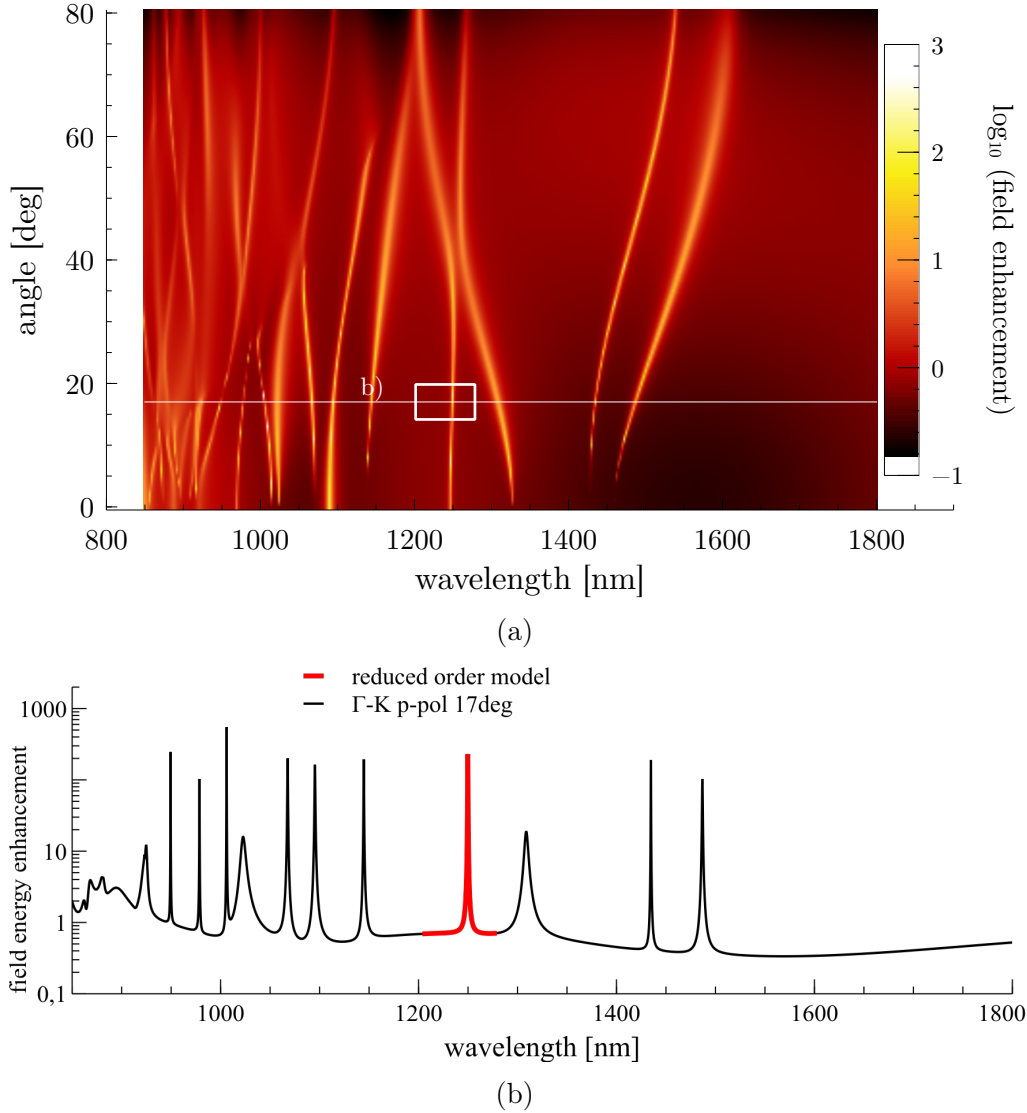
(a)

(b)

Figure 6.1.: (a): Simulated field enhancement pattern of the nanohole array on log-
arithmic scale. The field enhancement is measured in the cavity and
100 nm above the array and normalized with the field energy of a plane
wave in the respective volume. The incident wave is p-polarized and
tilted along the $\Gamma - K$ direction. The white line marks the cut shown
in b). The rectangle marks the limits of the parameter domain of the
reduced order model discussed in this section.
(b): Simulated electric field enhancement for p-polarized light at 17°
incidence angle in $\Gamma - K$ direction on a logarithmic scale (data adapted
from [Becker et al., 2014]). The reduced order model contains the sec-
tion of the spectrum shown in red. The resonance in this interval has
a field enhancement larger than 230 and a full width half maximum
smaller than 1.5 nm.
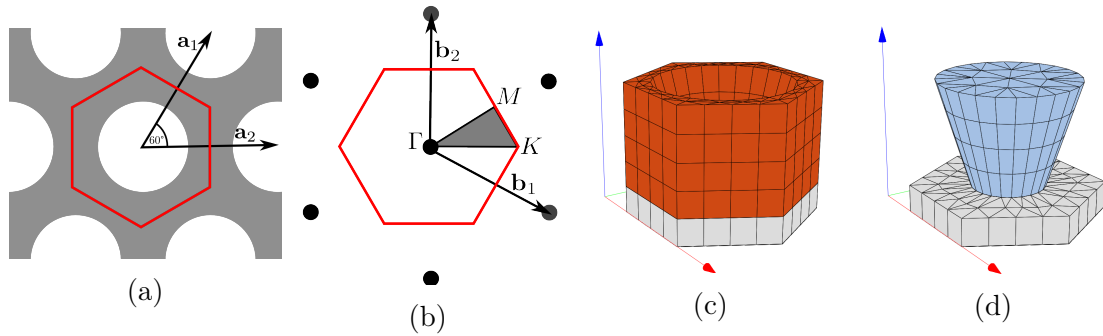
6.1.2. Optical model

Figure 6.2.: Schematic of the unit cell of the hexagonal nanohole array with 600 nm pitch in real space (a) and k-space (b). The high-symmetry points of the irreducible Brillouin zone (gray) are marked. (b) The silicon slab (orange) sits on a glass substrate (gray) and is 390 nm thick. (c) The conical hole (blue) is centered in the unit cell with a sidewall angle of 17° and has a diameter of of 385 nm at the center of the slab. An air layer (100 nm thick, not shown) completes the cell. In $\pm z$ directions transparent boundary conditions are applied.

We use exactly the same setup as in [Becker et al., 2014]. The unit cell model of the investigated periodic structure is shown in Figure 6.2. The cell has a pitch of 600 nm and the conical hole has a sidewall angle of 17 ° inherent to the fabrication process. The diameter of the hole is 385 nm at the center of the 390 nm thick slab. The unit cell is split into four subdomains: the silicon slab, the cavity, the glass substrate and the air layer of 100 nm thickness above the array. In $\pm Z$ directions transparent boundary conditions are applied, i.e. the air and glass domains are extended via PML-layers. The p-polarized illumination from the upper half-space is varied in wavelength λ and incidence angle θ along the Γ-K-direction. The parameterization used is

$$\boldsymbol{E}_{in}(\lambda, \theta) = \begin{pmatrix} 0 \\ -\cos(\theta) \\ -\sin(\theta) \end{pmatrix} \quad , \quad \boldsymbol{k}_{in}(\lambda, \theta) = \begin{pmatrix} 0 \\ \sin(\theta) \\ -\cos(\theta) \end{pmatrix} \frac{2\pi n_{glass}}{\lambda}.$$

The refractive index of silicon (taken from [Palik, 1998]) is dispersive but real-valued in the investigated wavelength range and $n_{air} = 1, n_{glass} = 1.53$ are kept constant. The FEM discretization with fourth-order elements and adaptive, accurate PML-settings yields a system with $\mathcal{N} = 249\,540$ unknowns.

6.1.3. Reduced basis assembly

In order to study the effectivity and the convergence properties of our reduced basis implementation, we build a reduced basis for the illumination parameters λ and θ in the parameter domain $\mathfrak{D} = [1200 \text{ nm}, 1280 \text{ nm}] \times [14°, 20°]$ with the self-adaptive assembly with the Greedy algorithm described in Section 5.6 and 5.6.1. As the computational requirements of this model problem are relatively small (240 s of cpu time for a snapshot and 16 GB memory) no restrictions to the number of snapshots are prescribed. We chose an estimated accuracy of $5 \cdot 10^{-6}$ in the output quantities as the stopping criterion. The reduced model is build for three output quantities simultaneously:

- the Fourier transform in z direction to compute the reflection of the array,

- the Fourier transform in -z direction to compute the transmission of the array,

- the electric field energy density integration to compute field enhancements in the subdomains of the array.

Due to the small pitch, only the 0th order Fourier mode is propagating in $\pm Z$ direction. The quadratic output quantity *electric field energy* is computed for the four subdomains. We will refer to these quantities again by the corresponding post process names in JCMsuite: *FourierTransform* and *DensityIntegration*.

The training set $\mathfrak{D}_{train}$ used for the various Greedy searches is chosen to be quite dense to adequately resolve all features within $\mathfrak{D}$. It initially comprises 101×21 sampling points in a equidistant grid along λ and θ axis.

The EIM approximation is executed using a tolerance of $\epsilon_{EIM} = 1 \cdot 10^{-7}$. The statistics of the EIM approximation are listed in Table 6.1. For the empirical interpolation of the system matrix $Q_A = 3$ snapshots are required leading to an estimated error of $\delta_{EIM}^A = 7.45 \cdot 10^{-12}$ over the training set $\mathfrak{D}_{train}$. Using the same training set, we find requirements of $Q_b = 8$ and $Q_{PP} = 2$ for the empirical interpolation of the source terms and the quadratic post processes. The resulting approximation errors over $\mathfrak{D}_{train}$ are $\delta_{EIM}^b = 9.42 \cdot 10^{-8}$ and $\delta_{EIM} = 7.24 \cdot 10^{-13}$ respectively.

Table 6.1.: EIM approximation summary - number of terms Q employed in expansion and error estimate δ of approximation for different functionals.

EIM	system matrix	right hand side	post process
Q	3	8	2
δ	$7.449 \cdot 10^{-12}$	$9.424 \cdot 10^{-8}$	$7.237 \cdot 10^{-13}$

In the offline phase 30 snapshots are computed to build the reduced basis for the parameter space $\mathfrak{D} = [1200 \text{ nm}, 1280 \text{ nm}] \times [14°, 20°]$. The same training set $\mathfrak{D}_{train}$ of cardinality 2021 is used for the empirical interpolation and the Greedy step in the
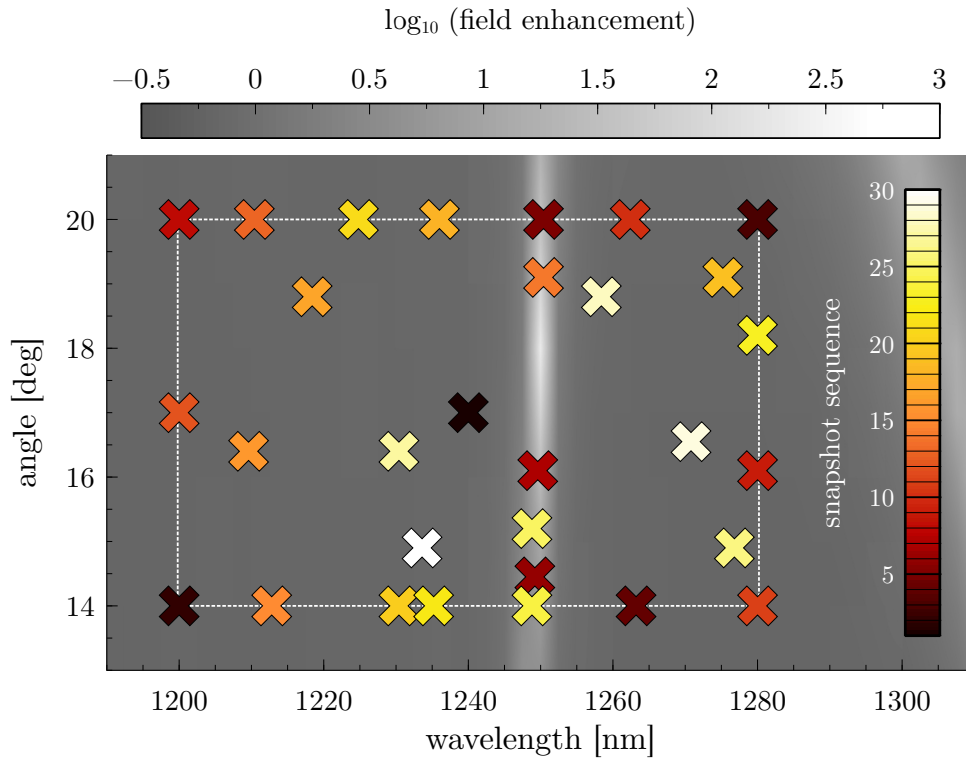
Figure 6.3.: Snapshot positions in parameter space are marked as crosses. They are superimposed on a gray-scale logarithmic plot of the field enhancement shown in Figure 6.1a. The color of the marker indicates the sequence of snapshot selection from darker to lighter colors. The first snapshot chosen is the center of the parameter domain. Most snapshots are located at the boundaries (dashed white line) of the parameter domain. A cluster of snapshots lies along the resonance band at approximately 1250 nm.

reduced basis offline phase. Figure 6.3 depicts the location of the chosen snapshots (crosses) in the parameter domain. The color coding indicates the sequence in which the snapshots were chosen (dark to light markers). The first snapshot is chosen in the center of the parameter domain and the subsequent snapshots are determined by the Greedy algorithm. The choice of snapshot locations follows the boundaries of $\mathfrak{D}$. This is in line with other publications where similar observations were made [Eftang et al., 2010b]. The first selected snapshots cover the extreme positions (1200, 14) and (1280, 20). Along the resonance band we find 6 snapshots in total with the first 3 snapshots chosen in iterations 5-7.

(a)

(b)   (c)   (d)
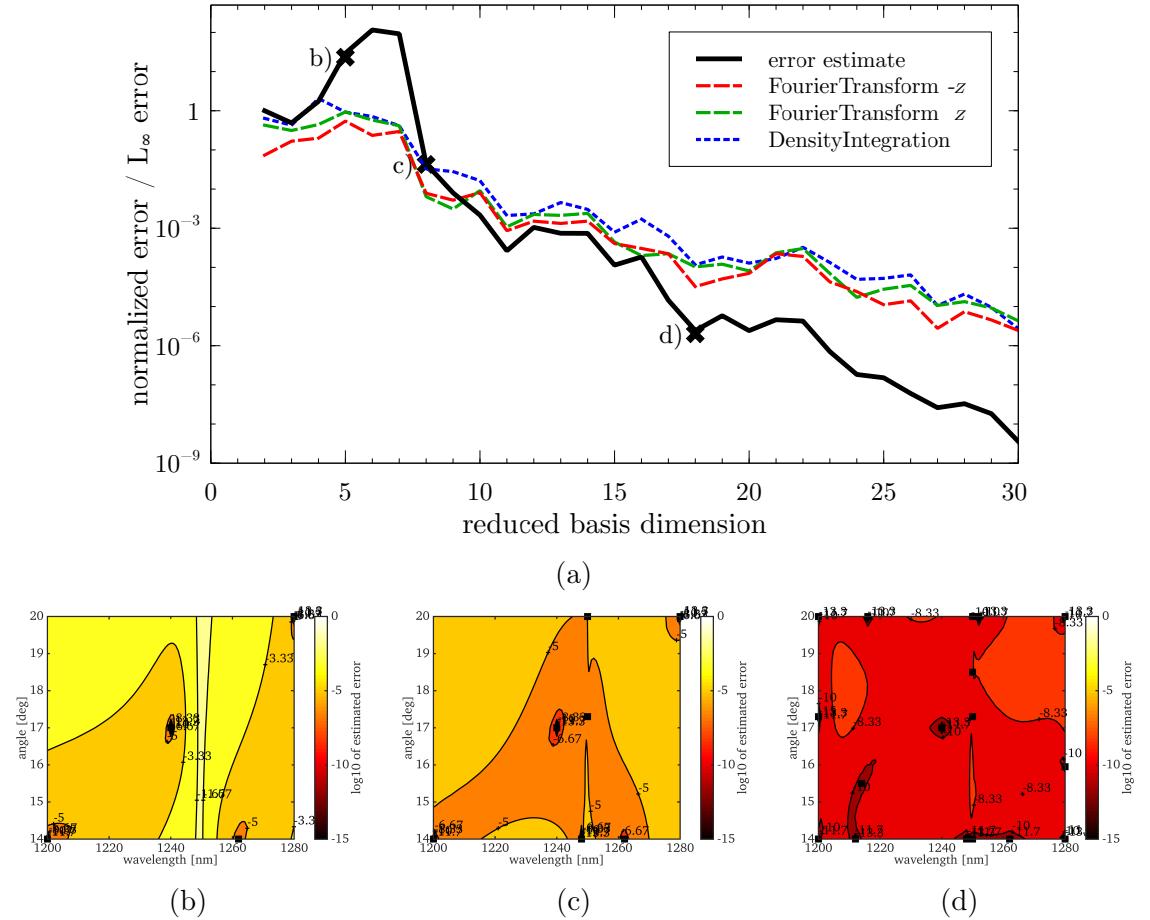
Figure 6.4.: (a): Error estimates with increasing reduced basis dimension in a semi-logarithmic plot. The residual error estimate (black) is normalized with the estimate for $N = 1$ (see Section 5.4.2 for definitions of the error estimators). The error estimates $\eta^l(N)$ and $\eta^q(N)$ for the FourierTransforms (red, green) and DensityIntegration (blue) measure the L_∞-norm. (b)-(d): Contours of the residual error estimate on a logarithmic scale with 4 (b), 7 (c) and 17 (d) snapshots.

The reduced basis offline phase chooses the snapshots according to a Greedy strategy depending on the error estimate for the worst-resolved parameter in the training set. Hence the estimated error generally decreases with increasing Greedy iterations. In Figure 6.4a the error estimates with increasing reduced basis dimension is shown in a semi logarithmic plot. The black line shows the normalized residual error estimate (5.11) for increasing reduced basis dimension N. The maximum of the error estimate in the first Greedy iteration is used as a normalization factor. The error first increases to a maximum of 115.62 at $N = 6$ before dropping to a level of 0.0440 at $N = 8$. Subsequently we observe exponential convergence of this error estimate up to a level of $3.59 \cdot 10^{-9}$. The increase is caused by the resonance band traversing the parameter domain as the false color contour plots of the estimated error in $\mathfrak{D}$ in subfigures b)-d) show. The labels in Figure 6.4a correspond to the subfigures. Figure 6.4b shows contours of the error estimate using 4 snapshots (whose locations are depicted as black squares). Clearly recognized by the estimator is the resonance band traversing the parameter domain at ≈ 1250 nm. As this area is poorly approximated by the first snapshots, the error estimate increases momentarily, leading to the maximum in Figure 6.4a. The error estimator does not recognize this resonance band and underestimates the true error in this region. In Figure 6.4c, using 7 snapshots, the resonance band is much better resolved and the error level decreases globally. The maximum is no longer found in the proximity of the resonance band. The last contour plot in Figure 6.4d corresponds to a global error level of 10^{-6}.

The dashed red and green graphs for the *FourierTransform* in *-z* and *z* directions and the blue graph for the *DensityIntegration* depict the errors $\eta^l(N)$ and $\eta^q(N)$ defined in Section 5.4.2 in the L_∞-norm. The graphs again start at $N = 2$ as the errors $\eta^l(1), \eta^q(1)$ are not defined. All three graphs exhibit an exponential reduction of the error over the training set up to approximately $2 \cdot 10^{-6}$.

6.1.4. Approximation errors

The error of reduced basis approximation can be measured differently. In general the reduced basis should approximate the truth solution itself more accurately with increasing reduced basis dimensions. In most applications the error in the output quantities is of particular interest. In our RBM we have to distinguish between the error of the reduced basis and the additional approximation introduced by the empirical interpolation (cf. Section 5.5.1). We thus compare the reduced basis approximation and two sets of reference solutions for two randomly chosen parameter ensembles $\Xi_{1,2} \subset \mathfrak{D}_{train}$ of 500 parameters each. Figure 6.7 shows the distribution of the parameter locations Ξ_1 as crosses. The diagram itself is discussed later in Section 6.1.5. For these parameters $\mu \in \Xi_1$ we solve the full FEM problem without any approximation i.e. these solution fulfill the truth approximation 6 on page 65. Note that these reference solutions are not solutions of the truth approximation 8 on page 78 which includes the EIM approximation of the system matrix and right-hand sides. We compute a second set of reference solutions over the parameter ensemble $\Xi_2 \subset \mathfrak{D}_{train}, \Xi_1 \neq \Xi_2$ as solutions of the truth approximation 8 including

the empirical interpolation for the system matrix and right-hand side.

Output quantities   We begin by comparing the output quantities for the first kind of reference solutions. We measure errors in the L_∞ norm, i.e. for vector components in the Fourier transform the errors are taken component wise. In Figure 6.5 the relative errors are depicted for the two linear quantities (FourierTransform in z and -z direction) and the quadratic quantities of interest (the density integration in the four subdomains) as dashed lines. Each plot shows the maximum error over Ξ_1 (red) and the mean error (blue). All output quantities exhibit an identical convergence trend. An initial plateau of the error is followed by a steep decrease of the error before a stagnation sets in at N=15. The maximum errors saturate at $1 \cdot 10^{-3}$ with the mean slightly lower. The errors in the Fourier transform in z direction are slightly higher. We do not observe any difference between the convergence rates of linear or quadratic output quantities up to the plateau. The stagnation is readily explained: The reference solutions used for comparison is not identical to the solution approximated by the reduced basis. The reference solution used for comparison here does not include the empirical interpolation error. Hence we cannot expect convergence of these quantities beyond the accuracy of the solution itself. At the resonances we are close to or at this accuracy limit as shown in the next section.

The reference solutions with the empirical interpolation included are the truth solutions approximated by the reduced basis itself. The error in the output quantities for these references are included in Figure 6.5 as solid lines. We observe a convergence behavior almost identical to the previous case up to $N = 10$. Here, the maximal error (red) decreases even beyond $N = 15$ and finally saturates at $1 \cdot 10^{-4}$. The error mean (blue) is almost an order of magnitude smaller. The saturation can be attributed to the empirical interpolation error introduced in the approximation of the quadratic post process and not to the convergence of the field solution itself as in the previous case. This is demonstrated in Figure 6.6.

Field solution   The output functionals are continuous functions of the field solution. Hence we do not expect a fundamentally different result in studying the approximation error of the field solution. In Figure 6.6 the convergence of the mean and maximum of the error in the H(**curl**,Ω) norm is shown as well as the relation between the reduced basis error estimate and the H(**curl**,Ω)-error. Here the two kinds of reference solutions are depicted separately but with the same axis scalings. The mean and maximum of the error over Ξ_1 have identical trends and fit those of the output quantities in Figure 6.5. The errors initially are constant before dropping 6 orders of magnitude at N=7. The maximum stagnates at a level $1 \cdot 10^{-3}$ at N=17. The mean error decreases only slowly beyond N=10 and to level of $1 \cdot 10^{-5}$. The drop of the error coincides with the inclusion of snapshots in the resonance band into the reduced basis (compare Figure 6.3 and the discussion in the previous section). Once these have been included in the basis, the errors are orders of magnitude smaller.
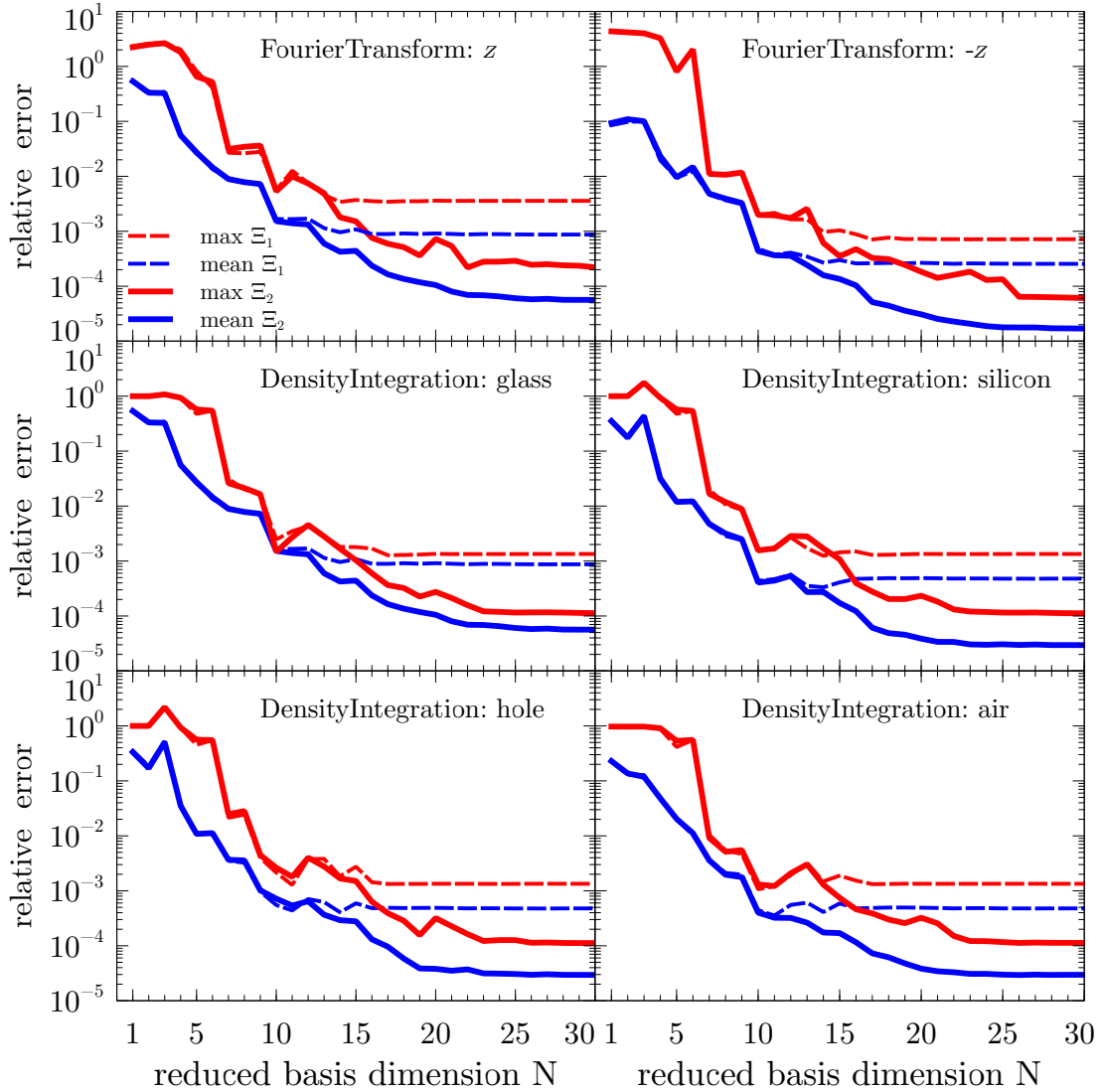
Figure 6.5.: Relative error in the output quantities over the reduced basis dimension measured between the reduced basis approximation and two reference solutions. There is one plot per output quantity which is indicated in the upper right of each axis. The first type of reference solutions fulfill the truth approximation 6 without empirical interpolation. The maximal (red dashed line) and mean (blue dashed line) relative errors to this reference over the set Ξ_1 stagnate beyond $N = 15$. The second type of reference solutions fulfill the truth approximation 8 with empirical interpolation and the maximal (red line) and mean (blue line) relative errors over the set Ξ_2 are smaller and still decrease with increasing N.

truth approximation without empirical interpolation

truth approximation with empirical interpolation
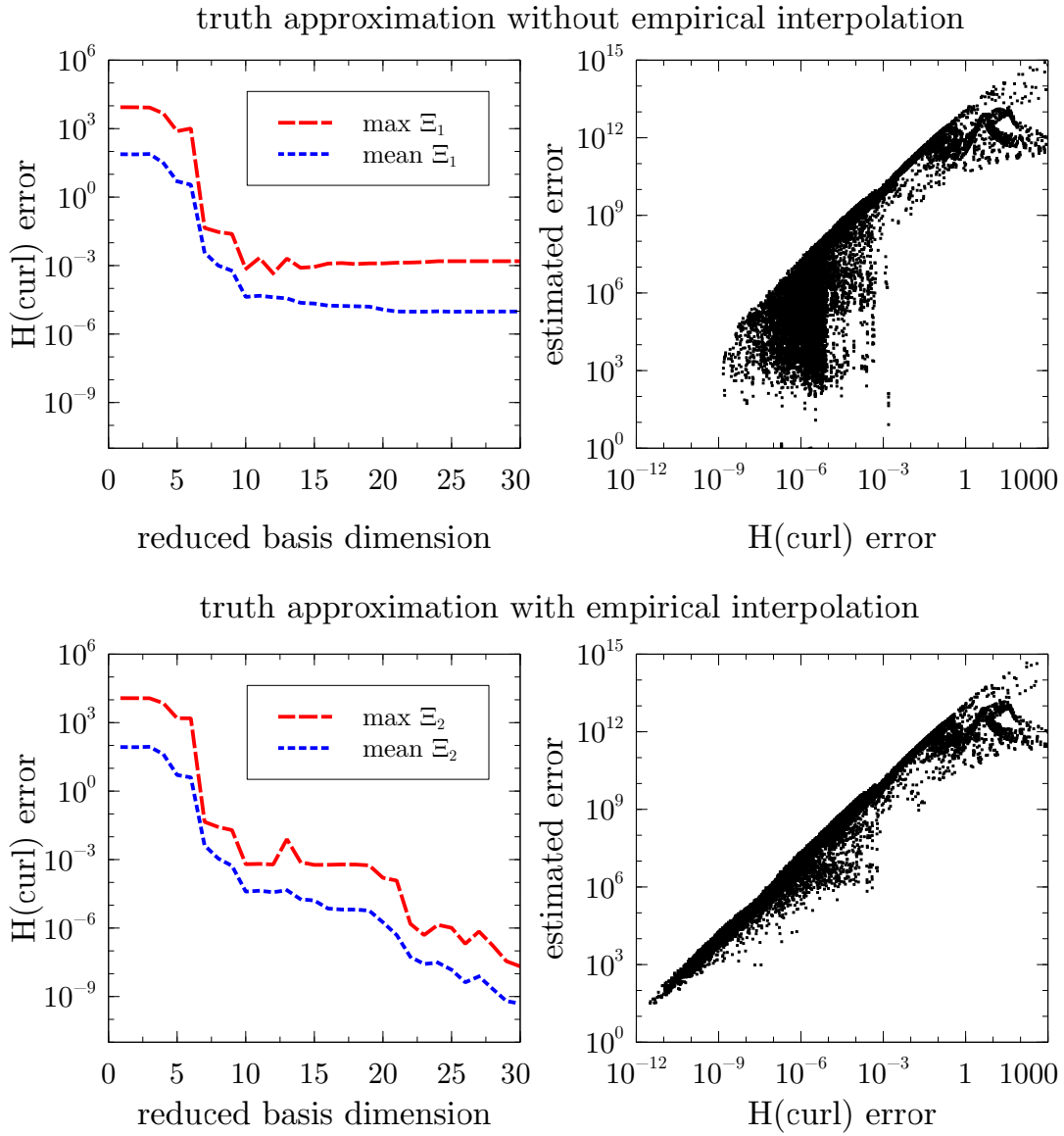
Figure 6.6.: Maximum and mean error of $\Xi_1 \subset \mathfrak{D}^N_{train}$ in H(**curl**,Ω) norm over the reduced basis dimension (left) and estimated reduced basis error over the error in H(**curl**,Ω) norm (right). The error is measured with respect to the reference solutions fulfilling the truth approximation without empirical interpolation 6 (top) and with empirical interpolation 8 (bottom).

Table 6.2.: Statistics of the H($\mathbf{curl}$,Ω) norm of the reference solutions over Ξ_1

mean	min	max	median	standard deviation
89.28	15.24	8840.50	17.37	525.48

The scatter plot relating estimated error and H($\mathbf{curl}$,Ω) error demonstrates the reasonable performance of the error estimate. The correlation coefficient $\rho = 0.86$ indicates a positive correlation. Especially for a low to medium accuracy the estimator works well. At higher accuracy, the efficiency seems to get worse. As mentioned earlier, the error shown here is measured between the reduced basis solution and the reference solution, not the discrete solution approximated by the reduced basis. This additional error is not accounted for by the error estimate shown here. Beyond this, the resonance structure of the field solution also has an effect. Due to the resonance, the H($\mathbf{curl}$,Ω) norm of the reference solutions differs greatly over the parameter domain. The statistics in Table 6.2 show this in detail. In relation to the norm of the solution, the approximations are orders of magnitude better than indicated by maximum of the absolute error shown here and in 6.6.

We conclude our investigation by comparing to the second kind of reference solutions fulfilling the truth approximation with the empirical interpolation of the discrete operators. These solutions are approximated by the reduced basis and hence the error should not stagnate as before. The resulting convergence of the mean and maximum of the error in the H($\mathbf{curl}$,Ω) norm and the scatter plot of reduced basis error estimate and H($\mathbf{curl}$,Ω)-error are depicted in the lower half of Figure 6.6. Compared the previous case shown on top, we observe clear similarities in the convergence of the H($\mathbf{curl}$,Ω) error for low reduced basis dimensions. The previously observed stagnation of the errors beyond N=17 is not found here. Instead, the errors decrease exponentially beyond N=21 up to a level of at most $2.09 \cdot 10^{-8}$ with a mean of $5.14 \cdot 10^{-10}$. Similarly, the correlation between the estimated and observed error is very good with a correlation coefficient $\rho > 0.96$. The errors are correctly approximated by the residual error estimate over the complete range of 15 orders of magnitude.

6.1.5. Error analysis

The approximation errors observed in the previous section are generally reduced with increasing dimension of the reduced basis. In the following we thus investigate the sources of the errors further. We determine the inf-sup constant first to justify its neglect (cf. Sections 5.4.2 and 5.4.3) and then investigate the errors introduced by the empirical interpolation of the system matrix and right-hand side in more detail.
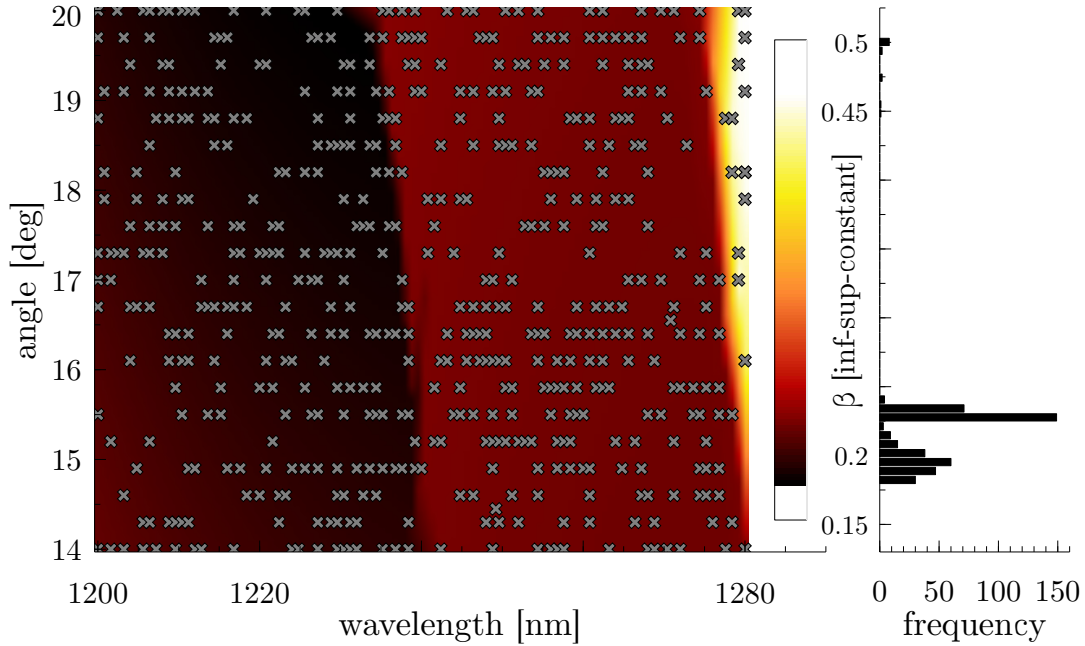
Figure 6.7.: The false color plot of the inf-sup constant β distribution in parameter space $\mathfrak{D}$ for 500 randomly selected values (indicated by crosses) of the finest training set $\mathfrak{D}_{train}^{N}$. The color bar axis coincides with the histogram on the right showing the clustering of β for the 500 data points.

Inf-sup constant estimation The residual error estimator used here does neither account for the empirical interpolation error nor the inf-sup constant β. As demonstrated, neglecting the empirical interpolation error is problematic at high accuracies. Neglecting the estimation of the inf-sup constant prevents the use of the term "certified" in the context of our reduced basis implementation, but comes at greatly reduced computational costs. In this example the inf-sup-constant varies between 0.18 and 0.50. The distribution of β over $\mathfrak{D}$ shown in Figure 6.7 exhibits a banded structure where β is constant within each of the two large stripes. This naturally follows from the frequency selective behavior of the investigated structure. The histogram shows the clustering around 0.19 and 0.23 which corresponds to the two stripes.

Empirical interpolation error The error introduced by the affine expansion of the sesquilinear form $a(\cdot, \cdot; \mu)$ and linear form $f(\cdot; \mu)$ with the Empirical Interpolation Method in Section 5.5.1 is measured and controlled in the L_{∞} norm. In Section 6.1.4 we found the errors in the H($\mathbf{curl}, \Omega$) norm to be much larger than the estimated L_{∞} errors of the EIM approximation listed in Table 6.1. This is why we investigate two errors related to the EIM approximation for a set $\Xi_{eim} \subset \mathfrak{D}$ of 500 parameters.

In the discretized system the matrix $\mathcal{A}$ is approximated by $\mathcal{A}_{eim}$ and the right

(a) Absolute error Δ_1 (logarithmic scale)

(b) Absolute error Δ_2 (logarithmic scale)

(c) Relative error δ_1 (logarithmic scale)

(d) Relative error δ_2 (logarithmic scale)

(e) Histogram of $\log_{10}(\Delta_1)$

(f) Histogram of $\log_{10}(\Delta_2)$
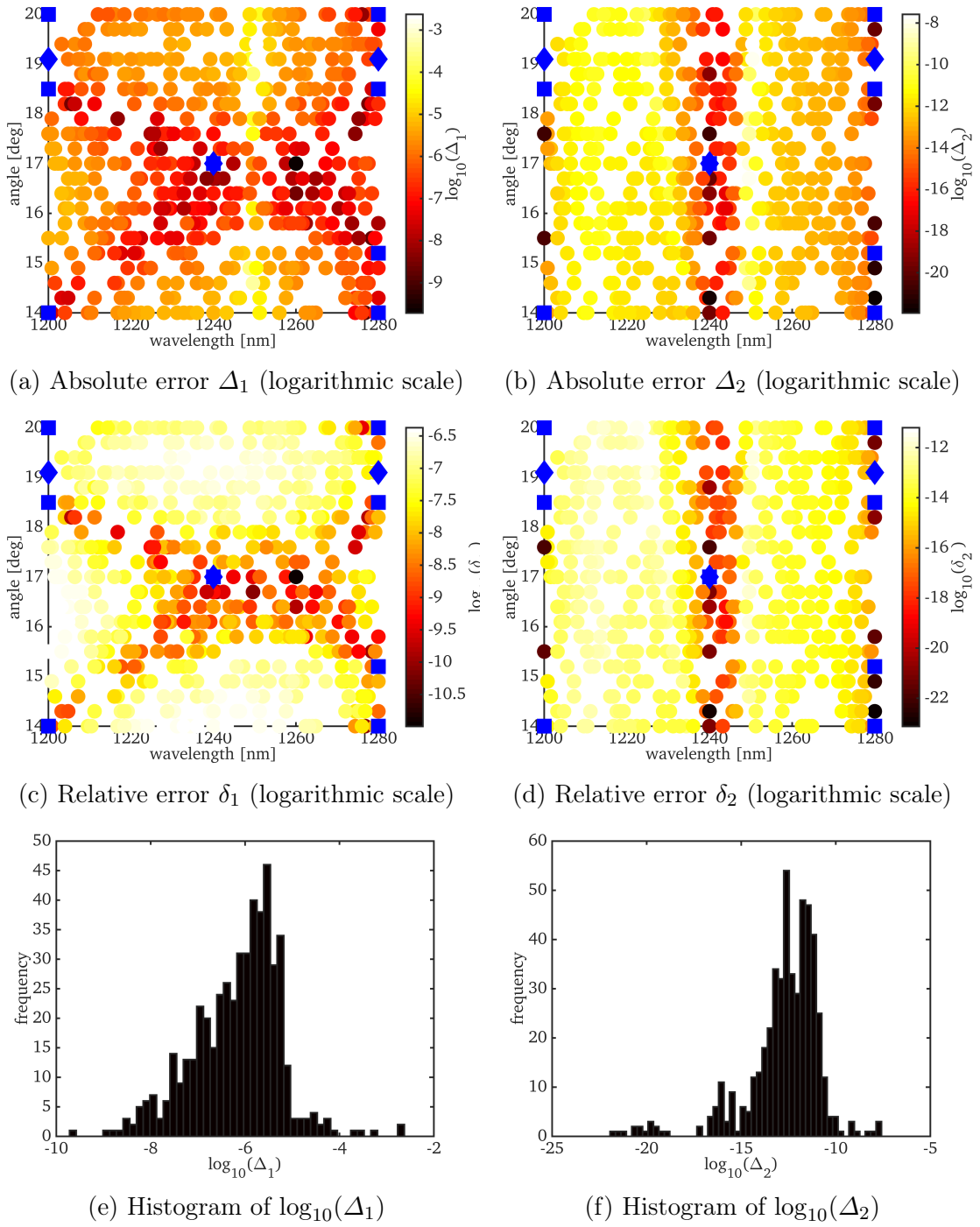
Figure 6.8.: (a)-(d): Scatter plots of the empirical interpolation error $\Delta_{1,2}$ (absolute) and $\delta_{1,2}$ (relative) for the set $\Xi_{eim} \subset \mathfrak{D}$ (see text for definitions). The positions of the EIM snapshots for the matrix (diamonds) and right-hand sides (squares) are marked blue. (e)-(f): Histograms of $\log_{10}(\Delta_1)$ and $\log_{10}(\Delta_2)$.

hand side $\boldsymbol{b}$ by $\boldsymbol{b}_{eim}$. We compare the solutions

$$\boldsymbol{x} = \mathcal{A}^{-1}\boldsymbol{b},$$
$$\boldsymbol{x}_{eim} = \mathcal{A}_{eim}^{-1}\boldsymbol{b}_{eim},$$
$$\tilde{\boldsymbol{x}} = \mathcal{A}^{-1}\boldsymbol{b}_{eim}.$$

This motivates the definition of the following absolute errors

$$\Delta_1 = \|\boldsymbol{x} - \boldsymbol{x}_{eim}\|_{\mathrm{H}(\mathbf{curl},\Omega)},$$
$$\Delta_2 = \|\tilde{\boldsymbol{x}} - \boldsymbol{x}_{eim}\|_{\mathrm{H}(\mathbf{curl},\Omega)}$$

and similarly relative errors

$$\delta_1 = \frac{\Delta_1}{\|\boldsymbol{x}_{eim}\|_{\mathrm{H}(\mathbf{curl},\Omega)}},$$
$$\delta_2 = \frac{\Delta_2}{\|\boldsymbol{x}_{eim}\|_{\mathrm{H}(\mathbf{curl},\Omega)}}.$$

The computed errors over Ξ_{eim} are shown in Figure 6.8 on logarithmic scales as scatter plots together with histograms. Δ_1 (Figure 6.8a) exhibits its maximal values along the resonance band. We find values larger than $1 \cdot 10^{-5}$ for Δ_1 in this region with a maximum of 0.0024. However, the relative error δ_1 at this parameter location is only $2.75 \cdot 10^{-7}$. Similarly, we observe δ_1 (Figure 6.8c) to be at most $4.28 \cdot 10^{-7}$ with a mean of $\approx 1 \cdot 10^{-7}$. The histogram Figure 6.8e confirms values of $\Delta_1 > 1 \cdot 10^{-5}$ to be the exception (23 out of 500 data points). The median of $\log_{10}(\Delta_1)$ -6.02 is close to the mean of -6.16.

The distribution of Δ_2 over Ξ_{eim} in Figure 6.8b differs distinctly from the distribution of Δ_1 (Figure 6.8a). A band along the central wavelength is well resolved for all incidence angles. Similarly, at the boundaries the error is minimal. Overall, we observe Δ_2 to smaller than $2.62 \cdot 10^{-8}$. The relative error distribution in (Figure 6.8d) is almost identical, albeit with error levels four magnitudes smaller. The median and mean of $\log_{10}(\Delta_2)$ in Figure 6.8f are ≈ -12.

In Figures 6.8a-(d) the positions of the EIM snapshots for the matrix and right-hand sides are marked as blue diamonds and squares. Their locations coincide with minima of both Δ_1 and Δ_2. Best observed in the relative errors δ_1 and δ_2 is the structure of the errors. Along the lines connecting the central snapshot and the snapshots on the boundaries in parameter space, the error is lowest. For the errors Δ_2, δ_2 we observe an anisotropy in the error along the wavelengths of the snapshots employed for the matrices. This is of little surprise, as this error measures the deviations in the inverse of $\mathcal{A}$ and $\mathcal{A}_{eim}$ acting on $\boldsymbol{b}_{eim}$, as

$$\Delta_2 = \|\tilde{\boldsymbol{x}} - \boldsymbol{x}_{eim}\|_{\mathrm{H}(\mathbf{curl},\Omega)} = \|\mathcal{A}^{-1}\boldsymbol{b}_{eim} - \mathcal{A}_{eim}^{-1}\boldsymbol{b}_{eim}\|_{\mathrm{H}(\mathbf{curl},\Omega)}$$
$$= \|(\mathcal{A}^{-1} - \mathcal{A}_{eim}^{-1})\boldsymbol{b}_{eim}\|_{\mathrm{H}(\mathbf{curl},\Omega)}. \tag{6.1}$$

As in this study the incidence angle and wavelength have been varied, the parameter dependency of the matrices are not as pronounced as the right-hand side dependency. This can be observed here in the different magnitudes of the errors Δ_1 and Δ_2.

We conclude that the relative errors introduced by the Empirical Interpolation Method approximation of the matrix and right-hand side are satisfyingly controlled. However, in the vicinity of the resonance band these errors might be substantial in absolute terms.

6.1.6. Online evaluation and results

In the online phase the reduced basis allows to evaluate the reduced order models in milliseconds instead of around 4 minutes which is the total time required to compute a single data point in the simulated field enhancement pattern shown in Figure 6.1a using a quad-core workstation. Due to limited computational capacities, the field pattern is computed on a coarse, equidistant cartesian grid with 381×81 points. This restriction is quite severe, as evident from Figure 6.9 where a detailed view of the field enhancement pattern in the parameter domain $\mathfrak{D}$ is shown. The depicted field enhancement is a linear interpolation of 33×7 values. As the resonance width is close to the distance between two grid points, it is unlikely to evaluate it at all or even judging its maximum enhancement. The resonance band is visible in Figure 6.9b but poorly resolved and exhibits a single peak.

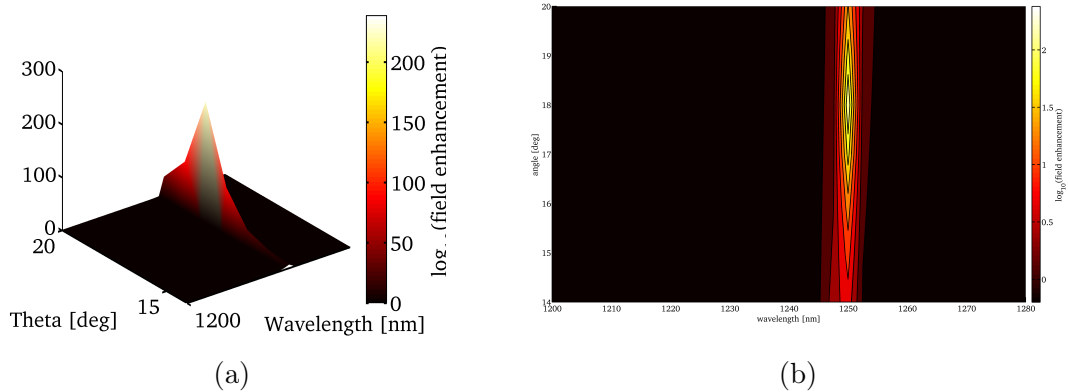(a)   (b)

Figure 6.9.: A detailed view of the reference field enhancements shown in Figure 6.1a for rectangular parameter domain $\mathfrak{D}$ as a surface plot (a) and as a contour plot with logarithmic scaling of the field enhancement (b).

The reduced basis allows to evaluate the field enhancement over $\mathfrak{D}$ much faster and with increased resolution in parameter space. We focus the evaluation to the vicinity of the resonance band between 1248 nm and 1251 nm and use 101×21 sampling points arranged in an equidistant grid. The evaluation of the reduced basis with the full dimension takes 205.62 s for the sampling set of 2021 evaluation points. The majority of the time is spent generating the input for the solver in MATLAB (105 s). Subsequently, each evaluation takes on average 358.4 ms on a single core for the full

field enhancement   contour (log scale)   error (log scale)

(a) N=4

(b) N=5

(c) N=11

(d) N=28
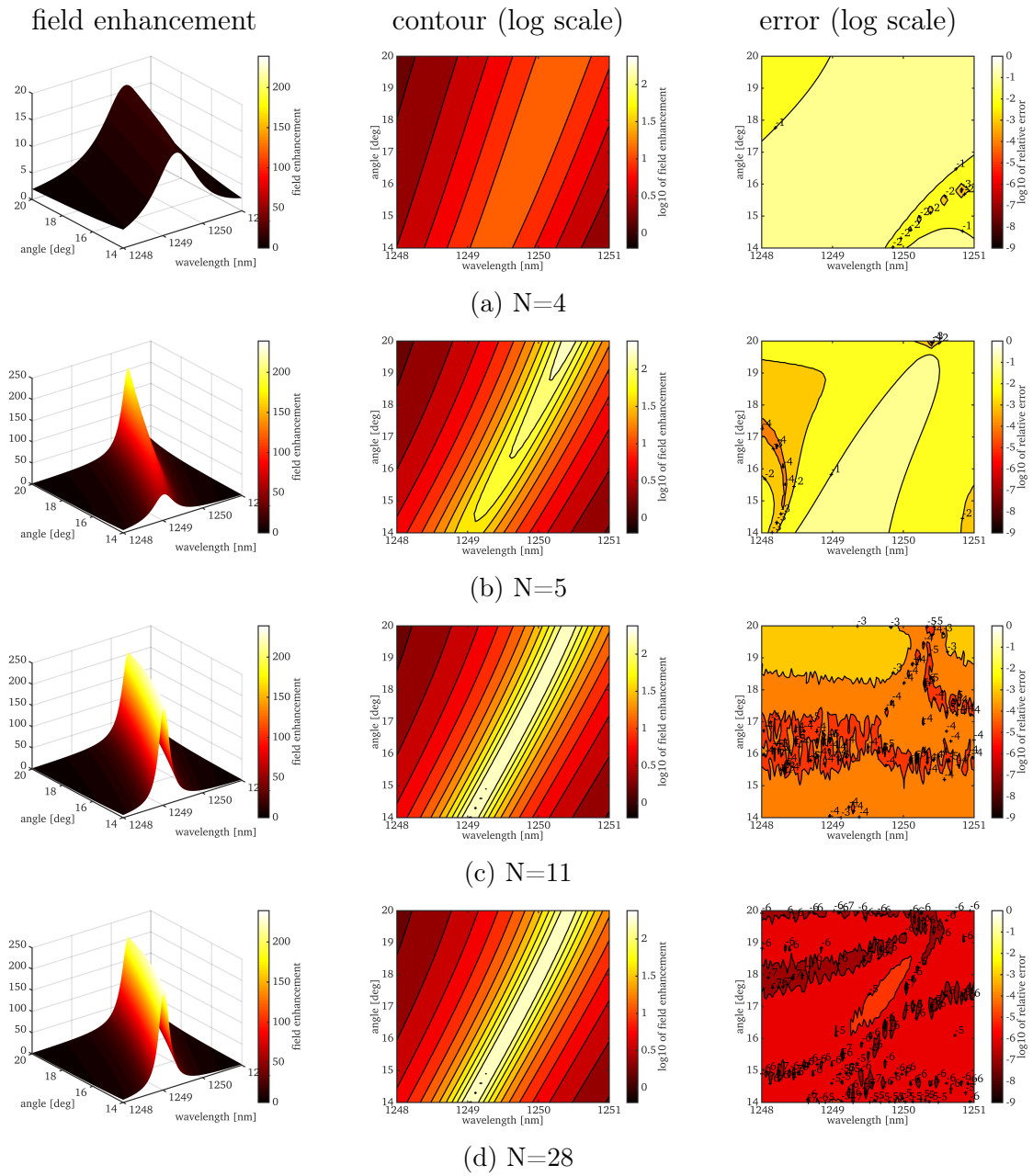
Figure 6.10.: Field enhancements computed by evaluation of the reduced basis in the vicinity of the resonance wavelength as surface plots (left column), contour plots (middle) and the relative deviations from the true solution (right). The rows correspond to using 4 snapshots (a), 5 snapshots (b), 11 snapshots (c) and 28 snapshots (d). Contour plots and error plots are logarithmically scaled.

reduced basis dimension. This includes inversion of the reduced system, the linear and quadratic post processing and writing of three separate output files. The speed up factor compared to the truth approximation is about 2300 for this example.

In Figure 6.10 the results of four evaluations using different numbers of snapshots are shown as surface plots on the left, as contour plots with logarithmic scaling in the middle and the contour of the relative error to the most accurate reconstruction on the right. In the first row (a) the reduced basis is evaluated using 4 snapshots. The field enhancement pattern is poorly recovered as none of the employed snapshot lies on or near the resonance band (cf. discussion of recognition of the resonance in the error estimate in the previous section and Figure 6.3). The error contour indicates large deviations along the resonance band. As the fifth selected snapshot lies on the resonance band, the field enhancement with 5 snapshots in the second row (b) is much better. The error contour still indicates deviations along the band. The resonance is correctly approximated in the third row (c) with 11 snapshots. The deviations are reduced globally by 2 orders of magnitude and the error contour has no longer a structure. The field enhancement and contour plots in the last row is visually identical to the previous row. Here 28 out of the 30 snapshots are used. The deviations are now negligible.

6.2. Incoherence in optical simulations of multi-junction thin-film silicon solar cells

In this example we investigate the domain decomposition algorithm for incoherent coupling presented in Chapter 4. The material of this example is adapted from [Hammerschmidt et al., 2013, Hammerschmidt et al., 2014a] where the presented model geometry is investigated in great detail. We present a convergence study for the finite element discretization first, comment on computational gains through use of hybrid meshes and control of polynomial degrees, and conclude with the incoherent coupling giving rise to a more realistic light-trapping approximation of the model.

6.2.1. Optical model

We us a xy-axis aligned unit cell with lateral dimension of 1 µm × 1 µm to model a thin-film silicon tandem solar cell. The solar cell geometry is described by a stack of layers with different material properties, separated by randomly textured interfaces. The investigated cell is a a-Si/µc-Si tandem solar cell in superstrate configuration, meaning the solar cell is illuminated through its glass substrate of several mm thickness. In this first setup light trapped between the solar cell back reflector and the substrate/air interface is not taken into account. Instead the glass substrate is modeled as a glass half-space in which the light is incident. The vertical device structure of the modeled cell is listed in Table 6.3 in sequence of illumination: A 600 nm thick FTO and a 130 nm thick FTO interlayer are used as a transparent

Table 6.3.: Multi-layer structure in illumination sequence with functional role in the solar cell, material and thickness of the layers.

function	material	thickness
substrate	glass	infinite
transparent front contact	FTO	600 nm
front intermediate layer	FTO	130 nm
p-doped layer 1	boron-doped a-Si	5 nm
p-doped layer 2	boron-doped a-Si	5 nm
top cell intrinsic layer	amorphous silicon	270 nm
n-doped layer	phosphorus-doped a-Si	30 nm
p-doped layer	boron-doped µc-Si	30 nm
bottom intrinsic absorber layer	micro-crystalline silicon	1600 nm
n-doped layer	phosphorus-doped µc-Si	30 nm
transparent back contact	zinc oxide	80 nm
silver back reflector	silver	200 nm
air	air	infinite

conductive oxide. Two p-type a-Si layers of 5 nm thickness each, a 270 nm thick intrinsic a-Si layer and 30 nm of n-type a-Si form the *top cell*. 30 nm of p- and n-type µc-Si enclose the intrinsic µc-Si *bottom cell* of 1600 nm thickness. The back contact is formed by a 80 nm zinc oxide (ZnO) layer with a 200 nm silver back reflector. The back side half-space is assumed to be filled with air. The optical constants for the absorbing materials were provided by PVcomB. The refractive indices of air and glass were set to $n_{air} = 1.0$ and $n_{glass} = 1.52$.

The glass/FTO interface and the FTO/FTO-interlayer interface are assumed to be planar. A random texture with the same RMS roughness and autocorrelation length as FTO separates the FTO-interlayer and the top cell p-layer. The same texture is used to separate all following cell layers corresponding to a material growth in vertical direction. In Figure 6.11a a mesh of the unit cell is shown. Based on previous findings [Lockau, 2012] the lateral dimensions of the unit cell were found to be a compromise between modeling accuracy and computing capacities.

Periodic boundary conditions are applied in x- and y-directions and adaptive perfectly matched layers (cf. Section 3.2.3 or [Zschiedrich, 2009]) are used in $\pm z$ directions as transparent boundary conditions. Plane waves in $+z$ direction are used as incident fields which model solar irradiance reasonably well [Lockau, 2012].

6.2.2. Convergence in volume absorption

The short-circuit current density is the quantity of interest for optimizing the optical properties of thin-film solar cells. It is computed as the (volume) absorption within
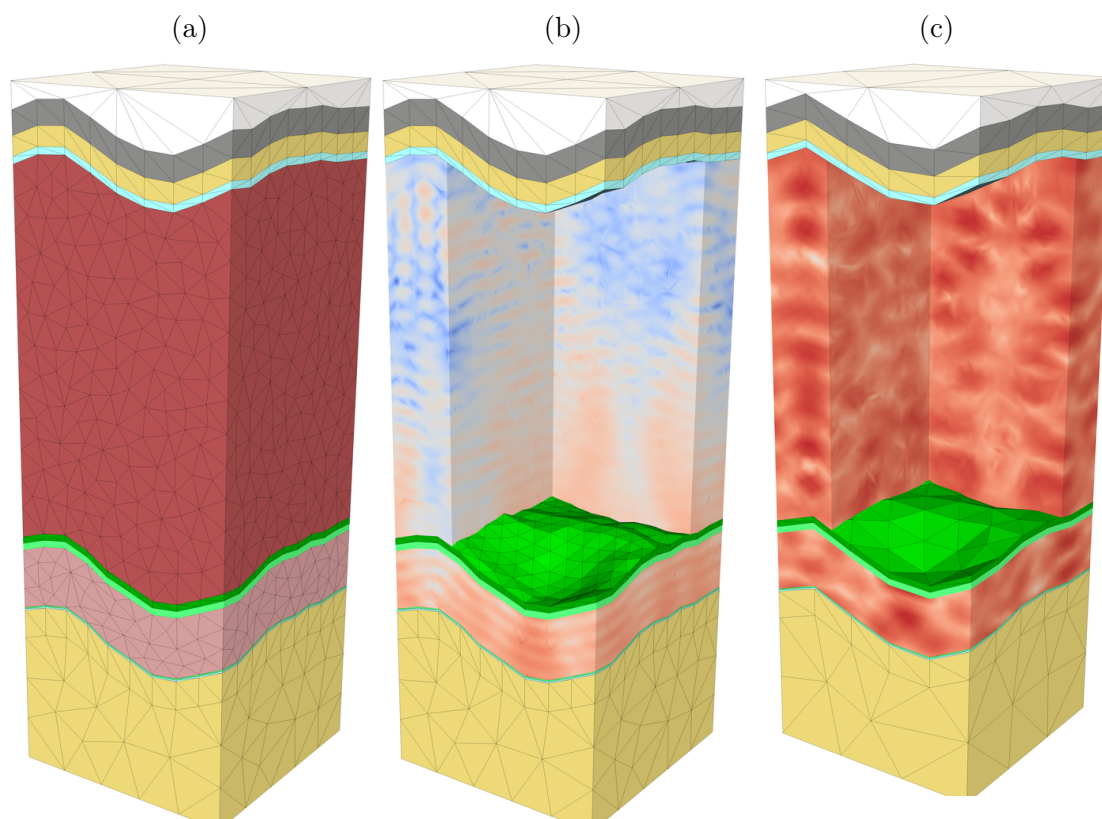
Figure 6.11.: Finite element mesh of an a-Si/µc-Si tandem solar cell illuminated from the bottom (a). Unstructured grids allow a good resolution also of the highly doped thin p-type layers inside the device. Electric field energy density is shown in a false-color plot on a logarithmic scale at 600 nm (b) and 900 nm (c) wavelength.

Table 6.4.: Computation times and number of unknowns for the convergence study shown in Figure 6.12. Computations were executed on a multi-core computer using 20 cores. In this example the cpu time required is roughly proportional to the square of the number of unknowns.

FEM degree	total time [s]	# unknowns	cpu time per unknown [ms]	cpu time per unknown^2 [ns]
1	6	55 034	0.53	9.56
2	81	258 894	2.34	9.03
3	553	736 815	7.90	10.84
4	2617	1 619 232	17.89	11.05
5	7963	3 121 880	28.83	9.23
6	23148	5 341 218	47.58	8.91

the absorber layer weighted by the spectral solar photon flux and is an upper bound for the achievable short-circuit current densities and thus the theoretical efficiency of the solar cell. To estimate the reliability of our computed results, we perform a showcase convergence study at 700 nm wavelength. Figure 6.12 shows the relative error in volume absorption for a uniform p-refinement compared to the most accurate solution computed. Exponential convergence of the relative error in volume absorption can be observed in all cell layers with increasing polynomial order p of the finite element ansatz functions. In particular the bottom cell i-layer (red line) exhibits a perfectly exponential decrease. The other cell layers exhibit a similar trend. A polynomial degree of $p = 4$ is required for the relative errors in all cell layers to less then $1 \cdot 10^{-3}$ (marked by dotted line). An error level of 1%, which is sufficient for most applications, is reached for $p = 3$. The cpu times listed in Table 6.4 for this study exhibit an approximately quadratic increase with the number of unknowns. These times include assembly and solution of the linear system.

6.2.3. Hybrid meshes and hp-adaptivity

Most optimization problems in thin-film PV aim at optimizing the short-circuit current density or increasing the EQE over the solar spectrum. This requires the solution of the forward problem (5.2) for many frequencies in order to estimate EQE curves and compute short-circuit current densities. Hence the computational effort for every solution should be minimized for a given level of accuracy. As a means to reduce computational effort, we investigate four hybrid meshes of the same geometry with different numbers of prismatic and tetrahedral elements and their influence on accuracy and computational effort. Hybrid finite element meshes contain unstructured and structured meshed subdomains, i.e. both triangular prismatic and
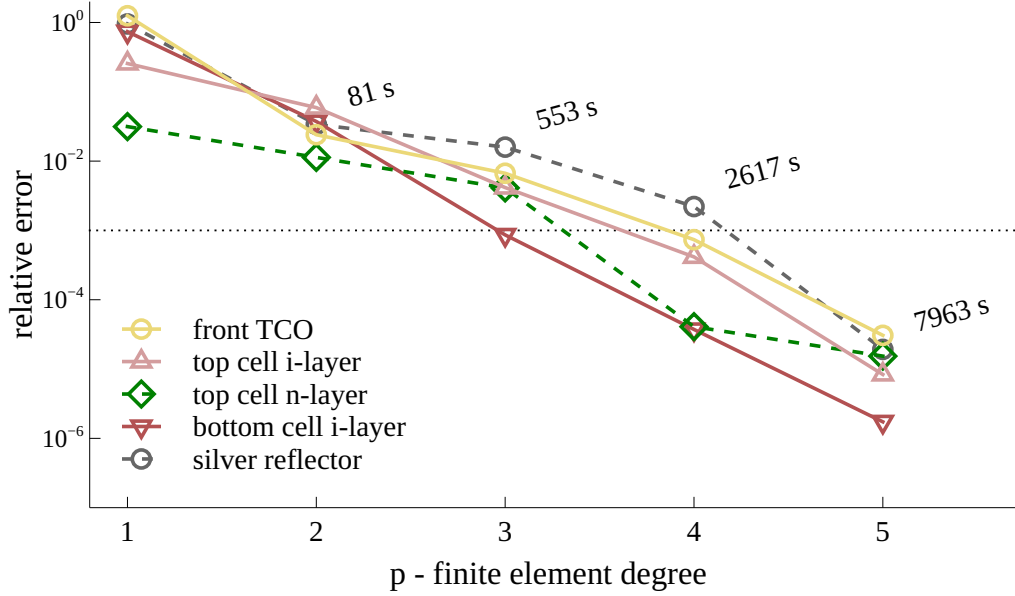
Figure 6.12.: Relative error in volume absorption at 700 nm wavelength compared to a reference solution with polynomial degree 6. In addition the computation time in seconds for each of the simulations is shown.

tetrahedral elements and allow to combine advantages of element types. The meshes shown in Figure 6.11a exhibit adaption to different permittivities and wavelengths as different mesh constraints have been used within the different cell layers. Furthermore, only one or two layers of tetrahedrons are necessary to resolve the thinner doped silicon layers (green) or the back TCO layer (soft yellow). The p-doped a-Si layers of the top cell are not even visible as their layer thicknesses are too small (5 nm) to be resolved at this scale. In Figure 6.13) a magnification of these layers is shown. These layers are oftentimes neglected in optical simulations, but are important for optimization purposes [Deceglie et al., 2012] especially in tandem cells. In the tetrahedral sample mesh A (cf. Figure 6.13) 1404 out of a total 10 756 tetrahedral elements are employed to resolve these thin layers. The assumed conformal layer growth of the solar cell permits the use of a structured mesh with 468 prismatic elements for these layers in mesh B, reducing the total number of elements to 9820 (cf. Table 6.5 and inset in Figure 6.13). For mesh C (also shown in Figure 6.13) the remaining doped silicon and the back contact layers are meshed with prisms as well, further reducing the total number of elements to 7480. Mesh D contains prisms in all layers but the FTO layer, the FTO interlayer and the air super space, using a minimal total number of 6241 elements.

In Figure 6.14(a) the number of unknowns used in the simulations with meshes A-D is shown normalized by the number of unknowns for the tetrahedral mesh A. The reduction in number of geometrical elements does not directly translate to a

Table 6.5.: Number of tetrahedrons, prisms and total number of elements employed in hybrid meshes A-D

mesh	# tetrahedrons	# prisms	# elements
A	10 756	0	10 756
B	9352	468	9820
C	5842	1638	7480
D	1561	4680	6241
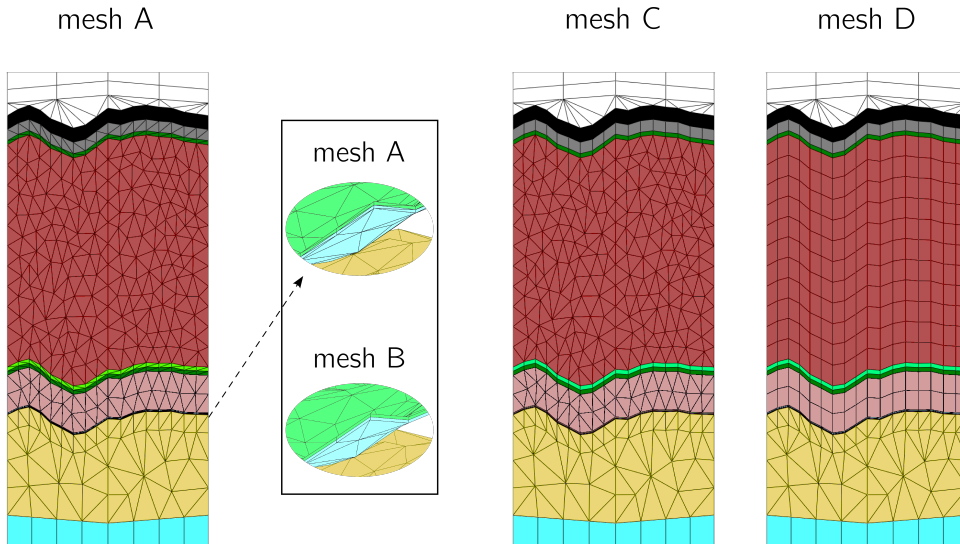
Figure 6.13.: Hybrid finite element meshes with triangular prismatic and tetrahedral elements. Mesh A contains only tetrahedrons. Mesh C is a hybrid grid and with five cell layers discretized by prisms. The absorber layers are meshed with tetrahedral elements. In mesh D all but the first (FTO and FTO interlayer) and last (air super space) cell layers are meshed with prisms. Mesh B is identical to A except for the two barely visible top cell p-layers (cyan and light green). A magnification of these layers in meshes A and B without surrounding layers is visible in the inset.

reduction in degrees of freedom as can be seen in Table 3.1. Hence we observe a different behavior of the fourth mesh D compared to the other three. The lines for meshes B and C lie below the black graph for mesh A indicating a reduction in the number of unknowns whereas the blue graph (mesh D) shows a monotonic increase up to 1.26 for $p = 6$. Thus only the use of prisms for the meshing of thin layers results in a significant reduction in computational costs.

A particular advantage of the used prismatic elements is the possibility to choose different polynomial degrees $p_\parallel$ and $p_\perp$ for the triangular basis and the translation direction. Using this technique three additional computations have been executed on meshes B and C (included as hollow diamond and square markers in Figure 6.14(a)) with a greatly reduced computational effort (up to 35% reduction). For the simulations labeled B1, B2 and C1, C2 the polynomial degree $p = p_\parallel = 4$ was kept constant for the triangular basis and $p_\perp$ reduced to 1 (B1, C1) and 2 (B2, C2) respectively on prismatic elements smaller than half the wavelength. In simulations B3 and C3 $p_\parallel = 3$ and $p_\perp = 2$ was used. The relative error in top and bottom cell volume absorption compared to the reference computed on the tetrahedral mesh A for $p = 4$ are smaller than $1 \cdot 10^{-3}$ for B1-3 and C2, C3. The relative error in the top cell absorption for simulation C1 is one order of magnitude larger. These error levels are the same when compared to the solutions for $p = 4$ on meshes B and C respectively.

Figure 6.14(b) shows the convergence of the volume absorption in top and bottom cell at 700 nm wavelength to the solution computed on mesh A. In general we observe a very similar convergence behavior for the top and bottom cell as all of the dotted lines, marking top cell absorption, closely follow their continuous counterparts, marking bottom cell absorption. The solution computed on mesh B is closest to the reference solution on mesh A and for $p = 3, 4$ the bottom cell absorptions deviate relatively in the order of $1 \cdot 10^{-7}$. The green line for mesh C show a similar trend as the red line for mesh B. The relative error is slightly greater in the order of $1 \cdot 10^{-5}$. As both meshes B and C are very much alike in their structure - both have absorber layer meshed with tetrahedrons - this is the expected and desired behavior. The blue line for mesh D shows a monotonically decreasing relative error down to a level of $1 \cdot 10^{-3}$ which is in the order of the accuracy we find for the solution for $p = 6$ on the relatively coarse mesh A.

The lines in Figure 6.14 indicate that a reduction in numerical effort can be achieved when combining tetrahedral and prismatic elements. Especially for thin cell layers prism meshing is advantageous as the reduction in computational complexity does not come at a great loss in accuracy. Furthermore it allows to lower the computational costs by means of tuning the polynomial degree specifically for very thin prismatic elements.
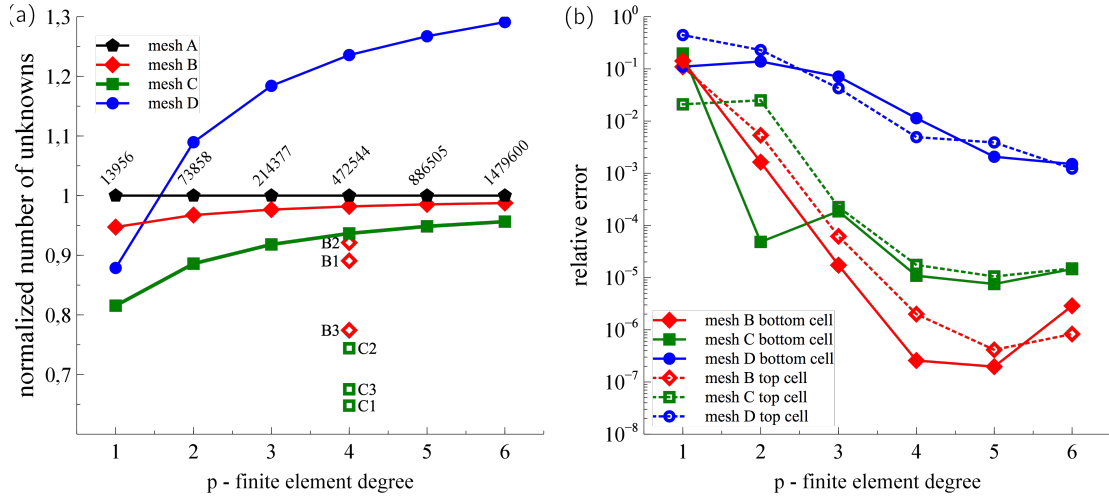
Figure 6.14.: (*a*) The lines show the number of unknowns for the investigated meshes A-D normalized with the number of unknowns for the tetrahedral mesh A which are printed as labels to the black graph. The lines for meshes B and C lie below the black graph for mesh A indicating a reduction in the number of unknowns. The blue graph (mesh D) shows a monotonic increase up to 1.26 for $p = 6$. For meshes B and C additional simulations with adapted polynomial degrees for the prismatic elements have been executed and included into the plot as additional data points B1-3 and C1-3. (*b*) The relative error in volume absorption at 700 nm wavelength for the three different hybrid meshes B-D compared to the solution with the respective polynomial degree for mesh A shows convergence. The lines marking top cell (dashed line) and bottom cell (continuous line) absorption show similar behavior for all of the regarded meshes. The red and green lines (meshes B and C) converge to an error level of $1 \cdot 10^{-5}$ whereas mesh D converges to an error level of $1 \cdot 10^{-3}$.
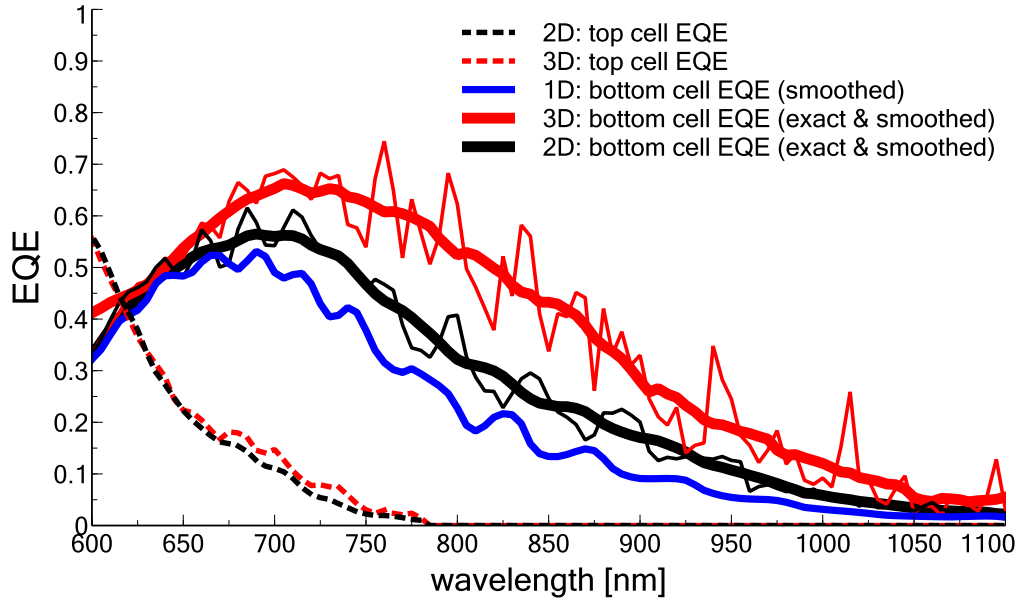
Figure 6.15.: Simulated EQEs of top and bottom cells in three different setups labeled 1D (flat reference), 2D (1D line roughness) and 3D (full 2D roughness) between 600 nm and 1100 nm wavelength. All lines are smoothed using a centered moving average filter. The unsmoothed curves for 2D and 3D simulations are shown as thinner lines of the same color.

6.2.4. Usability of 2D simulations for assessment of light-trapping of random textures

The investigated cells are deposited on FTO substrates with a random texture. Using the texture generation method described in Section 2.2.2, we can generate sets of random textures with any given autocorrelation function. Furthermore, this method is in not restricted to 2D (generating height coordinates over a cartesian plane), but can be employed to generate textures in 1D (resembling line roughnesses or grating like structures). Using the same circular autocorrelation based on the root mean squared roughness of 50 nm at 327 nm autocorrelation length of the FTO topography, we simulated a complete EQE curve with 2D and 3D simulations to assess the usability of 2D simulations to determine the light-trapping efficiency of the random textures.

Figure 6.15 depicts the simulated bottom cell EQE curves (thin lines) between 600 nm and 1100 nm incident wavelength. The moving average (MA) filtered lines (thick lines) offer easier comparison, but interference fringes are slightly shifted in wavelength(observable for example at 880 nm between 1D and 2D simulation).

The blue graph shows the corresponding planar reference stack labeled 1D Simu-

lation without any roughness and therefore no light-trapping. This leads to highly oscillatory bottom cell EQE curves (omitted). The graph shows the filtered bottom cell EQE instead. The black lines mark the results of the 2D simulation with line roughness. These simulations were done in a significantly larger computational domain of 15μm width and averaged over 10 Monte Carlo samples. The full 3D cell simulation results are plotted in red. In addition, the top cell EQE for 3D and 2D simulations are plotted using dotted lines in red and black, respectively.

The two shown top cell EQE curves for 2D and 3D simulations are nearly indistinguishable below 650 nm. At larger wavelengths the 3D simulation shows slightly higher absorption, but the difference is small. This effect is due to the shallow roughness of the simulated textured interface (see Figure 6.13) which leads to poor light-trapping compared to other TCOs such as BZO [Dominé et al., 2008]. In contrast, the three curves for the bottom cell EQE show a clear trend. Absorption within the bottom cell in 3D simulation is higher at every simulated wavelength compared to the corresponding 1D/2D simulations. The simulated bottom cell current density is 32.65% higher in the 3D simulation than the 2D simulation which in turn is 18.5% higher than the flat reference. This is to be expected as the reference has planar material interfaces and therefore no light trapping at all. The 2D simulations exhibit light trapping effects, but to a far lesser extent as with the full 2D roughness in 3D simulations. The 2D simulations underestimate the bottom cell absorption at the band edge by a factor of

$$\frac{\int_{1000 \ nm}^{1100 \ nm} A_{BC,3D}(\lambda) \, \mathrm{d}\lambda}{\int_{1000 \ nm}^{1100 \ nm} A_{BC,2D}(\lambda) \, \mathrm{d}\lambda} \approx 2.$$

This dimension effect in light trapping efficiency is readily explained as the 2D and 3D modeling corresponds to different physics. Following the derivation of theoretical limits (cf. Section 2.2.1) derived in [Yablonovitch, 1982, Yu et al., 2010b] in 2D instead of 3D we find the maximum of the above cited relation to be $\frac{4}{\pi} n \approx 4.46$. The difference to the theoretical limit can be attributed to parasitic absorption, the omitted superstrate light-trapping effects and the imperfect overall light-trapping efficiency of the simulated structure due to the shallow roughness.

In general the dimension reduction from 3D to 2D does not yield the same light-scattering results even if the surface morphology has identical statistics. The autocorrelation function considered here only accounts for the height distribution of the surface morphology but the distribution of surface angles is not controlled. In the 2D simulation light cannot be scattered out of the simulation plane in contrast a 3D simulation. The light scattering properties of a surface morphology that is invariant in one spatial direction (i.e. a grating) is thus fundamentally limited.

6.2.5. Absorptance in cell layers

The simulation yields not only EQE curves for top and bottom cell absorber layers, but absorptance numbers for all cell layers included. In Figure 6.16 these are
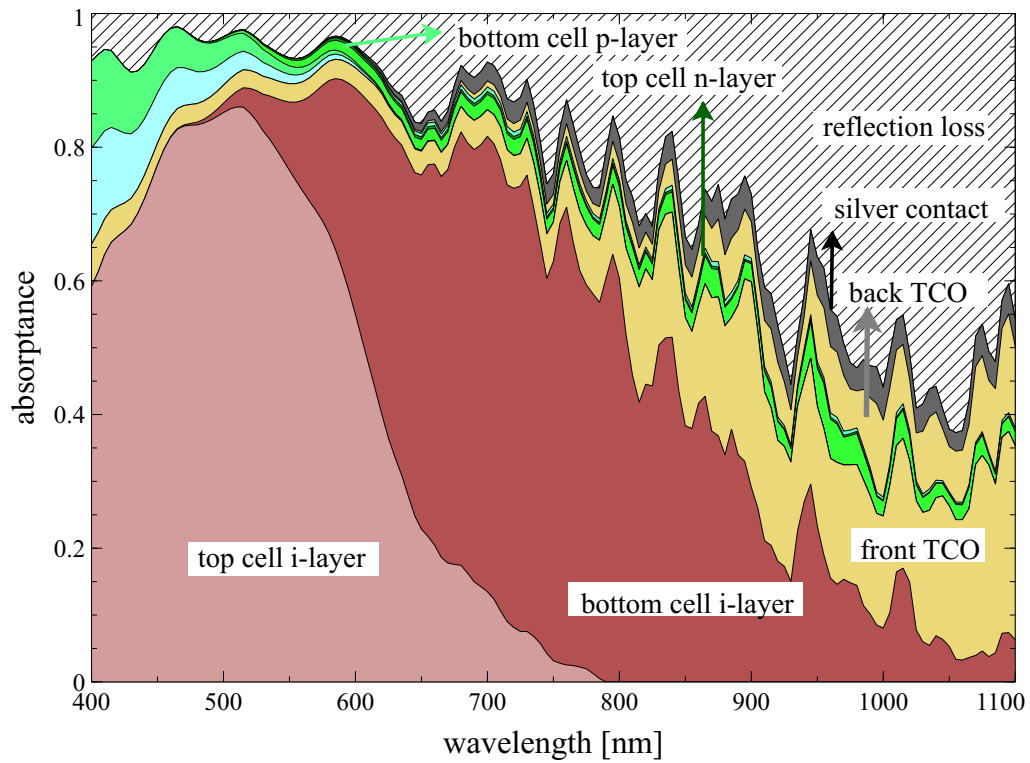
Figure 6.16.: Stacked area plot of absorptance in cell layers. The absorptance of the top and bottom cell layer is shown at the bottom of the plot. The absorptance of the remaining cell layers is ordered in deposition sequence from bottom to top. The reflectance is shown as a hatched area. There is no transmittance.

visualized in an area plot. The absorptance in the intrinsic silicon layers is shown on the bottom, followed by the TCO layer, the doped layers and finally the back reflector layers. The hatched area corresponds to the reflected energy flux obtained from the Fourier transform of the electric field in the exterior domain. This plot is well suited to visualize parasitic and reflection losses. Several observations can be made: The interference fringes in total absorptance (or 1-reflectance) are clearly visible. Below 500 nm parasitic losses in the 5 nm thin p-doped silicon layers reduce top cell absorptance. The top cell absorptance is maximal at 520 nm and drops off drastically beyond 600 nm. The combined absorptance of top and bottom cell reaches its maximum at 610 nm and gradually drops down. The front TCO absorptance becomes significant in the infrared part of the spectrum and the reflection losses are clearly the dominant effect beyond 900 nm. For the simulated cell we find top and bottom cell current densities of 11.25 mA cm^{-2}and 12.52 mA cm^{-2}. Having access to all information allows to quantify losses in terms of lost short circuit current density in this wavelength interval. The major loss mechanisms are reflection losses of 9.07 mA cm^{-2}and parasitic absorption loss in the FTO of 4.23 mA cm^{-2}, the silver back reflector (.97 mA cm^{-2}) and the back TCO layer (1.28 mA cm^{-2}). The combined absorptance of the p-layers accounts for 0.96 mA cm^{-2}.

6.2.6. Incoherent light trapping in a textured thin-film silicon tandem solar cell

Simulations in the previous sections did not take the contribution of light trapped by total internal reflection between the solar cell back reflector and the substrate/air interface on the illumination side into account. The glass substrate was instead modeled as a glass half-space and the calculated quantities were corrected with the Fresnel coefficient of the air/substrate interface. The *Fresnel-corrected* results are hence obtained by scaling the computed quantities with a factor of $c = (1 - R_{air/glass})^{-1} = (1 - (\frac{1-1.52}{1+1.52})^2)^{-1} = 1.0445$. The inclusion of incoherence into rigorous simulations was discussed in detail in Chapter 4 with the special focus on incoherent coupling of subdomains. Before investigating this algorithm in the context of the previously investigated model cell, we mention the relation of the previously applied MA filter to other incoherence modeling approaches. The graph in Figure 6.17 depicts the generation rate of both subcells combined between 600 and 1100 nm (black line). In addition 5 graphs of the same data are shown, each labeled with the according coherence time (5 fs - 200 fs). These are generated from the coherent data with a parameter dependent, Gaussian MA filter identical to the convolution with the incoherence function (4.2) presented for the illumination model presented in [Sarrazin et al., 2013]. The chosen coherence times were taken from this reference. Coherence times smaller than 90 fs distort the profile visibly. The spectral averaging with the 200 fs filter is roughly equivalent to a Gaussian filter with a few nm bandwidth and agrees in its shape approximately with the profiles in Figures 6.15 and 6.18 (iv) and (vi) which were generated by the applying a simple MA filter.
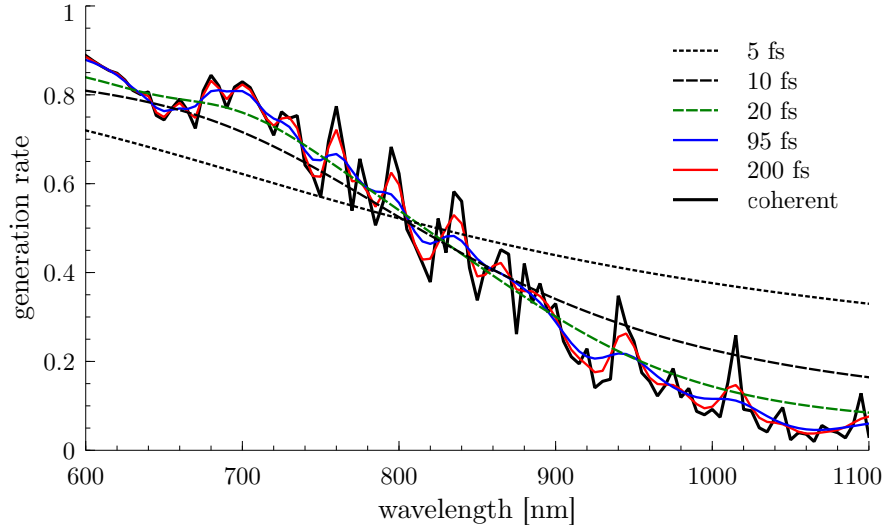
Figure 6.17.: The combined absorptance of both top and bottom cell (black line) is plotted together with MA filtered versions of the same profile according to different coherence times (5 fs - 200 fs).

In Figure 6.18 the absorptance of all tandem cell layers is shown in the form of area plots, together with the reflectance (shaded area). In subplot (i), the results of Fresnel corrected coherent simulations are shown, not taking the light trapping in the encapsulating glass layer into account. The sampling rate was 5 nm and the relative error in volume absorption was kept below 1%. The inclusion of all doped layers in combination with a low scattering efficiency of the relatively smooth texture lead to many narrow width interference fringes in the total absorptance (1-R). The same data is shown in (ii) with a simple MA filter (over 5 data points or 20 nm) applied. The simulation presented in (iii) includes the substrate in a coherent simulation leading to much more pronounced, narrow width interference fringes. For this simulation the wavelength sampling grid, the same as in (i), is too coarse to resolve the fringes accurately. This simulation is again presented in (iv) with the MA filter applied. The same simulation with the incoherent superstrate light trapping, shown in (v) and filtered in (vi), has broader and less pronounced fringes. The inclusion of the superstrate yields a reduced reflectance best observed in both (iv) and (vi). The bottom cell absorption is improved as well. When comparing subplots (iv) and (vi), we observe that the local maxima appearing in total absorptance at 1040 nm and 1080 nm are broader and slightly shifted in the incoherent case.

A natural figure of merit to compare these different spectra is the implied photo current density over the wavelength range. Table 6.6 lists the current densities for selected layers. As expected, the top cell current is not affected by light trapping - coherent or incoherent. The reflection on the other hand is significantly reduced. The bottom cell current increases slightly by 3.9% due to the incoherent light trapping to 12.09 mA cm^{-2}. The coherent light-trapping leads to marginally higher currents
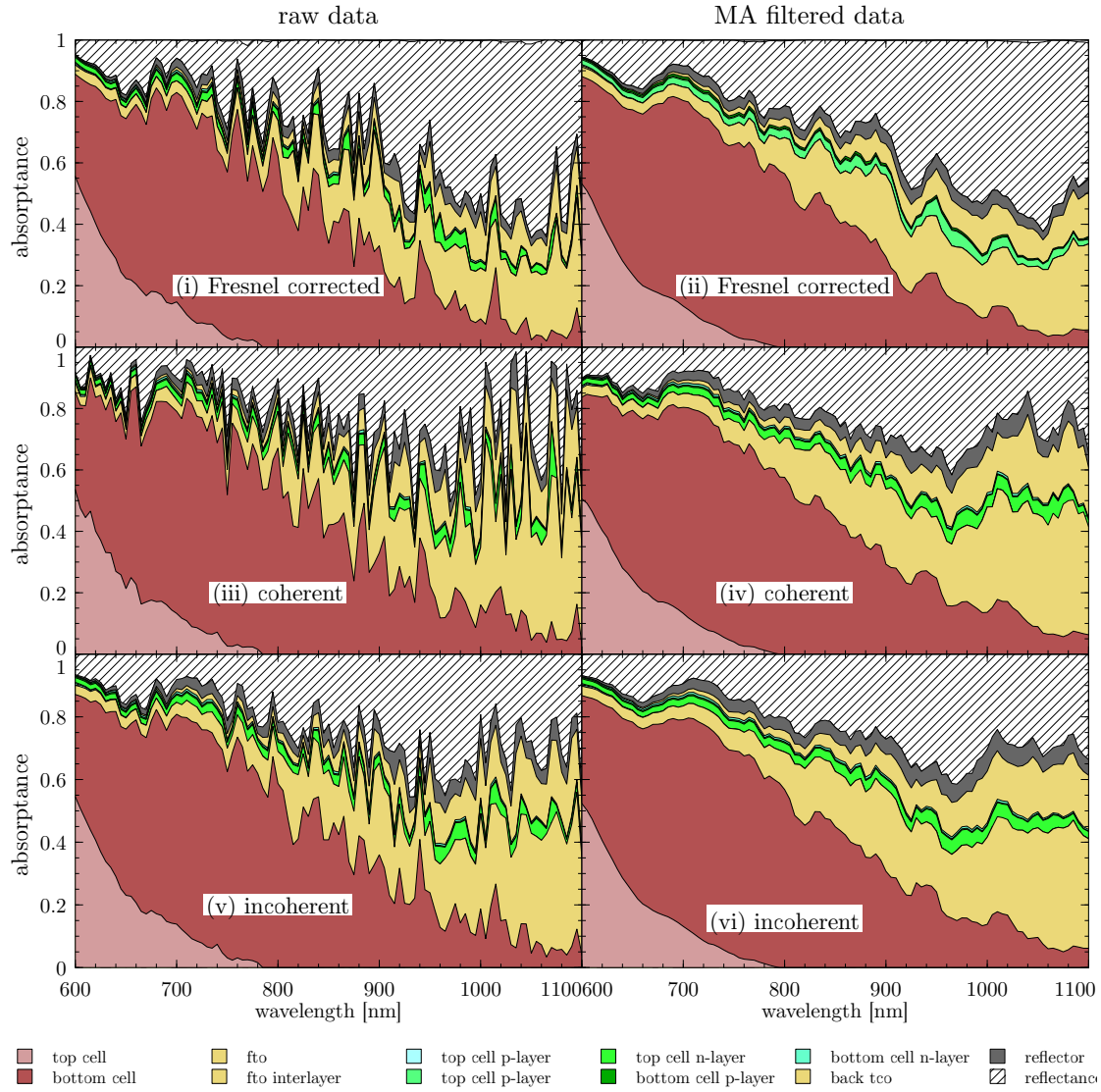
Figure 6.18.: Absorptance plots for the tandem cell in Figure 6.11. *Left column:* In (i) the coherent simulation is shown without light trapping in the encapsulating glass layer and a Fresnel correction. The simulation data in (iii) includes the substrate in a coherent simulation leading to much more pronounced narrow width interference fringes. The simulation with the incoherent light trapping in the encapsulating glass layer shown in (v) has broader and less pronounced fringes. *Right column:* The same data as in the left column is plotted with a moving average filter applied. The inclusion of the glass layer yields a reduced reflectance in both (iv) and (vi) compared to (ii). The bottom cell absorption is improved as well. In contrast to (iv) the local maxima in the total absorptance at 1040 nm and 1080 nm in (vi) are broader and slightly shifted.

Table 6.6.: Implied photo current densities for selected cell layers. The reflection is significantly reduced when light-trapping is included leading to higher absorption in the bottom cell and FTO layers. The coherent light-trapping leads to marginally higher currents compared to the incoherent light-trapping.

layer	Fresnel correction [mA cm⁻²]	incoherent [mA cm⁻²]	coherent [mA cm⁻²]
top cell	2.32	2.32	2.31
bottom cell	11.64	12.09	12.14
FTO	3.87	4.77	4.95
back TCO	1.33	1.78	1.83
silver reflector	0.96	1.19	1.22
reflection	8.38	6.07	5.89

compared to the incoherent light-trapping. This might be an artifact depending on individual resonances which depend on the chosen wavelength sampling and thickness of the glass substrate. In the incoherent coupling the thickness of the glass layer no longer has an influence. In general the sampling rate is insufficient to resolve all interference fringes. The sampling rate of 5 nm is a compromise to keep the computational costs reasonable yet resolve the absorptance spectra adequately of the whole spectrum. An adaptive sampling scheme as presented in [Hammerschmidt et al., 2014b] does not work considerably better in case of highly oscillatory spectra. A reduced basis (cf. Chapter 5 and Sections 6.1 and 6.3) for the wavelength can be employed to improve the sampling.

6.3. Intermediate reflector layer optimization with a reduced basis

The following numerical example demonstrates the efficacy of the Reduced Basis Method for Maxwell's equation for the optimization of the optical properties of a large nanostructured thin-film silicon solar cell. This section is structured as follows. We present a short motivational review of previous work, before presenting the optical model the reduced basis is built on. A detailed discussion and analysis of the approximation errors are presented next. The simulation results of the reduced model conclude this section.

6.3.1. Review and motivation

The limiting factor to multi-junction silicon solar cells is the light fraction absorbed by the top cell which should absorb as much of the higher energy part of the solar spectrum as possible. The bottom cell with the lower bandgap absorbs the high-energy photons transmitted through the top cell which in turn are lost for the top cell current thus limiting the maximal achievable top cell current. Due to serial connection of the subcells the minimum current of the subcells limits the overall current to be extracted from the tandem device. In a tandem cell configuration this is the a-Si top cell which is limited in its thickness and hence absorption efficiency. A trade-off between good electronic properties and high cell currents has to be found. In practice, the thickness is thus limited to 200-300 nm [Kirner et al., 2014] which is insufficient to overcome tandem cell efficiencies of ~12%. Strategies to improve top cell currents while restricting layer thickness comprise optimizing the TCOs texturing which provides light trapping by scattering light away from the incidence angle thus increasing the light path within the absorber. The ideal topography of the scattering structure depends on the TCOs and absorber materials involved and takes material growth and possibly decreased material quality into account. Another promising strategy is to introduce an intermediate reflector layer (IRL) made of silicon oxide between top and bottom cell [Dominé et al., 2008]. This leads to an improved performance of the top cell as light is reflected back from the IRL which has a lower refractive index. This gain in top cell absorption depends on the light trapping properties of the rough TCO used as a front contact as well as the thickness of the IRL. As both the feature size of the texture and the IRL thickness d_{irl} are in the order of the wavelengths of interest optical simulations resolving wave phenomena are required. Figure 6.19 depicts the electric field energy density distribution at 625 nm wavelength for d_{irl}=5 nm, 62.5 nm and 120 nm. We observe the effect of the intermediate reflector layer in the more pronounced interference patterns in the top cell for larger d_{irl}.

In a planar system, a variation of the IRL thickness d_{irl} introduces an interference in the reflectance. The reflectance exhibits maxima which are $\lambda/2$ apart. The computation of an optimal d_{irl} as the first maximum is trivial as the following maxima are smaller in amplitude due to absorption. A change in incidence angle effects the resonance condition which depends only on the normal component of the incident wave vector. As it gets smaller, the optimal thickness increases. A textured TCO leads to much improved light scattering, but as the solar cell is no longer a planar material stack, 1D models no longer provide sufficiently accurate descriptions of the interaction between scattering by the TCO topography and the IRL [Dominé et al., 2006, Rockstuhl and Lederer, 2009].

In [Kirner et al., 2014] we systematically investigated the interaction of three different TCOs (FTO, BZO and AZO) commonly used in TFSSC and the ideal IRL thickness experimentally and numerically. This required enormous computational effort and the optimizations were limited to a few wavelengths and a rough sampling of the IRL thickness. Using synthetic topographies generated by the method

Table 6.7.: Multi-layer structure in illumination sequence with functional role in the solar cell, material and thickness of the layers. This is a simplification of Table 6.3 where the doped layers are omitted for the purpose of optical optimization of the IRL.

function	material	thickness
substrate	glass	infinite
transparent front contact	zinc oxide	600 nm
top cell absorber layer	amorphous silicon	290 nm
intermediate reflector layer	silicon oxide	5 nm-120 nm
bottom cell absorber layer	micro-crystalline silicon	1800 nm
transparent back contact	zinc oxide	80 nm
silver back reflector	silver	100 nm
air	air	infinite

described in Section 2.5 instead of AFM data we could analyze the most commonly used parameters in characterizing TCOs and their scattering efficiencies - roughness and autocorrelation length - independently. We could obtain good qualitative agreements between simulations and experiments in determining optimal d_{irl} for the three investigated TCOs. Furthermore we concluded that roughness alone is not a solid figure of merit in predicting IRL performance and the lateral feature size is probably as influential. This conclusion is based on simulation results of synthetic surface morphologies indicating that the highest gain in top cell EQE for a given roughness is found at lower autocorrelation lengths. The highest gain (both experimentally and numerically) obtained for a BZO substrate could thus be improved by further reducing the ACL. However, experimentally this will probably lead to problems in depositing these layers and reduce material quality.

6.3.2. Optical model

A reduced basis for these parameters can significantly improve on simulation times and provide additional confidence in the results by controlling sampling errors within the investigated parameter domain. We use a model adapted from [Kirner et al., 2014] which is a simplification of the model presented in the previous section for the purpose of optical optimization of the IRL. Here, the doped layers are omitted to reduce complexity. We use the cell materials and thicknesses listed in Table 6.7. The sequence of materials in illumination direction is TCO, a-Si, IRL, μc-Si, AZO, Ag. The cell was modeled in a superstrate configuration with glass and air half-spaces in $\pm z$ directions, respectively. The cell is modeled using periodic boundary conditions at a pitch of 1.7 μm×1.7 μm. The texture employed is generated using a RMS roughness of 144 nm and autocorrelation length of 327 nm. These values correspond to the statistics found for a BZO texture. The tetrahedral finite element
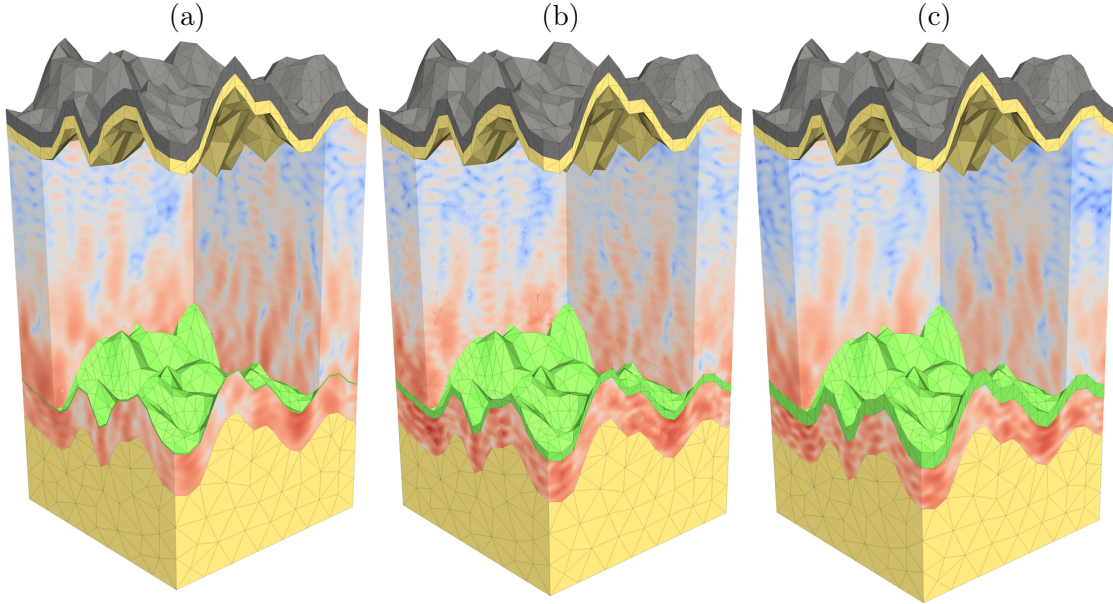
Figure 6.19.: Finite element meshes of the modeled a-Si/µc-Si tandem solar cell illuminated from the bottom. The substrate roughness resembles a BZO substrate. The electric field energy density at 625 nm illumination wavelength is shown in a false-color plot on the same logarithmic scale for different thicknesses of the intermediate reflector layer: 5 nm (a), 62.5 nm (b) and 120 nm (c). The fields show clear similarities. In contrast to (a), stronger interference patterns and higher intensities are visible in the top cell in (b) and (c).

mesh is parameterized and allows to vary the thickness d_{irl} of the IRL. In Figure 6.19 the mesh is shown for d_{irl}=5 nm, 62.5 nm and 120 nm with the corresponding electric field energy density distribution at 625 nm wavelength. These are the minimum, center and maximum of the d_{irl} interval investigated in the following.

The p-polarized illumination from the lower half-space is varied in wavelength λ. The parameterization of the illumination is

$$\boldsymbol{E}_{in}(\lambda) = \begin{pmatrix} 1 \\ 0 \\ 0 \end{pmatrix} \quad , \quad \boldsymbol{k}_{in}(\lambda) = \begin{pmatrix} 0 \\ 0 \\ 1 \end{pmatrix} \frac{2\pi n_{glass}}{\lambda}.$$

The refractive indices of all materials but glass and air ($n_{air} = 1, n_{glass} = 1.53$) are dispersive and provided by our collaboration partners from PVcomB and HZB. The FEM discretization with third- and fifth-order elements and adaptive, accurate PML-settings yield a system with $\mathcal{N} = 2\,327\,777$ unknowns.

Table 6.8.: EIM summary - number of terms Q employed in expansion and error estimate δ of approximation for different functionals. The quantities are defined in Section 5.5.1

EIM	system matrix	right hand side	post process
Q	15	1	11
δ	$1.566 \cdot 10^{-7}$	$5.530 \cdot 10^{-16}$	$1.716 \cdot 10^{-7}$

6.3.3. Reduced basis assembly

We build a reduced basis for the wavelength λ of the incident light and the thickness of the intermediate reflector layer d_{irl} in the parameter domain $\mathfrak{D} = [600 \text{ nm}, 650 \text{ nm}] \times [5 \text{ nm}, 120 \text{ nm}]$ with $\lambda \in [600 \text{ nm}, 650 \text{ nm}]$ and $d_{irl} \in [5 \text{ nm}, 120 \text{ nm}]$ with the self-adaptive assembly with the Greedy algorithm described in Section 5.6 and 5.6.1. As the computation requirements are significant for this model problem (ca. 21.7 hours of CPU time or ~ 90 min on a 16 core machine and >100 GB of memory for a single snapshot), the number of snapshots is restricted to 80. The reduced model is built for three output quantities simultaneously:

- the Fourier transform in -z direction to compute the reflection of the solar cell,

- the Fourier transform in z direction to compute the transmission of the solar cell,

- the electric field energy density integration to compute absorption in the sub-domains of the solar cell.

21 Fourier modes are propagating in z direction and 45 in -z direction. The quadratic output quantity "electric field energy" is computed for the seven subdomains. We will commonly refer to these quantities by the corresponding post process names in JCMsuite: *FourierTransform* and *DensityIntegration*.

The training set $\mathfrak{D}_{train}$ used for the Greedy searches initially comprises 20×116 sampling points in an equidistant grid along λ and d_{irl} axis. This corresponds to a 5 nm sampling of the wavelength interval and a 1 nm sampling of the d_{irl} interval and should be sufficiently dense to resolve the optical phenomena.

The EIM approximation is carried out using a tolerance level of $2 \cdot 10^{-7}$ as a threshold. The statistics of the approximation are listed in Table 6.8. The empirical interpolation of the system matrix requires $Q_A = 15$ snapshots with an estimated approximation error of $\delta_{EIM}^A = 1.566 \cdot 10^{-7}$ over the training set $\mathfrak{D}_{train}$. The quadratic post process requires the approximation of the permittivity tensors in the different subdomains. Using the same training set $\mathfrak{D}_{train}$ and error threshold this requires $Q_{PP} = 11$ with an estimated error of $\delta_{EIM}^{PP} = 1.716 \cdot 10^{-7}$. Due to the constant incidence angle and polarization, the right-hand side does not depend on
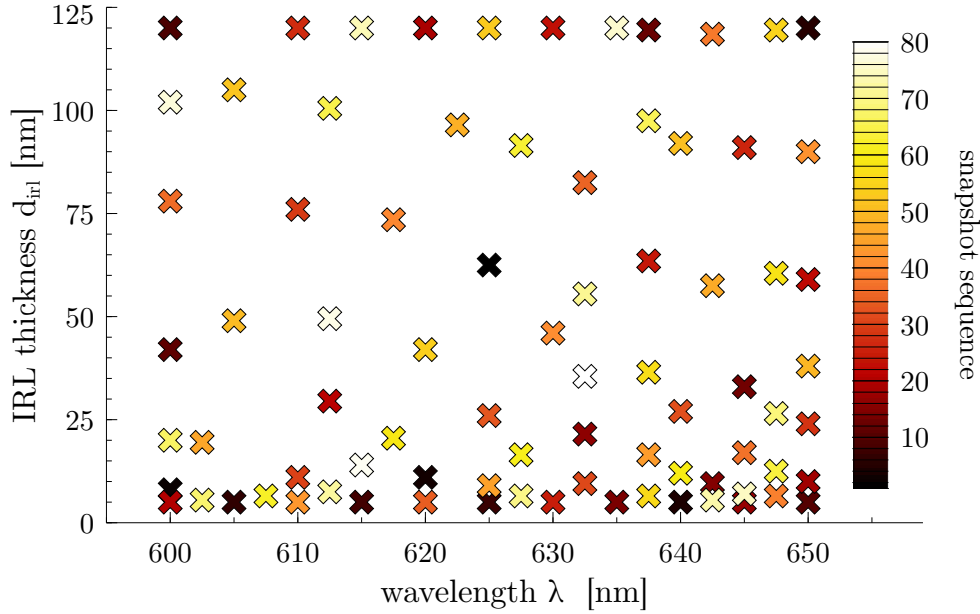
Figure 6.20.: Snapshot positions in parameter space are marked as crosses. The color of the marker indicates sequence of snapshot selection from darker to lighter colors. The first snapshot chosen is the center of the parameter domain. The distribution of snapshots follows the boundaries of the parameter domain. A clustering along the wavelength axis can be observed.

the parameters. Hence a single snapshot is sufficient to approximate all right-hand sides.

In the offline phase 80 snapshots are computed to form the reduced basis for the parameter space $\mathfrak{D}$. The Greedy search employs the same initial training set $\mathfrak{D}_{train}$ of cardinality 2320 as the EIM approximation. In Figure 6.20 the locations of the selected snapshots are depicted as crosses. The color coding indicates the sequence in which they were chosen from darker to lighter colors. The first snapshot is positioned in the center of the parameter domain. All subsequent snapshots are chosen by the Greedy algorithm. The chosen snapshots follow the boundaries of $\mathfrak{D}$ and cluster for small values of d_{irl} but are almost uniformly distributed along the λ-axis. Out of the first 10 snapshot locations chosen by the Greedy strategy, 7 have a d_{irl} coordinate less then 11. Two more are located in the extreme positions in the corners at d_{irl}=60 nm.

The Greedy algorithm 3 (cf. Section 5.6.1) determines the selection of snapshots according to the reduced basis error estimate (cf. Section 5.4.2) over the training set $\mathfrak{D}_{train}$. The selection of the worst resolved parameter location in every iteration leads to a decrease of the error estimated. We observe a monotonic decrease in the estimated error depicted in Figure 6.21. Here the normalized residual error estimate (black line) is shown in a semi-logarithmic plot, indicating the expected exponential
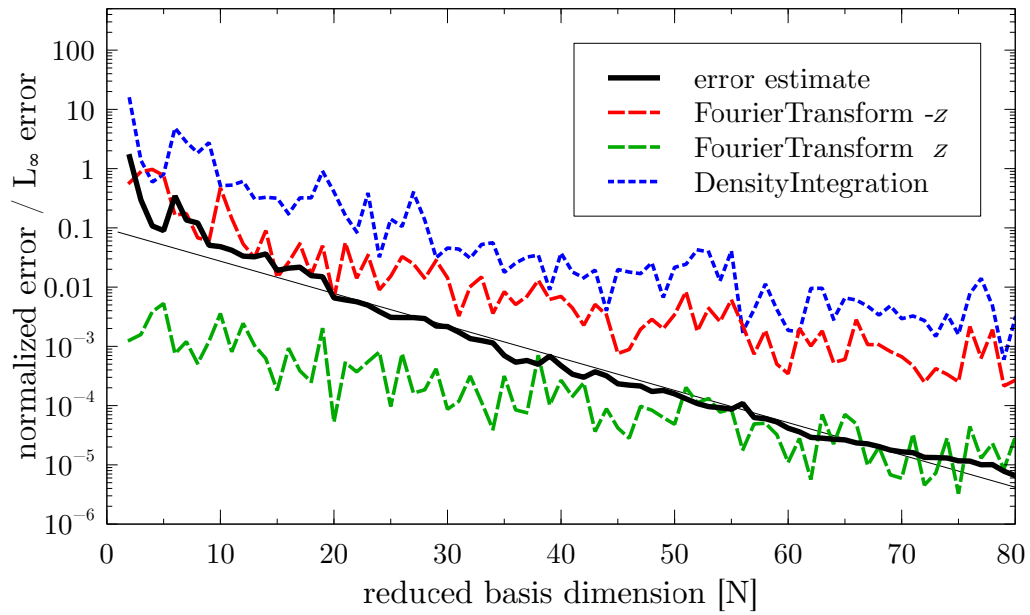
Figure 6.21.: Error estimates with increasing reduced basis dimension in a semi-logarithmic plot. The residual error estimate (thick black line) is normalized with the estimate for $N = 1$. The errors $\eta^l(N)$ and $\eta^q(N)$ for the FourierTransforms (red, green) and DensityIntegration (blue) are measured in the L_∞-norm (see Section 5.4.2 for definitions of the error estimators). An exponential fit of the residual error is shown as a thin black line.

decrease in the error with increasing reduced basis dimension N. The maximum of the error estimate in the first Greedy iteration is used as a normalization factor. The graph exhibits a steep decrease followed by an increase at $N = 6$. Subsequently, it follows an exponentially decaying function $f(N) = 0.096 \cdot 10^{-0.0545 \cdot N}$. The graph of this function is shown as a thin, black line.

The dashed red and green lines for the *FourierTransform* in *-z* and *z* directions and the blue line for the *DensityIntegration* depict the errors estimates $\eta^l(N)$ and $\eta^q(N)$ defined in Section 5.4.2 in the L_∞-norm. The graphs start at $N = 2$ as the errors estimates $\eta^l(1), \eta^q(1)$ are not defined. All three graphs exhibit an exponential reduction of the error estimate over the training set. The decay rates are comparable to the residual error estimate although in different norms. The *Fourier-Transform* in z direction exhibits a significantly lower error. As the modeled cell is illuminated from the bottom not much light is transmitted by the structure at all, deviations here are minimal and are usually neglected anyway. The error estimate of the *FourierTransform* in *-z* direction, describing the reflected light field, and the *DensityIntegration* error estimate are almost parallel and finish with an estimated error of approximately $3 \cdot 10^{-4}$ and $3 \cdot 10^{-3}$.

6.3.4. Approximation errors

The reduced basis should approximate the truth solution itself more accurately with increasing reduced basis dimensions as indicated by the error estimate in Figure 6.21. In order to quantify errors introduced by the reduced basis approximation we compute a set of reference solutions. The parameter locations $\mu_i \in \Xi \subset \mathfrak{D}$ are chosen at random. We compare the results of the reduced basis approximation and the full FEM problem without any approximation. These reference solutions thus do not fulfill the truth approximation 8 on page 78 with the affine expansion resulting from the empirical interpolation procedure but the truth approximation 6 on page 65. We distinguish between errors in the output quantities and the field solution itself.

Field solution   We begin the analysis of the approximation errors by comparing the fields. In Figure 6.22 the convergence of the mean and maximum of the error in the H(**curl**,Ω) norm is shown in addition to the relation between the reduced basis error estimate and the H(**curl**,Ω) error. The mean and maximum of the error over Ξ have identical trends and fit those of the output quantities shown in Figure 6.23 discussed hereafter. The errors decreases by about two orders of magnitude up to $N = 30$. The maximum subsequently stagnates at a level of $0.77 \cdot 10^1$ beyond $N = 40$. The mean error exhibits a similar decrease up to $N = 40$ before the stagnation is observed.

The scatter plot in Figure 6.22 relating estimated error and H(**curl**,Ω) error demonstrates the reasonable performance of the error estimate for large errors. As the approximation by the reduced basis becomes more accurate the estimated error and the H(**curl**,Ω) errors are no longer correlated for all parameters in Ξ. This is

truth approximation without empirical interpolation
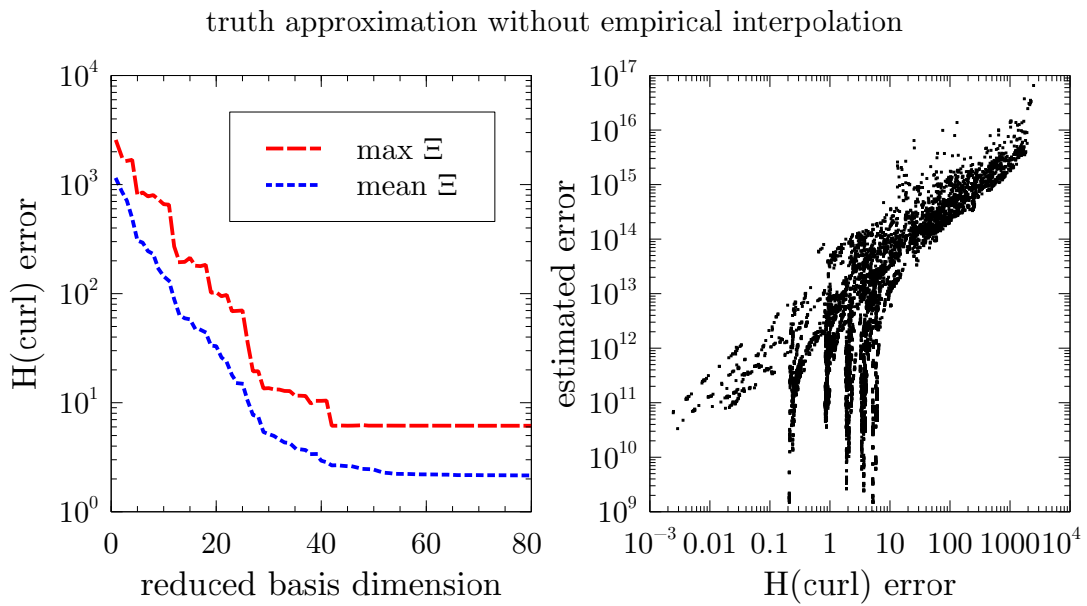

Figure 6.22.: Maximum and mean error of $\varXi \subset \mathfrak{D}_{train}^{N}$ in H(**curl**,Ω) norm over the reduced basis dimension (left) and estimated reduced basis error over the error in H(**curl**,Ω) norm (right). The error is measured with respect to the reference solutions fulfilling the truth approximation 6 on page 65 without empirical interpolation.

Table 6.9.: Statistics of the H(**curl**,Ω) norm of the reference solutions over Ξ

mean	min	max	median	standard deviation
1807.4	1507.1	2216.1	1741.2	213.6

reflected in the correlation coefficient $\rho = 0.62$ over all data points. At some parameter locations the H(**curl**,Ω) norm of the error does not decrease beyond $\sim 1 \cdot 10^1$. In relation to the norm of the solution, the approximations are orders of magnitude better than indicated by the absolute error shown here. In relative terms, the error is still below $1 \cdot 10^{-3}$ when considering the magnitudes of the H(**curl**,Ω) norms of the reference solutions listed in Table 6.9. As seen in the previous example in Section 6.1.4 the stagnation for some parameter values can be attributed to the error introduced by the empirical interpolation. As noted there, the reduced basis and the reference solutions fulfill different truth approximations and this additional error is not accounted for by the error estimate shown here. This results in the observed deviation from the diagonal in this plot.

Output quantity The output functionals are continuous functions of the field solution. Hence we expect a similar results in studying the errors in the output quantities. For this example, the transmission, the absorption within the air and IRL layer are negligible. The maximum and mean of the relative errors over Ξ for the remaining quantities are depicted in Figure 6.23 as red and blue dashed lines. The relative errors decrease in all quantities with increasing reduced basis dimension. The density integration in the ZnO and Ag layer exhibits a distinctive drop at $N = 26$. This corresponds to the inclusion of a snapshot at 650 nm. Subsequently this parameter location is much better resolved and the errors decrease. Overall we observe a stagnation in the errors beyond $N = 40$. This fits the discussion above where the field error was observed to be large for specific parameter location. The stagnation of the errors in the output quantities can be attributed for the most part to these specific locations as well.

The slight difference of the reference problems used here (these solve Problem 6) and the corresponding problems approximated by the reduced basis (solving Problem 8) explains the observed approximation errors in the field solution and the output quantities. These observations are identical to the discussion in Section 6.1.4 where the same stagnation is observed and could be attributed to the different reference solutions. This explanation is strengthened by the convergence properties of the second type of reference solutions fulfilling the truth approximation 8 with empirical interpolation over the set Ξ_{eim} used in the next sections. The maximum and mean of the relative errors over Ξ_{eim} with respect to these reference solutions are depicted in Figure 6.23 as red and blue solid lines. Both mean and maximum errors convergence exponentially with a rate of approximately $10^{-.036}$ which is identical to the estimated
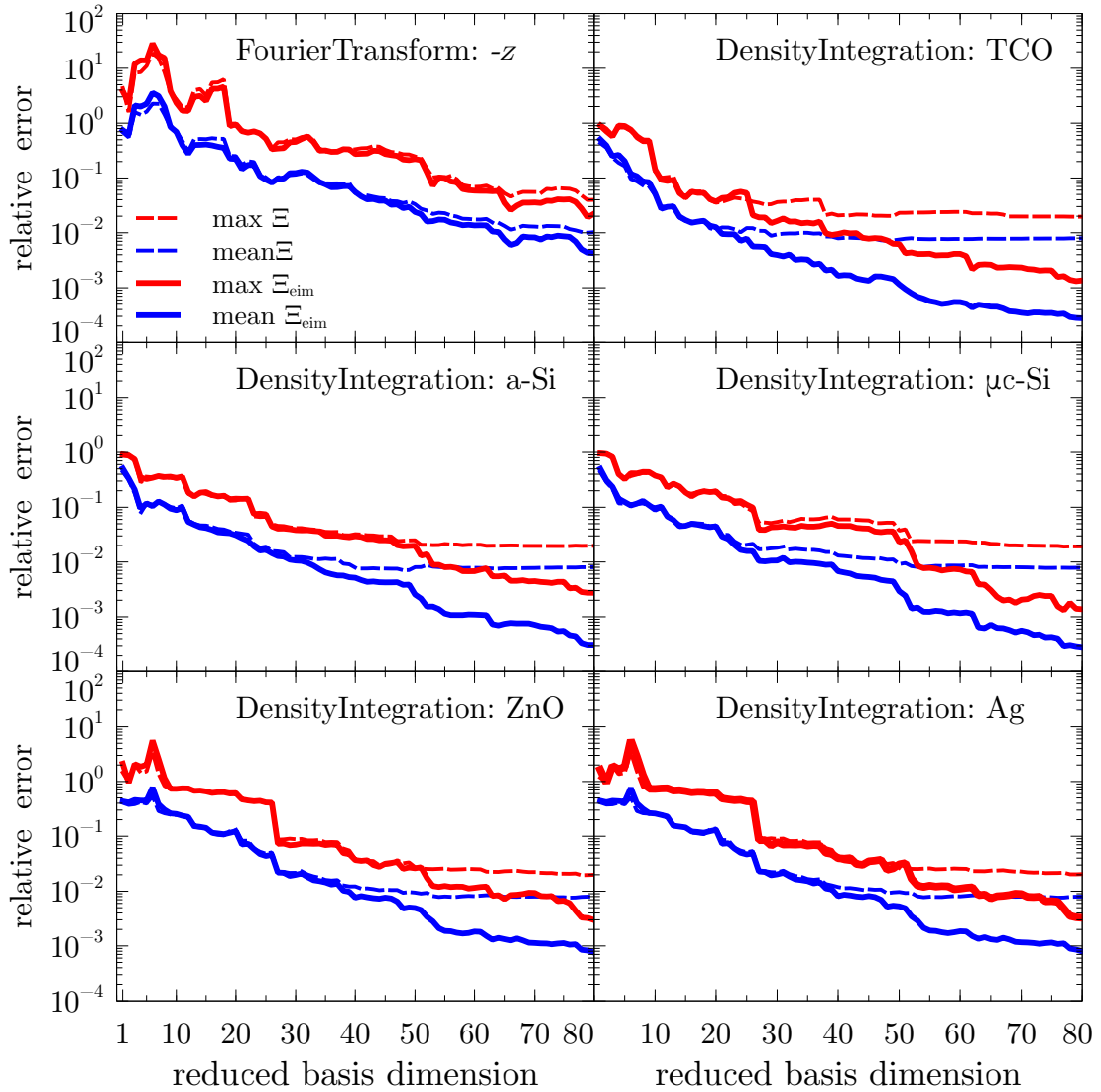
Figure 6.23.: Relative error in the output quantities over the reduced basis dimension measured between the reduced basis approximation and two reference solutions. There is one plot per output quantity which is indicated in the upper right of each axis. The maximal (red dashed) and mean (blue dashed) relative errors to the references fulfilling the truth approximation 6 without empirical interpolation over the set Ξ stagnate beyond $N = 15$. The maximal (red solid line) and mean (blue solid line) relative errors to the reference solution fulfilling the truth approximation 8 with empirical interpolation over the set Ξ_2 are smaller and stagnate at a lower error level for large N.

rate derived from Figure 6.21.

6.3.5. Error analysis

The approximation errors observed in the previous section are generally reduced with increasing dimension of the reduced basis. In the following we thus investigate the sources of the errors further. We determine the inf-sup constant first to justify its neglect (cf. Sections 5.4.2 and 5.4.3) and then investigate the errors introduced by the empirical interpolation of the system matrix and right-hand side in more detail.

Inf-sup constant estimation   The residual error estimator does not account for the inf-sup constant β. In this example the inf-sup-constant varies marginally between 0.1 and 0.7. The distribution of β over $\mathfrak{D}$ shown in Figure 6.24 depends mainly on the wavelength. The distribution exhibits three distinct areas with rugged boundaries instead of the sharp boundaries observed in Figure 6.7 for another example. This is likely an artifact of the interpolation of the coarser sampling points. Below ca. 615 nm the values of β are larger than .45 independently of the value of d_{irl}. Similarly above 645 nm the values are again larger than .45. In between β has values between .1 and .2. The histogram exhibits two clusters: one between $\beta = .1$ and $\beta = .2$ and one between $\beta = .45$ and $\beta = .7$. We conclude that the neglect of the inf-sup constant is not a great loss in accuracy as the variations in β are limited to at most a factor of 7.

Empirical interpolation error   The error introduced by the affine expansion of the sesquilinear form $a(\cdot, \cdot; \mu)$ and linear form $f(\cdot; \mu)$ with the Empirical Interpolation Method in Section 5.5.1 is measured and controlled in the L_∞ norm. In Section 6.3.4 we found the errors in the $H(\mathbf{curl}, \Omega)$ norm to be much larger than the estimated L_∞ errors of the EIM approximation listed in Table 6.8. We investigate the errors defined in Section 6.1.5 related to the EIM approximation for a set $\Xi_{eim} \subset \mathfrak{D}$ of 100 parameters.

The computed errors over Ξ_{eim} are shown in Figure 6.25 on logarithmic scales as scatter plots together with histograms. Δ_1 (Figure 6.25a) exhibits errors larger than $1 \cdot 10^{-1}$ over the whole parameter domain except for the central frequency where the errors are below $1 \cdot 10^{-8}$ independent of d_{irl}. Outside this line this absolute error is quite large and the relative error δ_1 takes values between $1 \cdot 10^{-4}$ and $1 \cdot 10^{-2}$ with a mean of $1.6 \cdot 10^{-4}$. The histogram Figure 6.25e shows this split between the 9 data points at the central wavelength and the other data points. The median of $\log_{10}(\delta_1)$ is -2.97.

The distribution of Δ_2 over Ξ_{eim} in Figure 6.25b differs distinctly from the distribution of Δ_1 (Figure 6.25a). We do not observe any structure in the distribution. The errors differ between $2 \cdot 10^{-10}$ and $6 \cdot 10^{-8}$. The relative error distribution in
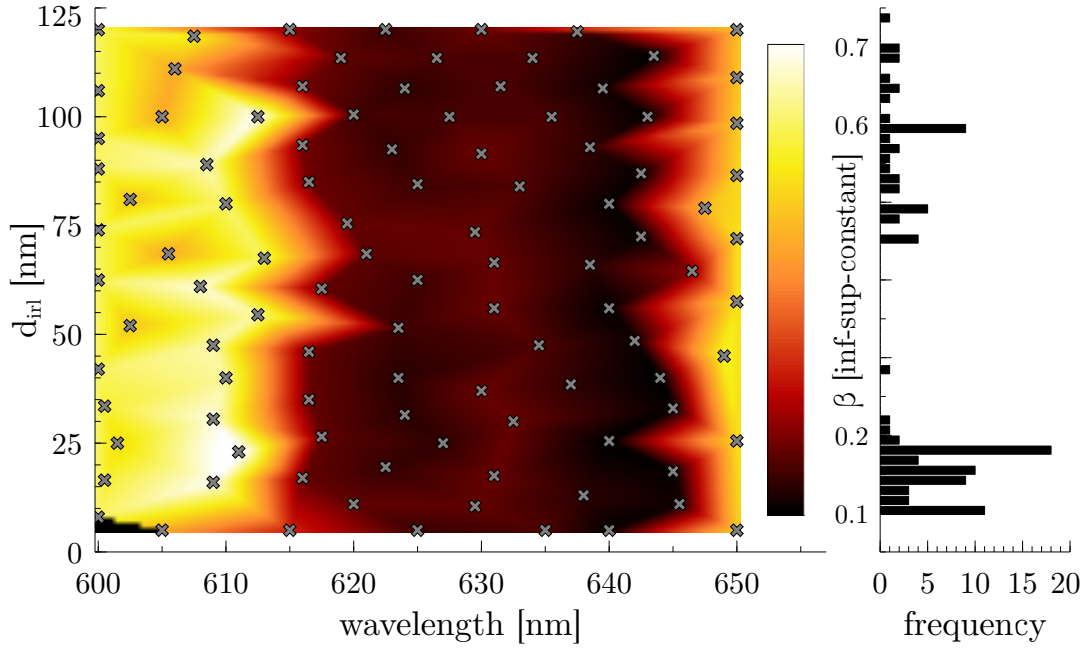
Figure 6.24.: The false color plot of the inf-sup constant β distribution in parameter space $\mathfrak{D}$ computed at the snapshot locations (indicated by crosses). The color bar axis coincides with the histogram on the right showing the clustering of β for the 80 data points.

Figure 6.25d is almost identical, albeit with error levels three magnitudes smaller. The median and mean of $\log_{10}(\delta_2)$ in Figure 6.25f are approximately -11.5.

The distribution of Δ_1, Δ_2 can in part be explained by the location of the empirical interpolation snapshots for the matrix (blue diamonds in Figures 6.25a-(d)) and the right hand side (a single blue square in the center). The error Δ_2 measures the error introduced by the empirical interpolation of the right hand side as detailed in (6.1) on page 107. As in this study the incidence angle is kept constant and only the wavelength is varied, the right hand side does not depend on the parameter and the empirical interpolation requires only a single snapshot. Subsequently the errors are negligible. The system matrix $\mathcal{A}$ depends on the geometrical parameter d_{irl} as well as the wavelength. Even though its entries are approximated well by the empirical interpolation the induced error Δ_1 is substantial if the wavelength does not coincide with the empirical interpolation snapshots for both the system matrix and the right hand side.

6.3.6. Online evaluation and results

The figure of merit in optimizing the intermediate reflector layer thickness is the gain in current density generated by the top cell. In [Kirner et al., 2014] our investigations were limited to 3 wavelengths (600 nm, 650 nm and 700 nm) and 7 values of d_{irl} for every sample as every evaluation has computational costs of ca.

(a) Error Δ_1 (logarithmic scale)

(b) Error Δ_2 (logarithmic scale)

(c) Error δ_1 (logarithmic scale)

(d) Error δ_2 (logarithmic scale)

(e) Histogram of $\log_{10}(\delta_1)$

(f) Histogram of $\log_{10}(\delta_2)$
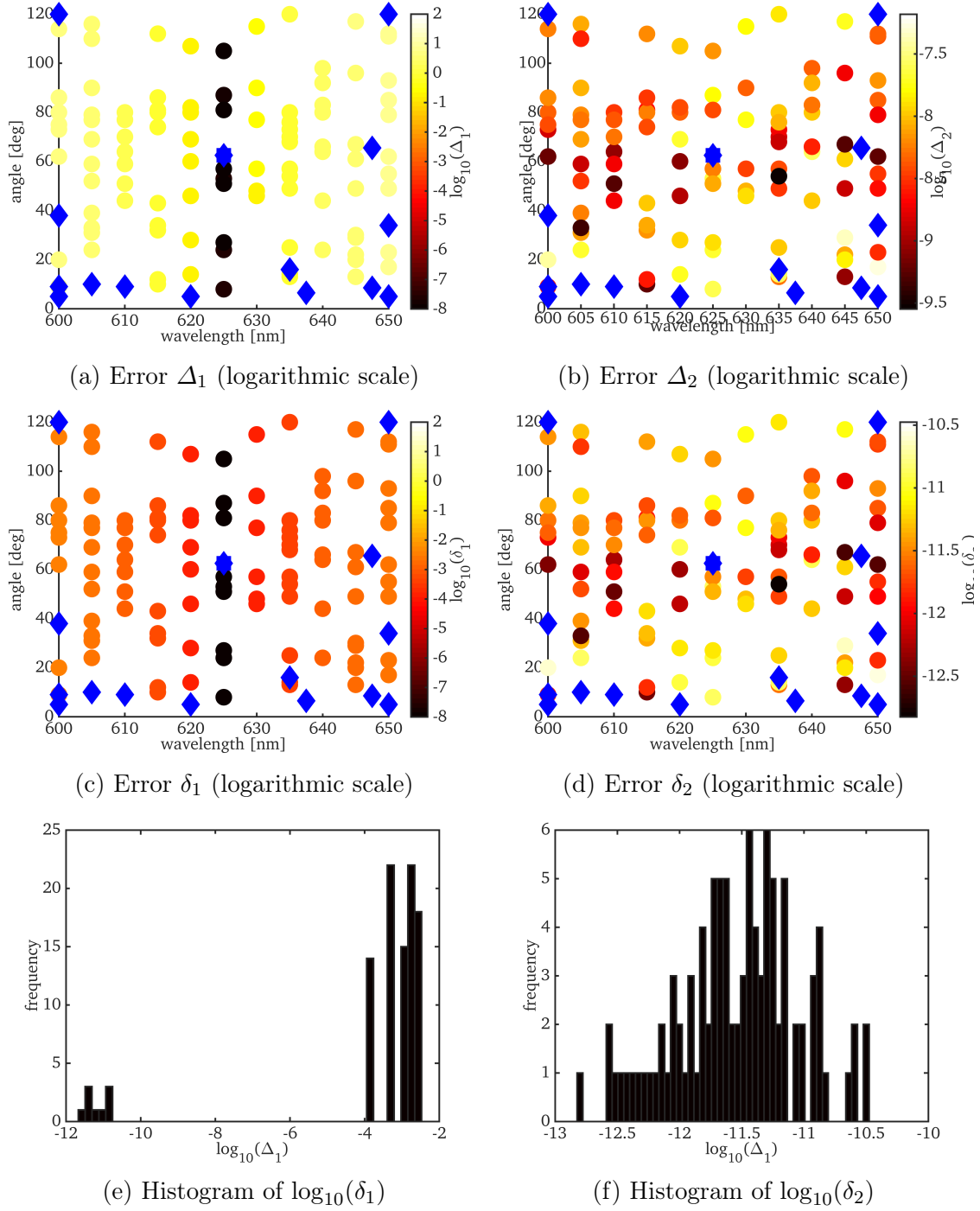
Figure 6.25.: (a)-(d): Scatter plots of the empirical interpolation error $\Delta_{1,2}$ (absolute) and $\delta_{1,2}$ (relative) for the set $\Xi_{eim} \subset \mathfrak{D}$ (see text for definitions). The positions of the EIM snapshots for the matrix (diamonds) and right-hand side (square) are marked blue. (e)-(f): Histograms of $\log_{10}(\delta_1)$ and $\log_{10}(\delta_2)$.
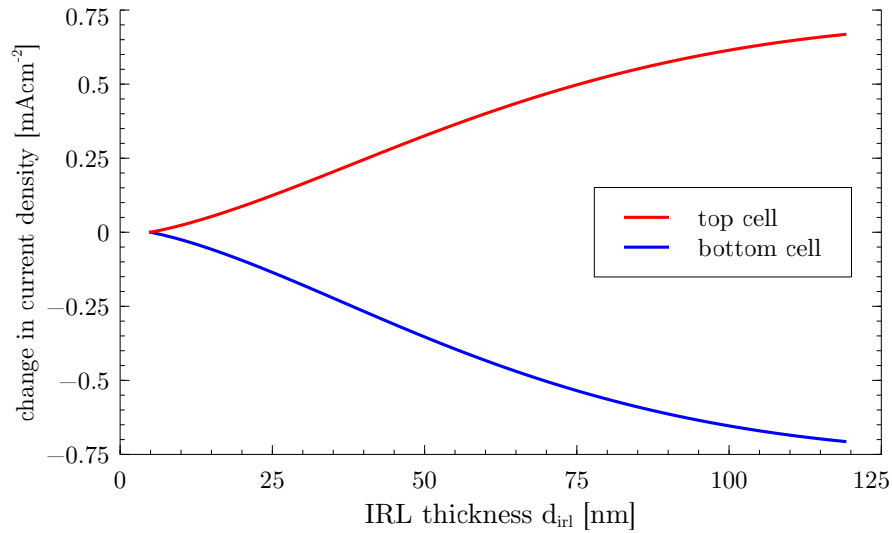
Figure 6.26.: Change in current density relative to a 5 nm thick IRL. The current densities considered here are restricted to wavelengths between 600 nm and 650 nm.
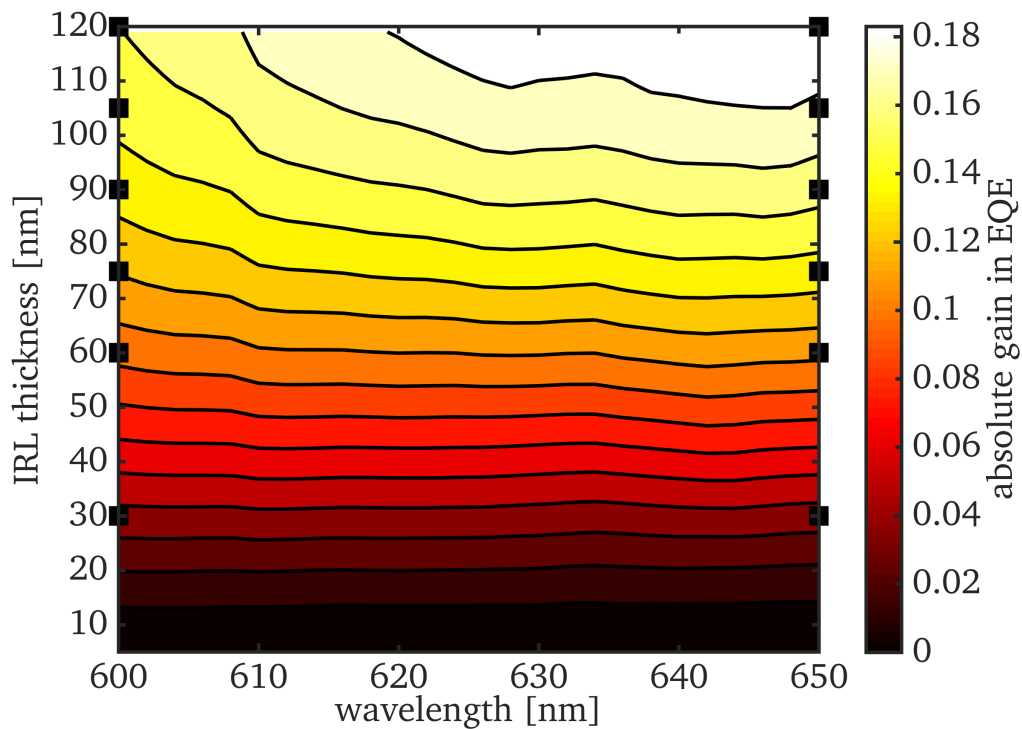
Figure 6.27.: Contour plot of the absolute gain in top cell EQE over the rectangular parameter domain $\mathfrak{D}$. The gain is computed with respect to $d_{irl}=5$ nm instead of $d_{irl}=0$ nm as in [Kirner et al., 2014]. The parameter locations used in [Kirner et al., 2014] are marked as black squares.

21.7 cpu hours or 1.43 hours total on a 16 core workstation. In the online phase the reduced basis allows to evaluate the reduced order model for a sample in approximately 300 milliseconds instead of hours. The speed up factor compared to the truth approximation is about 260 000 for this example. This allows to sample the parameter domain with a high resolution. Figure 6.26 depicts the computed change in implied photo current density generated between 600 nm and 650 nm wavelength with increasing thickness of the IRL. In contrast to the cited reference the gains and losses are computed with respect to the value for d_{irl}=5 nm ($j_{sc}^{TC}|_{600 \text{ nm}}^{650 \text{ nm}} = 1.48$ mA cm^{-2} and $j_{sc}^{TC}|_{600 \text{ nm}}^{650 \text{ nm}} = 2.01$ mA cm^{-2}) instead of d_{irl}=0 nm as it is not part of the parameter domain $\mathfrak{D}$. We observe an increase in top cell current density mirrored by a decrease in bottom cell current density. The results are not directly comparable to the experimentally obtained values as the current density here is only computed over part of the spectrum resulting in smaller values but the observed trends are similar. The wavelength resolved gain in top cell EQE is shown in Figure 6.27 over $\mathfrak{D}$. The parameter locations used in [Kirner et al., 2014] are marked as black squares. We observe almost horizontal contours for small values of d_{irl}. For longer wavelengths enough light reaches the IRL, is reflected and contributes substantially to the top cell current by increasing the EQE at 648 nm by .195 up to .492. The maximum top cell EQE for d_{irl}=60 nm is found at 600 nm with .715.

The resulting EQEs over the parameter domain for the top cell and bottom cell absorber are depicted in Figure 6.28 in the first two columns. The right column depicts the absorptance of the IRL. The rows correspond to a reduced basis evaluation using $N = \{10, 20, 40, 80\}$ snapshots. We observe the previously mentioned trade-off in top and bottom cell absorption in all rows. Maxima in top cell absorption correspond to minima in bottom cell absorption and vice versa. The IRL is non-absorptive beyond 610 nm wavelength. We do not observe larger differences for different reduced basis dimensions in this quantity. In estimating the top an bottom cell EQEs we find $N = 40$ to be a reasonable choice as there are distinct differences in the shape of the contours for $N = 10$ and $N = 20$.

The area plots in Figure 6.29 depict the stacked EQEs of all layers in the solar cell model and the reflectance. These plots are shown along two cross-sections through the center of the parameter domain. The left column corresponds to fixed d_{irl} of 61 nm. The right column corresponds to fixed wavelength of 624 nm. The central column shows the logarithm of the normalized error estimate of the reduced basis approximation over the parameter domain. The cross sections are marked as black lines through the center. The rows again show the approximation using $N = \{10, 20, 40, 80\}$ snapshots.

For the fixed wavelength of 624 nm we find a good approximation for all investigated thicknesses. The error in energy conservation is relatively small as observed by the small white areas where the EQEs and reflectance do not sum to one. In these plots the shown reflection only accounts for the specular reflection such that the real error in energy conservation is actually smaller than indicated. The trade-off between top and bottom cell absorption is clearly visible and well approximated even with a reduced basis dimension of $N = 10$. Conversely by keeping the thickness

(a) $N = 10$

(b) $N = 20$

(c) $N = 40$

(d) $N = 80$
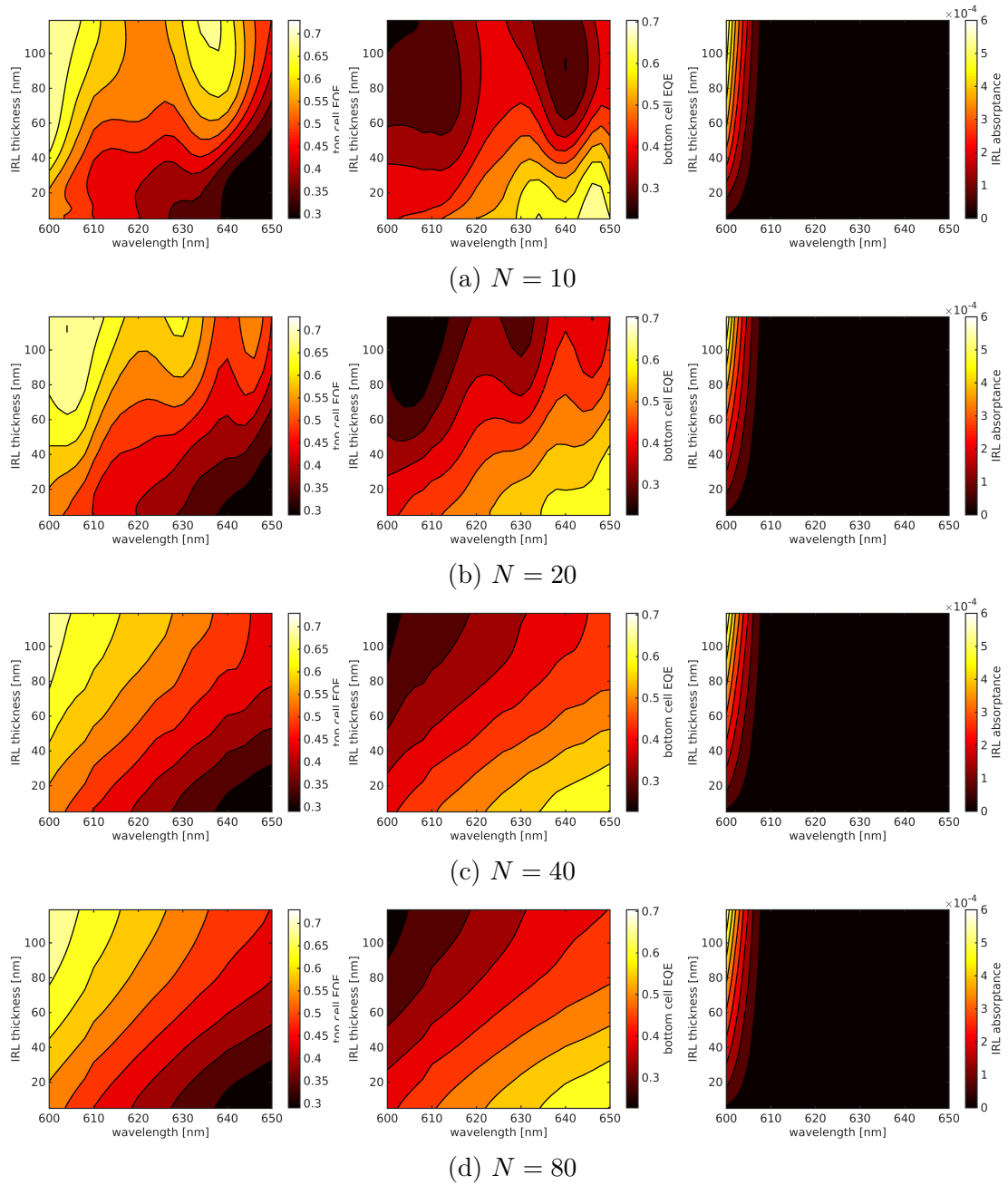
Figure 6.28.: Top and bottom cell EQEs (left and center column) and the absorption of the IRL (right) over the parameter domain $\mathfrak{D}$. The rows correspond to the evaluation of the reduced basis using 10 snapshots (a), 20 snapshots (b), 40 snapshots (c) and 80 snapshots (d).
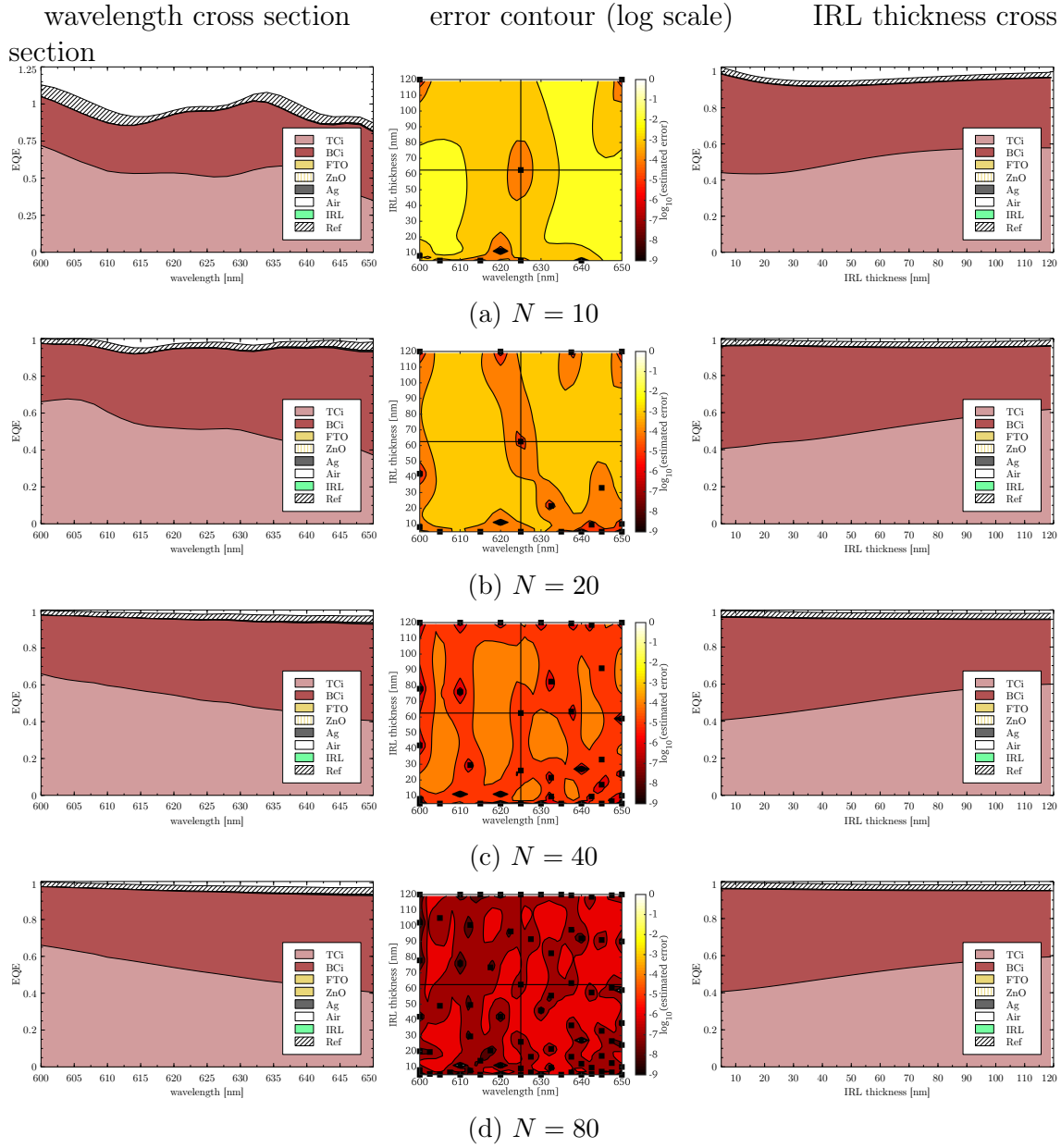
Figure 6.29.: Area plots of layer resolved absorptance over wavelength (left column) and IRL thickness (right column). The contour of the logarithm of the normalized residual error estimate is shown in the central column. The snapshot positions are marked as black squares. Additional black lines indicate the cross-sections at $d_{irl} = 61$ nm and $\lambda = 624$ nm depicted left and right. The rows correspond to using N=10 snapshots (a), N=20 snapshots (b), N=40 snapshots (c) and N=80 snapshots (d).

constant we observe larger errors in energy conservation. This is best observed by the oscillations in the plot for $N = 10$ in the left column. Using twice the number of basis functions reduces the oscillations until they are no longer visible for $N = 40$. Again, we do not observe visible differences between using a reduced basis dimension of 40 and 80.

Especially for the very low dimensional reduced basis approximation depicted in the first two rows, we observe an anisotropy in the estimate error. In part this may serve as an explanation of the previously discussed errors in energy conservation. At $N = 10$ the reduced basis exhibits larger errors below 610 nm and above 635 nm along the cross-section d_{irl}=60 nm. This corresponds to regions of larger oscillations in the area plot. In contrast the errors are lower in the other parameter direction which reflects in the smaller energy conservation error observed in the area plot.

7. Conclusion

In silicon photovoltaics advanced cell concepts and photonic structures must be found to trap light inside the solar cell absorber, as silicon based solar cells suffer from insufficient absorption of the incident solar irradiation. Predictive simulations of optical processes and complex nanostructured devices have become omnipresent in recent years in several fields of current research and industrial applications, not limited to the field of photovoltaics. In many applications devices or processes are optimized with respect to a certain objective where the underlying physical processes are described by partial differential equations. In the field of wave optics electromagnetic fields are investigated which are governed by Maxwell's equations.

In this work we developed a reduced basis method for the solution of the parameter dependent electromagnetic scattering problem with arbitrary parameters. The method was developed with the specific challenges arising in optical simulations of thin-film silicon solar cells in mind. These are generally large in domain size and have a complex three-dimensional structure, making optimization tasks infeasible due to high computational effort if a high accuracy of the electromagnetic field solution is required.

The specific modeling demands of solar cells were addressed in this work. This comprised the improvement of the reduced basis implementation to include also non-geometric parameters such as the incidence angle or wavelength of the illumination source by employing an empirical interpolation method. Its application allow for parameters not only to vary geometries as before, but also material tensors and source fields. Likewise, the non-linear post-processing steps of the electromagnetic field to derive energy fluxes or volume absorption were developed and included. In numerical examples the computational costs could be reduced by as much as five orders of magnitude compared to efficient finite element solvers.

In addition, an efficient tailored domain decomposition algorithm was presented in Chapter 4 allowing to model incoherent layers or illuminations in optical systems. This is of particular interest for solar cells in superstrate configuration where the absorber is illuminated through a glass substrate.

In this thesis we employed the developed methods in application examples taken from collaborations with experimentalists from the Helmholtz-Zentrum Berlin für Materialien und Energie active in the joint lab "BerOSE"[1]. The optical model of a thin-film silicon multi-junction with incoherent light-trapping was characterized in great detail in Section 6.2. The necessity to simulate three dimensional models of thin-film solar cells for results with predictive power was demonstrated. The

---

[1]Berlin Joint Lab for Optical Simulations for Energy Research (BerOSE)

7. Conclusion

computational gains through hybrid, *hp* adaptive finite elements were studied and the incoherent domain decomposition algorithm applied to model a more realistic light-trapping by the substrate.

The numerical examples of a hexagonal nano-hole array in Section 6.1 and multi-junction solar cell with a tunable intermediate reflector layer in Section 6.3 showed that the reduced basis method is well suited as a forward solver for modeling and optimization tasks arising in photovoltaics and photonics. Reduced models for illumination and geometric parameters can be be built with high accuracy compared to the reference models, while providing savings in computational costs of roughly three orders of magnitude. Even in the presence of resonance phenomena in the hexagonal nano-hole array, representing a photonic crystal, the method worked well and adapted itself automatically to a detected resonance in the field enhancement. Here, the employed residual error estimator worked reasonably well and we found high correlations between the observed and estimated errors.

The fast and efficient evaluation of the reduced model allowed to investigate the effect of changes in the intermediate reflector layer thickness over a broad wavelength spectrum and to compute changes in the current densities. This is in stark contrast to the previously encountered restrictions for this model problem where simulations were limited to a few wavelengths and thickness. A speed up of five orders of magnitude allows for a much finer resolved wavelength scan and the computation of short circuit current densities.

Future improvements are required on several fronts: Currently, the error estimator does not account for the error introduced by the empirical interpolation. Thus work is needed to develop a rigorous estimate to bound this error as well. Secondly, the offline phase requires possibly large computer resources. Parallelization on computing clusters can save wall clock time in this step if efficient ways to employ their full capacity are found.

8. Zusammenfassung

Die Beschreibung elektromagnetischer Felder durch die Maxwell-Gleichungen in der Wellenoptik ist beispielhaft für physikalische Prozesse, denen partielle Differentialgleichungen zugrunde liegen. Häufig werden Parameter bezüglich eines Zielfunktionals optimiert oder in inversen Problemen rekonstruiert. Die Parameterräume sind oftmals groß und hochdimensional oder es bestehen Echtzeitanforderungen an die Berechnung. Insbesondere für 3D-Probleme ist dies mit den verfügbaren Maxwell-Lösern auf Basis der Finite-Elemente-Methode (FEM) häufig nicht erreichbar.

Durch Nanostrukturierung und Abstimmung der optischen Komponenten kann die Einkopplung des Sonnenlichtes in Silizium-Dünnschichtsolarzellen verbessert werden. Studien zur Optimierung dieser Zellen erfordern daher neben genauen und schnellen Simulationen die Behandlung spezifischer Eigenschaften des Sonnenlichts. Im Fokus dieser Arbeit sind daher Methoden um die Optik nanostrukturierter Solarzellen schnell und effizient zu simulieren.

In dieser Arbeit wird eine Reduzierte-Basis-Methode (RBM) für allgemeine Parameterabhängigkeiten des elektromagnetischen Streuproblems entwickelt. Sie erlaubt, das parametrisierte Streuproblem in Echtzeit zu lösen, indem der Lösungsprozess in zwei Phasen gegliedert wird: In der aufwendigen *Offline*-Phase wird das Problem einmalig für einige wenige Parameter gelöst und daraus eine niedrigdimensionale Basis erstellt, die die Lösung über dem Parameterbereich gut approximiert. In der schnellen *Online*-Phase wird nur das reduzierte - von der FEM-Dimension unabhängige - System gelöst. Eine verlässliche Schätzung und Kontrolle des Approximationsfehlers ist im selbstadaptiven Aufbau der Basis unverzichtbar. Ziel der Nutzung der RBM für Solarzellen ist die Berechnung der Absorptions- und Reflexionsspektren, wofür reduzierte (nicht-)linearen Auswertefunktionale benötigt werden.

Des Weiteren wird eine Methode zur Modellierung von Inkohärenz präsentiert, die auf Gebietszerlegung basiert. Sie kann genutzt werden um das durch Totalreflexion gefangene Licht zu berücksichtigen. Direkte Simulation der spektralen Zerlegung führt zu einer Vielzahl von Simulationen und Auswertungen von nichtlinearen Funktionalen. Eine orthogonale Zerlegung zur beschleunigten Auswertung dieser Funktionale wird beschrieben.

In Beispielen aus Kooperationen mit dem JointLab "BerOSE"[1] werden die vorgestellten Methoden detailliert untersucht. Die Modellreduktion erlaubt eine um Größenordnungen schnellere Berechnung der physikalischen Größen in einem Solarzellenmodell. Damit sind detailliertere Parameterstudien möglich, die aufgrund des numerischen Aufwands zuvor nicht durchgeführt werden konnten.

---

[1]Berlin Joint Lab for Optical Simulations for Energy Research (BerOSE)

A. Appendix

A.1. Coupling of two domains
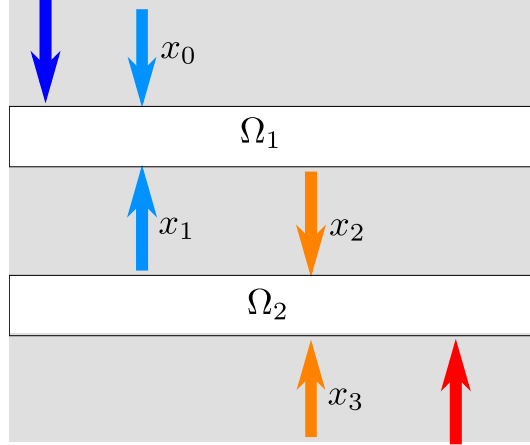
Figure A.1.: Schematic of the coupling in a stack of two domains Ω_1 and Ω_2. Illumination of the stack is only possible from the top and/or bottom as indicated by the blue and red arrows. In each domain fields are incident from both the bottom or the top (indicated by light blue and orange arrows). The scattered fields excited by $\boldsymbol{x}_0$ and $\boldsymbol{x}_1$ equal $\boldsymbol{x}_2$. Conversely, the scattered fields excited by $\boldsymbol{x}_2$ and $\boldsymbol{x}_3$ equal $\boldsymbol{x}_1$.

We consider the domain decomposition method introduced in Section 3.3 for most simple case where the domain Ω is decomposed into two domains Ω_1 and Ω_2. This case is depicted schematically in Figure A.1 where the notation used in the following is introduced. For each domain we can compute scattering matrices $\mathcal{T}^1, \mathcal{T}^2$, respectively. We only require the blocks $\mathcal{T}^1_{2,1}, \mathcal{T}^1_{2,2}$ and $\mathcal{T}^2_{1,2}, \mathcal{T}^2_{1,1}$ of the two scattering matrices for the coupling as we must balance the field only across the common boundary. The remaining blocks are used to determine the reflection and transmission of the stack once the solution is computed. Using the abbreviations $\mathcal{T}_1 = \mathcal{T}^1_{2,1}, \mathcal{R}_1 = \mathcal{T}^1_{2,2}$ and $\mathcal{T}_2 = \mathcal{T}^2_{1,2}, \mathcal{R}_2 = \mathcal{T}^2_{1,1}$ to simplify notation of these matrix blocks, we obtain the stack matrix

$$\mathcal{S} = \begin{pmatrix} \mathcal{I} & & & \\ -\mathcal{T}_1 & -\mathcal{R}_1 & \mathcal{I} & \\ & \mathcal{I} & -\mathcal{R}_2 & -\mathcal{T}_2 \\ & & & \mathcal{I} \end{pmatrix} \tag{A.1}$$

with the identity matrix $\mathcal{I}$. Here $\mathcal{T}$ and $\mathcal{R}$ symbolize transmission and reflection of the domains if fields are incident from the shared boundary.

The global illumination field E_{in} incident on the stack is encoded in $\boldsymbol{x}_0$ and $\boldsymbol{x}_3$ and can be expressed as $\boldsymbol{s}_{in} = (\boldsymbol{x}_0, 0, 0, \boldsymbol{x}_3)^{\mathsf{T}}$. Exploiting the linearity of the system we can restrict our consideration to the simpler case of a single incident field from the top, i.e. a right-hand side $\boldsymbol{s}_{in} = (\boldsymbol{i}_0, 0, 0, 0)^{\mathsf{T}}$. We find the following system for $\boldsymbol{x} = (\boldsymbol{x}_0, \boldsymbol{x}_1, \boldsymbol{x}_2, \boldsymbol{x}_3)$ as a block equation system from $\mathcal{S}\boldsymbol{x} = \boldsymbol{s}_{in}$

$$\boldsymbol{x}_0 = \boldsymbol{i}_0$$
$$\boldsymbol{x}_1 = \mathcal{R}_2 \boldsymbol{x}_2$$
$$\boldsymbol{x}_2 = \mathcal{T}_1 \boldsymbol{i}_0 + \mathcal{R}_1 \boldsymbol{x}_1$$
$$\boldsymbol{x}_3 = 0$$

which is equivalent to

$$\boldsymbol{x}_2 = \mathcal{T}_1 \boldsymbol{i}_0 + \mathcal{R}_1 \mathcal{R}_2 \boldsymbol{x}_2$$
$$\Longleftrightarrow \mathcal{T}_1 \boldsymbol{i}_0 = (\mathcal{I} - \mathcal{R}_1 \mathcal{R}_2) \boldsymbol{x}_2$$
$$\Longrightarrow \boldsymbol{x}_2 = (\mathcal{I} - \mathcal{R}_1 \mathcal{R}_2)^{-1} \mathcal{T}_1 \boldsymbol{i}_0$$

$$\boldsymbol{x}_1 = \mathcal{R}_2 \mathcal{T}_1 \boldsymbol{i}_0 + \mathcal{R}_2 \mathcal{R}_1 \boldsymbol{x}_1$$
$$\Longleftrightarrow \mathcal{R}_2 \mathcal{T}_1 \boldsymbol{i}_0 = (\mathcal{I} - \mathcal{R}_2 \mathcal{R}_1) \boldsymbol{x}_1$$
$$\Longrightarrow \boldsymbol{x}_1 = (\mathcal{I} - \mathcal{R}_2 \mathcal{R}_1)^{-1} \mathcal{R}_2 \mathcal{T}_1 \boldsymbol{i}_0$$

As $\mathbb{C}^M$ is a Banach space and $\mathcal{R}_1 \mathcal{R}_2$ is a linear (thus continuous and bounded) operator in said space, the infinite Neumann series converges provided $\|\mathcal{R}_1 \mathcal{R}_2\|_{\mathbb{C}^M} < 1$. Hence $\mathcal{I} - \mathcal{R}_1 \mathcal{R}_2$ is invertible (cf. Theorem II.1.11 in [Werner, 2011] and we have

$$(\mathcal{I} - \mathcal{R}_1 \mathcal{R}_2)^{-1} = \sum_{j=0}^{\infty} (\mathcal{R}_1 \mathcal{R}_2)^j.$$

The infinite series shows a relation to iterative domain decomposition algorithms. In terms of optical systems, it can be interpreted as a series of light passes through the domains. In every pass light is reflected by one domain into the other. If no light is lost, i.e. both domains contain a perfect mirror, the system does not converge, but as long as there are losses a solution exists.

A.2. Absorption in layered media

The electric field energy in a layered media can be explicitly computed provided we have a plane wave expansion of the electric field. In this case we have $E(\boldsymbol{r}) = \sum_{\boldsymbol{k}_\perp} \widehat{\boldsymbol{E}}_{\boldsymbol{k}_\perp} e^{ik_z(\boldsymbol{k}_\perp) \cdot r}$ as detailed in Section 3.3.1. To compute the electric field energy

contained in a bounded domain Ω with a twofold periodicity along grid vector $\boldsymbol{a}_1$ and $\boldsymbol{a}_2$ we have to compute

$$\int_\Omega E \cdot \overline{D}\, \mathrm{d}\boldsymbol{r} = \int_z \int_{\Omega_\perp} E \cdot \overline{D}\, \mathrm{d}\boldsymbol{x}_\perp\, \mathrm{d}z \tag{A.2}$$

where we assumed the computational domain to be oriented along the z axis and $\Omega_\perp$ is the unit cell spanned by $\boldsymbol{a}_1, \boldsymbol{a}_2$ in the z-hyperplane. The inner integral simplifies in case of a Fourier plane wave basis as they form an orthogonal basis over $\Omega_\perp$. The inner integral in (A.2) thus becomes

$$\int_{\Omega_\perp} E \cdot \overline{D}\, \mathrm{d}\boldsymbol{x}_\perp = \int_{\Omega_\perp} \left(\sum_{\boldsymbol{k}_\perp} \widehat{\boldsymbol{E}}_{\boldsymbol{k}_\perp} e^{ik_z(\boldsymbol{k}_\perp)z + i\boldsymbol{k}_\perp \cdot \boldsymbol{x}_\perp} \right) \cdot \overline{\left(\varepsilon \sum_{\boldsymbol{k}'_\perp} \widehat{\boldsymbol{E}}_{\boldsymbol{k}'_\perp} e^{ik_z(\boldsymbol{k}'_\perp)z + i\boldsymbol{k}'_\perp \cdot \boldsymbol{x}_\perp} \right)}\, \mathrm{d}\boldsymbol{x}_\perp$$

$$= \sum_{\boldsymbol{k}_\perp} \sum_{\boldsymbol{k}'_\perp} e^{i(k_z(\boldsymbol{k}_\perp) - \overline{k_z(\boldsymbol{k}'_\perp)})z} \int_{\Omega_\perp} \widehat{\boldsymbol{E}}_{\boldsymbol{k}_\perp} \cdot \overline{\left(\varepsilon \widehat{\boldsymbol{E}}_{\boldsymbol{k}'_\perp} \right)} e^{i\left(\boldsymbol{k}_\perp \boldsymbol{x}_\perp - i\overline{\boldsymbol{k}'_\perp} \right) \cdot \boldsymbol{x}_\perp}\, \mathrm{d}\boldsymbol{x}_\perp$$

$$= |\Omega_\perp| \sum_{\boldsymbol{k}_\perp} \widehat{\boldsymbol{E}}_{\boldsymbol{k}_\perp} \cdot \overline{\left(\varepsilon \widehat{\boldsymbol{E}}_{\boldsymbol{k}_\perp} \right)} e^{i(k_z(\boldsymbol{k}_\perp) - \overline{k_z(\boldsymbol{k}_\perp)})z} \tag{A.3}$$

In general E will not only contain upward or downward propagating components. However, for these $k_z(\boldsymbol{k}_\perp)$ differs only by a sign to determine propagation direction. The two plane waves do not necessarily have the same zero phase plane uniquely fixed by z_0, but instead z_t and z_b for top and bottom. In Section 3.3.4 this case is depicted in Figure 3.4 by black dots marking the zero-phase points. In this case (A.3) will take the following form for a fixed $\boldsymbol{k}_\perp$:

$$\left(\widehat{\boldsymbol{E}}_{\boldsymbol{k}_\perp}^+ e^{ik_z(\boldsymbol{k}_\perp)(z - z_b)} + \widehat{\boldsymbol{E}}_{\boldsymbol{k}_\perp}^- e^{-ik_z(\boldsymbol{k}_\perp)(z - z_t)} \right) \cdot \overline{\left(\varepsilon \left(\widehat{\boldsymbol{E}}_{\boldsymbol{k}_\perp}^+ e^{ik_z(\boldsymbol{k}_\perp)(z - z_b)} + \widehat{\boldsymbol{E}}_{\boldsymbol{k}_\perp}^- e^{-ik_z(\boldsymbol{k}_\perp)(z - z_t)} \right) \right)}$$

$$= \widehat{\boldsymbol{E}}_{\boldsymbol{k}_\perp}^+ \cdot \overline{\left(\varepsilon \widehat{\boldsymbol{E}}_{\boldsymbol{k}_\perp}^+ \right)} e^{i(k_z(\boldsymbol{k}_\perp) - \overline{k_z(\boldsymbol{k}_\perp)})(z - z_b)}$$

$$+ \widehat{\boldsymbol{E}}_{\boldsymbol{k}_\perp}^+ \cdot \overline{\left(\varepsilon \widehat{\boldsymbol{E}}_{\boldsymbol{k}_\perp}^- \right)} e^{i(k_z(\boldsymbol{k}_\perp) + \overline{k_z(\boldsymbol{k}_\perp)})z - ik_z(\boldsymbol{k}_\perp)z_b - i\overline{k_z(\boldsymbol{k}_\perp)}z_t}$$

$$+ \widehat{\boldsymbol{E}}_{\boldsymbol{k}_\perp}^- \cdot \overline{\left(\varepsilon \widehat{\boldsymbol{E}}_{\boldsymbol{k}_\perp}^+ \right)} e^{-i(k_z(\boldsymbol{k}_\perp) + \overline{k_z(\boldsymbol{k}_\perp)})z + ik_z(\boldsymbol{k}_\perp)z_t + i\overline{k_z(\boldsymbol{k}_\perp)}z_b}$$

$$+ \widehat{\boldsymbol{E}}_{\boldsymbol{k}_\perp}^- \cdot \overline{\left(\varepsilon \widehat{\boldsymbol{E}}_{\boldsymbol{k}_\perp}^- \right)} e^{-i(k_z(\boldsymbol{k}_\perp) - \overline{k_z(\boldsymbol{k}_\perp)})(z - z_t)}$$

$$= \widehat{\boldsymbol{E}}_{\boldsymbol{k}_\perp}^+ \cdot \overline{\left(\varepsilon \widehat{\boldsymbol{E}}_{\boldsymbol{k}_\perp}^+ \right)} \Phi_1(z) + \widehat{\boldsymbol{E}}_{\boldsymbol{k}_\perp}^+ \cdot \overline{\left(\varepsilon \widehat{\boldsymbol{E}}_{\boldsymbol{k}_\perp}^- \right)} \Phi_2(z) + \widehat{\boldsymbol{E}}_{\boldsymbol{k}_\perp}^- \cdot \overline{\left(\varepsilon \widehat{\boldsymbol{E}}_{\boldsymbol{k}_\perp}^+ \right)} \Phi_3(z) + \widehat{\boldsymbol{E}}_{\boldsymbol{k}_\perp}^- \cdot \overline{\left(\varepsilon \widehat{\boldsymbol{E}}_{\boldsymbol{k}_\perp}^- \right)} \Phi_4(z)$$

$$\tag{A.4}$$

To compute the integral over the z dependence we stick to integrating the Φ_i terms

A. Appendix

separately. We note that Φ_2 and Φ_3 are complex conjugates of each other.

$$\int_{z_0}^{z_1} \Phi_1(z)\, \mathrm{d}z = \int_{z_0}^{z_1} e^{i(k_z(\boldsymbol{k}_\perp) - \overline{k_z(\boldsymbol{k}_\perp)})(z - z_b)}\, \mathrm{d}z = \int_{z_0}^{z_1} e^{-2\mathfrak{Im}(k_z(\boldsymbol{k}_\perp))(z - z_b)}\, \mathrm{d}z$$

$$= \begin{cases} \frac{1}{-2\mathfrak{Im}(k_z(\boldsymbol{k}_\perp))}\left[e^{-2\mathfrak{Im}(k_z(\boldsymbol{k}_\perp))(z_1 - z_b)} - e^{-2\mathfrak{Im}(k_z(\boldsymbol{k}_\perp))(z_0 - z_b)} \right] & \text{if } \mathfrak{Im}(k_z(\boldsymbol{k}_\perp)) \neq 0, \\ z_1 - z_0 & \text{if } \mathfrak{Im}(k_z(\boldsymbol{k}_\perp)) = 0. \end{cases}$$

$$\text{(A.5)}$$

$$\int_{z_0}^{z_1} \Phi_2(z)\, \mathrm{d}z = \int_{z_0}^{z_1} e^{i(k_z(\boldsymbol{k}_\perp) + \overline{k_z(\boldsymbol{k}_\perp)})z - i k_z(\boldsymbol{k}_\perp) z_b - i\overline{k_z(\boldsymbol{k}_\perp)} z_t}\, \mathrm{d}z$$

$$= \int_{z_0}^{z_1} e^{2i\mathfrak{Re}(k_z(\boldsymbol{k}_\perp))z} e^{-i k_z(\boldsymbol{k}_\perp) z_b - i\overline{k_z(\boldsymbol{k}_\perp)} z_t}\, \mathrm{d}z$$

$$= \begin{cases} \frac{e^{-i k_z(\boldsymbol{k}_\perp) z_b - i\overline{k_z(\boldsymbol{k}_\perp)} z_t}}{2i\mathfrak{Re}(k_z(\boldsymbol{k}_\perp))}\left[e^{2i\mathfrak{Re}(k_z(\boldsymbol{k}_\perp))z_1} - e^{2i\mathfrak{Re}(k_z(\boldsymbol{k}_\perp))z_0} \right] & \text{if } \mathfrak{Re}(k_z(\boldsymbol{k}_\perp)) \neq 0, \\ e^{-i k_z(\boldsymbol{k}_\perp) z_b - i\overline{k_z(\boldsymbol{k}_\perp)} z_t}(z_1 - z_0) & \text{if } \mathfrak{Re}(k_z(\boldsymbol{k}_\perp)) = 0. \end{cases}$$

$$\text{(A.6)}$$

$$\int_{z_0}^{z_1} \Phi_3(z)\, \mathrm{d}z = \int_{z_0}^{z_1} e^{-i(k_z(\boldsymbol{k}_\perp) + \overline{k_z(\boldsymbol{k}_\perp)})z + i k_z(\boldsymbol{k}_\perp) z_t + i\overline{k_z(\boldsymbol{k}_\perp)} z_b}\, \mathrm{d}z$$

$$= \int_{z_0}^{z_1} e^{-2i\mathfrak{Re}(k_z(\boldsymbol{k}_\perp))z} e^{+i k_z(\boldsymbol{k}_\perp) z_t + i\overline{k_z(\boldsymbol{k}_\perp)} z_b}\, \mathrm{d}z$$

$$= \begin{cases} \frac{e^{+i k_z(\boldsymbol{k}_\perp) z_t + i\overline{k_z(\boldsymbol{k}_\perp)} z_b}}{-2i\mathfrak{Re}(k_z(\boldsymbol{k}_\perp))}\left[e^{-2i\mathfrak{Re}(k_z(\boldsymbol{k}_\perp))z_1} - e^{-2i\mathfrak{Re}(k_z(\boldsymbol{k}_\perp))z_0} \right] & \text{if } \mathfrak{Re}(k_z(\boldsymbol{k}_\perp)) \neq 0, \\ e^{+i k_z(\boldsymbol{k}_\perp) z_t + i\overline{k_z(\boldsymbol{k}_\perp)} z_b}(z_1 - z_0) & \text{if } \mathfrak{Re}(k_z(\boldsymbol{k}_\perp)) = 0. \end{cases}$$

$$\text{(A.7)}$$

$$\int_{z_0}^{z_1} \Phi_4(z)\, \mathrm{d}z = \int_{z_0}^{z_1} e^{-i(k_z(\boldsymbol{k}_\perp) - \overline{k_z(\boldsymbol{k}_\perp)})(z - z_t)}\, \mathrm{d}z = \int_{z_0}^{z_1} e^{2\mathfrak{Im}(k_z(\boldsymbol{k}_\perp))(z - z_t)}\, \mathrm{d}z$$

$$= \begin{cases} \frac{1}{2\mathfrak{Im}(k_z(\boldsymbol{k}_\perp))}\left[e^{2\mathfrak{Im}(k_z(\boldsymbol{k}_\perp))(z_1 - z_t)} - e^{2\mathfrak{Im}(k_z(\boldsymbol{k}_\perp))(z_0 - z_t)} \right] & \text{if } \mathfrak{Im}(k_z(\boldsymbol{k}_\perp)) \neq 0, \\ z_1 - z_0 & \text{if } \mathfrak{Im}(k_z(\boldsymbol{k}_\perp)) = 0. \end{cases}$$

$$\text{(A.8)}$$

List of publications

Articles and Conferences

- Hammerschmidt, M., Lockau, D., Burger, S., Schmidt, F., Schwanke, C., Kirner, S., Calnan, S., Stannowski, B., and Rech, B. (2012). 3D optical modeling of thin-film a-Si/mc-Si tandem solar cells with random textured interfaces using FEM. In *Renewable Energy and the Environment Optics and Photonics Congress*

- Hammerschmidt, M., Lockau, D., Burger, S., Schmidt, F., Schwanke, C., Kirner, S., Calnan, S., Stannowski, B., and Rech, B. (2013). FEM-based optical modeling of silicon thin-film tandem solar cells with randomly textured interfaces in 3D. In *Proc. SPIE*, volume 8620

- Hammerschmidt, M., Lockau, D., Zschiedrich, L., and Schmidt, F. (2014a). Optical modelling of incoherent substrate light-trapping in silicon thin film multi-junction solar cells with finite elements and domain decomposition. In *Proc. SPIE*, volume 8980

- Hammerschmidt, M., Pomplun, J., Burger, S., and Schmidt, F. (2014b). Adaptive sampling strategies for efficient parameter scans in nano-photonic device simulations. In *Proc. SPIE*, volume 8980

- Hammerschmidt, M., Herrmann, S., Pomplun, J., Zschiedrich, L., Burger, S., and Schmidt, F. (2015b). Reduced basis method for Maxwell's equations with resonance phenomena. In *Proc. SPIE*, volume 9630

- Hammerschmidt, M., Herrmann, S., Burger, S., Pomplun, J., and Schmidt, F. (2015a). Reduced basis method for the optimization of nano-photonic devices (submitted). *Optical and Quantum Electronics*

- Becker, C., Wyss, P., Eisenhauer, D., Probst, J., Preidel, V., Hammerschmidt, M., and Burger, S. (2014). 5 x 5 cm² silicon photonic crystal slabs on glass and plastic foil exhibiting broadband absorption and high-intensity near-fields. *Scientific reports*, 4:5886

- Kirner, S., Hammerschmidt, M., Schwanke, C., Lockau, D., Calnan, S., Frijnts, T., Neubert, S., Schopke, A., Schmidt, F., Zollondz, J.-H., Heidelberg, A., Stannowski, B., Rech, B., and Schlatmann, R. (2014). Implications of TCO Topography on Intermediate Reflector Design for a-Si/μc-Si Tandem

A. Appendix

Solar Cells -Experiments and Rigorous Optical Simulations. *IEEE Journal of Photovoltaics*, 4(1):10–15

- Lockau, D., Hammerschmidt, M., Blome, M., and Schmidt, F. (2014a). Optics of thin film solar cells. In Deuflhard, P. and al., E., editors, *MATHEON-Mathematics for Key Technologies*, volume 1, pages 278–279. European Mathematical Society Publishing House, Zuerich, Switzerland

- Lockau, D., Hammerschmidt, M., Haschke, J., Blome, M., Ruske, F., Schmidt, F., and Rech, B. (2014b). A comparison of scattering and non-scattering anti-reflection designs for back contacted polycrystalline thin film silicon solar cells in superstrate configuration. In *Proc. SPIE*, volume 9140

- Burger, S., Gutsche, P., Hammerschmidt, M., Herrmann, S., Pomplun, J., Schmidt, F., Wohlfeil, B., and Zschiedrich, L. (2015). Hp-finite-elements for simulating electromagnetic fields in optical devices with rough textures. In *Proc. SPIE*, volume 9630

Talks

- 24/10/2012: *Modeling of thin-film silicon tandem solar cells with random roughness*, Max Planck Institute for the Science of Light, Erlangen

- 19/2/2013: *Benefits of hp-finite element techniques for simulating solar cells with super-thin layers*, 6th Annual Meeting Photonic Devices, Zuse Institute Berlin (ZIB)

- 17/6/2013: *Vom Licht zum Strom*, Lange Nacht der Wissenschaften, ZIB

- 18/9/2013: *Incoherent domain coupling*, Euro-Regional-Workshop, "Characterization and Modelling of Silicon based Thin-film Solar Cells and Modules", Monschau

- 6/2/2014: *Optical modelling of incoherent substrate light-trapping in silicon thin-film multi-junction solar cells with finite elements and domain decomposition*, SPIE Photonics West 2014, San Franscisco, USA

- 17/2/2014: *A fast method for rigorous incoherent substrate modelling in nano-optics*, 7th Annual Meeting Photonic Devices, ZIB

- 20/5/2014: *Computing incoherent substrate light-trapping in thin-film solar cells with domain decomposition*, Division Seminar, ZIB

- 26/11/2014: *Computational nanooptics for renewable energy research*, ZIB evaluation,ZIB

- 8/12/2014: *Efficient optical simulation of complex nanostructred solar cells with a reduced basis method*, Workshop "Nanostructures for Photovoltaics and Energy Storage", TU Berlin

- 17/2/2015: *A reduced basis method for fast optical simulations*, 8th Annual Meeting Photonic Devices, ZIB

- 10/9/2015: *Reduced basis method for optimization of nano-photonic devices*, Numerical Simulation of Opto-Electronic Devices NUSOD 2015, Taipei, Taiwan

Bibliography

[Abass et al., 2013] Abass, A., Trompoukis, C., Leyre, S., Burgelman, M., and Maes, B. (2013). Modeling combined coherent and incoherent scattering structures for light trapping in solar cells. *Journal of Applied Physics*, 114(3):033101.

[Abdi et al., 2013] Abdi, F. F., Han, L., Smets, A. H. M., Zeman, M., Dam, B., and van de Krol, R. (2013). Efficient solar water splitting by enhanced charge separation in a bismuth vanadate-silicon tandem photoelectrode. *Nature communications*, 4:2195.

[Afonso et al., 2009] Afonso, S. M. B., Lyra, P. R. M., Albuquerque, T. M. M., and Motta, R. S. (2009). Structural analysis and optimization in the framework of reduced-basis method. *Structural and Multidisciplinary Optimization*, 40(1-6):177–199.

[Almroth et al., 1978] Almroth, B. O., Stern, P., and Brogan, F. A. (1978). Automatic choice of global shape functions in structural analysis. *AIAA Journal*, 16(5):525–528.

[Amsallem et al., 2009] Amsallem, D., Cortial, J., Carlberg, K., and Farhat, C. (2009). A method for interpolating on manifolds structural dynamics reduced-order models. *International Journal for Numerical Methods in Engineering*, 80(9):1241–1258.

[Barrault et al., 2004] Barrault, M., Maday, Y., Nguyen, N. C., and Patera, A. T. (2004). An 'empirical interpolation' method: application to efficient reduced-basis discretization of partial differential equations. *Comptes Rendus Mathematique*, 339(9):667–672.

[Becker et al., 2014] Becker, C., Wyss, P., Eisenhauer, D., Probst, J., Preidel, V., Hammerschmidt, M., and Burger, S. (2014). 5 x 5 cm² silicon photonic crystal slabs on glass and plastic foil exhibiting broadband absorption and high-intensity near-fields. *Scientific reports*, 4:5886.

[Benner and Schneider, 2013] Benner, P. and Schneider, J. (2013). Uncertainty Quantification for Maxwell's Equations Using Stochastic Collocation and Model Order Reduction. Preprint MPIMD/13-19, Max Planck Institute Magdeburg.

[Berenger, 1994] Berenger, J.-P. (1994). A perfectly matched layer for the absorption of electromagnetic waves. *Journal of Computational Physics*, 114(2):185–200.

Bibliography

[Bergot et al., 2010] Bergot, M., Cohen, G., and Duruflé, M. (2010). Higher-order Finite Elements for Hybrid Meshes Using New Nodal Pyramidal Elements. *Journal of Scientific Computing*, 42(3):345–381.

[Bergot and Duruflé, 2013] Bergot, M. and Duruflé, M. (2013). High-order optimal edge elements for pyramids, prisms and hexahedra. *Journal of Computational Physics*, 232(1):189–213.

[Bergot and Marc, 2013] Bergot, M. and Marc, M. (2013). Approximation of H(div) with High-Order Optimal Finite Elements for Pyramids, Prisms and Hexahedra. *Communications in Computational Physics*, 14(5):1372–1414.

[Binev et al., 2011] Binev, P., Cohen, A., Dahmen, W., DeVore, R., Petrova, G., and Wojtaszczyk, P. (2011). Convergence Rates for Greedy Algorithms in Reduced Basis Methods. *SIAM Journal on Mathematical Analysis*, 43(3):1457–1472.

[Born and Wolf, 1999] Born, M. and Wolf, E. (1999). *Principles of Optics: Electromagnetic Theory of Propagation, Interference and Diffraction of Light*. Cambridge University Press, 7th edition.

[Braess, 2007] Braess, D. (2007). *Finite Elemente: Theorie, Schnelle Loser und Anwendungen in der Elastizitatstheorie*. Springer-Lehrbuch Masterclass Series. Springer-Verlag Berlin Heidelberg, 3rd edition.

[Bui-Thanh et al., 2008] Bui-Thanh, T., Willcox, K., and Ghattas, O. (2008). Model Reduction for Large-Scale Systems with High-Dimensional Parametric Input Space. *SIAM Journal on Scientific Computing*, 30(6):3270–3288.

[Burger et al., 2015] Burger, S., Gutsche, P., Hammerschmidt, M., Herrmann, S., Pomplun, J., Schmidt, F., Wohlfeil, B., and Zschiedrich, L. (2015). Hp-finite-elements for simulating electromagnetic fields in optical devices with rough textures. In *Proc. SPIE*, volume 9630.

[Campbell and Green, 1987] Campbell, P. and Green, M. A. (1987). Light trapping properties of pyramidally textured surfaces. *Journal of Applied Physics*, 62(1):243.

[Cecot et al., 2003] Cecot, W., Rachowicz, W., and Demkowicz, L. F. (2003). An hp-adaptive finite element method for electromagnetics. Part 3: A three-dimensional infinite element for Maxwell's equations. *International Journal for Numerical Methods in Engineering*, 57(7):899–921.

[Chaturantabut and Sorensen, 2009] Chaturantabut, S. and Sorensen, D. C. (2009). Discrete Empirical Interpolation for nonlinear model reduction. In *Proceedings of the 48h IEEE Conference on Decision and Control (CDC) held jointly with 2009 28th Chinese Control Conference*, pages 4316–4321. IEEE.

156

[Chaturantabut and Sorensen, 2010] Chaturantabut, S. and Sorensen, D. C. (2010). Nonlinear Model Reduction via Discrete Empirical Interpolation. *SIAM Journal on Scientific Computing*, 32(5):2737–2764.

[Chen et al., 2011] Chen, Y., Hesthaven, J. A. N. S., and Maday, Y. (2011). A seamless reduced basis element method for 2D Maxwell's problem: an introduction. In Hesthaven, J. S. and Rønquist, E. M., editors, *Spectral and High Order Methods for Partial Differential Equations*, volume 76 of *Lecture Notes in Computational Science and Engineering*, pages 141–152. Springer Berlin Heidelberg, Berlin, Heidelberg.

[Chen et al., 2008] Chen, Y., Hesthaven, J. S., Maday, Y., and Rodríguez, J. (2008). A monotonic evaluation of lower bounds for inf-sup stability constants in the frame of reduced basis approximations. *Comptes Rendus Mathematique*, 346(23-24):1295–1300.

[Chen et al., 2009] Chen, Y., Hesthaven, J. S., Maday, Y., and Rodríguez, J. (2009). Improved successive constraint method based a posteriori error estimate for reduced basis approximation of 2D Maxwell's problem. *ESAIM: Mathematical Modelling and Numerical Analysis*, 43(6):1099–1116.

[Christesen et al., 2012] Christesen, J. D., Zhang, X., Pinion, C. W., Celano, T. a., Flynn, C. J., and Cahoon, J. F. (2012). Design principles for photovoltaic devices based on Si nanowires with axial or radial p-n junctions. *Nano Letters*, 12(11):6024–6029.

[Deceglie et al., 2012] Deceglie, M. G., Ferry, V. E., Alivisatos, A. P., and Atwater, H. A. (2012). Design of nanostructured solar cells using coupled optical and electrical modeling. *Nano letters*, 12(6):2894–900.

[Demkowicz, 2006] Demkowicz, L. F. (2006). *Computing with hp-ADAPTIVE FINITE ELEMENTS: Volume 1 One and Two Dimensional Elliptic and Maxwell Problems.* Chapman & Hall/CRC Applied Mathematics & Nonlinear Science. CRC Press.

[Demkowicz et al., 2007] Demkowicz, L. F., Kurtz, J., Pardo, D., Paszenski, M., Rachowicz, W., and Zdunek, A. (2007). *Computing with hp-ADAPTIVE FINITE ELEMENTS: Volume II Frontiers: Three Dimensional Elliptic and Maxwell Problems with Applications.* Chapman & Hall/CRC Applied Mathematics & Nonlinear Science. CRC Press.

[Deuflhard and Hohmann, 1993] Deuflhard, P. and Hohmann, A. (1993). *Numerische Mathematik I. Eine algorithmisch orientierte Einführung. (Numerical mathematics I. An algorithmically oriented introduction).* de Gruyter, 2nd edition.

Bibliography

[Dominé et al., 2006] Dominé, D., Bailat, J., Steinhauser, J., Shah, A., and Ballif, C. (2006). Micromorph Solar Cell Optimization using a ZnO Layer as Intermediate Reflector. In *2006 IEEE 4th World Conference on Photovoltaic Energy Conference*, volume 2, pages 1465–1468. IEEE.

[Dominé et al., 2008] Dominé, D., Buehlmann, P., Bailat, J., Billet, A., Feltrin, A., and Ballif, C. (2008). Optical management in high-efficiency thin-film silicon micromorph solar cells with a silicon oxide based intermediate reflector. *physica status solidi (RRL) - Rapid Research Letters*, 2(4):163–165.

[Drohmann et al., 2011] Drohmann, M., Haasdonk, B., and Ohlberger, M. (2011). Adaptive Reduced Basis Methods for Nonlinear Convection–Diffusion Equations. In Fořt, J., Fürst, J., Halama, J., Herbin, R., and Hubert, F., editors, *Finite Volumes for Complex Applications VI Problems & Perspectives*, volume 4 of *Springer Proceedings in Mathematics*, pages 369–377. Springer Berlin Heidelberg, Berlin, Heidelberg.

[Eftang et al., 2010a] Eftang, J. L., Grepl, M. A., and Patera, A. T. (2010a). A posteriori error bounds for the empirical interpolation method. *Comptes Rendus Mathematique*, 348(9-10):575–579.

[Eftang et al., 2010b] Eftang, J. L., Patera, A. T., and Rønquist, E. M. (2010b). An "hp" Certified Reduced Basis Method for Parametrized Elliptic Partial Differential Equations. *SIAM Journal on Scientific Computing*, 32(6):3170–3200.

[Fahr et al., 2011] Fahr, S., Kirchartz, T., Rockstuhl, C., and Lederer, F. (2011). Approaching the Lambertian limit in randomly textured thin-film solar cells. *Optics express*, 19(S4):A865–74.

[Fahr et al., 2009] Fahr, S., Rockstuhl, C., and Lederer, F. (2009). Metallic nanoparticles as intermediate reflectors in tandem solar cells. *Applied Physics Letters*, 95(12):121105.

[Farhat et al., 2014] Farhat, C., Avery, P., Chapman, T., and Cortial, J. (2014). Dimensional reduction of nonlinear finite element dynamic models with finite rotations and energy-based mesh sampling and weighting for computational efficiency. *International Journal for Numerical Methods in Engineering*, 98(9):625–662.

[Ferry et al., 2011] Ferry, V. E., Verschuuren, M. A., van Lare, M. C., Schropp, R. E. I., Atwater, H. A., and Polman, A. (2011). Optimized Spatial Correlations for Broadband Light Trapping Nanopatterns in High Efficiency Ultrathin Film a-Si:H Solar Cells. *Nano Letters*, 11(10):4239–4245.

[Goodman, 2000] Goodman, J. W. (2000). *Statistical optics*. Wiley-Interscience, 1st edition.

[Green et al., 2015] Green, M. A., Emery, K., Hishikawa, Y., Warta, W., and Dunlop, E. D. (2015). Solar cell efficiency tables (Version 45). *Progress in Photovoltaics: Research and Applications*, 23(1):1–9.

[Grepl et al., 2007] Grepl, M. A., Maday, Y., Nguyen, N. C., and Patera, A. T. (2007). Efficient reduced-basis treatment of nonaffine and nonlinear partial differential equations. *ESAIM: Mathematical Modelling and Numerical Analysis*, 41(03):575–605.

[Gutsche, 2014] Gutsche, P. (2014). Convergence Study of the Fourier Modal Method for Nano-optical Scattering Problems in Comparison with the Finite Element Method. Master's thesis, Computational Quantum Physics, Physics, Eberhard Karls University Tübingen.

[Haasdonk et al., 2011] Haasdonk, B., Dihlmann, M., and Ohlberger, M. (2011). A training set and multiple bases generation approach for parameterized model reduction based on adaptive grids in parameter space. *Mathematical and Computer Modelling of Dynamical Systems*, 17(4):423–442.

[Haasdonk et al., 2012] Haasdonk, B., Salomon, J., and Wohlmuth, B. (2012). A Reduced Basis Method for the Simulation of American Options. In *Numerical Mathematics and Advanced Applications 2011*, chapter 11, pages 821–829. Springer Berlin Heidelberg, Berlin, Heidelberg.

[Hammerschmidt et al., 2015a] Hammerschmidt, M., Herrmann, S., Burger, S., Pomplun, J., and Schmidt, F. (2015a). Reduced basis method for the optimization of nano-photonic devices (submitted). *Optical and Quantum Electronics*.

[Hammerschmidt et al., 2015b] Hammerschmidt, M., Herrmann, S., Pomplun, J., Zschiedrich, L., Burger, S., and Schmidt, F. (2015b). Reduced basis method for Maxwell's equations with resonance phenomena. In *Proc. SPIE*, volume 9630.

[Hammerschmidt et al., 2012] Hammerschmidt, M., Lockau, D., Burger, S., Schmidt, F., Schwanke, C., Kirner, S., Calnan, S., Stannowski, B., and Rech, B. (2012). 3D optical modeling of thin-film a-Si/mc-Si tandem solar cells with random textured interfaces using FEM. In *Renewable Energy and the Environment Optics and Photonics Congress*.

[Hammerschmidt et al., 2013] Hammerschmidt, M., Lockau, D., Burger, S., Schmidt, F., Schwanke, C., Kirner, S., Calnan, S., Stannowski, B., and Rech, B. (2013). FEM-based optical modeling of silicon thin-film tandem solar cells with randomly textured interfaces in 3D. In *Proc. SPIE*, volume 8620.

[Hammerschmidt et al., 2014a] Hammerschmidt, M., Lockau, D., Zschiedrich, L., and Schmidt, F. (2014a). Optical modelling of incoherent substrate light-trapping in silicon thin film multi-junction solar cells with finite elements and domain decomposition. In *Proc. SPIE*, volume 8980.

Bibliography

[Hammerschmidt et al., 2014b] Hammerschmidt, M., Pomplun, J., Burger, S., and Schmidt, F. (2014b). Adaptive sampling strategies for efficient parameter scans in nano-photonic device simulations. In *Proc. SPIE*, volume 8980.

[Harbecke, 1986] Harbecke, B. (1986). Coherent and incoherent reflection and transmission of multilayer structures. *Applied Physics B Photophysics and Laser Chemistry*, 39(3):165–170.

[Herman et al., 2014] Herman, A., Sarrazin, M., and Deparis, O. (2014). The fundamental problem of treating light incoherence in photovoltaics and its practical consequences. *New Journal of Physics*, 16(1):013022.

[Hermeline, 2004] Hermeline, F. (2004). A finite volume method for solving Maxwell equations in inhomogeneous media on arbitrary meshes. *Comptes Rendus Mathematique*, 339(12):893–898.

[Hess et al., 2014] Hess, M., Grundel, S., and Benner, P. (2014). Estimating the Inf-Sup Constant in Reduced Basis Methods for Time-Harmonic Maxwell's Equations. Preprint MPIMD/14-19, Max Planck Institute Magdeburg.

[Hesthaven and Warburton, 2010] Hesthaven, J. S. and Warburton, T. (2010). *Nodal Discontinuous Galerkin Methods: Algorithms, Analysis, and Applications (Texts in Applied Mathematics)*. Springer.

[HLRN, 2015] HLRN (2015). Norddeutscher Verbund für Hoch- und Höchstleistungsrechnen (HLRN): The HLRN-III Cray System. `https://www.hlrn.de/home/view/System3/CrayHardware`. Accessed 2015-10-23.

[Hohage et al., 2003a] Hohage, T., Schmidt, F., and Zschiedrich, L. (2003a). Solving Time-Harmonic Scattering Problems Based on the Pole Condition I: Theory. *SIAM J. Math. Anal.*, 35(1):183–210.

[Hohage et al., 2003b] Hohage, T., Schmidt, F., and Zschiedrich, L. (2003b). Solving Time-Harmonic Scattering Problems Based on the Pole Condition II: Convergence of the PML Method. *SIAM J. Math. Anal.*, 35(3):547–560.

[Hollaus et al., 2010] Hollaus, K., Feldengut, D., Schöberl, J., Wabro, M., and Omeragic, D. (2010). Nitsche-type Mortaring for Maxwell's Equations. In *PIERS Proceedings 2010 Cambridge*.

[Huynh and Patera, 2007] Huynh, D. B. P. and Patera, A. T. (2007). Reduced basis approximation and a posteriori error estimation for stress intensity factors. *International Journal for Numerical Methods in Engineering*, 72(10):1219–1259.

[Huynh et al., 2007] Huynh, D. B. P., Rozza, G., Sen, S., and Patera, A. T. (2007). A successive constraint linear optimization method for lower bounds of parametric coercivity and inf-sup stability constants. *Comptes Rendus Mathematique*, 345(8):473–478.

[Iapichino et al., 2012] Iapichino, L., Quarteroni, A., and Rozza, G. (2012). A reduced basis hybrid method for the coupling of parametrized domains represented by fluidic networks. *Computer Methods in Applied Mechanics and Engineering*, 221-222(07):63–82.

[Iapichino et al., 2014] Iapichino, L., Quarteroni, A., Rozza, G., and Volkwein, S. (2014). Reduced basis method for the Stokes equations in decomposable domains using greedy optimization. Universität Konstanz, `http://nbn-resolving.de/urn:nbn:de:bsz:352-279961`.

[IEA, 2015] IEA (2015). A Snapshot of Global PV (1992-2014). Technical report, International Eenergy Agency Photovoltaic Power Systems Programme, `http://www.iea-pvps.org/fileadmin/dam/public/report/technical/PVPS_report_-_A_Snapshot_of_Global_PV_-_1992-2014.pdf`.

[Isabella et al., 2014] Isabella, O., Sai, H., Kondo, M., and Zeman, M. (2014). Full-wave optoelectrical modeling of optimized flattened light-scattering substrate for high efficiency thin-film silicon solar cells. *Progress in Photovoltaics: Research and Applications*, 22(6):671–689.

[Jabbar and Azeman, 2004] Jabbar, M. and Azeman, A. (2004). Fast Optimization of Electromagnetic-Problems: The Reduced-Basis Finite Element Approach. *IEEE Transactions on Magnetics*, 40(4):2161–2163.

[Jäger, 2012] Jäger, K. (2012). *On the Scalar Scattering Theory for Thin-Film Solar Cells*. Phd thesis, TU Delft.

[Jäger et al., 2012] Jäger, K., Fischer, M., van Swaaij, R. A. C. M. M., and Zeman, M. (2012). A scattering model for nano-textured interfaces and its application in opto-electrical simulations of thin-film silicon solar cells. *Journal of Applied Physics*, 111(8):083108.

[Jäger et al., 2015] Jäger, K., Linssen, D. N., Isabella, O., and Zeman, M. (2015). Ambiguities in optical simulations of nanotextured thin-film solar cells using the finite-element method. *Optics Express*, 23(19):A1060.

[Jänich, 2005] Jänich, K. (2005). *Vektoranalysis (Springer-Lehrbuch)*. Springer, 5th edition.

[Joannopoulos et al., 2011] Joannopoulos, J. D., Johnson, S. G., Winn, J. N., and Meade, R. D. (2011). *Photonic Crystals: Molding the Flow of Light (Second Edition)*. Princeton University Press.

[Jovanov et al., 2013] Jovanov, V., Xu, X., Shrestha, S., Schulte, M., Hüpkes, J., Zeman, M., and Knipp, D. (2013). Influence of interface morphologies on amorphous silicon thin film solar cells prepared on randomly textured substrates. *Solar Energy Materials and Solar Cells*, 112:182–189.

Bibliography

[Kettner, 2012] Kettner, B. (2012). *Detection of spurious modes in resonance mode computations: pole condition method.* Phd thesis, Freie Universität Berlin.

[Kirner et al., 2014] Kirner, S., Hammerschmidt, M., Schwanke, C., Lockau, D., Calnan, S., Frijnts, T., Neubert, S., Schopke, A., Schmidt, F., Zollondz, J.-H., Heidelberg, A., Stannowski, B., Rech, B., and Schlatmann, R. (2014). Implications of TCO Topography on Intermediate Reflector Design for a-Si/μc-Si Tandem Solar Cells -Experiments and Rigorous Optical Simulations. *IEEE Journal of Photovoltaics*, 4(1):10–15.

[Knezevic and Peterson, 2011] Knezevic, D. J. and Peterson, J. W. (2011). A high-performance parallel implementation of the certified reduced basis method. *Computer Methods in Applied Mechanics and Engineering*, 200(13-16):1455–1466.

[Kowalczewski et al., 2013] Kowalczewski, P., Liscidini, M., and Andreani, L. C. (2013). Light trapping in thin-film solar cells with randomly rough and hybrid textures. *Optics express*, 21(S5):A808–20.

[Koynov et al., 2006] Koynov, S., Brandt, M. S., and Stutzmann, M. (2006). Black nonreflecting silicon surfaces for solar cells. *Applied Physics Letters*, 88(20):203107.

[Krč et al., 2003] Krč, J., Smole, F., Topič, M., Krč, J., Smole, F., and Topič, M. (2003). Analysis of light scattering in amorphous Si:H solar cells by a one-dimensional semi-coherent optical model. *Progress in Photovoltaics: Research and Applications*, 11(1):15–26.

[Krč et al., 2011] Krč, J., Čampa, A., Luxembourg, S. L., Zeman, M., and Topic, M. (2011). Periodic Structures for Improved Light Management in Thin-film Silicon Solar Cells. *MRS Proceedings*, 1101:1101–KK08–01.

[Krč et al., 2003] Krč, J., Zeman, M., Kluth, O., Smole, F., Topič, M., Krč, J., Zeman, M., Kluth, O., Smole, F., and Topič, M. (2003). Effect of surface roughness of ZnO:Al films on light scattering in hydrogenated amorphous silicon solar cells. *Thin Solid Films*, 426(1-2):296–304.

[Lass and Volkwein, 2013] Lass, O. and Volkwein, S. (2013). POD Galerkin Schemes for Nonlinear Elliptic-Parabolic Systems. *SIAM Journal on Scientific Computing*, 35(3):A1271–A1298.

[Lavrinenko et al., 2014] Lavrinenko, A. V., Laegsgaard, J., Gregersen, N., Schmidt, F., and Soendergaard, T. (2014). *Numerical Methods in Photonics.* CRC Press.

[Leblanc et al., 1994] Leblanc, F., Perrin, J., and Schmitt, J. (1994). Numerical modeling of the optical properties of hydrogenated amorphous-silicon-based p-i-n solar cells deposited on rough transparent conducting oxide substrates. *Journal of Applied Physics*, 75(2):1074.

162

[Lee et al., 2012] Lee, W., Lee, S.-Y., Kim, J., Kim, S. C., and Lee, B. (2012). A numerical analysis of the effect of partially-coherent light in photovoltaic devices considering coherence length. *Opt. Express*, 20(S6):A941—-A953.

[Li and Huang, 2012] Li, J. and Huang, Y. (2012). *Time-Domain Finite Element Methods for Maxwell's Equations in Metamaterials (Springer Series in Computational Mathematics)*. Springer.

[Li, 1996] Li, L. (1996). Formulation and comparison of two recursive matrix algorithms for modeling layered diffraction gratings. *Journal of the Optical Society of America A*, 13(5):1024.

[Lockau, 2012] Lockau, D. (2012). *Optical modeling of thin film silicon solar cells with random and periodic light management textures*. Phd thesis, TU Berlin.

[Lockau et al., 2014a] Lockau, D., Hammerschmidt, M., Blome, M., and Schmidt, F. (2014a). Optics of thin film solar cells. In Deuflhard, P. and al., E., editors, *MATHEON-Mathematics for Key Technologies*, volume 1, pages 278–279. European Mathematical Society Publishing House, Zuerich, Switzerland.

[Lockau et al., 2014b] Lockau, D., Hammerschmidt, M., Haschke, J., Blome, M., Ruske, F., Schmidt, F., and Rech, B. (2014b). A comparison of scattering and non-scattering anti-reflection designs for back contacted polycrystalline thin film silicon solar cells in superstrate configuration. In *Proc. SPIE*, volume 9140.

[Lockau et al., 2013] Lockau, D., Sontheimer, T., Becker, C., Rudigier-Voigt, E., Schmidt, F., and Rech, B. (2013). Nanophotonic light trapping in 3-dimensional thin-film silicon architectures. *Opt. Express*, 21:A42–A52.

[Lockau et al., 2014c] Lockau, D., Sontheimer, T., Preidel, V., Ruske, F., Hammerschmidt, M., Becker, C., Schmidt, F., and Rech, B. (2014c). Advanced microhole arrays for light trapping in thin film silicon solar cells. *Solar Energy Materials and Solar Cells*, 125.

[Lockau et al., 2011] Lockau, D., Zschiedrich, L., Burger, S., Schmidt, F., Ruske, F., and Rech, B. (2011). Rigorous optical simulation of light management in crystalline silicon thin film solar cells with rough interface textures. In *Proc. SPIE*, volume 7933.

[LRZ, 2015] LRZ (2015). LRZ - Leibniz-Rechenzentrum der Bayerischen Akademie der Wissenschaften: SuperMUC Petascale System. `https://www.lrz.de/services/compute/supermuc/systemdescription/`. Accessed 2015-10-23.

[Maday et al., 2007] Maday, Y., Nguyen, N.-C. N., Patera, A. T., and Pau, G. (2007). A general, multipurpose interpolation procedure: the magic points. *Communications on Pure and Applied Analysis*, 8(1):383–404.

Bibliography

[Maday et al., 2002] Maday, Y., Patera, A. T., and Turinici, G. (2002). Global a priori convergence theory for reduced-basis approximations of single-parameter symmetric coercive elliptic partial differential equations. *Comptes Rendus Mathematique*, 335(3):289–294.

[Maday and Rønquist, 2002] Maday, Y. and Rønquist, E. M. (2002). A reduced-basis element method. *Journal of scientific computing*, 17(1-4):447–459.

[Maday and Stamm, 2013] Maday, Y. and Stamm, B. (2013). Locally Adaptive Greedy Approximations for Anisotropic Parameter Reduced Basis Spaces. *SIAM Journal on Scientific Computing*, 35(6):A2417–A2441.

[Mancini and Volkwein, 2013] Mancini, R. and Volkwein, S. (2013). An inverse scattering problem for the time-dependent Maxwell equations: nonlinear optimization and model-order reduction. *Numerical Linear Algebra with Applications*, 20(4):689–711.

[Mavrokefalos et al., 2012] Mavrokefalos, A., Han, S. E., Yerci, S., Branham, M. S., and Chen, G. (2012). Efficient light trapping in inverted nanopyramid thin crystalline silicon membranes for solar cell applications. *Nano letters*, 12(6):2792–6.

[Monk, 2003] Monk, P. (2003). *Finite Element Methods for Maxwell's Equations*. Numerical Mathematics and Scientific Computation. Clarendon Press.

[Moser et al., 2014] Moser, P., Wolf, P., Larisch, G., Li, H., Lott, J. A., and Bimberg, D. (2014). Energy-efficient oxide-confined high-speed VCSELs for optical interconnects. In *Proc. SPIE*.

[NASA, 2015] NASA (2015). Solar System Exploration: Sun - Facts and Figures. `http://solarsystem.nasa.gov/planets/profile.cfm?Display=Facts&Object=Sun`. Accessed 2015-05-20.

[Nedelec, 1980] Nedelec, J. C. (1980). Mixed finite elements in $\mathbb{R}^3$. *Numerische Mathematik*, 35(3):315–341.

[Nolting, 1990] Nolting, W. (1990). *Grundkurs: Theoretische Physik - Elektrodynamik (Band 3)*. Verlag Zimmermann-Neufang, Ulmen, 3 edition.

[Noor and Peters, 1980] Noor, A. K. and Peters, J. M. (1980). Reduced Basis Technique for Nonlinear Analysis of Structures. *AIAA Journal*, 18(4):455–462.

[NREL, 2015] NREL (2015). NREL - Renewable Resource Data Center: Solar Spectra: Air Mass Zero. `http://rredc.nrel.gov/solar/spectra/am0/`. Accessed 2015-06-24.

[Paetzold, 2013] Paetzold, U. W. (2013). *Light trapping with plasmonic back contacts in thin-film silicon solar cells*. PhD thesis, RWTH Aachen.

[Palik, 1998] Palik, E. D. (1998). *Handbook of Optical Constants of Solids*. Academic Press handbook series. Academic Press.

[Paulus and Martin, 2001] Paulus, M. and Martin, O. J. (2001). Green's tensor technique for scattering in two-dimensional stratified media. *Physical review. E, Statistical, nonlinear, and soft matter physics*, 63(6):066615.

[Pfleging et al., 2014] Pfleging, W., Kohler, R., and Pröll, J. (2014). Laser generated microstructures in tape cast electrodes for rapid electrolyte wetting: new technical approach for cost efficient battery manufacturing. In *Proc. SPIE*, volume 8968.

[Pierce and Giles, 2000] Pierce, N. a. and Giles, M. B. (2000). Adjoint Recovery of Superconvergent Functionals from PDE Approximations. *SIAM Review*, 42(2):247–264.

[Pomplun, 2006] Pomplun, J. (2006). *Rigorous FEM-Simulation of Maxwell's Equations for EUV-Lithography Diplomarbeit*. Master's thesis, Freie Universität Berlin.

[Pomplun, 2010] Pomplun, J. (2010). *Reduced basis method for electromagnetic scattering problems*. Phd thesis, Freie Universität Berlin.

[Pomplun et al., 2007] Pomplun, J., Burger, S., Zschiedrich, L., and Schmidt, F. (2007). Adaptive Finite Element Method for Simulation of Optical Nano Structures. *Physica Status Solidi (B)*, 244(10):3419–3434.

[Pomplun and Schmidt, 2010] Pomplun, J. and Schmidt, F. (2010). Accelerated a posteriori error estimation for the reduced basis method with application to 3D electromagnetic scattering problems. *SIAM J. Sci. Comput.*, 32:498–520.

[Prentice, 2000] Prentice, J. (2000). Coherent, partially coherent and incoherent light absorption in thin-film multilayer structures. *Journal of Physics D: Applied Physics*, 33(2000):3139–3145.

[Quarteroni and Valli, 1999] Quarteroni, A. and Valli, A. (1999). *Domain Decomposition Methods for Partial Differential Equations*. Oxford University Press, Oxford, UK, 1st edition.

[Rockstuhl and Lederer, 2009] Rockstuhl, C. and Lederer, F. (2009). Photon management by metallic nanodiscs in thin film solar cells. *Applied Physics Letters*, 94(21):213102.

[Rockstuhl et al., 2007] Rockstuhl, C., Lederer, F., Bittkau, K., and Carius, R. (2007). Light localization at randomly textured surfaces for solar-cell applications. *Applied Physics Letters*, 91(17):171104.

[Rozza et al., 2008] Rozza, G., Huynh, D. B. P., and Patera, A. T. (2008). Reduced Basis Approximation and a Posteriori Error Estimation for Affinely Parametrized Elliptic Coercive Partial Differential Equations. *Archives of Computational Methods in Engineering*, 15(3):229–275.

Bibliography

[Saga, 2010] Saga, T. (2010). Advances in crystalline silicon solar cell technology for industrial mass production. *NPG Asia Materials*, 2(3):96–102.

[Santbergen et al., 2013] Santbergen, R., Smets, A. H. M., and Zeman, M. (2013). Optical model for multilayer structures with coherent, partly coherent and incoherent layers. *Optics express*, 21(S2):A262–7.

[Sarrazin et al., 2013] Sarrazin, M., Herman, A., and Deparis, O. (2013). First-principle calculation of solar cell efficiency under incoherent illumination. *Optics express*, 21(S4):A616–30.

[Schaadt et al., 2005] Schaadt, D. M., Feng, B., and Yu, E. T. (2005). Enhanced semiconductor optical absorption via surface plasmon excitation in metal nanoparticles. *Applied Physics Letters*, 86(6):063106.

[Schädle et al., 2007] Schädle, A., Zschiedrich, L., Burger, S., Klose, R., and Schmidt, F. (2007). Domain decomposition method for Maxwell's equations: Scattering off periodic structures. *Journal of Computational Physics*, 226(1):477–493.

[Schmid et al., 2014] Schmid, M., Andrae, P., and Manley, P. (2014). Plasmonic and photonic scattering and near fields of nanoparticles. *Nanoscale Research Letters*, 9(1):50.

[Schmid and Manley, 2014] Schmid, M. and Manley, P. (2014). Nano- and microlenses as concepts for enhanced performance of solar cells. *Journal of Photonics for Energy*, 5(1):057003.

[Schmidt, 2002] Schmidt, F. (2002). *A New Approach to Coupled Interior-Exterior Helmholtz-Type Problems: Theory and Algorithms*. Habilitation thesis, Freie Universität Berlin.

[Schmitt et al., 2012] Schmitt, S. W., Schechtel, F., Amkreutz, D., Bashouti, M., Srivastava, S. K., Hoffmann, B., Dieker, C., Spiecker, E., Rech, B., and Christiansen, S. H. (2012). Nanowire arrays in multicrystalline silicon thin films on glass: A promising material for research and applications in nanotechnology. *Nano Letters*, 12(8):4050–4054.

[Schur, 1909] Schur, I. (1909). Über die charakteristischen Wurzeln einer linearen Substitution mit einer Anwendung auf die Theorie der Integralgleichungen. *Mathematische Annalen*, 66(4):488–510.

[Sen, 2007] Sen, S. (2007). *Reduced Basis Approximation and A Posteriori Error Estimation for Non-Coercive Elliptic Problems: Application to Acoustics*. PhD thesis, Massachusetts Institute of Technology.

[Shockley and Queisser, 1961] Shockley, W. and Queisser, H. J. (1961). Detailed Balance Limit of Efficiency of p-n Junction Solar Cells. *Journal of Applied Physics*, 32(3):510.

166

[Sommer et al., 2015] Sommer, A., Farle, O., and Dyczij-Edlinger, R. (2015). Certified dual-corrected radiation patterns of phased antenna arrays by offline–online order reduction of finite-element models. *Journal of Computational Physics*, 299:22–44.

[Sprafke and Wehrspohn, 2012] Sprafke, A. N. and Wehrspohn, R. B. (2012). Light Trapping Concepts for Photon Management in Solar Cells. *Green*, 2(4):177–187.

[Stannowski et al., 2013] Stannowski, B., Gabriel, O., Calnan, S., Frijnts, T., Heidelberg, A., Neubert, S., Kirner, S., Ring, S., Zelt, M., Rau, B., Zollondz, J. H., Bloess, H., Schlatmann, R., and Rech, B. (2013). Achievements and challenges in thin film silicon module production. *Solar Energy Materials and Solar Cells*, 119:196–203.

[Taflove and Hagness, 2005] Taflove, A. and Hagness, S. C. (2005). *Computational Electrodynamics: The Finite-Difference Time-Domain Method*. Artech House, 3rd edition.

[Čampa et al., 2013] Čampa, A., Krč, J., and Topic, M. (2013). Two approaches for incoherent propagation of light in rigorous numerical simulations. *Progress In Electromagnetics Research*, 137(February):187–202.

[Čampa et al., 2009] Čampa, A., Krč, J., Topič, M., Krč, J., and Topič, M. (2009). Analysis and optimisation of microcrystalline silicon solar cells with periodic sinusoidal textured interfaces by two-dimensional optical simulations. *Journal of Applied Physics*, 105(8):83107.

[Werner, 2011] Werner, D. (2011). *Funktionalanalysis*. Springer-Lehrbuch. Springer.

[Wirth, 2015] Wirth, H. (2015). Aktuelle Fakten zur Photovoltaik in Deutschland. Technical report, Fraunhofer ISE, `https://www.ise.fraunhofer.de/de/veroeffentlichungen/veroeffentlichungen-pdf-dateien/studien-und-konzeptpapiere/aktuelle-fakten-zur-photovoltaik-in-deutschland.pdf`.

[Wohlmuth, 2000] Wohlmuth, B. I. (2000). A Mortar Finite Element Method Using Dual Spaces for the Lagrange Multiplier. *SIAM Journal on Numerical Analysis*, 38(3):989–1012.

[Wolff et al., 2015] Wolff, S., Jansen, D., Terlinden, H., Kelestemur, Y., Mertin, W., Demir, H. V., Bacher, G., and Nannen, E. (2015). Implementation of graphene multilayer electrodes in quantum dot light-emitting devices. *Applied Physics A*, 120(3):1197–1203.

[Wu, 2000] Wu, J.-J. (2000). Simulation of rough surfaces with FFT. *Tribology International*, 33(1):47–58.

Bibliography

[Würfel, 2009] Würfel, P. (2009). *Physics of Solar Cells: From Basic Principles to Advanced Concepts.* Wiley-VCH, 2nd edition.

[Yablonovitch, 1982] Yablonovitch, E. (1982). Statistical ray optics. *Journal of the Optical Society of America*, 72(7):899.

[Yablonovitch, 1993] Yablonovitch, E. (1993). Photonic band-gap structures. *Journal of the Optical Society of America B: Optical Physics*, 10(2):283–295.

[Yee and Others, 1966] Yee, K. S. and Others (1966). Numerical solution of initial boundary value problems involving Maxwell's equations in isotropic media. *IEEE Trans. Antennas Propag*, 14(3):302–307.

[Yu et al., 2010a] Yu, Z., Raman, A., and Fan, S. (2010a). Fundamental limit of light trapping in grating structures. *Optics express*, 18 Suppl 3:A366–A380.

[Yu et al., 2010b] Yu, Z., Raman, A., and Fan, S. (2010b). Fundamental limit of nanophotonic light trapping in solar cells. *Proceedings of the National Academy of Sciences of the United States of America*, 107(41):17491–6.

[Zaglmayr, 2006] Zaglmayr, S. (2006). *High order finite element methods for electromagnetic field computation.* Phd thesis, Johannes Kepler Universität Linz.

[Zeng et al., 2006] Zeng, L., Yi, Y., Hong, C., Liu, J., Feng, N., Duan, X., Kimerling, L. C., and Alamariu, B. A. (2006). Efficiency enhancement in Si solar cells by textured photonic crystal back reflector. *Applied Physics Letters*, 89(11):111111.

[Zschiedrich, 2009] Zschiedrich, L. (2009). *Transparent boundary conditions for Maxwells equations: numerical concepts beyond the PML method.* Phd thesis, Freie Universität Berlin.

[Zschiedrich et al., 2012] Zschiedrich, L., Greiner, H., Pomplun, J., Hammerschmidt, M., Burger, S., and Schmidt, F. (2012). FEM simulations of light extraction from nanostructured organic light-emitting diodes. In *Renewable Energy and the Environment Optics and Photonics Congress*. OSA.

CURRICULUM VITAE

For reasons of data protection, the Curriculum vitae is not published in the online version